University of Alberta

Performance Evaluation, Wake Study, and Flow Visualization of Air and Large Diameter Water Droplets around the Blade of a Micro Horizontal Axis Wind Turbine

by

Graeme Ian Comyn

A thesis submitted to the Faculty of Graduate Studies and Research
in partial fulfillment of the requirements for the degree of

Master of Science

Mechanical Engineering

Spring 2011
Edmonton, Alberta

Examining Committee

Roger W. Toogood, Mechanical Engineering

Brian A. Fleck, Mechanical Engineering

David S. Nobes, Mechanical Engineering

Mark Loewen, Civil and Environmental Engineering

Abstract

This thesis presents a performance evaluation of a micro horizontal axis wind turbine, investigates the use of particle image velocimetry (PIV) to capture the flow field around a rotating blade and to track water droplets in the flow. The testing was done in a low speed wind tunnel in a highly blocked configuration. The turbine was instrumented to measure rotational speed of the rotor, axial thrust and power output. Wind speed of the wake was measured with a Kiel probe. Performance characteristics were calculated and compared with the manufacturer's published data and to power predictions by axial momentum theories. The turbine was shown to perform well and the manufacturer's published data are accurate. Axial momentum theory over-predicts power by approximately 50%.

It is shown that good PIV results can be obtained using a fog machine to seed the flow. Improved illumination and optics will be required to measure 3D flow close to the blade. Water droplets can be tracked but a shadowgraphy arrangement should be used to better visualize the droplets. The droplets also affect the rotational speed of the rotor such that capturing the blade in a consistent point in the field of view is problematic.

Acknowledgements

I would like to thank my supervisor, Dr. Brian Fleck, and my co-supervisor, Dr. David Nobes, for welcoming me back to academia and providing funding to make it possible. Dr. Fleck's enthusiasm encouraged me and he gave me the freedom to explore my new field of study. Dr. Nobes' practical mentorship took care to focus my goals and ensured my deadlines were met. Together they made a good team and I am proud to have worked with them.

Ray Moon and BMT Fleet Technology were very generous in their support of my career change and the gift of a computer and software.

Of course, I would never have attempted this degree if it were not for Christine. Her constant desire for social change and knack for critical analysis forces me to see the world with new perspectives every day. She challenges us to always think of others and the environment first and it is this that gives me hope that I can practice engineering in an environmentally-friendly way. I am never without her support and encouragement and love. Always love.

Table of Contents

List of Tables

List of Figures

Nomenclature

Variables

A	area of rotor disc
A_0	area of undisturbed streamtube
A_W	area of wake streamtube
B_U	systematic error in wake wind speed measurement
a	axial induction factor
C_{TOR}	coefficient of torque
C_P	coefficient of power
C_T	coefficient of thrust
c	chord length
D	diameter
dt	time separation between PIV image pairs
E	modulus of elasticity
F	force
I	current
I_M	moment of inertia
L	length
M	moment
P	power
P_{atm}	atmospheric pressure
P_d	dynamic pressure
P_s	static pressure
P_t	total pressure
P_U	random error in wake wind speed measurement
Q	peak ratio
R	reaction force
R_{air}	gas constant of air
Ra	radius
Re	Reynold's number
Rs	resistance
r	radial distance from rotor centreline
T	thrust on rotor disc
T_{air}	temperature of air
Tor	rotor torque
T_S	thrust at standard conditions
T_T	thrust at test conditions
TSR	tip speed ratio
U	wind speed through rotor disc
U_0	freestream wind speed
U_a	axial component of wake velocity
U_B	bypass wind speed
U_{rel}	relative wind speed
U_{rot}	blade speed due to rotation
U_W	wake wind speed

U_θ	tangential component of wake velocity
V	voltage
W	drag force
Z	section modulus
α	wake speed ratio
β	ratio of average pressure upstream of rotor to average pressure downstream of rotor
γ	blade angle of attack
ΔU	velocity deficit
δ	power factor
ε	strain
ϵ	ratio of rotor disc area to wind tunnel cross-sectional area
ζ_x	error in measurement x
λ	tip speed ratio
μ	dynamic viscosity
ρ	density
ρ_S	density at standard conditions
ρ_T	density at test conditions
σ	stress
σ_B	bending stress
σ_{Ba}	allowable bending stress
σ_S	shear stress
σ_Y	yield stress
τ	bypass flow ratio
φ	blade angle of twist
ω	rotational speed of rotor

Abbreviations

2D	two-dimensional
3D	three-dimensional
AC	alternating current
BEM	blade element momentum
CCD	charge-coupled device
CFD	computational fluid dynamics
C.L.	centreline
CMM	coordinate measuring machine
DAQ	data acquisition
DC	direct current
DOF	depth of field
FOV	field of view
f#	f-number
IR	infrared
LED	light emitting diode
LWC	liquid water content
MECE	mechanical engineering
MVD	mean volume diameter

NACA	National Advisory Committee for Aeronautics
Nd:YAG	neodymium-doped yttrium aluminum garnet
NPT	national pipe thread
PDF	probability density function
PIV	particle image velocimetry
PTU	programmable timing unit
rms, RMS	root mean square
RPM	revolutions per minute
S.F.	safety factor
SNR	signal-to-noise ratio
STP	standard temperature and pressure
TTL	transistor-transistor logic

1 Introduction

Small wind turbines are generally considered to be machines that generate less than 100 kW of power and micro (or mini) wind turbines are the subset that generate less than 30 kW (eFormative Options, LLC & Entegrity Wind Systems, Inc. 2006). They can be connected to the grid to offset electrical load for rural homes, farms or businesses. They can be connected to battery banks or hybridized with solar or diesel generators for places without access to the grid or where getting access would be extremely expensive, such as in the Arctic or onboard a sailboat. Canada, with its large rural areas and remote northern communities, has the opportunity to expand the number of small wind turbine installations and significantly reduce fossil-fuel based electrical consumption (Marbek Resource consultants Ltd. & GPCo Inc. 2005).

There has been growing public interest in small wind turbines since the late 1990s (Gipe 2004). There are three main reasons for this: environmental, economic, and security (Baring-Gould and Corbus 2007). Not only are people becoming more environmentally conscious but new, stricter regulations are being imposed on the transport and storage of diesel fuel and on the CO_2 emissions from coal-fired generating plants. This and rising costs of fossil fuels are forcing people to seek ways to reduce their consumption.

Remote rural communities must also consider the security of their power generation. If connection to the grid is lost, or the supply of fuel runs out, power might not be restored for a significant amount of time. During the winter in Canada, a power failure could have disastrous results. People are seeking ways to reduce their impact on the environment, save money and to diversify their sources of power and small wind turbines can fill this role.

Small wind turbine installations, however, are not simple systems and there is much to learn. There is a large array of choices and considerations to be made including the type of turbine, tower options, electrical components, placement and noise considerations. In Canada, the cold climate is an additional challenge that is not yet well understood. With the prevalence of diesel generators, there are very few wind turbine installations providing operational feedback (Baring-Gould and Corbus 2007). Material selection, construction, lubrication and increased loading due to air density, ice and snow are all serious factors that need investigation.

Though independent testing of small wind turbines has improved the quality of manufacturer's published data (Gipe 2007) (National Renewable Energy Laboratory 2007) (Huot 2009), the technical specifications and ratings can be confusing to the general public. The optimum practice of wind power systems is still being developed by professionals in the field. A recent study illustrates that most small wind turbine installations produce much less power than predicted (The Cadmus Group, Inc. 2008). This highlights the need for a better understanding of small wind power systems and

their interactions with their electrical components, the surrounding terrain, and environmental conditions to improve reliability and efficiency.

This thesis is part of increasing efforts toward small wind turbine research in the Mechanical Engineering Department at the University of Alberta. Edmonton, Alberta has a long history of cold-weather research and the ultimate goal for this specific project was to begin investigating the problem of icing on wind turbine blades. However, the project started with acquiring a small wind turbine, installing it in the low-speed wind tunnel and evaluating its performance. Along with confirming the manufacturer's performance claims of the turbine, it was decided that the best way to gain understanding in the field was to experience first-hand (through experimentation) the fundamental models of early wind turbine theory.

After this preliminary work was done, then methods could be developed for modern measurement techniques, such as particle image velocimetry (PIV), for future experiments. A method to visualize the air flow around the rotating blades would be useful when designing new blade shapes using the blade element momentum (BEM) methodology, for example. A method to capture images of water droplets impinging and otherwise interacting with the rotating blades would be useful for the study of blade icing. Evaluating the feasibility of setting up these measurement techniques for a turbine in the wind tunnel was part of the work presented here.

1.1 Performance Evaluation and Wake Study

The fundamental expression of a wind turbine's power output uses axial momentum theory across an ideal rotor or actuator disc. This theory ignores wake rotation and heat transfer. The ideal rotor has no drag and an infinite number of blades. The application of this theory led to the Lanchester-Betz limit that demonstrated how the maximum power an ideal rotor can extract from the wind is approximately 59% of the total kinetic energy available in the wind and occurs when the speed of the wake is reduced to 1/3 of the wind speed upstream of the rotor (Hansen 2008).

There have been many attempts to improve upon the axial momentum theory. Glauert included the rotational velocity in the wake and showed that the maximum power extracted by the rotor is reduced as tip speed ratio (λ) decreases. This is because at low rotational speeds of the rotor the tangential component of velocity in the wake is greater (Hansen 2008). The effect of swirl in the wake on the power coefficient is predicted to be small for λ above 5, but the analysis depends on defining the hub vortex, which has not been experimentally measured to date (Wood 2007). A rotor with a finite number of blades has been considered and it is shown that the smaller the number of blades the less power can be extracted from the wind (Okulov and Sørensen 2008). Including the presence of a channel around the ideal rotor has been developed for use with tidal turbines (Garrett and Cummins 2007). However, it can also apply to wind turbines being tested inside wind tunnels. An expression has been developed for

the additional power available to the rotor based on the ratio of the area of the rotor to the cross-sectional area of the channel.

Wind turbine wakes have been measured since the early days of wind turbine research. The primary goal at that time was to examine the effect of a wind turbine's wake on other wind turbines installed in a wind farm. A comprehensive review and discussion of these measurements is available in Vermeer, Sørensen and Crespo (2003). Though the wake measurements for this project used a simple pitot-tube method to measure the wake speed, there have been others that have improved the amount of information that can be extracted from the turbine wake. A numerical analysis to model a wake with momentum sinks is compared to field measurements in Magnusson (1999), and three dimensional velocity components in the wake are measured with hot-wire anemometry in Haans, et al. (2005).

In the experiment of this thesis there were several differences to the axial momentum theory. The main difference was that the rotor was not an ideal rotor. The rotor has a finite number of blades, the blades experience drag and there was a hub. In fact, the hub was large compared to the rotor diameter, with a hub diameter to rotor diameter ratio of 0.246. In addition, flow out of the rotor was not confined to the axial direction; the turbine wake rotates and air moved radially along the blades due to centripetal force and variations in pressure distribution along the blade span (Bertin and Smith 1979). These effects account for a certain amount of energy lost to the rotor that was not accounted for in the Betz theory. Finally, the wind turbine was contained within an enclosed tunnel which caused blockage effects. The restriction prevented the streamtube passing through the rotor from diverging freely, forcing more air through the rotor which caused the turbine to produce more power than if it were in free air.

1.2 Particle Image Velocimetry

Particle image velocimetry (PIV) and Stereo PIV are measurement systems that can capture the instantaneous velocity field of a fluid as images. All that is required is a source of illumination, cameras, a fluid seeded with particles that follow the flow and can scatter light, and a computer to carry out the computations.

PIV and Stereo PIV have become a standard measurement system in the field of fluid mechanics. The equipment required for these measurement systems are readily available and modern computing power is capable of handling large amounts of data in a short amount of time. The equipment can be arranged in many different ways such that researchers are only limited by their ingenuity for determining a method of applying these measurement systems to determine the velocity fields in their experiments. The results obtained are generally considered to be reliable. For these reasons, PIV and Stereo PIV have penetrated the field of fluid mechanics experimentation.

As Willert (1997) points out, the information gathered through PIV and Stereo PIV have greatly improved the understanding of fluid flows. The ability to capture the instantaneous velocity field of a fluid in a relatively short amount of time has allowed researchers to study unsteady flow phenomena and examine both large and small scale structures within the flow. It has also become a very useful tool for validating the results from computational fluid dynamics (CFD) and other numerical method models.

PIV has been used since the early 1990s to measure velocity fields around wind turbines and propellers. Grant, Smith and Liu, et al. (1991) were early pioneers, examining the flow around a wind turbine blade and in the rotor wake in a wind tunnel using a PIV system. Grant, Smith and Infield, et al. (2005) refined their previous work with more modern equipment many years later and even attempted to capture PIV information in the field. Whale and Anderson (1993) and Whale, Anderson and Bareiss et al. (2000) used simple models of wind turbines in a water tank to study the rotor vortex structures in the wake in order to verify numerical model simulations. Becker, et al. (2005) used a PIV system to measure the flow field in the wake of a propeller in a cryogenic wind tunnel. Experiments on wind turbines in wind tunnels using Stereo PIV were not found.

Stereo PIV has, however, been used to study the velocity fields around other types of rotors. Anschau and Mach (2007) examined the wake behind a ship's propeller in a water tank, finding deficiencies in the CFD model that was being used. This is a good example of collecting 3D velocity vectors in a turbine wake but seeding in water flow is not as challenging as in air. The particles can be much larger and therefore more reflective than the small particles required in an air flow. Cho, et al. (2005) use a phase-locking technique to study the flow through the rotating impeller of a multiblade fan. Raffel, et al. (2006) use micro-Stereo PIV to get high-resolution velocity data of the separated flow at the leading edge a helicopter rotor in a wind tunnel. The multiblade fan experiment records data around a rotating machine, but only around the inlet cone and not the individual blades. The helicopter blade was fixed in a wind tunnel and not rotating. The area of interest was a specific part of the blade and used a telescopic lens to resolve small particles in a small field of view. Siddiqui, Hangan and Rasouli (2008) did not measure flow velocities around a rotor but their experiences with Stereo PIV in a wind tunnel while measuring flow velocities over model topography highlighted the problems of tracer particle density. All of these experiments provide accounts of successes and challenges to overcome when planning a Stereo PIV experiment.

1.3 Blade Icing

The interest in adding water droplets into the air flow relates to the issues of rain and icing events on wind turbines. Rain and icing on rotor blades cause many problems for wind turbines in Canada and other northern climates. The primary problem with rain is that the additional mass of water droplets clinging to wind turbine blades causes a significant increase in the minimum wind speed required for start-up (Sharman 2009). Heavy rain can coat the airfoil with a wavy surface and form rivulets that will increase

surface roughness, affect the interaction with the boundary layer, increase drag, and decrease maximum lift coefficient and stall angle of attack (Feo 1997).

Ice accretion on wind turbine blades causes an increase in surface roughness that seriously affects the aerodynamics of the airfoil. Drag can increase 250 to 365% and lift can be reduced by 40% at the blade tip (Hochart, Fortin and Perron 2008). The reduction of torque can stop the turbine altogether. Ice can also break free of the blade, becoming a safety hazard to nearby people and other wind turbines. This can also cause rotor imbalance vibrations that will damage the turbine (Hochart, Fortin and Perron 2008). Even if the turbine can keep running under icing conditions power output will be greatly reduced (Wang, Bibeau and Naterer 2007).

Blade icing usually forms in one of two ways. Glaze ice is a clear, high-density ice that will form in high liquid water content (LWC) atmospheric conditions when the temperature is only a few degrees below 0°C. In this condition, the convection of heat away from the accreting ice by the air flow is not sufficient to remove all the latent heat of the impinging water droplets. The droplet will only partially freeze on impact with the airfoil and the remaining water will run back along the airfoil (Ice Accretion Simulation December 1997). This run-back can subsequently freeze along the surface of the blade, most often on the pressure side. The suction side often remains ice-free except for a short section starting from the leading edge to 15% of blade chord (Bose 1992).

Rime ice is a white, low density ice that forms in low LWC conditions when the temperature is much below 0°C. The droplets freeze completely on impact with the blade surface. This can also occur if snow sticks to the blade surface and the temperature drops to below 0°C. Rime ice tends to break off easier than glaze ice because the additional air between the ice particles reduces the surface area of the bond (Ice Accretion Simulation December 1997).

There are several existing methods that the wind turbine industry uses to protect the machines from icing. Active measures include electrical resistance heating and heating of the blades internally with warm air. These techniques are not entirely desirable because wires in the blades can be subject to high stresses and will break, the heating elements can attract lightning, and often increase surface roughness of the blade. Heating with warm air becomes very inefficient with large blade size. Electrical costs for anti-icing are estimated to be 6-12% or even up to 25% of the maximum power of the turbine. Passive measures include using flexible blades to crack the ice, electro-expulsive techniques to induce vibrations and special coatings to prevent surface bonding. Only the coatings have seen much field testing (Dalili, Edrisy and Carriveau 2009).

Due to a lack of a nucleus to precipitate formation of ice, a cloud can carry large volumes of super-cooled droplets. For airplane airfoils, the vast majority of icing events occur when the mean volume diameter (MVD) of the droplets are less than 20 μm (Ice Accretion Simulation December 1997). However, for wind turbines icing events are common up to MVD of 40 μm (Hochart, Fortin and Perron 2008).

More recently, there has been more interest in super-cooled large droplet ice accretion in the aircraft industry due to some airplane accidents (Papadakis and Bidwell 1996). Large droplets are considered to be 50 to 400 μm diameter or up to 1000 μm if considering freezing drizzle (Ice Accretion Simulation December 1997). Large droplets impinge further back on the airfoil surfaces and contain more water for run-back and thus cause ice accretion to form further back on the airfoils. This ice extends beyond the range of standard anti-icing protection (Addy Jr., Miller and Ide 1996).

Computational simulations of ice accretion are available. LEWICE, CANICE (Morency, Tezok and Paraschivoiu 1999), and SIMPLE (Cao, Zhang and Sheridan 2008) were designed for aircraft wing airfoils. TURBICE was specifically designed for wind turbine airfoils (Makkonen, Laakso and Finstad 2001). These codes have shown good agreement with experimental results and continue to be improved. LEWICE has recently been updated to include large droplet impingement. One of the chief disagreements between the code and experimental results for large droplet icing was that the code assumed that after a droplet splashed at the leading edge, the smaller droplets ejected off the surface were lost to the air flow. However, these smaller droplets often re-impinge on the airfoil further downstream. LEWICE now uses an empirical equation to simulate the re-impingement of splashed droplets (Wright and Potapczuk 1996).

1.4 Objectives

This project has several objectives. First, to evaluate the performance of the small wind turbine that was purchased to act as a test bed for the experiments. Second, the axial momentum analysis of a streamtube through an ideal rotor will be used to calculate the power absorbed by the turbine by measuring the speed of the wake behind the turbine. Third, the three-dimensional velocity field of the flow of air around the rotating wind turbine blade will be measured with stereo particle image velocimetry. Lastly, in order to study the process of blade icing, the interaction of water droplets with the rotating wind turbine blade will be investigated using flow visualization techniques.

2 Wind Turbine Performance Evaluation and Wake Study

The intention of the first experiment with the Ampair 100 wind turbine was to commission the machine and confirm its global characteristics. The power curve of the machine was generated and compared with the manufacturer's published data. In addition, the velocity profile of the near wake was measured. From these data, one-dimensional momentum equations were used to determine the theoretical power extracted from the wind by the rotor. This was compared with the actual power being generated by the machine.

2.1 Experimental Setup

2.1.1 Experimental Apparatus

The Ampair 100 wind turbine was installed in the low-speed wind tunnel in the Department of Mechanical Engineering at the University of Alberta. The wind turbine was instrumented and a Kiel probe was mounted on a traverse system in the wake of the wind turbine. The wind tunnel ran at a constant wind speed while data were recorded. The experiment was repeated at several different wind speeds, from 3 to 25 m/s (7 to 56 mph).

The arrangement of the experiment can be seen in Figures 2.1 and 2.2. The mast of the wind turbine was located at 7.31 m (24'-0") downstream of the wind tunnel contraction. The centre of the wind turbine was located at the centre of the cross sectional area of the wind tunnel. The wind turbine generator output cable was connected to a load bank comprised of two variable-resistance 10 ohm resistors rated for 100 W.

A static-pitot tube was installed 5.21 m (17'-1") upstream of the wind turbine mast at the centre of the cross sectional area of the wind tunnel. This static-pitot tube was connected to a manometer in order to calculate the wind speed as described in Section 2.2.4.

The manometers used were from Dwyer Instruments Inc. For wind speeds up to 20 m/s (45 mph) the manometer with a 25 mm of H_2O full scale range was used. For wind speeds of 25 m/s (56 mph) the manometer with a 2" of H_2O full scale range was used.

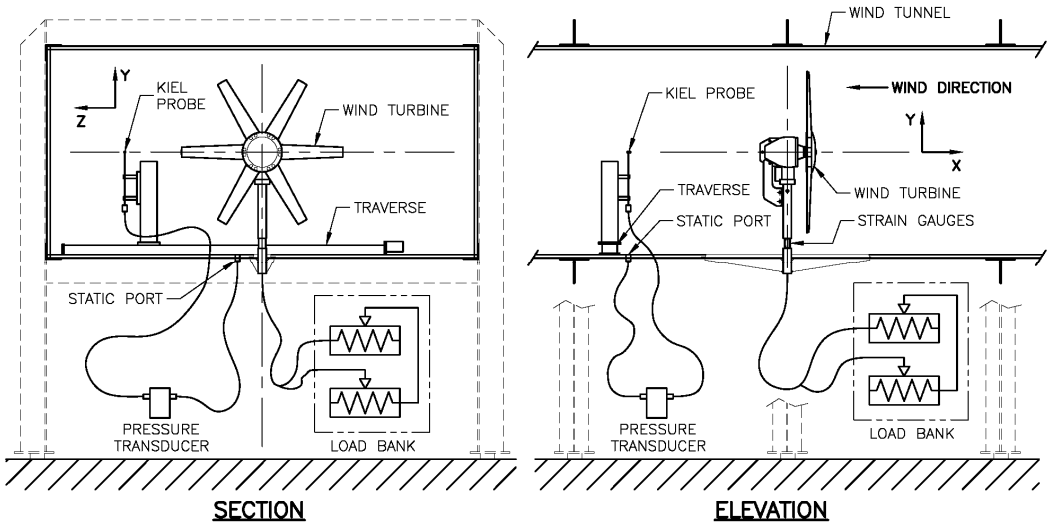

Figure 2.1 - General arrangement of wind turbine wake experiment

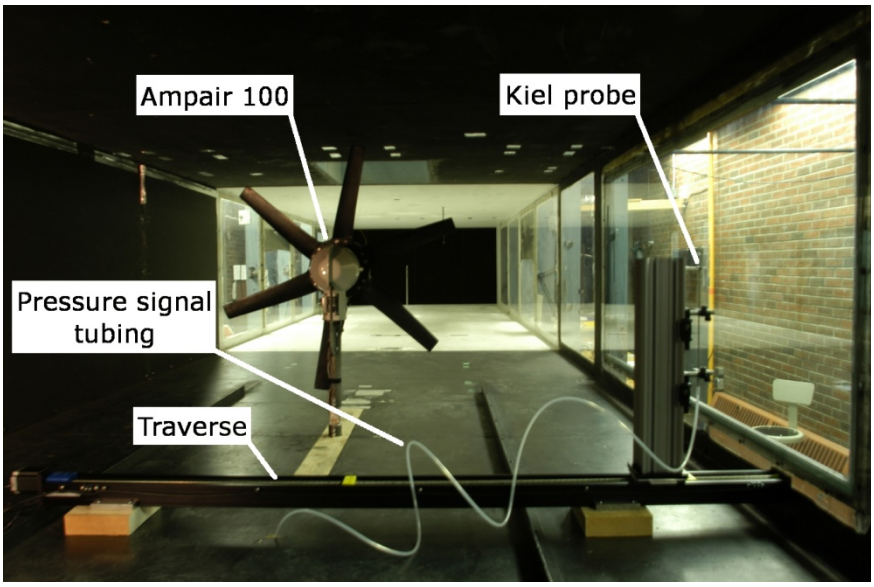

Figure 2.2 - Arrangement of Kiel probe on traverse in wake of wind turbine

Temperature of the air inside the wind tunnel was measured with a thermocouple on a digital readout at approximately 4.25 m (14’-0”) upstream of the mast. The thermocouple wires descended through a hole in the wind tunnel roof and hung in the air flow. Barometric pressure was measured with a mercury barometer located in the building and corrected for the elevation difference between the barometer and the wind tunnel, temperature difference between Standard Temperature and the temperature of the barometer, and for gravity variations (i.e. latitude of Edmonton).

The Kiel probe was mounted on a linear traverse system at one rotor diameter downstream of the wind turbine rotor. This distance was within the ‘near wake’ where

rotor characteristics are still able to be distinguished (Vermeer, Sørensen and Crespo 2003). The head of the Kiel probe was positioned at the same elevation as the centre of the wind turbine rotor. The traverse system could move the Kiel probe laterally from the wind tunnel centerline to the wind tunnel wall. A static port was located flush with the wind tunnel floor at the wind tunnel centerline. The Kiel probe and static port were connected to opposite sides of a differential pressure sensor with hard-walled polypropylene tubing.

2.1.2 Wind Turbine

The Ampair 100 is a horizontal axis wind turbine manufactured by Ampair in the UK and designed for trickle-charging batteries onboard a sailboat. It has a 928 mm (36.5") diameter, 6 -bladed rotor. The diameter of the hub is 228 mm (9"). The glass fibre reinforced polypropylene blades are fixed, tapered and twisted. The generator is rated for 100 W peak output with onboard rectifier circuits for 12 V DC. It uses two 6-pole permanent magnet rotors with stators staggered at 30° to minimize break-out torque (Ampair 2008).

2.1.2.1 *Wind Turbine Blades*

According to the manufacturer, lift and drag data for the specific airfoil shapes of the blades are no longer available. The manufacturer reverse-engineered them and found that near the tip the airfoil had the NACA 4-digit geometry parameters listed in Table 2.1 (Sharman, Personal email 2010).

Table 2.1 - Ampair 100 blade measurements provided by manufacturer

Maximum camber in percent of chord	Distance of max. camber from leading edge in tenths of percent of chord	Maximum thickness of airfoil in percent of chord (2 digits)
5.8	2.6	7.0

The shape of the blade was reverse-engineered using the Mechanical Engineering Department's Coordinate Measuring Machine (CMM). The measurement procedure and details can be found in Appendix A. It was determined from the CMM data that the blade has the characteristics listed in Table 2.2 and shown in Figure 2.3. Blade length in Table 2.2 is considered to be from the outer diameter of the hub, at rotor radius 114 mm (4.5"), to the full rotor radius. From approximately 20% blade length back to the root, the trailing edge begins to curl towards the low pressure side and the camber becomes 3rd order. This can no longer be defined as a NACA airfoil (Bertin and Smith 1979).

Characteristics of NACA airfoils are available online with an applet called JavaFoil (Hepperle 2007). A selection of the parameters calculated for NACA airfoils 6308 are given in Appendix B

Table 2.2 - Ampair 100 blade measurements from CMM

Airfoil location as % length	Chord (mm)	Max. camber as % chord	Distance to max. camber from leading edge in chord 10ths	Max. thickness as % chord	Twist (degrees from rotor plane)	Approx. NACA designation
95% (tip)	58.96	6.05	3.66	8.00	13.18	6308
90%	60.07	5.71	3.71	8.09	13.39	6308
75%	63.63	6.02	3.70	7.68	14.67	6308
50%	71.65	6.70	3.64	9.06	18.02	6309
25%	80.69	6.47	3.35	10.31	21.84	6310
10%	89.78	5.26	2.84	15.46	27.04	Not NACA
0% (root)	97.71	8.46	3.20	26.39	26.72	Not NACA

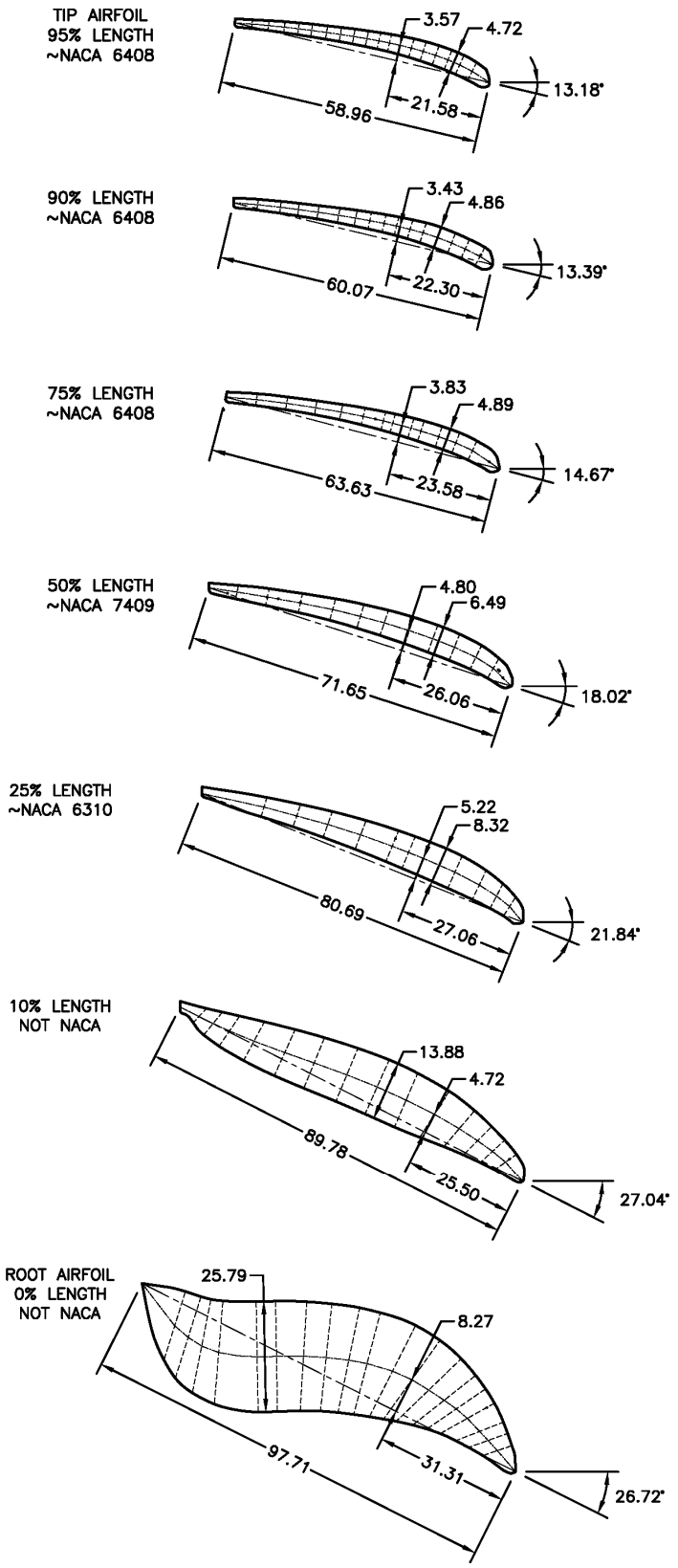

Figure 2.3 - Ampair 100 airfoils along blade length

2.1.3 Wind Tunnel

The low speed wind tunnel used for the experiment is a closed-loop system with a test section of constant rectangular cross section. The test section is 1.22 m (48") high by 2.44 m (96") wide and is approximately 11 m (36'-0") long. Stable winds up to 35 m/s (78 mph) are provided by an axial fan driven by a variable speed 150 kW (200 hp) electric motor. The wind tunnel was characterized in 2001 with a hotwire probe (0.004 mm diameter). From this characterization it was determined that the mean flow profile was essentially constant between boundary layers and turbulence intensity in the tunnel is <0.4% for wind speeds above 2 m/s (4.5 mph) (Johnson 2001).

2.1.3.1 *Static pressure change along test section*

Results obtained through experiments inside a wind tunnel will not be the same as if the measurements were done in free air due to the effects of the boundaries of the test section (Pope and Harper 1966). One such effect is the drop in static pressure along the length of the test section due to the growing boundary layer thickness. The slow moving air of the boundary layer effectively reduces the cross-sectional area of the tunnel. Thus, as the boundary layer grows the wind speed along the length of the test section will increase. Since the speed of the air in the wind tunnel was measured upstream of the wind turbine, this value was corrected for the increase due to the distance to the rotor.

Prior to the wind turbine being installed the wind tunnel was tested to determine the static pressure drop along the length of the test section for different wind speeds. Measurements were taken by a static-pitot pressure probe connected to a manometer. The probe was located at the centerline of the wind tunnel test section. For each wind speed selected at the fan controller, the probe was moved along the length of the test section at 6 different locations listed in Table 2.3.

Table 2.3 - Static pressure test locations

Position	Distance from Wind Tunnel Contraction (m)	Distance from Wind Tunnel Contraction (in.)
1	2.100	82.68
2	3.820	150.39
3	4.768	187.72
4	6.725	264.76
5	8.243	324.53
6	9.743	383.58

At each location, the static pressure was measured against atmospheric pressure by connecting the static port of the probe to one side of the manometer and leaving the

other side open to atmosphere. In addition, the dynamic pressure was measured by connecting both probe ports across the manometer. The velocity in the wind tunnel at each location was calculated using Equation 4 (see Section 2.2.4).

The static pressure along the length of the wind tunnel proved to be a linear relationship indicating a constant drop in pressure along the wind tunnel test section as expected (Pope and Harper 1966). The increase in wind speed in the tunnel due to increasing boundary layer thickness is shown in Figure 2.4. These curves were used to correct for the difference in wind speed from the measurement location to the wind turbine.

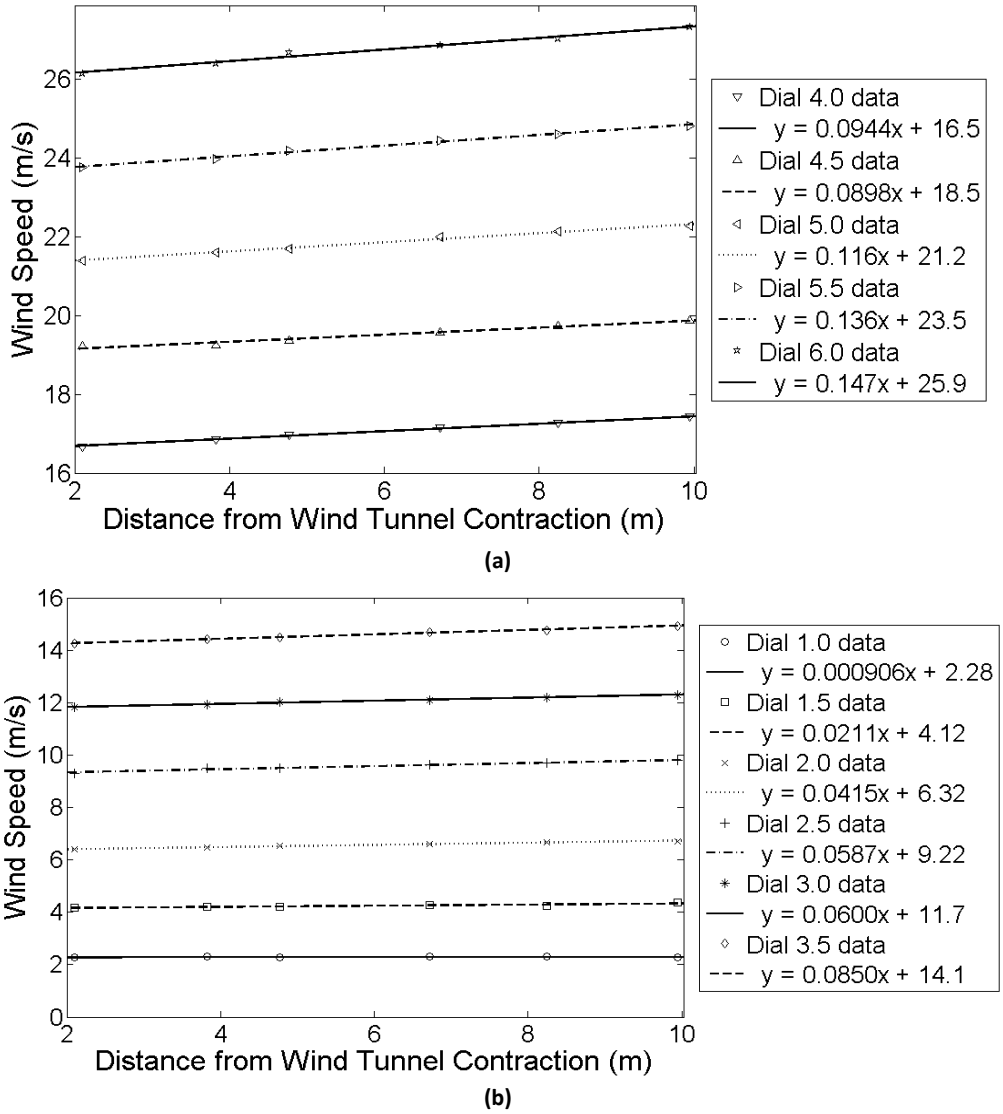

Figure 2.4 – Wind speed increase along wind tunnel test section. (a) shows data measured from wind tunnel dial settings 4.0-6.0 (b) shows data measured from wind tunnel dial settings 1.0-3.5.

2.1.4 Wind Turbine Mast

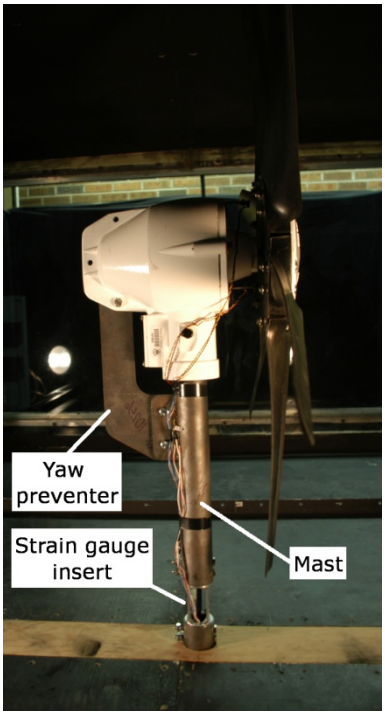

Figure 2.5 - Wind turbine mounted on mast in wind tunnel

There was no existing structure to install a wind turbine in the wind tunnel. A mast for the wind turbine was designed and installed in the wind tunnel for this project. The calculations and construction drawings can be found in Appendix C. A photograph of the final installation is shown in Figure 2.5.

The Ampair 100 wind turbine is mounted on a pipe mast such that the centre of the turbine is at the centre of the wind tunnel test section cross-sectional area. A yaw preventer ensures that the wind turbine faces upstream at all times. An aluminum insert, instrumented with strain gauges, is fitted at the base of the mast in order to measure wind force on the wind turbine.

The location inside the wind tunnel test section was chosen to be at the middle of the existing glass window installed in the side wall. The glass window would allow for clearer view for the cameras of the planned particle image velocimetry (PIV) experiment. At this location there is also a window in the floor of the wind tunnel with an aluminum frame 975 mm (38.375”) long x 152 mm (6”) wide with 21 tapped holes for 5 mm (3/16”) cap screws. The base of the mast was designed to fit this frame. The pipe mast penetrated the base plate and was bracketed from below to avoid obstructions inside the test section of the wind tunnel. The penetration also allowed for the output cable from the wind generator to freely exit the wind tunnel.

The Ampair 100 wind turbine was designed to fit inside a standard 1-1/2" (38 mm) diameter Schedule 40 steel pipe mast. The manufacturer's documentation specifies that the drag due to the wind turbine is about 22 kg (50 lbs) at 50 knots (25 m/s) (Ampair 2008). The stresses in the mast and mounting base plate at this wind force were calculated (see Appendix C) and were found to be acceptable.

The strain gauge insert piece was designed to fit easily into the pipe mast, allow for the generator cable to pass through the middle, and to be flexible enough to register enough strain that can easily be measured at the maximum loading at 25 m/s (56 mph) wind speed. Aluminum 6061-T6 was chosen for its availability and lower modulus of elasticity. The calculations and final dimensions of the insert can be seen in Appendix D and give a section modulus that allows for approximately 840 μstrain at maximum loading.

2.1.5 Electrical Arrangement

It was desirable for the planned PIV experiment that the rotor turn at a constant speed in order to capture images of the blades at the same phase angle. Some variation in speed of rotation was expected due to rotor imbalance, the passage of the generator permanent magnets, and wind tunnel turbulence, but these were expected to be small. If the generator were connected to a battery, the varying load as the battery charged would cause variation in the rotor speed. Therefore, the generator output cable was connected to a resistor load bank. The constant resistance was a constant load on the generator and kept the rotor at a constant speed.

2.2 Instrumentation

The wind turbine was instrumented to measure thrust on the rotor, rotational speed of the rotor, and the power output of the generator. The wind speed in the wind tunnel was measured by a static-pitot tube and manometer. The wind speed in the wake was measured by means of a Kiel probe and pressure transducer. All the signals, except for the wind tunnel speed, were collected by a data acquisition (DAQ) card and recorded by a computer.

2.2.1 Rotor thrust

The rotor thrust was measured by strain gauges mounted on the strain gauge insert piece in the mast. Details of the strain gauge arrangement and calibration are available in Appendix D. A strain gauge conditioner box, shown in Figure 2.6, supplied the bridge with an excitation voltage of 4.987 V and could control the balance and gain of the signal. The gain was set at 8.0 because it resulted in an output voltage of near the maximum 10 V when the maximum weight was applied during calibration. An example of the strain gauge signal recorded during the experiment is shown in Figure 2.7.

Figure 2.6 - Strain gauge insert with conditioner box

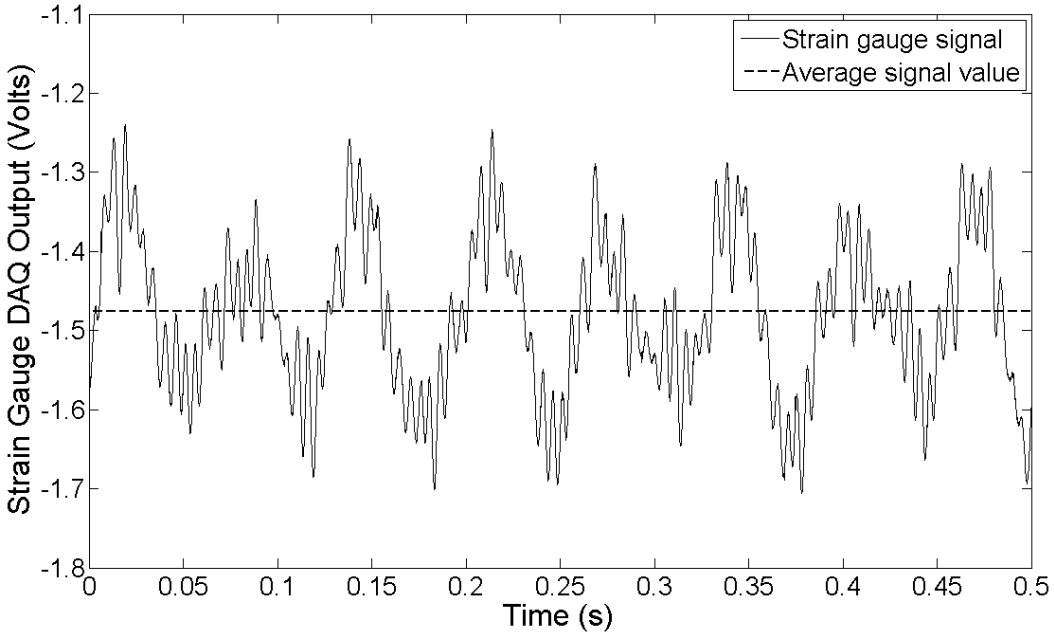

Figure 2.7 - Strain gauge example output signal, 10 m/s wind speed, Kiel probe radial position 18.000" (0.4572 m)

2.2.2 Rotor speed

The rotational speed of the rotor was determined with the use of an absolute position rotary encoder fabricated from two infrared (IR) reflective sensors. The details and specifications of the rotary encoder can be found in Appendix E. The output of the rotary encoder is two signals: one marking a complete revolution of the rotor, and one marking the passing of each blade. The signals are a negative voltage spike, examples of which are shown in Figures 2.8 and 2.9. These figures include the filtering performed by Matlab in order to count the number of revolutions or blade passes. The raw signal is shown in black, the filtered signal is shown in blue, and the minimum peaks are shown as red asterisks.

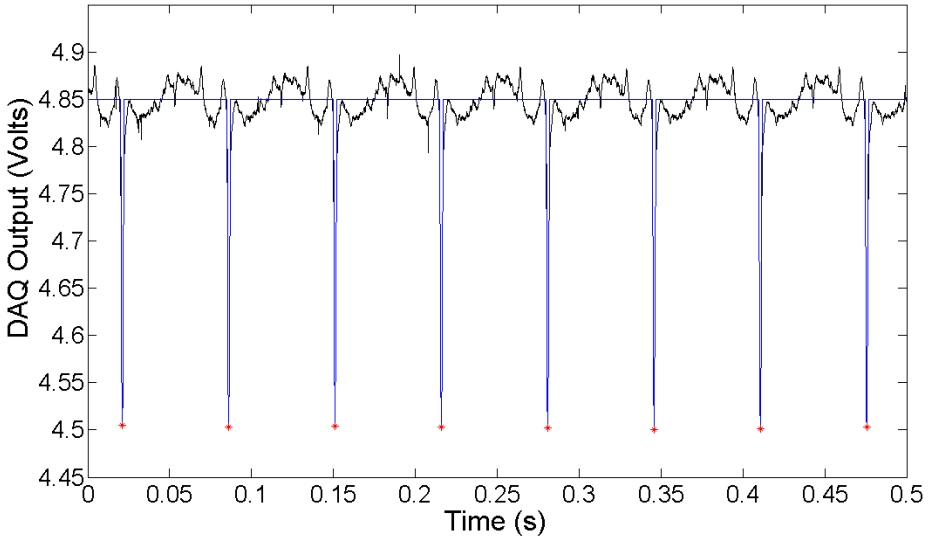

Figure 2.8 - IR sensor detecting full rotor revolution example output signal (in black), with filtering (in blue), 10 m/s wind speed, Kiel probe radial position 18.000" (0.4572 m). Voltage minima are marked with red asterisks.

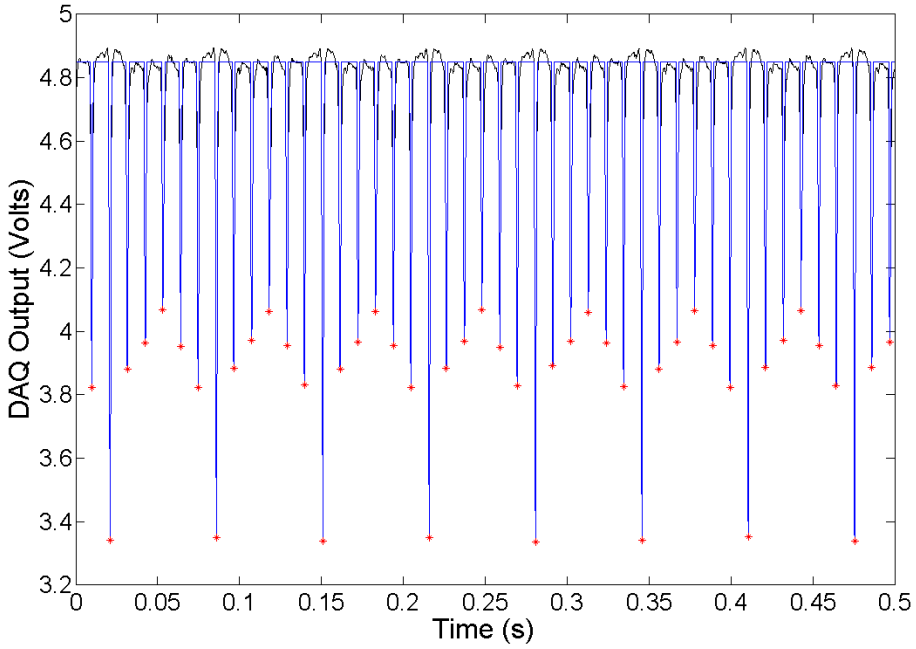

Figure 2.9 - IR sensor detecting blade passes example output signal (in black), with filtering (in blue), 10 m/s wind speed, Kiel probe radial position 18.000" (0.4572 m). Voltage minima are marked with red asterisks.

In order to determine the period of revolution or period of blade passes the points of minimum voltage had to be determined. The time between these minima was the time between revolutions (RPM) or the time between blade passes, depending on the IR sensor. A Matlab function for detecting maximums and minima in a signal (Aguilera

2007) was modified to detect only minima. The signal experienced noise of about ±0.05 V during the time between reflective marks. These local minima had to be ignored in order for Matlab to correctly determine the time between reflective marks. The signal was filtered by choosing a threshold value of 4.75 V for the revolution signal, and 4.60 V for the blade pass signal. When the signal was above this threshold, the signal was replaced with a value of 4.85 V. When the signal was below the threshold, the value of the signal was retained. In this way the signal noise between reflective peaks was replaced with a constant value with no minima that would add erroneously to the count.

For very high DAQ sampling rates there could be several data points recorded during the time it took for the reflective mark to pass the IR sensor. In these cases, signal noise would produce local minima at the bottom of the IR sensor signal spike. These local minima were removed by anticipating the time expected between them. For each wind speed a value was set such that if the time between minima was smaller than the set value they were eliminated from the data set. At a recording rate of 10,000 Hz the value of this threshold for each wind speed is shown in Table 2.4.

Table 2.4 - Time step threshold for each wind speed to avoid false minima when finding blade passes at 10,000 Hz recording rate

Wind Speed		Threshold
(m/s)	(mph)	(time steps @ 10,000 Hz)
3	7	100
4	9	100
5	11	50
6	13	50
7	16	50
8	18	20
9	20	20
10	22	10
15	34	10
20	45	10
25	56	10

2.2.3 Generator power

Each stator of the permanent magnet generator in the wind turbine creates an AC current that is full-wave rectified using a built-in diode bridge. The two stators are 90° out of phase to improve the voltage signal. The result is an approximation of DC current. This output voltage was recorded to calculate the output power from the wind turbine. An example of the voltage signal recorded during the experiment is shown in Figure 2.10.

The generator average output voltage is normally 15 V but the maximum input voltage of the DAQ card was only 10 V. It was therefore necessary to connect two variable (10 Ω maximum) resistors (depicted in Figure 2.11) in series as the load on the generator. If the load on a generator is too small (short-circuit) it will act to brake the generator. If the load is too large the generator will respond with increased voltage to overcome the resistance (Avallone and Baumeister III 1997). The manufacturer's curve of current vs. wind speed (power curve) indicated that the testing had been performed at a constant generator voltage of 15 V. This curve was therefore used to determine what resistance to set the load bank at for each wind speed. Table 2.5 shows the resistance of the load bank for each wind speed. Each resistor was set at half the total resistance required at each wind speed and thus each resistor witnessed half the total voltage. The voltage drop across a single resistor was recorded by the DAQ software. This value was later doubled for voltage drop across the entire load bank, V, and with the known resistance of the load bank, Rs, used to calculate power, P, using Ohm's Law shown in Equation 1.

Table 2.5 - Experimental wind speeds and load bank total resistance

Wind Speed		**Total Load Bank Resistance**
m/s	mph	Ohms
3	7	19.4
4	9	19.4
5	11	15.0
6	13	9.3
7	16	6.6
8	18	5.1
9	20	4.0
10	22	3.5
15	34	2.5
20	45	2.2
25	56	2.1

$$P = VI = \frac{V}{(Rs)^2} \qquad \text{(Eq. 1)}$$

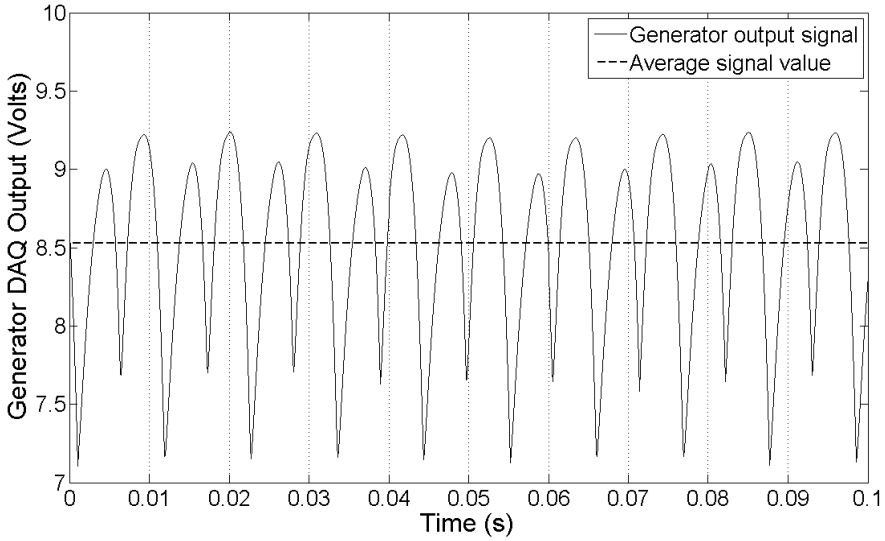

Figure 2.10 - Wind turbine generator example output signal, 10 m/s wind speed, Kiel probe radial position 18.000" (0.4572 m)

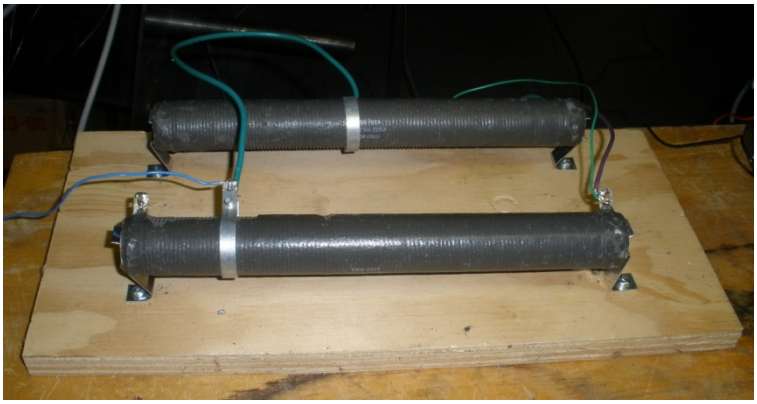

Figure 2.11 - Wind turbine load bank, two variable (10 Ohm max.) resistors connected in series

2.2.4 Wind Tunnel Wind Speed

A static-pitot tube was installed 5.21 m (17'-1") upstream of the wind turbine mast at the centre on the cross sectional area of the wind tunnel. It was connected to a manometer in order to calculate the wind speed inside the tunnel from dynamic pressure.

Total pressure, P_t, is the sum of static pressure, P_s, and dynamic pressure, P_d, as shown in Equation 2.

$$P_t = P_s - P_d \quad \text{(Eq. 2)}$$

$$\text{where } P_d = \frac{1}{2}\rho U_0^2 \quad \text{(Eq. 3)}$$

Total pressure is experienced at the tip of the pitot tube where the air comes to rest. Static pressure is experienced at the ports normal to the flow around the circumference

of the pitot tube tip. Connecting the two ports of the pitot tube across a U-tube manometer gives dynamic pressure as the difference in height between the two liquid columns. Once dynamic pressure is known simple rearrangement of Equation 3 gives the expression for the wind speed in the wind tunnel.

$$U_0 = \sqrt{\frac{2P_d}{\rho}} \quad \text{(Eq. 4)}$$

where U_0 is the velocity in the wind tunnel, P_d is dynamic pressure and ρ is air density defined by the Ideal Gas Law as

$$\rho = \frac{P_{atm}}{R_{air}T_{air}} \quad \text{(Eq. 5)}$$

where P_{atm} is atmospheric pressure, R_{air} is the gas constant for air, and T_{air} is the temperature of the air.

2.2.5 Wake velocity

A Kiel probe was used to measure the wind speed in the rotor wake. Due to the reaction of the forces on the rotor blades, the wake behind the rotor is rotating in the opposite direction of the rotor as well as being carried downstream (Hansen 2008). This motion means the Kiel probe is experiencing the wind direction at a significant angle from the freestream wind direction. A standard pitot tube for calculating air velocity from dynamic pressure change is only accurate for angles of attack up to 5° (United Sensor Corp. 1995). A Kiel probe is a type of pitot tube that measures total pressure at a point but due to a cowling around the probe tip can do so without significant error when the air flow is at a large angle from the direction it is facing. The Kiel probe used in the experiment can measure velocity pressure accurately within a range of ±63° in yaw and ±58° in pitch (United Sensor Corp. 1995). A drawing of the Kiel probe used in this experiment and its specifications can be found in Appendix F. A photograph of the Kiel probe mounted on the traverse system is shown in Figure 2.12.

Figure 2.13 shows a diagram of the velocity components of the wind turbine wake. The air in the wake consists of an axial component, U_a (which is the same as the freestream velocity, U_0, due to conservation of mass), and a tangential component, U_θ. The tangential component is dependent on the blade speed due to rotation, U_{rot}. At high rotational speeds the tangential component of the wake is small. The Kiel probe measures the combined velocity, U_W. Since the axial momentum theory assumes there is no rotation in the wake, the inclusion of the tangential component of the wake velocity will generate some error in the calculated power.

Figure 2.13 also shows angles important for the blade airfoil. The angle of attack of the blade airfoil, γ, is the difference between the blade twist angle, φ, and the angle at which U_{rel} meets the leading edge. The relationships between U_0, U_{rot}, U_{rel} and the blade angles are given in Equations 6, 7 and 8. The Reynolds number, Re, for an airfoil is

given in Equation 9. The lift and drag of an airfoil can be found at a specific Reynolds number and angle of attack.

$$U_{rot} = \pi D \omega \quad \text{(Eq. 6)}$$

where D is the rotor diameter and ω is the rotational speed of the rotor

$$U_{rel} = \sqrt{U_0^2 + U_{rot}^2} \quad \text{(Eq. 7)}$$

$$\gamma = arctan\left(\frac{U_0}{U_{rot}}\right) - \varphi \quad \text{(Eq. 8)}$$

$$Re = \frac{\rho_{air} U_{rel} c}{\mu} \quad \text{(Eq. 9)}$$

where c is the chord length of the airfoil and μ is the dynamic viscosity of air.

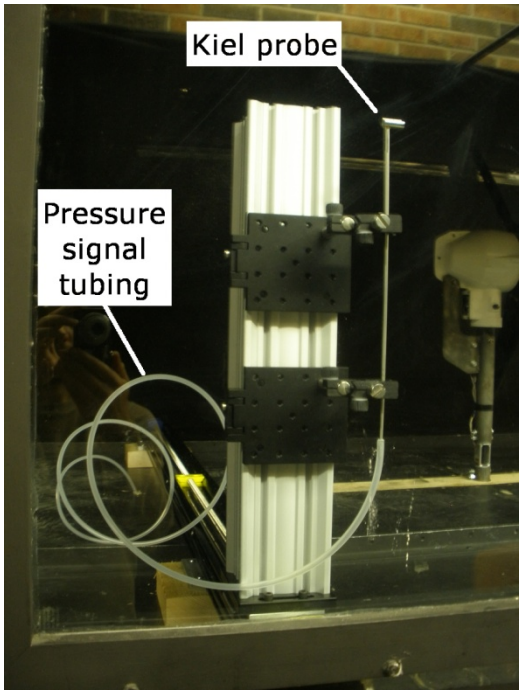

Figure 2.12 - Kiel probe mounted on traverse system to measure wind turbine wake speed

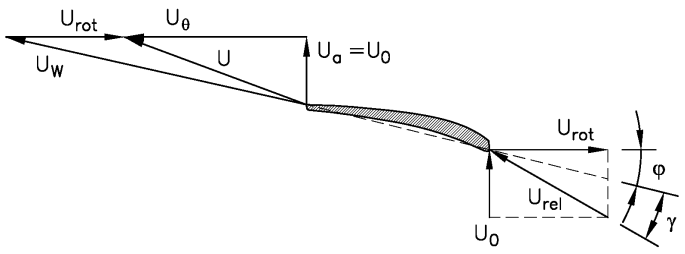

Figure 2.13 - Rotor velocity vectors

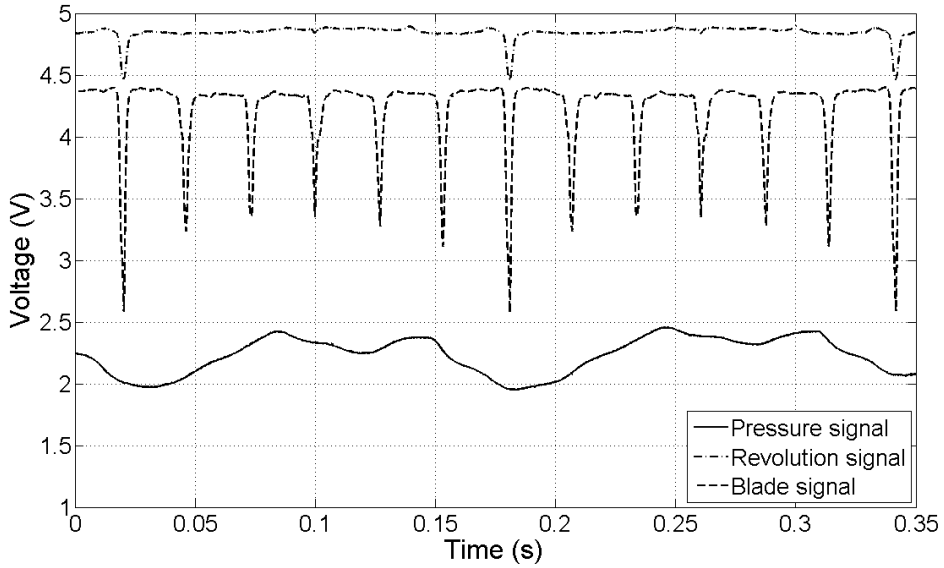

Figure 2.14 - Kiel probe pressure signal at 18.50" (470 mm) from centerline compared to simultaneous IR reflective sensor signals detecting individual blade passes and rotor revolutions. The revolution signal was shifted vertically on the Y-axis for clarity.

Previous wake studies often measure velocity using hot wire anemometry (Vermeer, Sørensen and Crespo 2003) (Haans, et al. 2005). The Kiel probe was used for wind speed measurements instead of hot-wire anemometry for several reasons. Pressure sensors were readily available and easily calibrated. The method of calculating wind speed with pitot tubes is simple and well understood. The fast time response of a hot-wire was not required to measure the average speed of the wake. The slow response time of the Kiel probe is illustrated in Figure 2.14. A distinguishable pressure fluctuation is expected for each blade pass even one rotor diameter downstream where the near wake is transitioning to the far wake. It is clear from the cyclic nature of the pressure signal that the Kiel probe is responding to the rotor but the system is too slow to react to the individual signals of the blades.

The Kiel probe measured total pressure, P_t, but dynamic pressure, P_d, was required to calculate wind speed. In order to measure dynamic pressure, static pressure was measured by a port flush with the floor of the wind tunnel such that the port opening was perpendicular to the direction of flow. The static port was located at the wind tunnel centreline at the same longitudinal location as the Kiel probe. Dynamic pressure was measured directly by connecting the Kiel probe (total pressure) and the static pressure port to opposite sides of a diaphragm-type differential pressure transducer.

The connecting tubing for each side was the same length so that pressure losses through each side were equal. Polypropylene tubing was chosen because it has rigid walls so less damping of the pressure signal would occur than if the tube could expand due to a soft flexible material such as vinyl. Table 2.6 lists the specifications of the tubing.

Table 2.6 - Specifications of pressure transducer signal tubing

Brand	Omega
Model	TYPP-1418-100
Inner Diameter	3.2 mm (1/8”)
Outer Diameter	6.4 mm (1/4”)
Material	polypropylene
Durometer, 15 secs.	75, Shore D
Specific Gravity	0.9
Operating Temperature	-40 to 121 °C (-40 to 250 °F)
Tensile Strength	3700 psig (25,511 kPag)

The pressure sensors used in the experiment were Validyne differential pressure diaphragm type transducers. The pressure ports are on either side of a diaphragm. A difference in pressure across the diaphragm causes it to deform and produces an output voltage proportional to the pressure. As stated above, the two pressure ports were connected to the Kiel probe and the static port in order to measure dynamic pressure for calculating wind speed. The pressure sensors were connected to a conditioning device that adjusted signal gain and offset.

The diaphragms inside the pressure transducers are rated for specific pressure differences. At the maximum wind speed of 25 m/s (56 mph), by Equation 3, a maximum dynamic pressure of 350 Pa (0.0508 psi) was expected. This pressure corresponds to the Validyne model DP45-16. However, in order to maximize the resolution of the voltage signal at low wind speeds three different pressure transducers were used. Table 2.7 indicates which pressure transducer was used for each wind speed.

Table 2.7 - Pressure transducers used for various wind speeds

Wind Speed (m/s)	**Pressure Transducer**	**Pressure range**	**Accuracy**
3-8	Validyne DP103-08	3.56-5.59 mm H_20 (0.14-0.22” H_20)	-0.25% Full Scale, Hysteresis 0.1% pressure excursion
9-20	Validyne DP45-14	13.97-22.61 mm H_20 (0.55-0.89” H_20)	±1% Full Scale
25	Validyne DP45-16	22.61-35.5 mm H_20 (0.89-1.40” H_20)	±1% Full Scale

The pressure transducers were calibrated as described in Appendix G. The pressure transducers were calibrated each time the ports or diaphragms were adjusted, or if the control box settings were changed.

2.3 Data acquisition

Data acquisition (DAQ) and control of the traverse was accomplished by a computer controlled DAQ card and custom software. The custom program, written by summer student Amanda Kotchon using National Instruments LabWindows/CVI development software, allowed data acquisition at a series of points in space to be visited by the traverse. The program also controlled the speed of data acquisition and the number of samples to be collected.

The card used was a National Instruments 6052 Series E connected to a National Instruments shielded desktop connector block model SCB-68. The DAQ card characteristics are listed in Table 2.8. The maximum sampling rate of the card (333 kS/s) was split between the 5 input signals: pressure transducer, strain gauges, IR reflective sensors (2), and turbine output voltage. Therefore the maximum sampling rate of each channel was 66.6 kHz, however, from experimentation the maximum frequency of the traverse/DAQ program was 10 kHz on each channel.

Table 2.8 - Specifications of DAQ card

Brand	National Instruments
Model	6052 series E
Bus	PCI, PXI, FireWire
Max Sampling rate	333 kS/s
Analog Inputs	16 SE / 8 DI
Input Resolution	16 bits
Input Range	±0.05 to ±10 V
Analog Outputs	2
Output Resolution	16 bits
Output rate	333 kS/s
Output Range	±10 V
Digital I/O	8
Counter/Timers	2

The experiment was repeated three times at different sampling rates. The initial data collection was 1000 samples at 1000 Hz on each channel. Once it was determined that good data were being collected by the system, a new set of data of 10,000 samples at 5,000 Hz on each channel was collected. Data collection was again successful. Trials run at 30,000 and 20,000 Hz sampling rate on all channels resulted in random numbers. The trial at 10,000 Hz on all channels recorded data successfully so all further experiments

were carried out at this sampling rate. In addition, the frequency response of the pressure transducers were 1st order and so 10,000 Hz sampling rate would be sufficiently high enough to be above the cutoff frequency of the measurement system.

The results from the three different sampling rates were compared to determine the effect of sampling rate. Force, power and rotor speed measurements all had similar results as shown in Figure 2.15. The variation in power at 20 m/s (45 mph) between 1,000 Hz and higher sampling rates is probably not due to sampling rate. The wind tunnel produces highly variable results at this wind speed in this configuration so no trends can be concluded from the data.

The Kiel probe measurements taken at 1,000 Hz had noticeable variation from higher sampling rates, as can be seen in Figure 2.16. However, the difference between 5,000 Hz and 10,000 Hz sampling rates were small. This suggests that increasing the sampling rate above 10,000 Hz would not significantly increase the accuracy of the experiments.

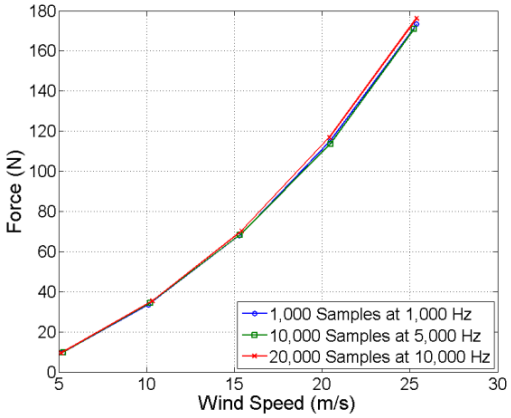

(a) Force measured by strain gauges.

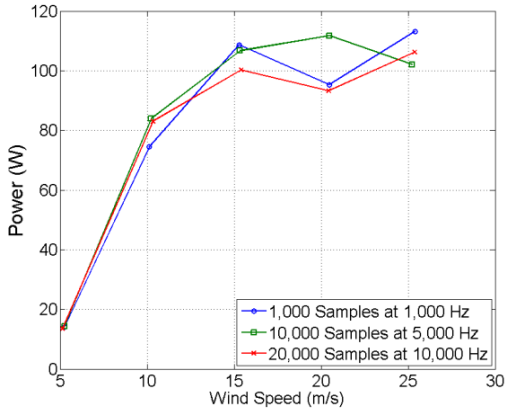

(b) Power, calculated from voltage across load bank.

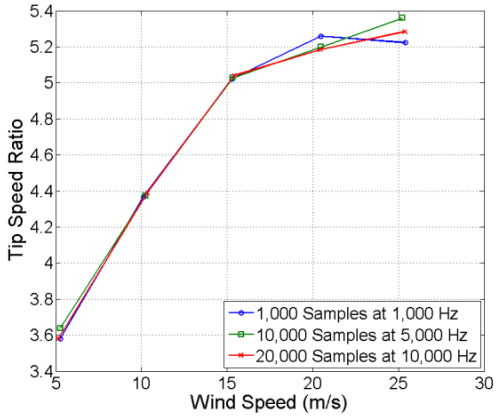

(c) Tip speed ratio, calculated from IR sensors.

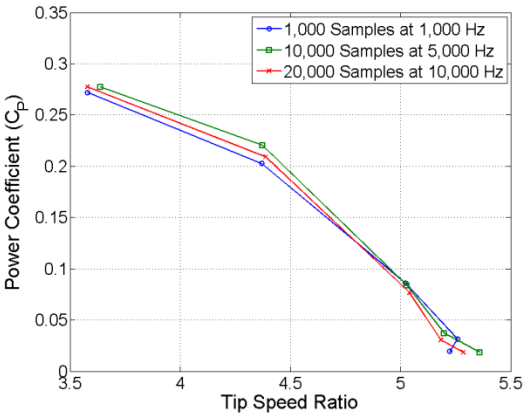

(d) Power coefficient

Figure 2.15 – Comparisons of results at different sampling rates.

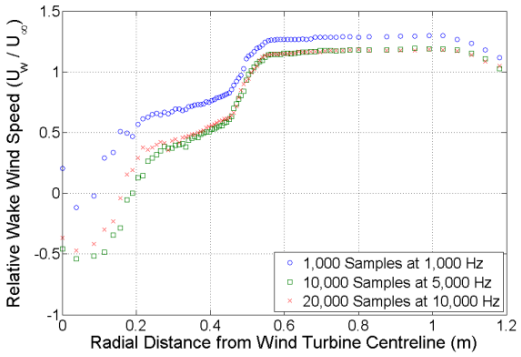

(a) U_0 = 5 m/s nominal

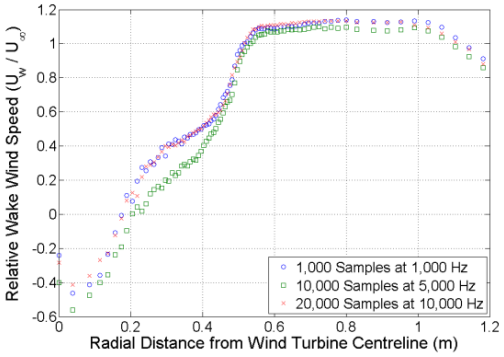

(b) U_0 = 10 m/s nominal

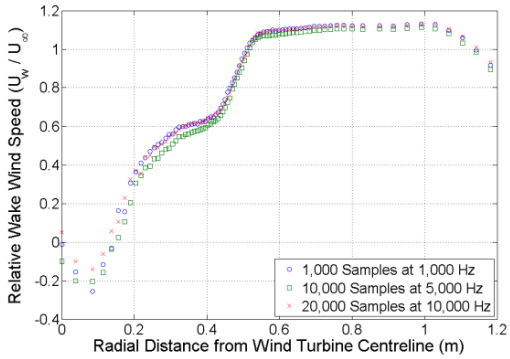

(c) U_0 = 15 m/s nominal.

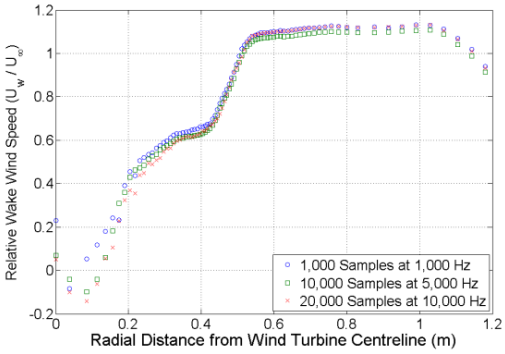

(d) U_0 = 20 m/s nominal

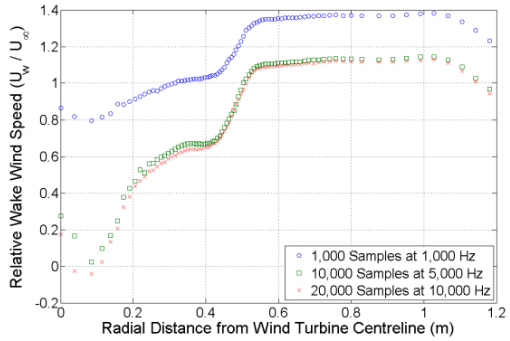

(e) U_0 = 25 m/s nominal

Figure 2.16 - Comparison of Kiel probe data at different sampling rates.

The points at which the probe was stopped for data acquisition were arranged to allow for more points to be sampled near the blade tip where the most change in readings were expected. Sampling density could be reduced near the hub and far beyond maximum rotor radius where less change in measurements were expected. The points were arranged as follows. Starting at 457 mm (18”), which is located near the wind turbine blade tip radius, the next adjacent point was chosen as 6 mm (1/4”) towards rotor centreline. These points can be considered radius points of concentric circles centred at the rotor centre. The area of the ring between these two points was used to determine the pattern of points toward the centreline. Each successive radius point was determined by moving inward an amount such that the difference in area between

adjacent circles would be equal. Moving outward from 457 mm (18”) to the wind tunnel wall the points were mirrored about the 457 mm (18”) point. Outward from 914 mm (36”) the steps became a constant 38 mm (1.5”) until the final point at 1181 mm (46.5”). The complete list of points can be found in Appendix H and the general layout is shown in Figure 2.17.

At each point the DAQ/traversing program stopped the traverse and recorded data from all 5 channels. The sampling rate and number of points were generally chosen to record data for 2 seconds. This allowed the rotor to make a number of revolutions, and 6 times as many identical blade passes, to average over. The numbers ranged from 6 revolutions or 36 blade passes at 3 m/s (7 mph) to 91 revolutions or 546 blade passes at 25 m/s (56 mph). The data were saved as text files which were processed by a custom Matlab script to calculate the wind turbine characteristics. An example of the Kiel probe pressure signal for one radial location is shown in Figure 2.18.

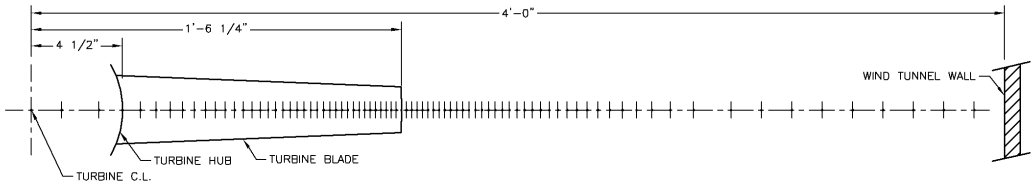

Figure 2.17 - Kiel probe radial measurement locations

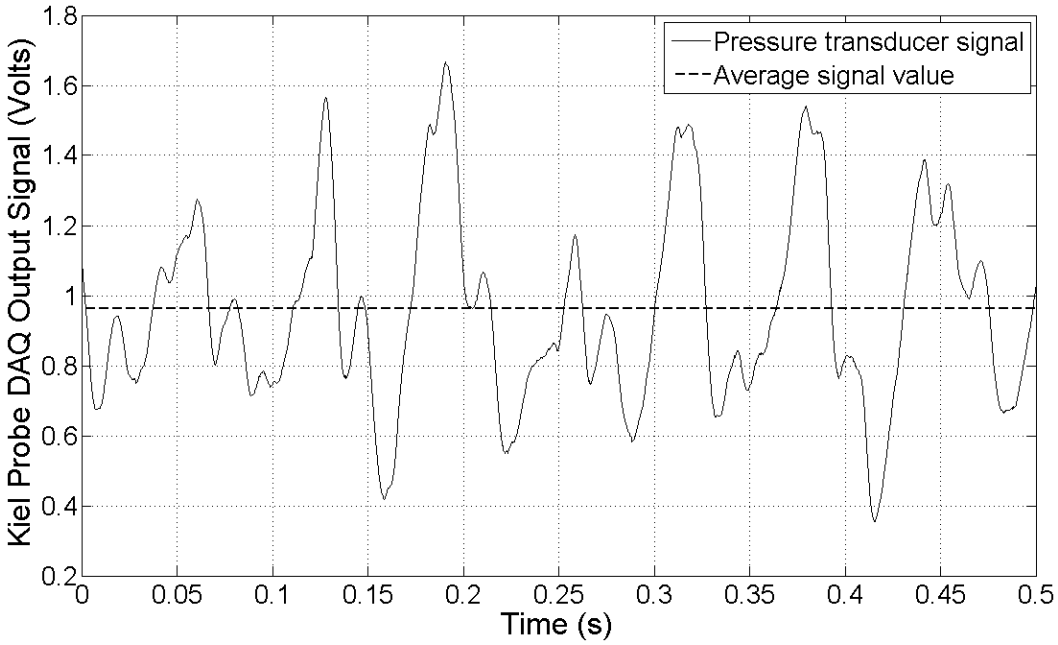

Figure 2.18 - Kiel probe example output signal, 10 m/s wind speed, Kiel probe radial position 18.000" (0.4572 m)

2.3.1 Matlab Processing

The data collected by the DAQ system were processed using custom MATLAB scripts. The complete scripts can be found in Appendix I.

2.4 Measurements/Results

The experiment was set up to accomplish two things. First, measure the global characteristics of the wind turbine and, second, map the average speed of the wind turbine wake. The global characteristics were compared to those given by the manufacturer to confirm that it was working correctly for future experiments. Information about the wake was used to calculate the theoretical power extracted from the wind by the rotor. This was compared to the power generated by the wind turbine.

2.4.1 Rotor Speed

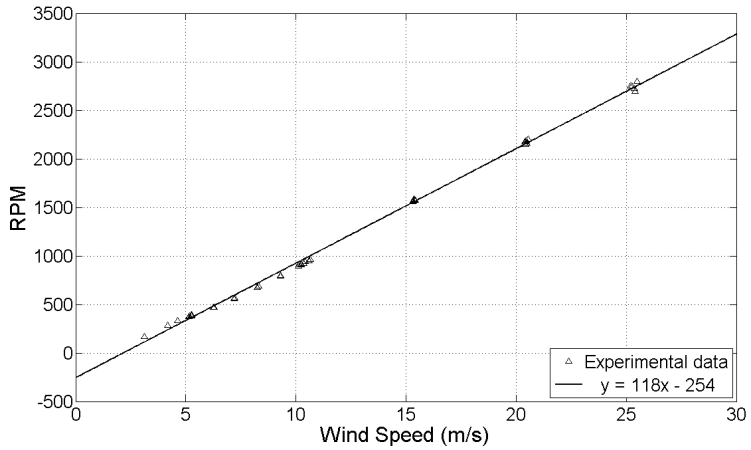

Figure 2.19 - Ampair 100 RPM vs. Wind Speed

The rotor revolution signal was used to calculate revolutions per minute. Revolution speed is plotted against wind speed in Figure 2.19. Rotor speed is a linear function of wind speed.

The signal measuring the time between blades is presented as probability density functions (PDF) in Figure 2.20. The highest peak of the PDF represents the most probable rotor revolution speed, and the spread represents the variation in rotor speed. At very low speeds there are 6 distinct peaks which is most likely due to the 6 permanent magnets in the generator. At low rotor speeds the magnetic attraction of the poles to the rotor are clearly interfering with smooth running of the generator. At higher speeds the inertia of the rotor is much less affected by the magnets. The very low counts noticeable in the 25 m/s (56 mph) wind speed data are errors due to false minima in the signal that were not filtered out by the Matlab script.

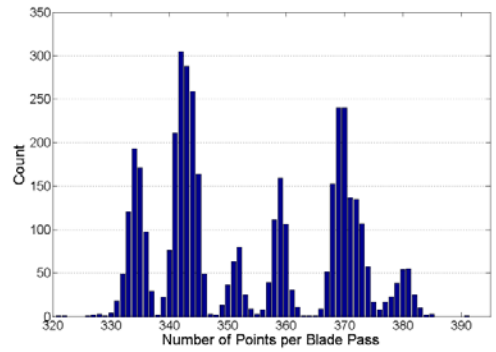

(a) 4 m/s nominal wind speed

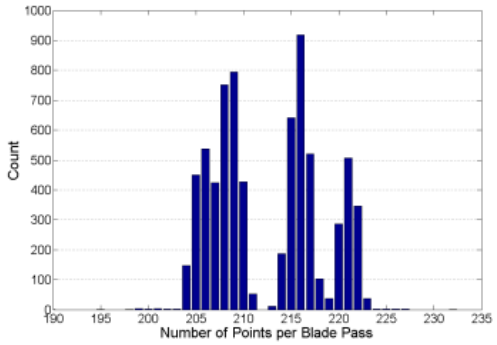

(b) 6 m/s nominal wind speed

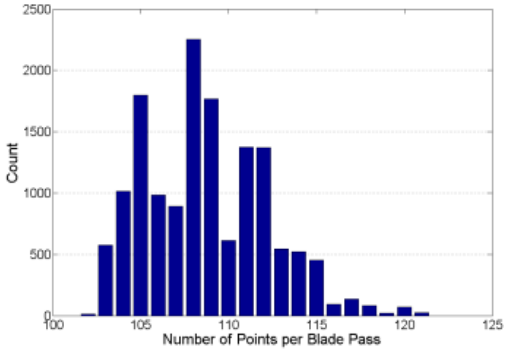

(c) 10 m/s nominal wind speed

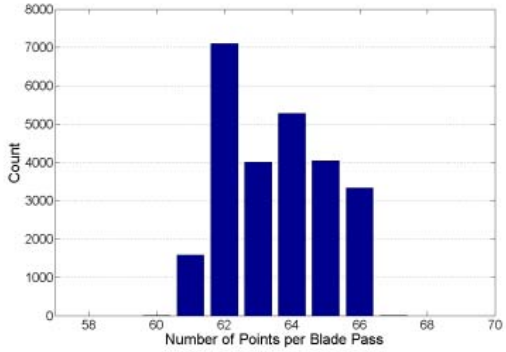

(d) 15 m/s nominal wind speed

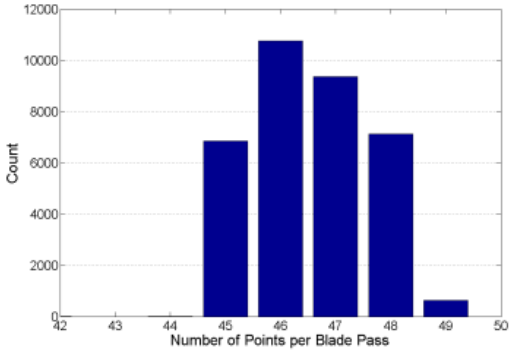

(e) 20 m/s nominal wind speed

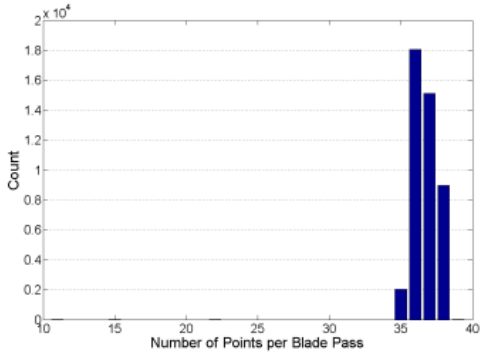

(f) 25 m/s nominal wind speed

Figure 2.20 - Rotor rotation probability density functions counting number of blade passes over 2 seconds.

2.4.1.1 *Airfoil Parameters*

Important airfoil parameters based on rotor speed are shown in Table 2.9 for all experiment runs. Many of the parameters are dependent on radial distance from turbine centerline but only the values at the blade tip (D = 0.928 mm) are presented. Dynamic viscosity of air was taken to be 1.983x10^{-5} kg/m s for the temperature range in the wind tunnel from 20-30°C.

It can be seen from Table 2.9 that the angle of attack is very close to zero degrees for freestream wind speeds above 5 m/s (11 mph). In fact, the calculated angles of attack (using Equation 8) become negative above freestream wind speeds above 9 m/s (20 mph), which suggests that, if the measurements from the CMM were accurate, the blade twist is too much at these wind speeds. The change to negative angles of attack could explain the discontinuity in bypass speeds around 9 m/s and increase in wake speeds above 9 m/s shown in Figure 2.24.

Table 2.9 - Ampair 100 blade tip airfoil parameters

Sample Rate	Nominal Wind Speed	U_0	ω	U_{rot}	U_{rel}	ρ_{air}	γ	Re
(Hz)	(m/s)	(m/s)	(RPM)	(m/s)	(m/s)	(kg/m^3)	(degrees)	
1000	5	5.26	381.7	18.55	19.28	1.051	2.65	5.800×10^4
1000	10	10.13	896.2	43.55	44.71	1.045	-0.08	1.354×10^5
1000	15	15.30	1556.5	75.63	77.16	1.045	-1.74	2.351×10^5
1000	20	20.47	2185.3	106.18	108.14	1.038	-2.27	3.279×10^5
1000	25	25.39	2693.5	130.88	133.32	1.053	-2.20	4.100×10^5
5000	5	5.26	387.7	18.84	19.56	1.053	2.42	5.902×10^4
5000	10	10.24	906.9	44.07	45.24	1.049	-0.10	1.375×10^5
5000	15	15.34	1562.4	75.92	77.45	1.045	-1.76	2.360×10^5
5000	20	20.49	2162.4	105.07	107.05	1.037	-2.14	3.424×10^5
5000	25	25.24	2747.7	133.51	135.87	1.024	-2.47	4.068×10^5
10000	3	3.11	167.7	8.15	8.72	1.059	7.71	2.567×10^4
10000	4	4.17	283.0	13.75	14.37	1.059	3.69	4.333×10^4
10000	5	5.14	373.0	18.12	18.84	1.058	2.65	5.705×10^4
10000	6	6.27	470.4	22.86	23.70	1.058	2.16	7.195×10^4
10000	7	7.18	558.6	27.14	28.07	1.059	1.64	8.552×10^4
10000	8	8.24	685.6	32.83	33.84	1.058	0.91	1.033×10^5
10000	9	9.29	790.0	38.39	39.49	1.063	0.42	1.214×10^5
10000	10	10.34	919.8	44.69	45.87	1.062	-0.15	1.412×10^5
10000	15	15.41	1574.4	76.50	78.04	1.057	-1.79	2.406×10^5
10000	20	20.42	2148.8	104.41	106.39	1.056	-2.11	3.280×10^5
10000	25	25.38	2724.6	132.39	134.80	1.049	-2.33	4.132×10^5

2.4.2 Thrust

The drag force acting on the wind turbine at different wind speeds is shown in Figure 2.21. The values for drag force on the entire wind turbine include thrust on rotor blades, hub and mast measured by the strain gauges. Also shown are drag force measurements done with the rotor blades removed. Subtracting the curve of the hub and mast alone from the curve with the rotor blades included gives an expression of the drag force of the rotor alone.

Thrust is a function of air density and, since wind turbine testing is required to correct for standard temperature and pressure (STP) (British Wind Energy Association 2008), the measured thrust was corrected by

$$T_S = T_T \frac{\rho_S}{\rho_T} \quad \text{(Eq. 10)}$$

where T_S is the thrust at standard conditions, T_T is the thrust at test conditions, ρ_S is the density of air at standard conditions and ρ_T is the density of air at test conditions.

The manufacturer indicates that the drag due to the turbine is 22 kg (216 N) at 25 m/s wind speed (Ampair 2008). From the experimental results the drag on the entire turbine at 25 m/s is 200 N.

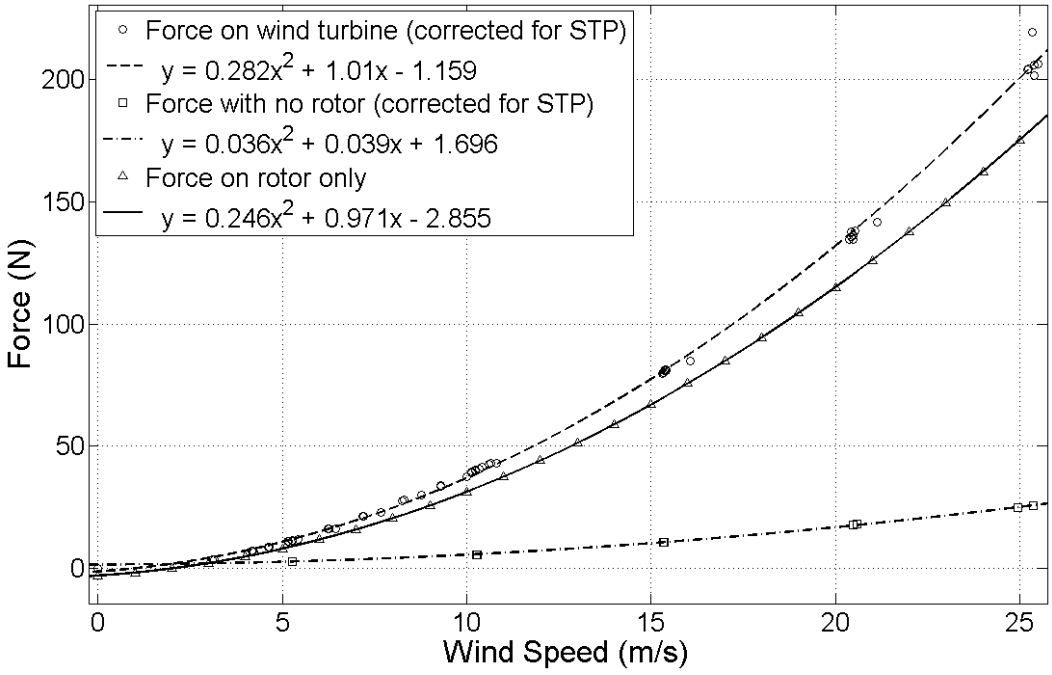

Figure 2.21 - Ampair 100 force curve. Estimated error ±1.5 N.

2.4.3 Current

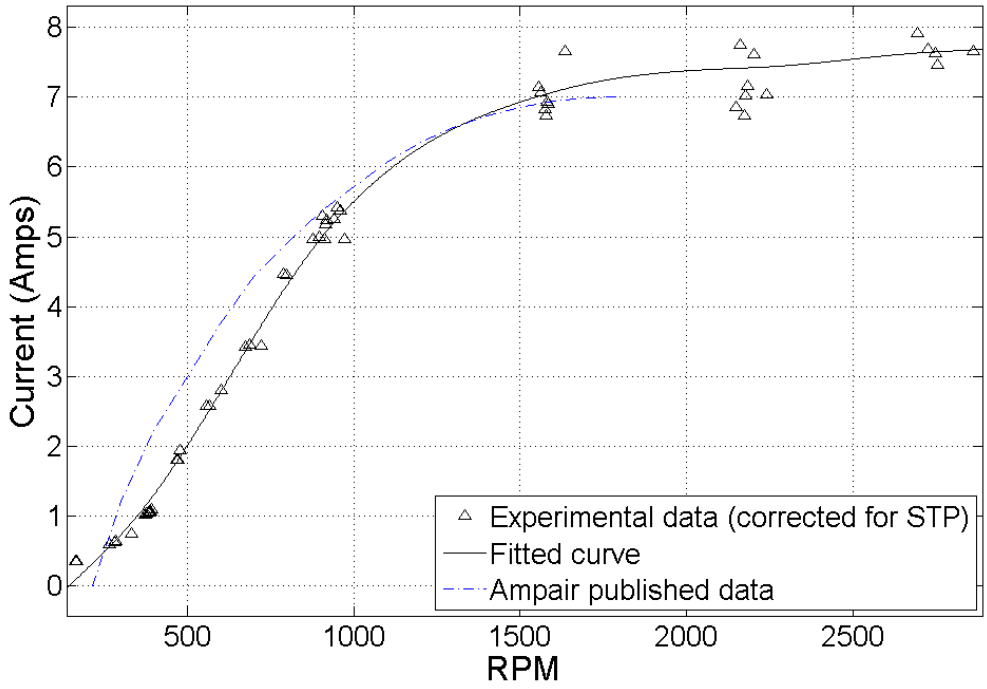

Figure 2.22 - Ampair 100 current curve, with manufacturer's published data. Estimated error at 2600 RPM: ±0.02 A.

The current produced in the load bank by the generator is shown in Figure 2.22 as a function of rotor speed. The current was calculated from Ohm's law (Eq. 1) using the measured generator output power corrected for standard air density and the known resistance of the load bank. Figure 2.22 shows that the wind turbine closely matches the published data. However, since the measured power exceeds the published data (see Figure 2.23) the current should do the same. This is because the generator in the turbine produces approximately 15 V but the manufacturer conservatively rates the machine at 12 V. At constant power, assuming a lower voltage will generate higher current. If the manufacturer had presented current based on 15 V the manufacturer's curve in Figure 2.22 would be below the experimental measurements.

2.4.4 Power

The power output from the turbine was calculated by measuring the voltage drop across the known resistance of the load bank as described in Section 2.2.3. This measured power was corrected to standard air density in the same manner as thrust was corrected above. This correction accounts for 15% additional power. The corrected power values are shown in Figure 2.23 and compared with the manufacturer's power curve. Up to 6 m/s (13 mph) wind speed the experimental results match the published data but at higher wind speeds the measured power exceeds the published data and even exceeds the rated power of the generator. Between 10 and 15 m/s (22-34 mph) the additional power was approximately 40%.

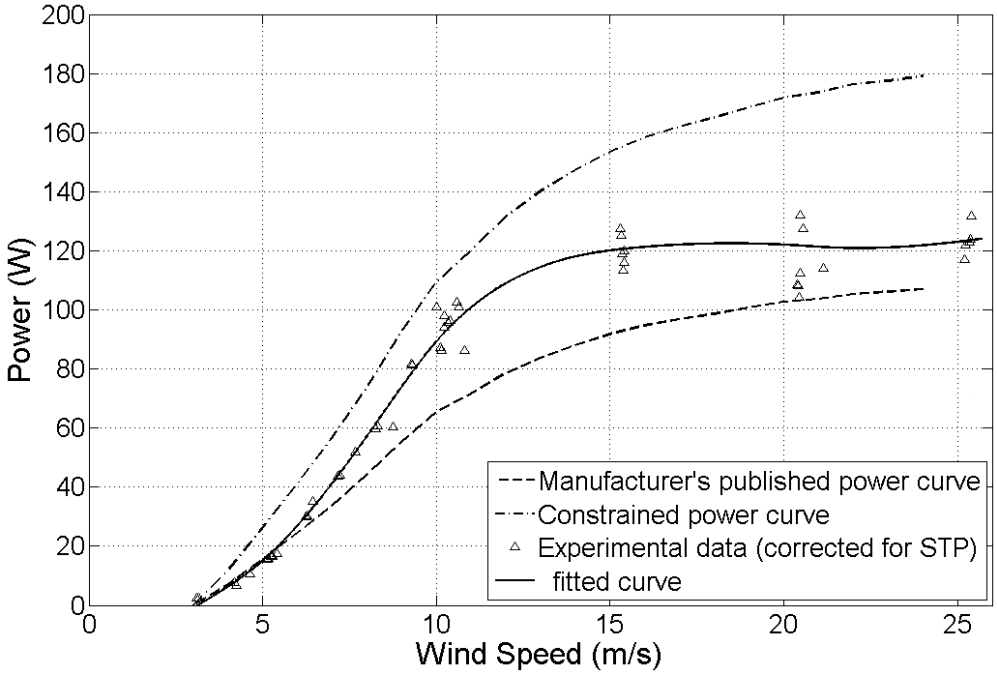

Figure 2.23 - Ampair 100 power curve, with manufactuer's published data. Estimated error at 25 m/s: ±0.32 W.

It should be noted that the grouping of the data points is widely scattered at the high wind speeds, especially at 20 m/s (45 mph). This is not unusual in wind turbine power curves taken from field data but it should not be so in the laminar flow and unchanging wind direction in the wind tunnel. Turbulence from the boundary layer may be responsible, but there might also be some irregularity with the wind tunnel at this speed as discussed in Chapter 3.

The boundary layer can be clearly seen in the flow profile plot and wake velocity plots (see Figure 2.24). From this plot, at 15 m/s (34 mph) wind speed, the boundary layer is approximately 190 mm (7.5") thick at the measurement plane. The clearance between the blade tips and the floor and ceiling of the wind tunnel is only 146 mm (5.75"). The turbulence effects, such as parcels of low speed air erupting from the boundary layer, at the top and bottom of the rotor may be causing uneven loading of the rotor resulting in the scatter in the power data.

In addition to the boundary layer, an uncertainty analysis of the wake wind speed shows much larger turbulence effects at 20 m/s (45 mph) than any other speed. The high uncertainty of the wake wind speed is chiefly due to the larger standard deviation of the Kiel probe pressure signal, indicating high turbulence at this wind speed. The complete uncertainty analysis of wake wind speed is presented in Appendix J.

(a)

(b)

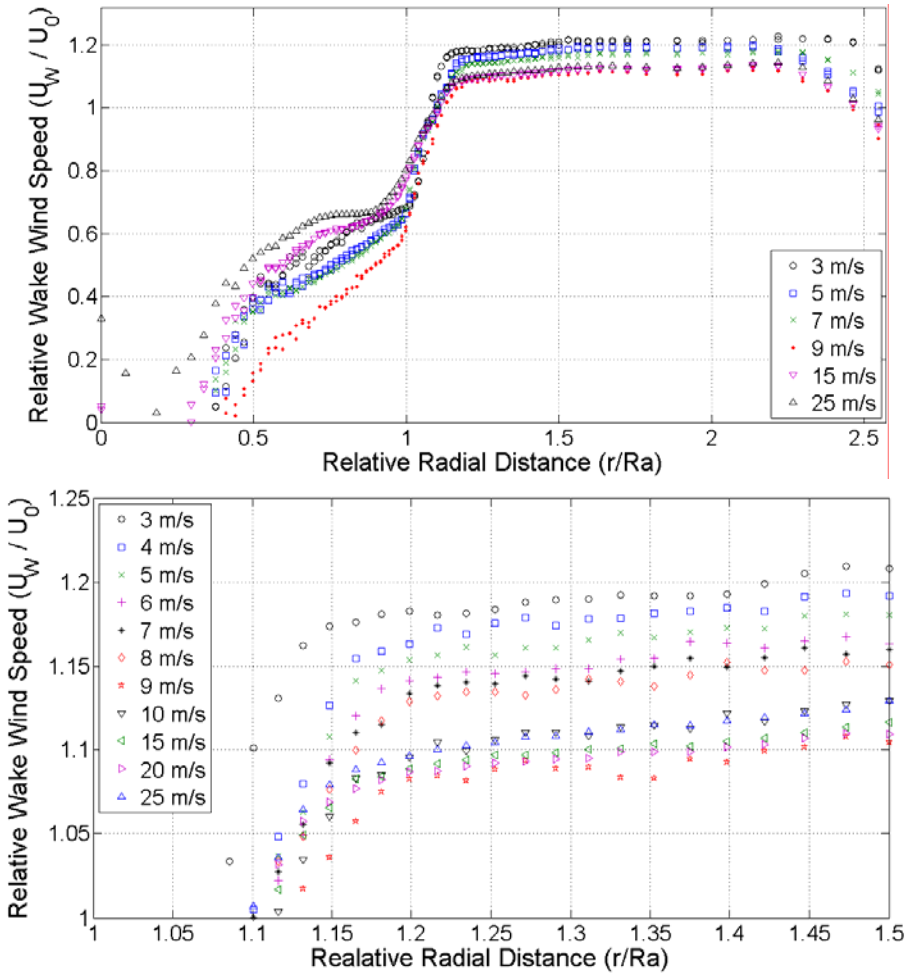

Figure 2.24 - (a) Relative wake wind speed at relative radial locations for various wind speeds. (b) Detail of bypass flow area outside of wake due to wake blocking.

It was expected that the power generated by the wind turbine inside the wind tunnel would be higher than what it could produce in open air. The wake is not free to diverge naturally, especially in the vertical direction. According to Equation 6:38 in Pope and Harper (1966) the expected increase in velocity due to this wake blocking was 6% meaning an additional 19% power contained in the wind.

Measurements show that the increase in velocity outside of the wake due to blocking is much higher than 6%. Figure 2.24(a) shows a plot of the Kiel probe wake speed measurements. Figure 2.24(b) shows a detail of the wake speed measurements in the bypass zone outside the wake, where relative radial distance is above 1.1. It can be seen that there is a discontinuity in the blocking trend between 8 and 9 m/s (18-20 mph) nominal upstream wind speed. From 3-8 m/s (7-18 mph) the average increase in wind speed outside the wake at the measurement plane was 18.7%. From 9-25 m/s (20-56 mph) the average increase was only 12.2%. In the latter group, this additional wind speed represents an additional 41.4% power in the wind.

By contrast, Garrett and Cummins (2007) give a theoretical power factor for a turbine constrained in a channel. By including a channel around the ideal rotor they rework the axial momentum theory. The result is identical to Betz except for an additional power factor, δ, of

$$\delta = (1-\epsilon)^{-2} \quad \text{(Eq. 11)}$$

where ϵ is the ratio of the area of the rotor to the area of the channel. In this experiment, the ratio of the area of the rotor disc (including hub) to the area of the wind tunnel cross section is 0.227 which results in a power factor of 1.67, or 67% additional power. This power factor is applied to the manufacturer's power curve for comparison with the measured output power in Figure 2.23. The power factor over-predicts output power by 20-30% from 6 to 11 m/s (13-25 mph) wind speed. Above this wind speed the measured power falls away from the theoretical line because the limit of the generator is reached.

The experimental results do not show any additional power above the published data for wind speeds of 6 m/s (13 mph) and below. This implies that in open air even less power would be produced. Since the typical wind speed will be less than 10 m/s (22 mph) for the majority of small wind turbine installations (Environment Canada 2003), it is important that accurate information be published in this low speed range.

Above 6 m/s (13 mph) the experimental results show power production in excess of the manufacturer's data. The additional power is what would be expected from the blockage of the wake inside the wind tunnel. It is not, however, as high as what would be predicted by the power factor on axial momentum theory for an ideal rotor in Garrett and Cummins (2007).

2.4.5 Non-Dimensional Parameters

In order to compare the wind turbine to other machines, the parameters need to be non-dimensionalized. Thrust coefficient (C_T), power coefficient (C_P), torque coefficient (C_{TOR}), and tip speed ratio (λ) are common parameters defined as

$$C_T = \frac{T}{\frac{1}{2}\rho A U_0^2} \quad \text{(Eq. 12)}$$

$$C_P = \frac{P}{\frac{1}{2}\rho A U_0^3} \quad \text{(Eq. 13)}$$

$$C_{TOR} = \frac{Tor}{\frac{1}{2}\rho A R a U_0^2} = \frac{C_P}{TSR} \quad \text{(Eq. 14)}$$

$$\lambda = \frac{\pi D \omega}{U_0} \quad \text{(Eq.15)}$$

where T is thrust on the rotor disc, P is power, ρ is air density, A is the area of the rotor disc including hub, U_0 is the undisturbed wind speed, Tor is rotor torque, Ra is rotor radius, D is rotor diameter, and ω is rotational speed of the rotor in revolutions per second.

2.4.5.1 *Blockage Corrections*

The walls of the wind tunnel constrain the divergence of the wake of the rotor disc. This results in a flow outside of the wake streamtube that is faster than the freestream air speed leading up to the rotor disc. Maskell (1963) developed a blockage factor for bluff bodies (such as a rotor disc) based on the additional drag these bodies would experience due to this faster bypass flow. From this Whelan *et. al.* (2009) provides blockage corrections for C_T and TSR.

$$C_{T_{(unblocked)}} = \left[\frac{C_T}{\tau^2}\right]_{(blocked)} \quad \text{(Eq. 16)}$$

$$\lambda_{(unblocked)} = \left[\frac{\lambda}{\tau}\right]_{(blocked)} \quad \text{(Eq. 17)}$$

where τ is the factor applied to the freestream flow to achieve the bypass flow, i.e.

$$U_B = \tau U_0 \quad \text{(Eq. 18)}$$

A blockage correction for C_P is not provided in Whelan *et. al.* (2009). Given the close relationship between thrust and power it seems reasonable that C_P should have a correction factor based on τ. However, Whelan *et. al.* (2009) shows good agreement between their model and experimental results for C_P at low λ (below 5) and so no correction is applied to these experimental results.

2.4.5.2 *Coefficient of Thrust*

The C_T vs. λ curves for the Ampair 100 are shown in Figure 2.25. The peak at $\lambda_{(unblocked)} = 3.4$ (corresponding to about 5 m/s wind speed) shows that the rotor is not as efficient at higher wind speeds. It is interesting that the unblocked data shows high outliers at about $\lambda_{(unblocked)} = 4$. This corresponds to wind speeds of about 10 m/s at which the turbine produces the most power.

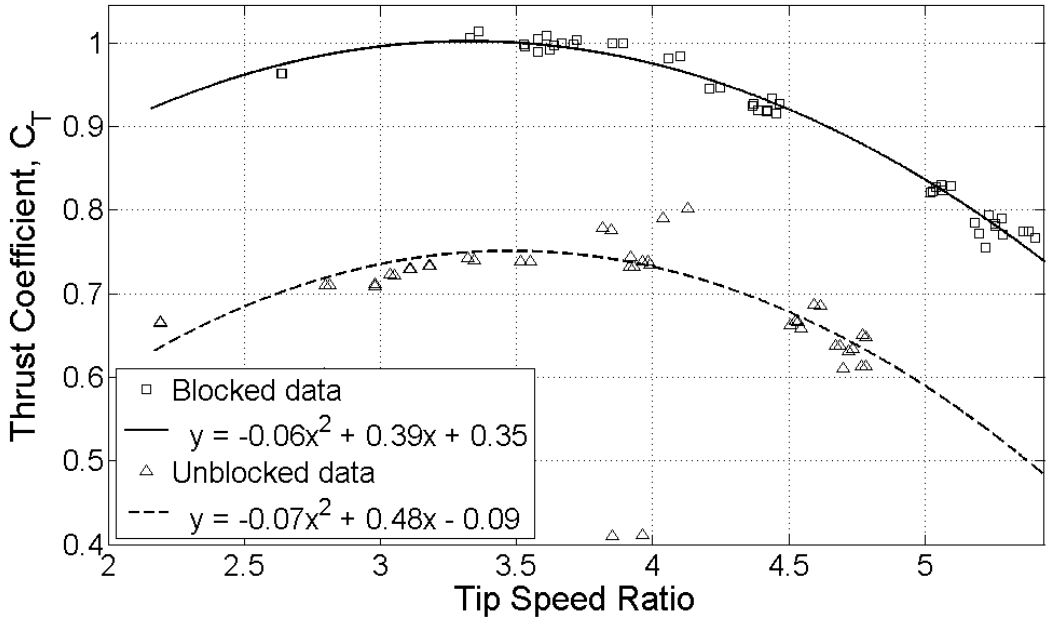

Figure 2.25 - Ampair 100 thrust coefficient curve

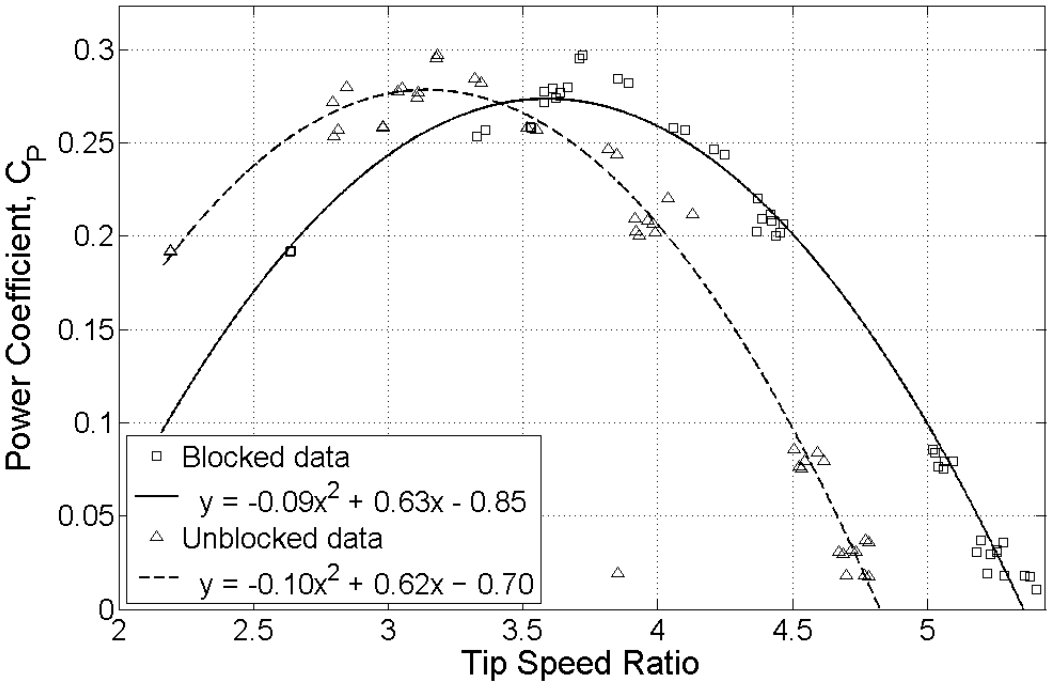

Figure 2.26 - Ampair 100 power coefficient curve

2.4.5.3 *Coefficient of Power*

The C_P vs. λ curve for the Ampair 100 is shown in Figure 2.26 with a peak C_P of 0.28 at a $\lambda_{(unblocked)}$ of 3.14. The Lanchester-Betz limit determines a maximum C_P possible of 0.59. Glauert applies a factor of 0.92 at this λ due to wake rotation, resulting in a maximum C_P of 0.543. Okulov and Sørensen (2008) show the maximum C_P for a 6 bladed rotor at λ = 3.14 is 0.48. However, due to the constraining walls of the wind tunnel, applying the power factor from Garrett and Cummins (2007) results in a maximum C_P of 0.83 for this experiment. According to Hau (2006) this wind turbine falls in the category of low-speed, high-torque machines, as expected from its many-bladed, small diameter rotor, which typically have a C_P of approximately 0.30. Therefore, this wind turbine is performing well for its small size.

2.4.5.4 *Coefficient of Torque*

The C_{TOR} vs. λ curve is shown in Figure 2.27. The turbine produces a C_{TOR} of 0.093 at a $\lambda_{(unblocked)}$of 2.53. According to Hau (2006) low-speed, high-torque machines typically have C_{TOR} range from 0.15-0.02. However, for such small blades this turbine performs well.

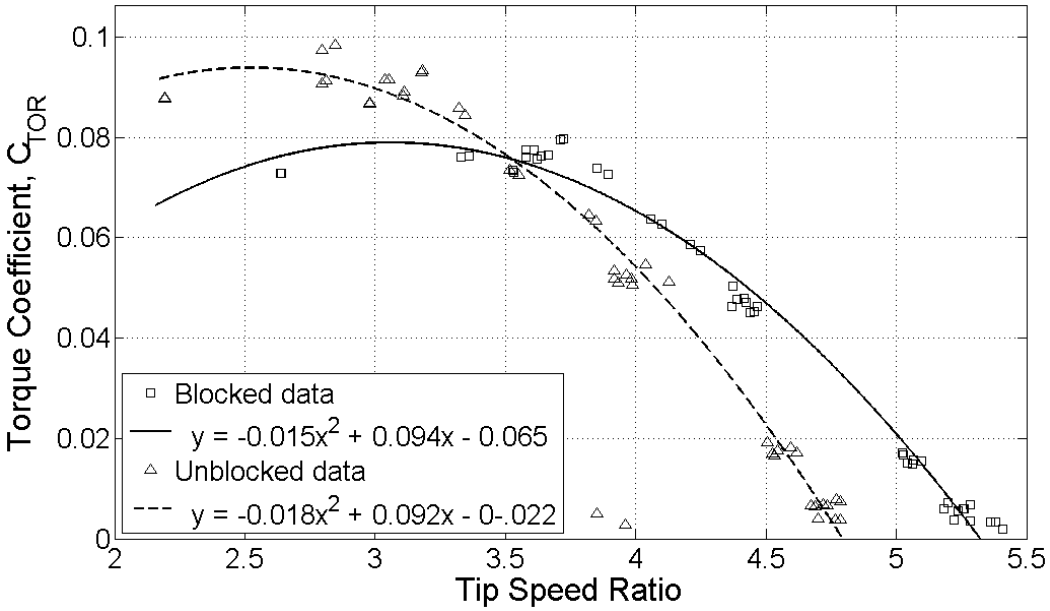

Figure 2.27 - Ampair 100 torque coefficient curve

2.5 Near Wake Characteristics

2.5.1 The unconstrained ideal rotor disc model

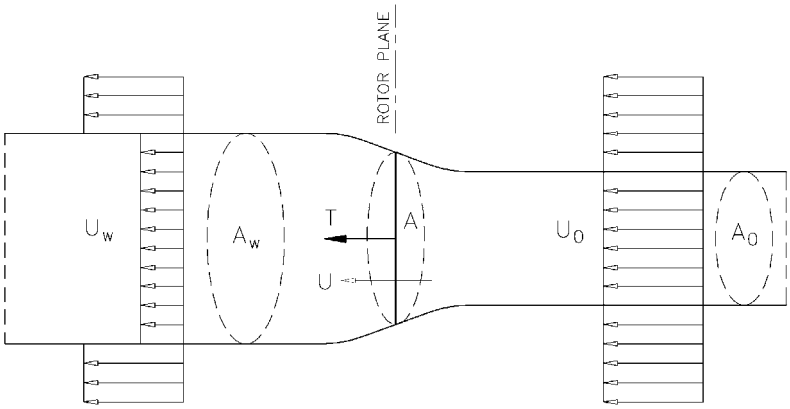

Figure 2.28 - Axial momentum theory control volume

Hansen (2008) provides a summary of the one-dimensional axial momentum theory for an ideal rotor disc that is commonly used for wind turbines. A simple diagram of the control volume considered is shown in Figure 2.28. Using the Bernoulli equation in two instances: from far upstream of the rotor to the rotor, and from far downstream of the rotor to the rotor, the equation for thrust on the rotor is

$$T = \rho A U (U_0 - U_W) \quad \text{(Eq. 19)}$$

where ρ is the density of air and A is the area of the rotor disc. The theory also demonstrates that the wind speed through the rotor plane, U, is the average of free stream velocity, U_0, and wake speed, U_W, as shown in Equation 20.

$$U = \frac{1}{2}(U_0 + U_W) \quad \text{(Eq. 20)}$$

Since thrust on the rotor was measured in the experiment, U_W can be calculated.

The power extracted from the wind by the rotor is defined from axial momentum theory as

$$P = \frac{1}{2}\rho A U (U_0^2 - U_W^2) \quad \text{(Eq. 21)}$$

2.5.2 Rotor disc constrained in a channel (wind tunnel) model

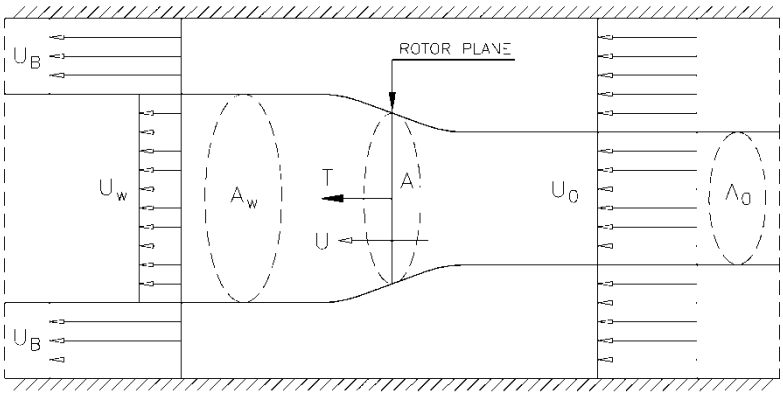

Figure 2.29 – Constrained axial momentum theory control volume

Garrett and Cummins (2007) adds channel walls to the axial momentum through an ideal rotor model. A simple diagram of the control volume considered is shown in Figure 2.29. The equation for thrust on the rotor is now

$$T = \frac{1}{2}\rho A(U_B^2 - U_W^2) \qquad \text{(Eq. 22)}$$

where U_B is the accelerated bypass flow outside of the wake. Wind speed through the rotor plane is then related to U_W, U_B and U_0, as shown in Equation 23.

$$U = \frac{U_W(U_B + U_W)}{U_B + 2U_W - U_0} \qquad \text{(Eq. 23)}$$

With constraining walls the power extracted from the wind by the rotor is

$$P = \frac{1}{2}\rho A U_W \frac{(U_B + U_W)(U_B^2 - U_W^2)}{U_B + 2U_W - U_0} \qquad \text{(Eq. 24)}$$

The wake velocity was measured along a single radial line from wind turbine centerline to wind tunnel wall. To calculate power, this line was assumed to represent the full circular cross-section of the wake streamtube despite the fact that the wind tunnel is much shorter than it is wide. In the vertical direction the wake was more constrained which would cause higher local wind speeds through the rotor. The effect of the assumption was to predict less total power for the rotor.

2.5.3 Wake speed

Axial momentum theory ignores rotation of the wake, however, the Kiel probe measures a resultant wind vector that includes axial and tangential components. The individual components cannot be resolved in this experiment so the measured wake speed includes the tangential vector and results in a higher wake speed being measured.

The tangential component of wake wind velocity is largest at low rotational speed (Hansen 2008). So, the error due to wake rotation is more pronounced at low rotational speeds.

By ignoring wake rotation the axial momentum theory over-predicts power absorbed by the rotor by the amount required to generate wake rotation. The higher wake speed measured by the Kiel probe results in a calculation error of less power being absorbed by the rotor. The Kiel probe measurements compensate for the deficiency in the theory but by how much is beyond the scope of this paper. Stereo PIV measurements of the rotor wake could give much more information of the three-dimensional components of wake speed.

The velocity profile of an actual wind turbine wake is not constant as assumed in the axial momentum theory. The wake can be considered as a jet of negative momentum (Magnusson and Smedman, Air flow behind wind turbines 1999) and should have maximum velocity deficit where the rotor blades are most efficient at generating lift and therefore extract the most power from the wind (Magnusson, Near-wake behavior of wind turbines 1999). Field studies, however, consistently show that maximum velocity deficit occurs at the hub (Vermeer, Sørensen and Crespo 2003) (Haans, et al. 2005) (Baker, Walker and Katen 1985) and develop into a Gaussian distribution in the far wake (Hau 2006). The numerical results in Magnusson (1999) show a distinct hump in the wake velocity deficit at 60% of the length of their blade model. This is where the blades are extracting maximum energy from the wind.

In Figure 2.30, the relative velocity deficit in the wake behind the wind turbine, defined in Magnusson (1999) as

$$\frac{\Delta U}{U_0} = \frac{(U_0 - U_W)}{U_0} \qquad \text{(Eq. 25)}$$

is plotted against relative radial position for wind tunnel speeds of 3-25 m/s (7 -56 mph). The wake velocity deficit profiles do not show humps along the rotor blade like those shown in Magnusson (1999) (besides the one representing the area directly behind the turbine hub). However, some of the data sets show a lessening of the slope (flattening) of the data from r/Ra =0.7 to r/Ra =0.9, which suggests the blades are most efficient near the tip. It is also clear that maximum velocity deficit (i.e. minimum wake velocity) occurs at approximately 9 m/s (20 mph) wind speed.

The hub of the wind turbine is one of the major differences between the axial momentum models and the experiment. It was attempted to remove the effects of the hub from the data in order to more resemble an ideal rotor. Wake measurements were done on the wind turbine hub alone (with the rotor blades removed). The wake speed plots of the wind turbine hub and their fitted Gaussian profiles are shown in Appendix K.

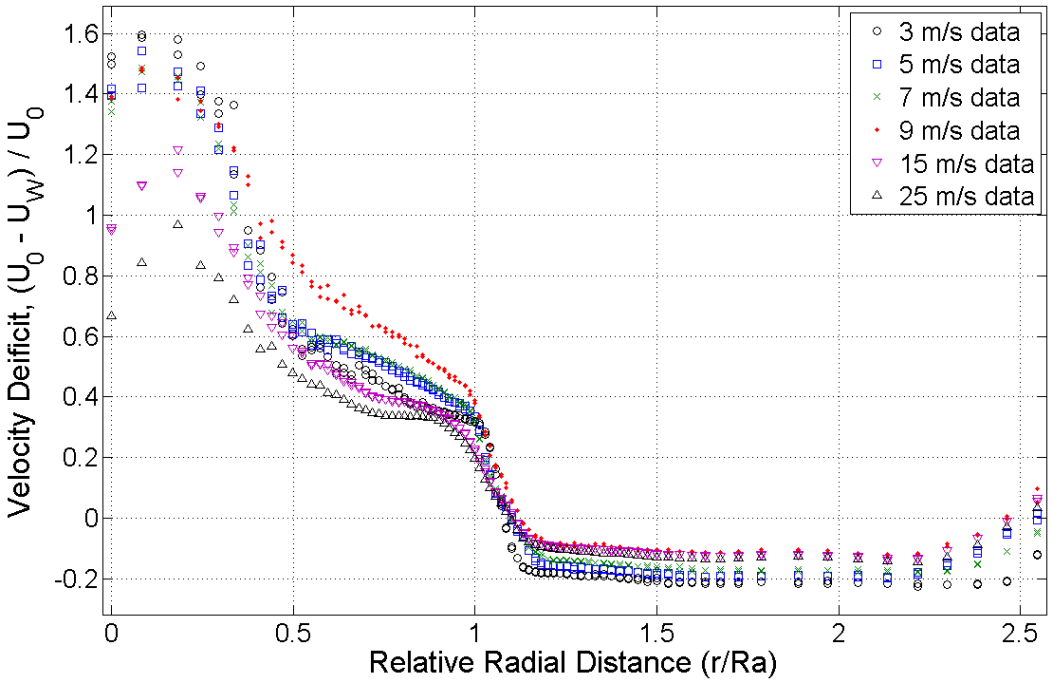

Figure 2.30 - Velocity deficit in the wake behind the Ampair 100 with rotor blades installed

The relative wake wind speed of the hub was subtracted from the data with the rotor in the manner shown in Equation 26 for each data sampling position on the Kiel probe path.

$$\left[\frac{U_W}{U_0}\right]_{Rotor\ only} = \left(1 - \left[\frac{U_W}{U_0}\right]_{Hub\ only}\right) + \left[\frac{U_W}{U_0}\right]_{Hub\ \&\ Rotor} \qquad \text{(Eq. 26)}$$

The results of subtracting the hub wake are shown in Figure 2.31. It can be seen that the subtraction is not perfect, especially in the high slope transition zone at the root of the blades. In addition, the resulting velocity profile in the wake is still far from constant as assumed in the axial momentum theory.

To use the axial momentum equations, a single wake speed is required. An average wake speed was calculated from the relative wake speed data. The wake of the hub and turbine was used in order to evaluate the performance of the wind turbine, but the wake of the rotor alone (with hub wake subtracted) was evaluated separately for comparison to the axial momentum theory. When using the average wake speed of the rotor only the calculated power was less than the calculated power using the average wake speed of the rotor including the hub (and therefore closer to measured values of power output). However, the difference was noticeable only at calculated powers greater than 150 W, which is beyond the range of the Ampair 100 generator.

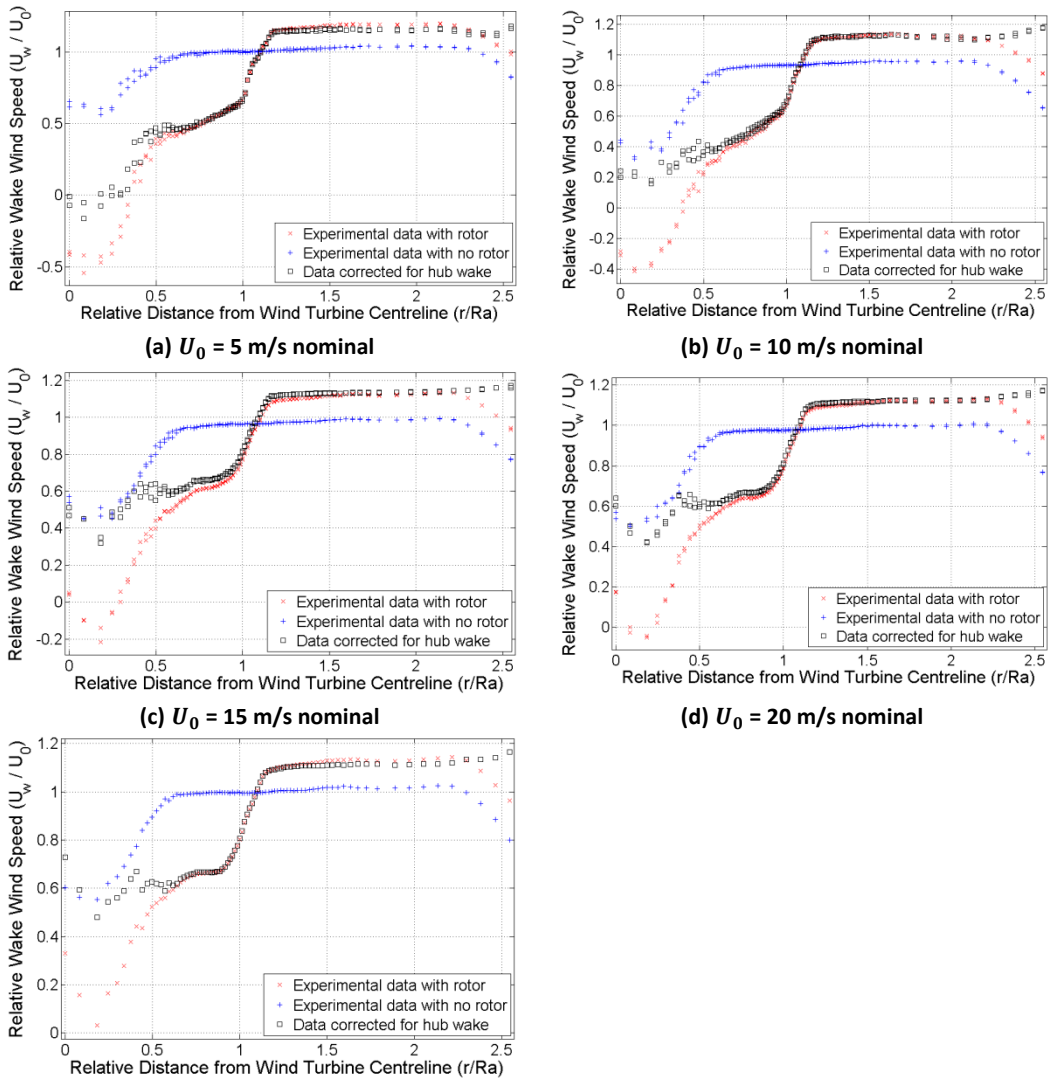

(a) U_0 = 5 m/s nominal

(b) U_0 = 10 m/s nominal

(c) U_0 = 15 m/s nominal

(d) U_0 = 20 m/s nominal

(e) U_0 = 25 m/s nominal

Figure 2.31 - Subtraction of hub wake from wind turbine rotor wake.

The wake is defined as the region between turbine centerline and the point before the transition back to free stream velocity. This point was consistently at a relative radius of 0.9853 for wind speeds of 5-9 m/s (11-20 mph). Above 9 m/s (20 mph) the transition point shifted to a relative radius of 0.9295. Below 5 m/s (11 mph) the transition point increased steadily to a relative radius of 1.0269 at 3 m/s (7 mph) wind speed. To calculate power, the wake velocity was determined by taking the area under the velocity curve in the wake region and dividing by the area of the wake the square of the wake radius. An example of the average wake speed is depicted in Figure 2.32.

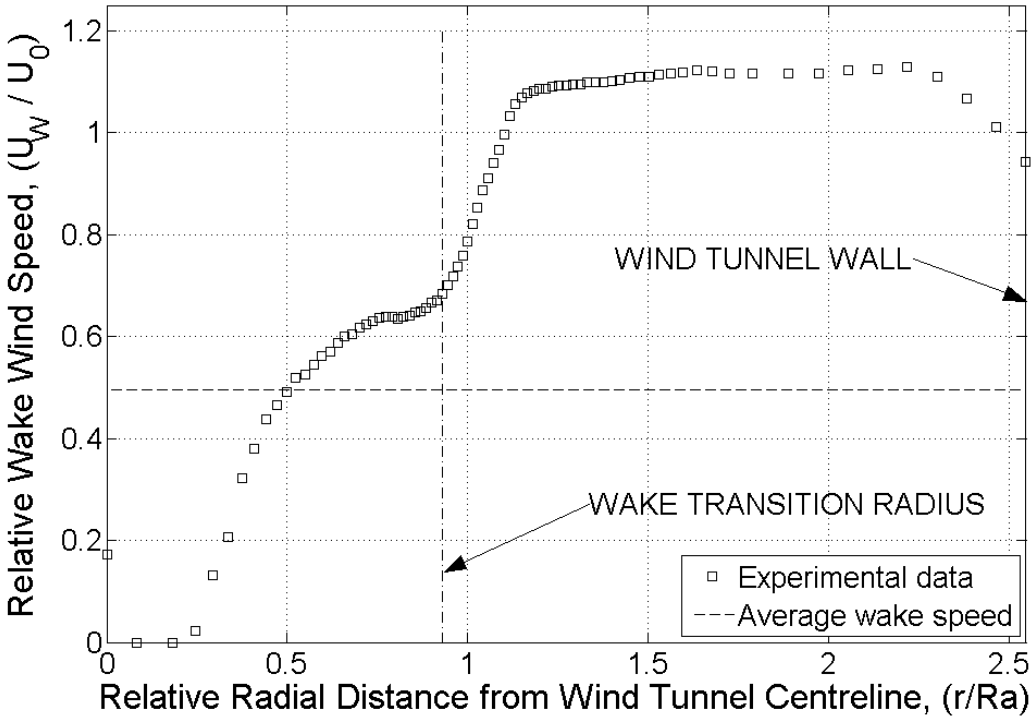

Figure 2.32 - Calculation of average wake speed for 20 m/s wind speed

2.5.4 Axial induction factor

For the axial momentum theory without constraining walls axial induction factor, a, is defined in terms of wake speed as

$$a = \frac{(U_0 - U_W)}{2U_0} \qquad \text{(Eq. 27)}$$

For a known thrust on the rotor the theoretical wake speed can be calculated by the axial momentum theory thrust equation (no walls). When walls are added the axial induction factor becomes

$$a = 1 - \left[\frac{U_W(U_B + U_W)}{U_0(U_B + 2U_W - U_0)}\right] \qquad \text{(Eq. 28)}$$

Axial induction factor is the relationship between wake speed and the freestream speed. In essence, it shows how effectively kinetic energy in the wind is being absorbed by the rotor (ignoring wake rotation). Higher a is obtained when the rotor is extracting more power resulting in low wake speeds. The axial momentum theory shows that the maximum power should occur when $a = 0.33$. However, it has been determined that the assumptions of the axial momentum theory are only valid for $a < 0.4$. Above this value there is a turbulent wake state in which the large jump from U_0 to U_W is so great

that the shear line at the edge of the wake becomes unstable and momentum is transferred from the free stream into the wake (Hansen 2008).

Axial induction factors calculated from wake speeds derived from the thrust equation (using Equations 19, 20 and 27) followed a power law as shown in Figure 2.33, asymptotic to a = 0.2. Axial induction factors calculated from Equation 28 followed two patterns. Above 10 m/s (22 mph) wind speed values followed a power law, but below 10 m/s (22 mph) values leveled off to a near constant value of 0.35. At 10 m/s (22 mph) a spike in a is noted. This shows that this rotor is most effective at generating power at this wind speed.

The change in pattern is related to U_B. Above 10 m/s (22 mph) the ratio τ remains nearly constant with increasing wind speed. Below 10 m/s (22 mph) it is the ratio of wake speed to freestream speed ($\alpha = U_W/U_0$) that remains nearly constant while U_B increases with decreasing wind speed, as shown in Figure 2.34. The low values of α at 10 m/s (22 mph) wind speed indicate that the maximum difference between U_W and U_0 is achieved at this point. This may suggest the turbulent wake state has been reached. The rotor reaches the limit of how much energy it can extract from the wind, the wind within the streamtube is slowed as much as possible, and so more air must be forced to bypass the rotor.

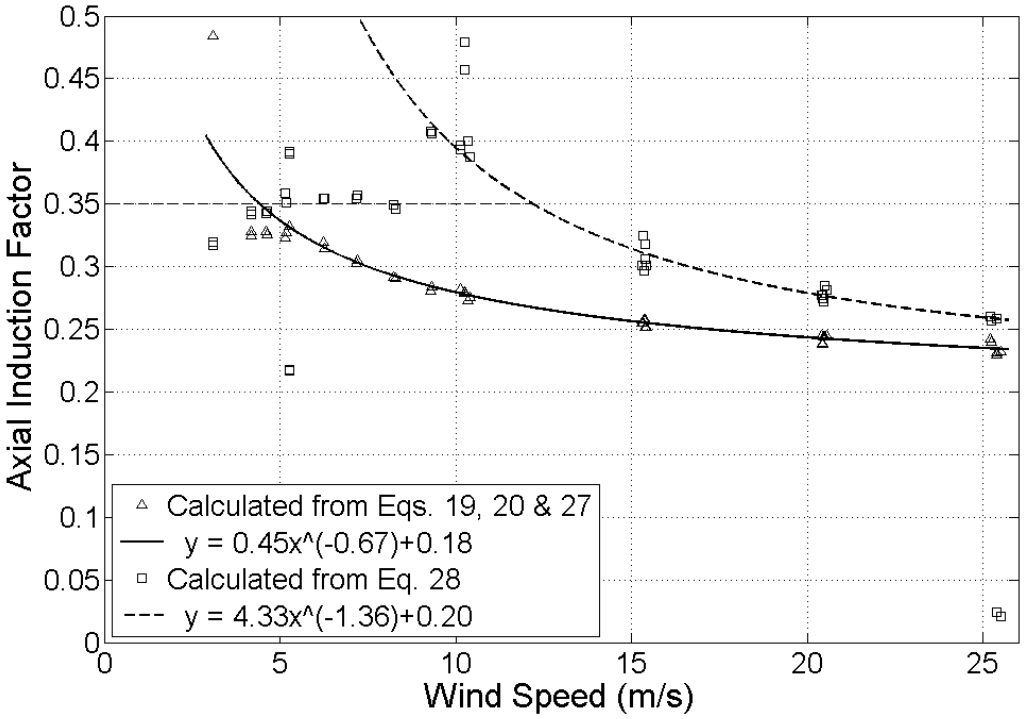

Figure 2.33 - Axial induction factors for the Ampair 100, calculated from axial momentum theory using measured rotor thrust and from axial momentum theory within a closed channel

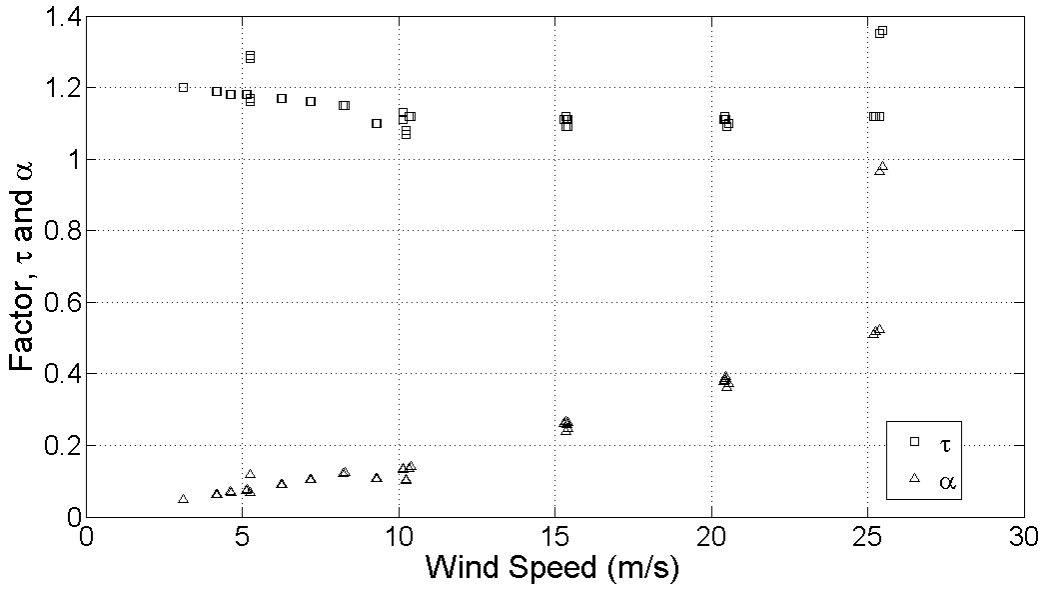

Figure 2.34 - Bypass wind speed factor, τ, and wake wind speed factor, α

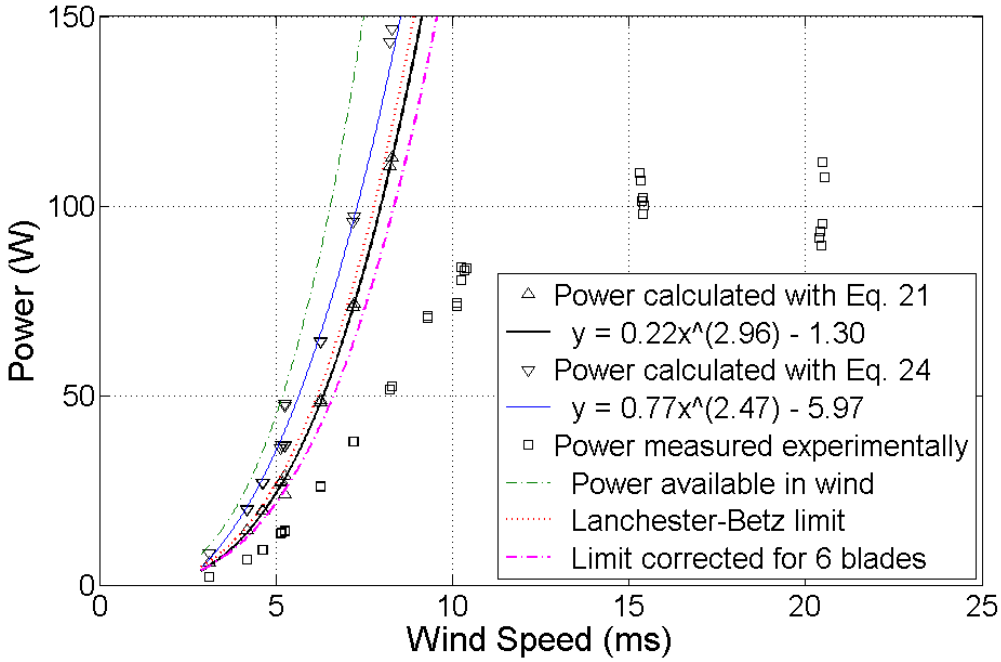

Figure 2.35 - Ampair 100 power calculated from wake speeds derived from thrust equation, average wake speed, and average wake speed corrected for hub wake, compared with measured generator output

2.5.5 Calculated power

Power was calculated using Equations 21 & 24 with the average wake speed and average bypass speed measured by the Kiel probe and is presented in Figure 2.35. As expected, the results followed a near-cubic relationship and the power calculated from Equation 24 predicted more power than the Lanchester-Betz limit.

The measured power output is also plotted and can be seen to roughly follow the axial momentum theory up until the limit of the generator rating, where it is forced to remain relatively constant. The measured output falls short of axial momentum theory by approximately 50%. Included in this deficiency are all the non-physical assumptions of the ideal rotor and the various mechanical and electrical losses of the generator and rectifiers. The theory also does not consider the existence of a hub. The area of the hub represents 6% of the total rotor area and this area is not generating power.

2.6 Conclusions

The global characteristics of the Ampair 100 micro wind turbine were derived from measurements in a low-speed wind tunnel. The power curve was shown to match the published power curve within experimental expectations. The constraints of the wind tunnel did cause power output to exceed the manufacturer's published data at wind speeds over 6 m/s but the results did not give the additional power factor derived for an ideal rotor in a channel given in Garrett and Cummins (2007). Since this power factor is applied directly to the axial momentum theory it is not surprising that it over-estimates actual power.

According to Magnusson (1999) the highest velocity deficit represents the highest efficiency of the rotor. From this, the Ampair 100 rotor is optimized for a wind speed of approximately 10 m/s (22 mph).

The original axial momentum theory for ideal rotors (without constraining walls) is shown to over-predict power absorbed by the Ampair 100 by approximately 50%. It is shown that using measurements of rotor thrust will predict similar values for power absorbed as by using measurements of average wake speed.

3 Static Pressure Across Wind Turbine Rotor

An experiment was performed to determine the effect of the wind turbine rotor on the static pressure in the wind tunnel. By the axial momentum ideal rotor model it was expected that the pressure would rise from atmospheric close upstream of the rotor, drop suddenly across the plane of the rotor, then rise back up to atmospheric pressure downstream of the rotor.

This experiment was carried out by lab assistant Benden Nielsen from June 2-10, 2010.

3.1 Experimental setup

Static pressure ports were drilled in the floor of the wind tunnel at the locations listed in Table 3.1. The locations were measured in terms of rotor diameters (D) and were 305mm (12") to one side of centerline in order to avoid the wind turbine mast support structure.

Table 3.1 - Static pressure port locations

Port No.	Location
1	3.00 D upstream
2	2.00 D upstream
2	1.50 D upstream
3	1.00 D upstream
4	0.75 D upstream
5	0.50 D upstream
6	0.25 D upstream
7	0.00 D upstream (in plane of rotor)
8	0.25 D downstream
9	0.50 D downstream
10	0.75 D downstream
11	1.00 D downstream
12	1.50 D downstream
13	2.00 D downstream
14	3.00 D downstream

The pressure ports were connected to the negative side of a differential pressure transducer by hard-walled polypropylene tubing (see Table 2.6 for specifications). The positive side of the pressure transducer was left open to atmosphere in order to measure static pressure in relation to atmospheric pressure.

The wind turbine was set up as previously described in Section 2.1. The only difference was that the traverse was not being used and therefore LabView was used to record the transducer signals instead of the traversing software.

3.2 Experimental procedure

The experiment was performed at various wind speeds from 3-25 m/s (7-56 mph). For each wind speed the resistor load bank was adjusted as described in Section 2.2.3 to match the manufacturer's power curve. Atmospheric pressure was recorded with the mercury barometer in room MECE 3-10 and corrected for temperature, elevation and gravity effects. Temperature in the wind tunnel was recorded with a thermocouple located 4.25 m (14'-0") upstream of the wind turbine rotor. Wind speed was measured with a hand-held Fluke flow meter as well as calculated with the pitot tube and manometer described in Section 2.1.

With the wind tunnel running at constant speed the pressure signal at each static pressure port was recorded in succession using LabView. The program recorded for 2 seconds at 10,000 Hz and the data were averaged over those 2 seconds using a Matlab script.

3.3 Results

A comparison was made between the measurements of wind speed obtained by the Fluke flow meter and the pitot tube/manometer combination. The two instruments are compared in Figure 3.1. It can be seen that the two instruments delivered very similar results.

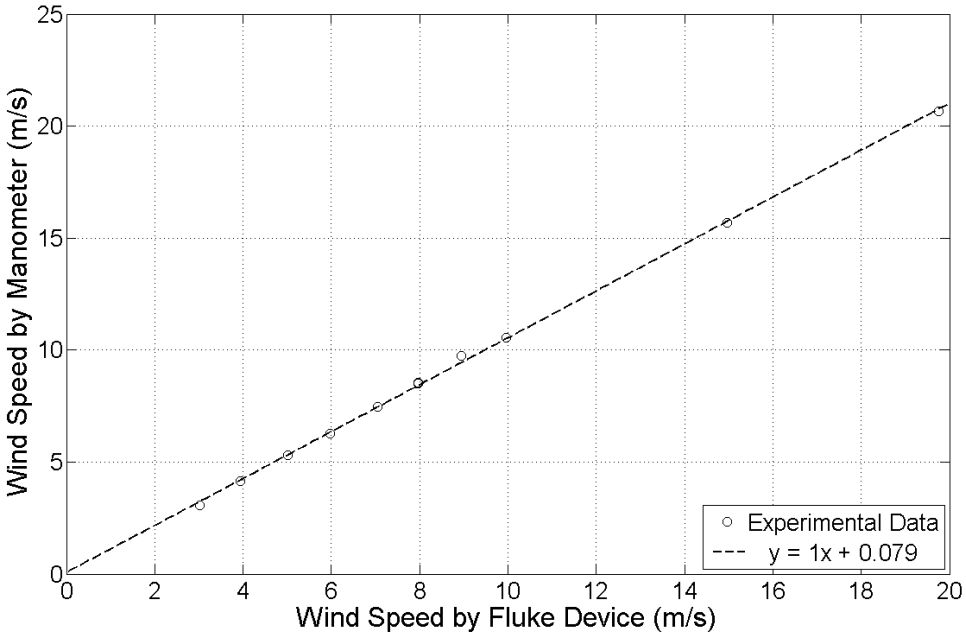

Figure 3.1 - Comparison of wind speed measurements made with Fluke flow meter and pitot tube/manometer combination

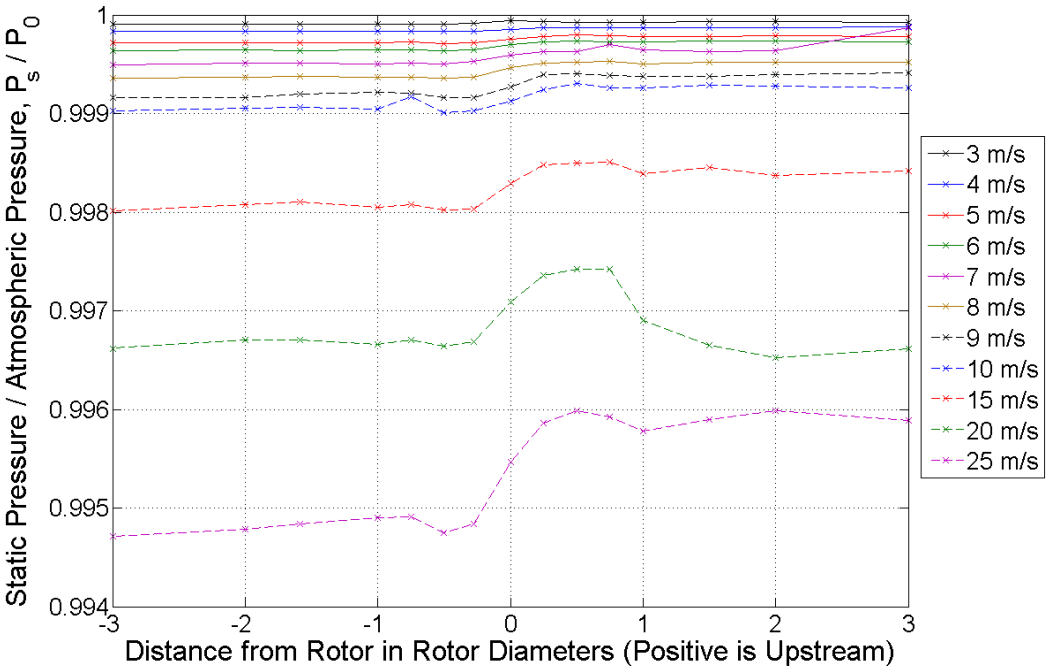

Figure 3.2 - Change in pressure across wind turbine rotor

The average static pressure at the static pressure ports for each wind speed is shown in Figure 3.2.

3.4 Discussion

The general form of the pressure change across the wind turbine rotor was as expected. The change in pressure across the wind turbine rotor shown in Figure 3.2 shows the static pressure staying relatively constant upstream of the rotor, drops across the rotor plane, and then remains at a constant value which is lower than the upstream pressure. At wind speeds above 8 m/s (18 mph) a rise in pressure upstream of the rotor is visible, as is a slight recovery in pressure downstream of the large pressure drop across the rotor. This is consistent with the axial momentum ideal rotor theory.

The results for 20 m/s (45 mph) wind speed are anomalous. The data set shows a rise in pressure as the air approaches the rotor upstream that is much greater than any of the other data sets, including at 25 m/s (56 mph) wind speed. From the figure, this seems to be due to the constant upstream pressure being abnormally low compared to other wind speeds. After the drop in pressure across the rotor the pressure returns to a constant value downstream that is slightly *higher* than the constant pressure upstream of the rotor.

This anomaly may help to explain the large variations in power being generated by the wind turbine at 20 m/s (45 mph) wind speed, as is seen in Figure 2.24. It is possible that the wind tunnel has some sort of critical value at around 20 m/s (45 mph) wind speed that is causing the unexplained results. This anomaly has not been reported in recent

previous studies though the studies were not carried out at wind speeds above 8 m/s (18 mph) (Johnson 2001) (Woods 2005). The anomaly might be caused by the presence of the wind turbine in the wind tunnel.

The measured pressures differ from the axial momentum ideal rotor theory in that they do not return to atmospheric pressure far upstream and downstream of the rotor plane. This is because only static pressure is being shown. The difference between static pressure and atmospheric pressure is the dynamic pressure due to the speed of the air inside the wind tunnel. The fact that downstream of the rotor the static pressure does not return to the same pressure as upstream of the rotor must be due to an increase in dynamic pressure resulting from the accelerated bypass flow due to the wake blocking in the wind tunnel. Figure 3.3 overlays the static pressure drop across the wind turbine rotor with the static pressure drop along the length of the empty wind tunnel. It can be clearly seen that the drop in static pressure is not simply due to the wind speed increase along the length of the wind tunnel due to increasing boundary layer thickness.

In the axial momentum ideal rotor theory, the change in pressure across the rotor is equal to the thrust on the rotor. The additional drop in static pressure seen here illustrates the additional thrust, or horizontal buoyancy, due to wake blocking described in Pope and Harper (1966). A parameter, β, to represent this blockage effect was calculated by taking the ratio of the average pressure from one to three diameters upstream of the rotor with the average pressure from one to three diameters downstream. This parameter is shown in relation to wind speed in Figure 3.4.

At low wind speeds, the relation between β and wind speed is linear. The datum point near 20 m/s (45 mph) has to be discounted due to the anomalous readings at this wind speed. At 25 m/s (56 mph) the wind turbine is at the extreme end of its operating envelope and the datum point at this wind speed should not be considered to be representative of normal operation.

Unfortunately, parameter β is much too small to account for the amount of wake blocking expressed in Pope (1966) or Whelan *et. al.* (2009). At 10 m/s (22 mph) β only predicts 0.02% blockage. This does not even account for the physical volume of the wind turbine in the wind tunnel (about 0.70%) much less the wake from a blunt body disc the size of the rotor.

(a)

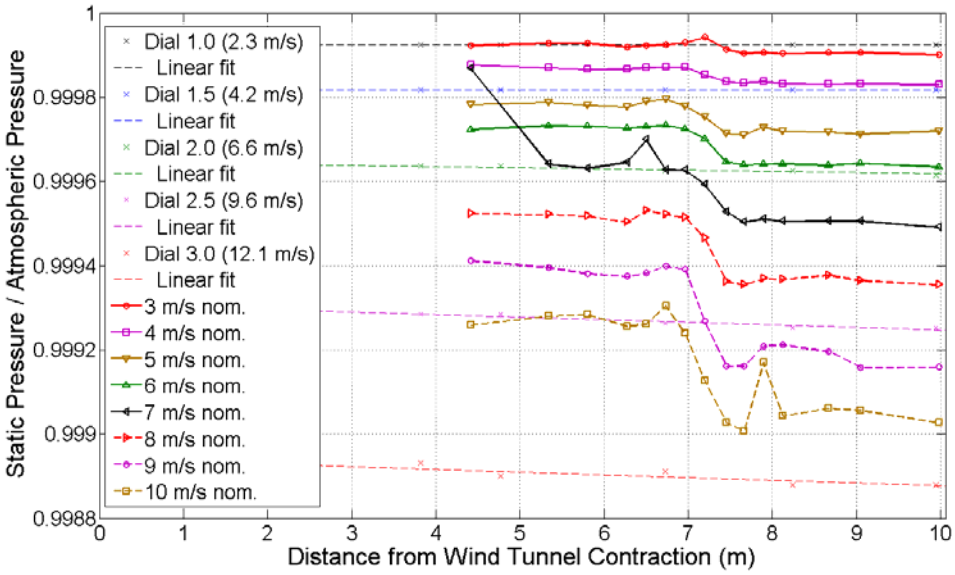

(b)

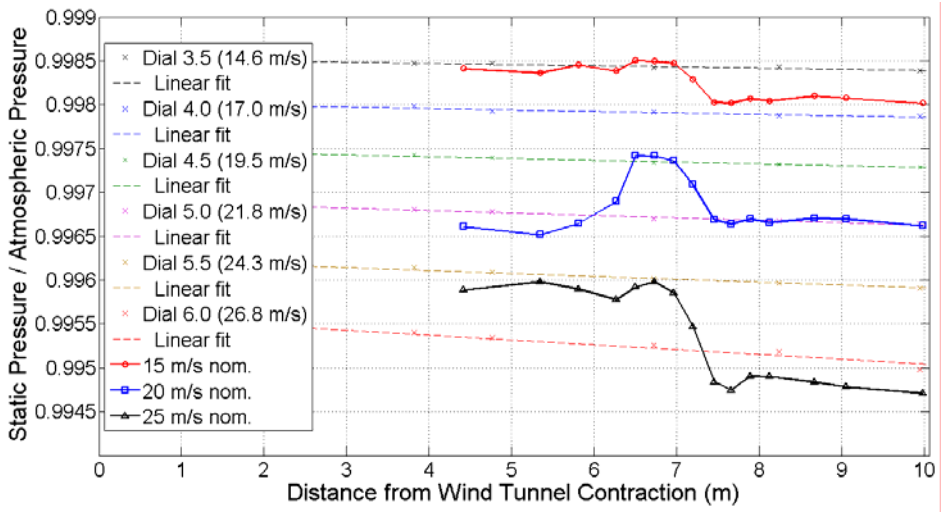

Figure 3.3 - Static pressure drop across wind turbine rotor compared with static pressure drop along wind tunnel length

(a) shows wind tunnel static pressure drop measured from wind tunnel dial settings 1.0-3.5

(b) shows wind tunnel static pressure drop measured from wind tunnel dial settings 4.0-6.0

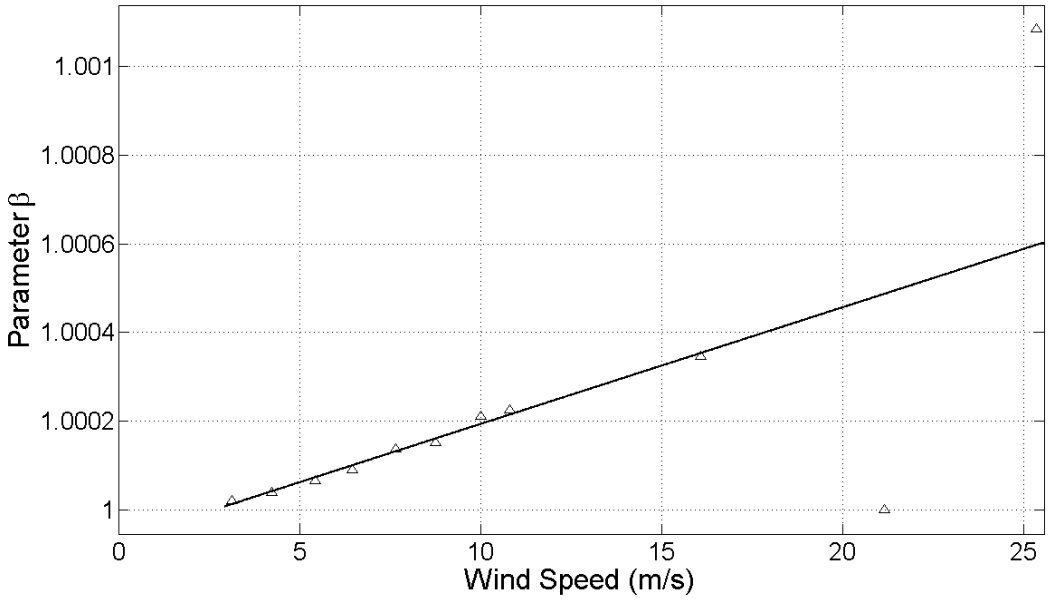

Figure 3.4 - Parameter β versus wind tunnel wind speed

3.5 Conclusions

The static pressure drop ahead of the wind turbine rotor, the subsequent pressure rise across the rotor plane, and the pressure drop in the wake of the turbine predicted by turbine theory is shown for the Ampair 100. However, the pressure in the wake does not return to atmospheric pressure within 3 rotor diameters as expected by axial momentum theory.

It is also shown that the low speed wind tunnel in the Mechanical Engineering building at the University of Alberta produces anomalous results at wind speeds of 20 m/s (45 mph). The static pressure measurements clearly do not follow the trends shown at all other wind speeds.

4 High Speed Photography of Water Droplets Hitting a Rotating Wind Turbine Blade

The purpose of this experiment was to begin to investigate the process of icing on small wind turbine blades. Wind turbine icing occurs when supercooled water droplets hit a wind turbine at temperatures below 0°C (Ice Accretion Simulation December 1997). Without access to a refrigerated wind tunnel the investigation was performed simply with water droplets that were not supercooled.

The goal of the experiment was to get a sense of the interaction between a water droplet being carried by the freestream air flow and the rotating blade of a wind turbine. High speed photography is used to capture this interaction at a moment in time. The goal of the experiment was to determine where the water droplets impact on the blade, if the droplets are affected by the changing flow field around the blade, and what happens to the water of the droplet after impact.

4.1 Experimental Setup

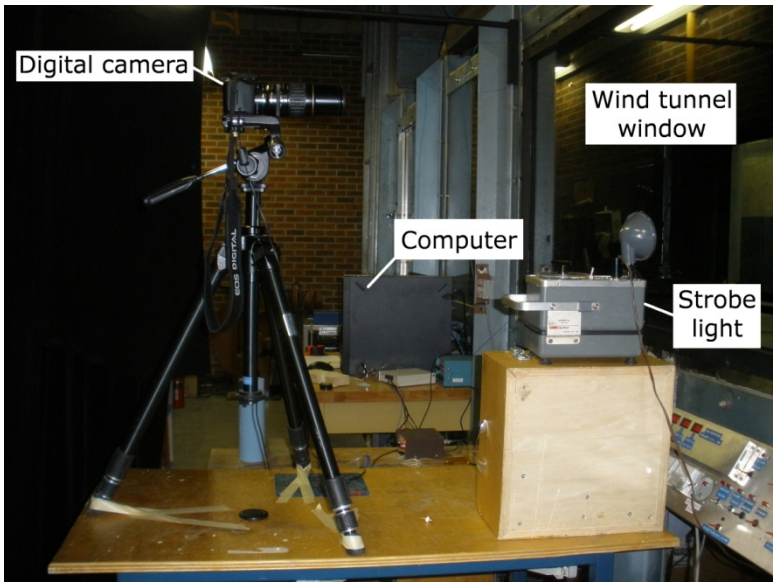

Figure 4.1 - Photograph of camera and strobe light arrangement outside of the wind tunnel

An experiment was set up to photograph water droplets as they impacted on a rotating wind turbine blade. The arrangement of the experiment can be seen in Figure 4.1.

4.1.1 Wind Tunnel

The wind tunnel was the Department of Mechanical Engineering low-speed wind tunnel described in Section 2.1.3.

4.1.2 Wind Turbine

The wind turbine was the Ampair 100 described in Section 2.1.2 and installed as described in Section 2.1.4.

4.1.3 Droplet Generator

A droplet generator was constructed from a BD Ultra-Fine 1cc insulin syringe. It had a ¼" (6 mm) outer diameter body with a 29 gauge, 13 mm (1/2") long needle. The syringe plunger was removed and the finger flanges were cut off to allow it to be connected to a ¼" (6 mm) outer diameter polypropylene tubing with Swagelok compression fittings. A photograph of the droplet generator is shown in Figure 4.2. Specifications for the tubing can be found in Table 4.1. The tubing was connected to a domestic tap as a water source. A needle valve was connected between the water source and the syringe to as an isolation valve and flow throttle for the droplet generator.

Table 4.1 - Specifications of droplet generator tubing

Brand	Omega	
Model	TYPP-14170-100	
Inner Diameter	4.3 mm	(0.17")
Outer Diameter	6.4 mm	(1/4")
Material	polypropylene	
Durometer, 15 secs.	75, Shore D	
Specific Gravity	0.9	
Operating Temperature	-40 to 121 °C	(-40 to 250 °F)
Tensile Strength	3700 psig	(25,511 kPag)

The syringe was mounted to the ceiling of the wind tunnel approximately 1.7 m (5'-7") upstream of the wind turbine. It was mounted at 0.4 m (16") from wind turbine centerline so that the droplets would hit near the tip of the rotor blades.

The droplets were sized by first photographing a sheet of graph paper of 5x5 mm squares in the focal plane of the camera. The graph paper was used to calibrate number of pixels to millimeters. It was determined that the water droplets were, on average, 2.7 mm in diameter.

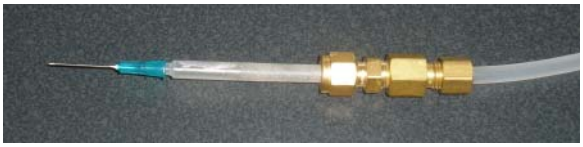

Figure 4.2 - Droplet generator

(a) **(b)**

Figure 4.3 - Photographs of droplets for sizing purposes

Figure 4.3 shows examples of the droplet photographs used to measure droplet diameter. The figure shows a nearly spherical droplet silhouetted against a light background. A silhouetted droplet was the easiest to use to determine the extents of the droplet for measurement purposes.

4.1.4 Illumination

Illumination for the photography was provided by a strobe light by General Radio Co. (GenRad) model Strobotac Type 1531. It was mounted outside of the wind tunnel with the bulb aligned to shine through the glass window in the wind tunnel wall.

The strobe light was actuated using a photodetector and delay box previously designed for high-speed photography by Bernie Faulkner, Specialist Technician in the Department of Mechanical Engineering shop. The photodetector was comprised of an infrared emitter and a detector pair mounted in the two prongs of a U-tube. The device was triggered if anything passed between the tips of the U-tube and interrupted the infrared beam. A delay box in the system allowed control of how much time would pass between the beam being interrupted and the trigger being fired.

The photodetector U-tube was mounted to the ceiling of the wind tunnel below and slightly downstream of the droplet generator. It was carefully positioned such that when the wind speed in the tunnel carried a water droplet through mid-height of the rotor plane there was a good chance the droplet would pass through the trigger beam. The delax box was set such that the strobe light fired when the water droplet was passing through the rotor plane.

4.1.5 Camera

Images of the droplet were captured with a Canon EOS Rebel XSi digital SLR camera. Specifications of this camera are listed in Table 4.2. It was fitted with a 200 mm lens with a 2x zoom teleconverter and was mounted on a tripod approximately 0.58 m (23") from the wind tunnel wall. The field of view was 86 mm x 57 mm. The camera was controlled remotely via USB cable using the EOS Utility software.

Table 4.2 - Specifications of the Canon EOS Rebel XSi camera

Type:	Digital, single-lens reflex, AF/AE camera with built-in flash
Image sensor:	High-sensitivity, high-resolution, large single-plate APS-C CMOS sensor, size 22.2 x 14.8 mm, 1.6x focal length multiplier
Effective pixels:	Approx. 12.20 megapixels
Total pixels:	Approx 12.40 megapixels
Aspect ratio:	3:2 (horizontal : vertical)
Colour filter system:	RGB primary colour filter
Low-pass filter:	Located in front of the image sensor, non-removable
ISO speed range	Basic Zone modes ISO 100-800 Creative Zone modes ISO 100-1600
Shutter type:	Electronically-controlled, focal plane shutter
Shutter speeds:	1/4000 sec to 1/60 sec, X-sync at 1/200 sec 1/4000 sec to 30 sec, bulb

The camera was set up to continually take a photograph every 5 seconds with an exposure of 2 seconds and ISO 1600. F-number was set at 5.26. All of the lights in the wind tunnel chamber were turned off so that the only illumination would be the strobe light if a droplet passed through the detector. It was only chance that determined if the strobe light fired during a camera exposure and if the droplet was captured impacting the wind turbine blade.

4.2 Results

Images of droplets near or impacting the wind turbine blade are shown in Figures 4.4 to 4.11. In these images the freestream wind speed is 6.8 m/s (15 mph). The rotor is turning at 560 rpm which results in a blade tip speed of 27.2 m/s (61 mph). The blade is moving up in the images. The large droplets are strongly affected by gravity and do not follow the flow streamlines. They are moving down and are being pushed to the left by the wind. They either pass through the rotor or are struck by a blade.

Figure 4.4 shows the droplet in the freestream with the blade is approaching from below. The images show the droplets are nearly spherical.

Figure 4.5 shows the droplet very close to or at the moment of impact with the suction side of the leading edge of the blade. The shape of the droplets remain nearly spherical.

The changing flow field over the airfoil does not seem to affect the shape of the droplet in any way. The droplet only begins to deform upon impact with the blade surface.

Figure 4.6 shows the droplet very close to or at the moment of impact with the pressure side of the leading edge of the blade. Again, the changing flow field over the airfoil does not seem to affect the shape of the droplet and the droplet only begins to deform upon impact with the blade.

Figure 4.7 shows the droplets after they have been struck by the leading edge of the blade. Water is splashed both upstream and downstream of the airfoil. As the blade passes through the droplet splashed water takes the form of a continuous stream or a dense cloud of smaller droplets. (Figure 4.7(a) also shows a ghost image of a whole droplet. This is due to an instance when the strobe flashed twice during the camera exposure to produce a double exposure. This droplet should be ignored. It is not present in the exposure that includes the blade.)

Figure 4.8 shows images several moments after a blade-droplet impact. The droplet has been struck by the suction side of the blade. The droplet has either struck near the leading edge and the water has flowed along the suction side of the blade (known as run-back) or the droplet was struck a glancing blow by the suction side of the blade some distance away from the leading edge. In Figure 4.8(a) the water visible seems to be separating from the blade surface but the secondary droplets seem to be re-impinging onto the blade towards the trailing edge. In Figure 4.8(b) the water visible is also separating from the blade surface but the secondary droplets seem to be re-entering the flow downstream of the blade.

Figure 4.9 shows post-impact water droplets near the trailing edge of the blade. Again, the water flowed some distance along the suction side of the blade and is now separating from the blade surface. In Figure 4.9(a) some water seems to be re-entering the flow. In Figure 4.9(b) the water seems to be re-impinging onto the blade surface.

Figure 4.10 shows water droplets after impact with the suction side of the blade as the run-back re-enters the flow beyond the trailing edge of the blade. Figure 4.10(a) shows the water leaving the surface as a nearly continuous sheet of water being spread out and pushed downstream by the air flow. Figure 4.10(b) shows the water streaming off the trailing edge as a series of smaller droplets and being pushed downstream.

Figure 4.11 shows the remains of a droplet impact on the pressure side of the blade. The water is not flowing along the surface of the blade. The water could have been ejected into the flow by an impact on the leading edge as shown in Figure 4.7 or the droplet could have hit somewhere on the pressure side of the blade and was dealt a glancing blow without sticking to the surface.

Literature on blade icing describe ice formations on the pressure side of the blade with ice only on the first 15% chord of the suction side (Bose 1992) (Hochart, Fortin and Perron 2008). This is because the icing events being simulated are using water droplets with a diameter of 20-40 µm. Droplets of this size follow the flow much better than the large droplets used in this experiment and so impact in the vicinity of the stagnation point on the leading edge, which is typically on the pressure side of the blade. Run-back then occurs chiefly on the pressure side. Studies of large droplet (40-400 µm) ice accretion on aircraft airfoils mention that ice accretes further along the airfoil but that icing favours the pressure side (Addy Jr., Miller and Ide 1996).

Many pictures captured the run-back of the droplet separating from the suction side of the blade and re-impinging (secondary impingement). Despite the orientation of the pressure side of the blade to the flow, very few of the photographs caught the droplet impacting on the pressure side. No photographs caught the splash on the pressure side, only the remains of the droplet after it had experienced a glancing blow with the pressure side. No run-back along the pressure side was evident in the photographs.

(a) **(b)**

Figure 4.4 - Blade approaching droplet

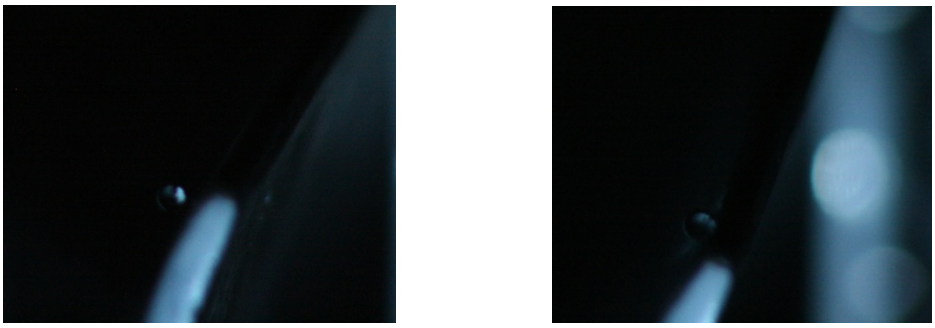

(a) **(b)**

Figure 4.5 - Droplet impacting blade on suction side

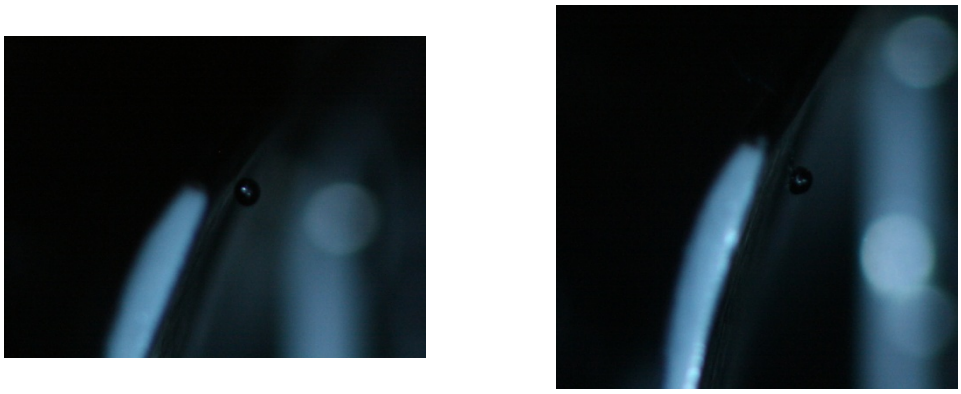

(a) (b)

Figure 4.6 - Droplet impacting blade on pressure side

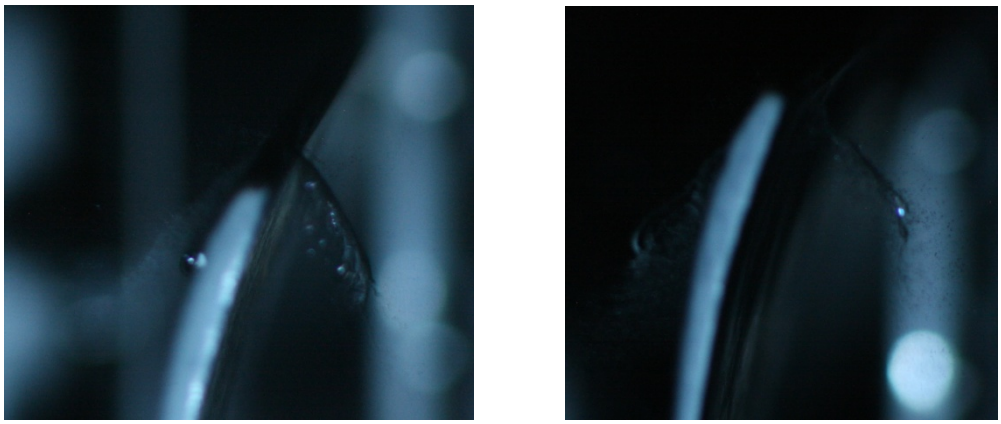

(a) (b)

Figure 4.7 - Droplet splash on leading edge

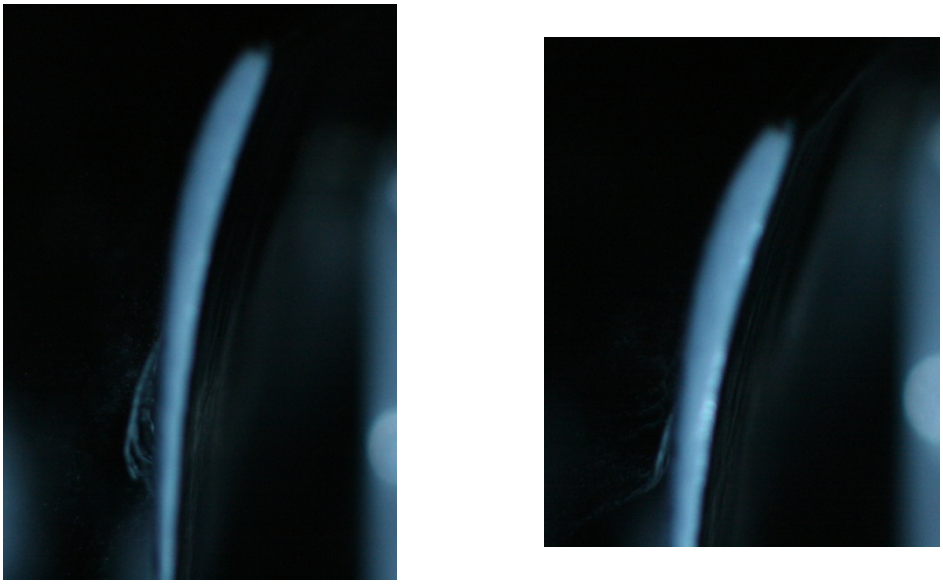

(a) (b)

Figure 4.8 - Droplet run-back on suction side of blade

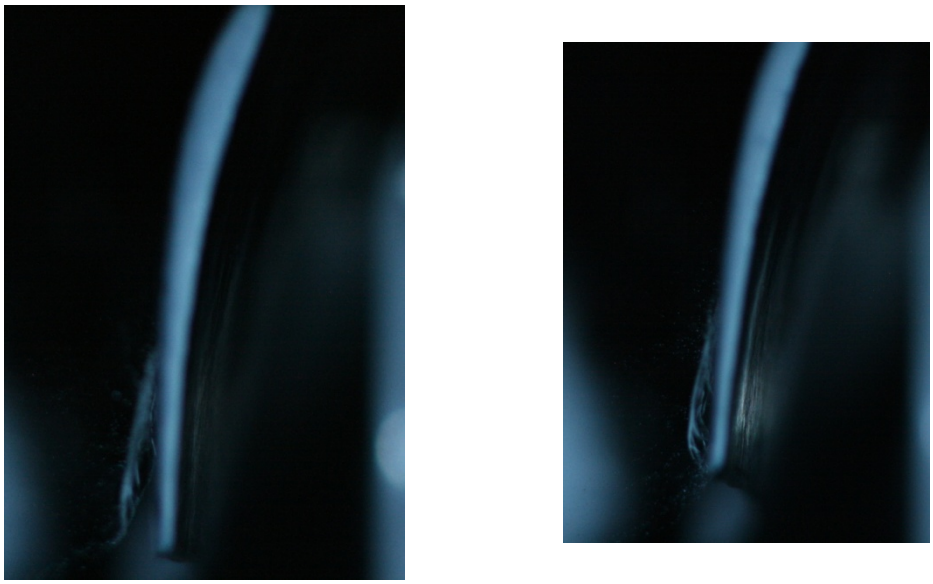

(a) **(b)**

Figure 4.9 - Droplet run-back on suction side of blade trailing edge

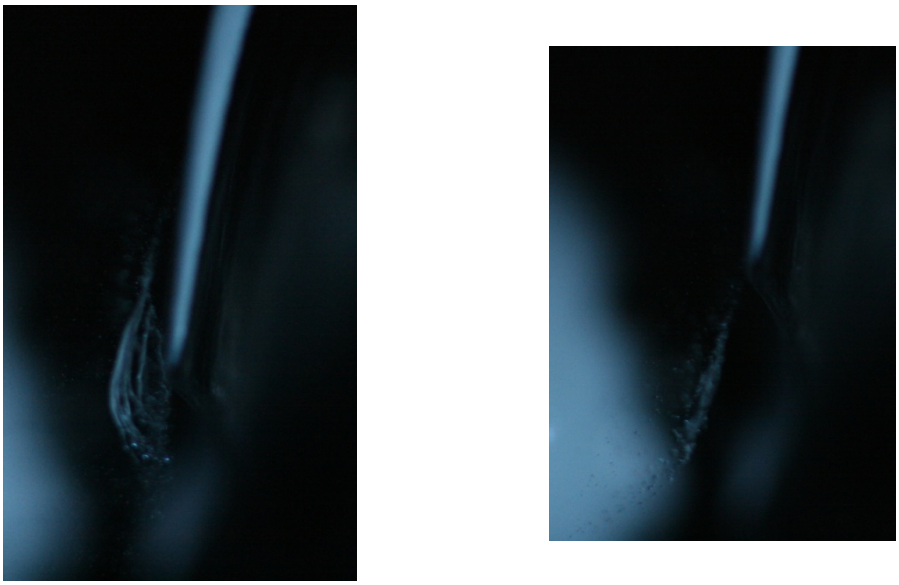

(a) **(b)**

Figure 4.10 - Droplet run-back re-entering flow from suction side

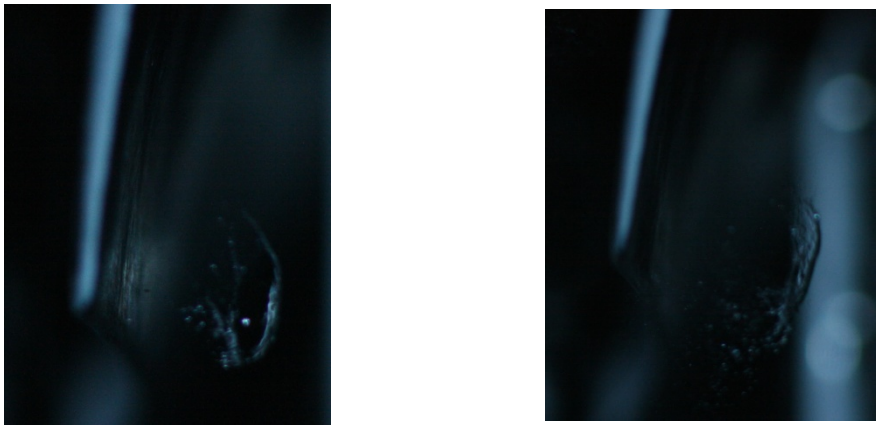

(a) (b)

Figure 4.11 - Droplet in flow after impact with pressure side of blade

4.3 Conclusions

The droplet generator used produced very large droplets with an average diameter of 2.7 mm. Droplet size should be reduced to more closely resemble icing events in the field. In order to resolve these smaller droplets different optics would be required that could provide a much smaller field of view at a focal distance of approximately 1.2 m.

Despite the literature reporting that icing occurs almost entirely on the pressure side of airfoils, for both wind turbine blades and airplane wings, the observed droplet impacts and water run-back occurred almost entirely on the suction side of the blades. No run-back was observed on the pressure side of the blade.

5 Flow Visualization of Air around a Rotating Wind Turbine Blade using Particle Image Velocimetry

The aim of the experiment was to develop an arrangement that would produce vector flow fields around a rotating wind turbine blade in a wind tunnel using stereo particle image velocimetry.

5.1 The PIV Methodology

5.1.1 Planar PIV

The most basic form of PIV is known as Planar PIV. Only a single camera is required and as such only the two-dimensional (2D) components of velocity of the particles in the flow projected onto the illumination plane can be determined. The third component of velocity out of the illumination plane is lost.

5.1.2 Experimental Apparatus

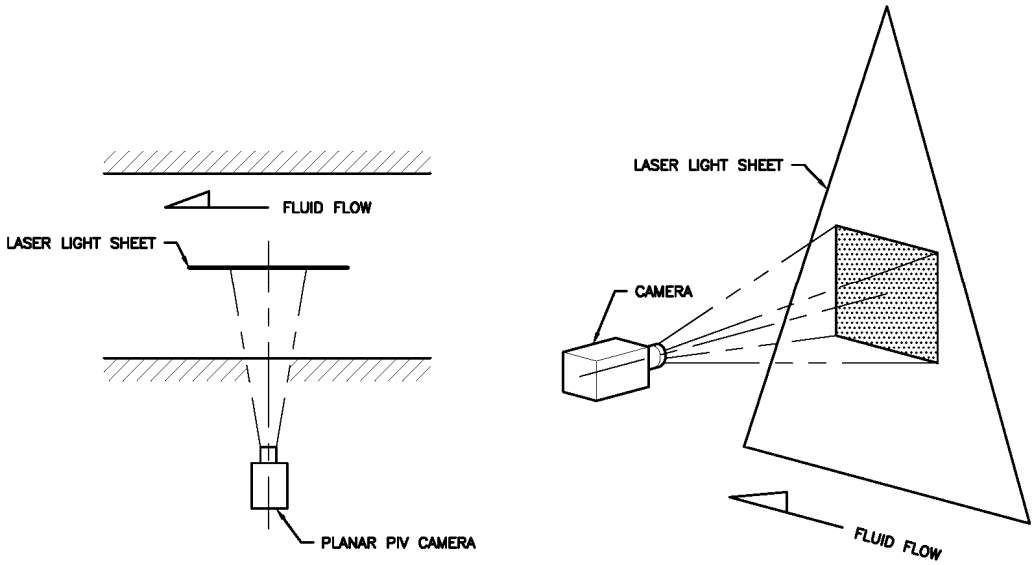

Figure 5.1 - Arrangement of planar PIV

The experimental apparatus is set up generally as shown in Figure 5.1. The flow is homogeneously seeded with tracer particles that are assumed to follow the fluid motion. The area in which the velocity field is desired is illuminated with the pulse of a laser, typically a high energy-density Nd:YAG (neodymium-doped yttrium aluminum garnet) laser. A camera is arranged perpendicular to the laser light sheet.

5.1.3 Calibration

A calibration process is performed first. The accuracy of the PIV system depends on how well the image of the object relates to the object itself. Errors can be introduced by

focusing errors of the lenses (spherical aberration, astigmatism, and coma) or by magnification errors caused by lens imperfections and refraction through objects between the camera and the laser sheet. A target, usually a grid of known dimensions is located in the plane of the laser light sheet. Using the target, the camera can be correctly focused and it can be seen if any distortion is being caused by the system optics. Computer software compares the image of the calibration target with the known dimensions of the target and calculates the appropriate corrections to ensure the object plane is mapped correctly to the image plane (Soloff, Adrian and Liu 1997).

5.1.4 Image Processing

The process of capturing the images involves illuminating the particles and capturing them as images. The laser produces a pulse of light in the order of 10 nanoseconds long to illuminate the particles in the fluid and capture them in that moment of time. At that moment a camera takes an image of a portion (defined by the camera's field of view) of the particles within the laser light sheet. Then, a known interval of time later, the laser pulses again and the camera takes a second image.

Before the velocity vectors can be calculated the images are digitally pre-processed. Calculation of the velocity vectors requires the computer to be able to correlate the change in position of particles between the two images separated by the known time interval. Factors that interfere with identifying this particle image pair are non-uniformities in the background (ambient light, reflections, etc.) and variations in the intensity of the laser pulses from one image to the next. Non-uniformities are removed by applying a highpass filter to the image. Variations in laser pulse intensity cause a variation in grey-scales of the particle image and this is corrected by binarizing the image. The filtered and binarized image is then ready for further processing to calculate the velocity vectors (Willert 1997).

The images are then digitally processed to calculate the velocity vectors. First, based on the calibration information taken earlier, the images are de-warped to reduce the effect of distortion due to the optical system. Then, using a process outlined in Willert and Gharib (1991) the images are compared to determine the distance and direction in which the particles moved in the time interval between images. Each image is sub-divided into a grid of interrogation windows of, for example, 32x32 pixels in size as shown in Figure 5.2. Each window of the first image is compared to the same window of the second image as shown in Figure 5.3. Using an algorithm that correlates light intensities between the two images, the particles are separated from background noise intensity as shown in Figure 5.4. A high peak indicates that the same particles in the first image are found in the second image. The distance and direction in the plane of the laser light sheet is calculated from the difference from the second image to the first as shown in Figure 5.5. An average of these displacements over the grid is determined to be the average velocity vector in the plane of the laser light sheet and is shown as a vector arrow for that grid as shown in Figure 5.6. An image composed of all the vectors

for each grid is produced to show the velocity profile of the fluid in the camera's field of view (FOV) in the plane of the laser light sheet as shown in Figure 5.7.

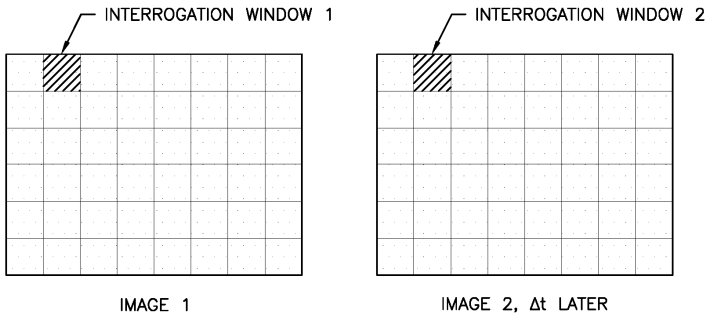

Figure 5.2 - Image pair divided into interrogation windows

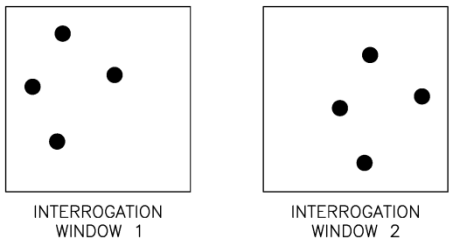

Figure 5.3 – Interrogation from each windows are compared

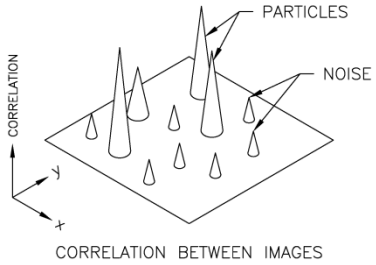

Figure 5.4 - Correlation algorithm is applied between images to detect particles

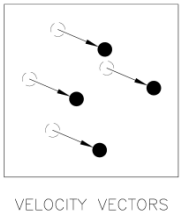

Figure 5.5 - Particle location shift between windows is used to calculate velocity vectors

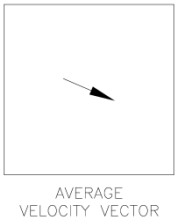

Figure 5.6 - Average velocity vector of all particles is displayed in the window

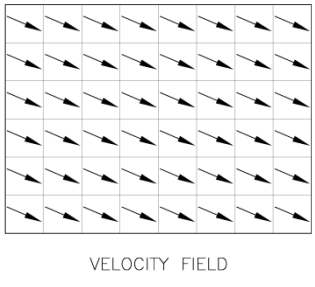

Figure 5.7 - The complete image made up of all average velocity vectors for each interrogation window

5.1.5 Stereo PIV

Stereo PIV is an improvement over Planar PIV. While Planar PIV determines a two component velocity vector in two-dimensional space, losing out-of-plane information, Stereo PIV can determine three component velocity vectors in two-dimensional space. Thus, the out-of-plane component of velocity within the thickness of the laser light sheet is calculated and retained. Prasad (2000) provides an excellent review paper on this subject, the key points of which are summarized below.

5.1.5.1 *Experimental Apparatus*

Stereo PIV uses the same basic process of Planar PIV except two cameras separated by a known angle view the same area of the laser light sheet at the same time as shown in Figure 5.8. The accuracy of the out-of-plane velocity vector increases as the separation angle approaches 90° (Willert 1997). The cameras view the illuminated plane from two separate locations which means the cameras can detect three-dimensional (3D) information similar to a pair of human eyes.

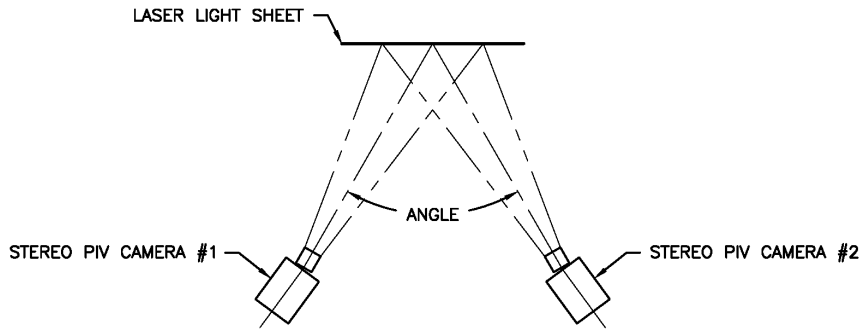

Figure 5.8 - Stereo PIV uses two cameras focused on the target with an angle between them

5.1.5.2 *Calibration*

Calibration of the camera system is required before the experiment can begin. De-warping like that for Planar PIV is required to correct for the distortion of the optical system. In addition, the de-warping procedure must account for the perspective effect of one edge of the laser light sheet being further away than the other. The target contains distinctive markings (such as a triangle and a square) which allows the computer software to directionally orient the image for each camera. The user manually selects the distinctive marks in order to allow the software to recognize the correct orientation. If a target with a known 3D component like that in Figure 5.9 is used, the calibration software can also use this information to determine the angle between the cameras. (Willert 1997) (Soloff, Adrian and Liu 1997) (Fei and Merzkirch 2004) (Wieneke 2005)

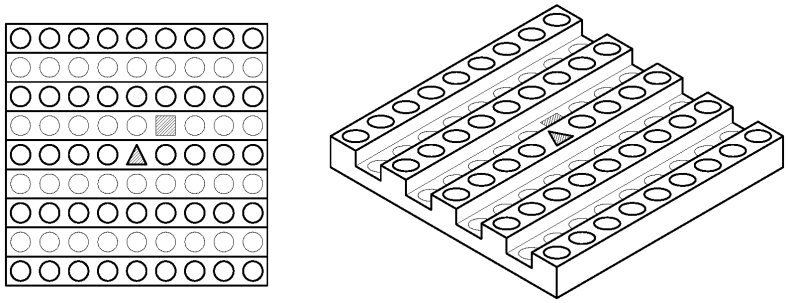

Figure 5.9 - Three-dimensional calibration target

The fact that the illumination plane is not perpendicular to the camera causes another problem specific to Stereo PIV. One edge of the laser light sheet is closer to the camera than the other as shown in Figure 5.10. Since the scattered light from the particles is generally of low intensity, the camera lenses need to be able to collect as much light as possible, which requires low f-numbers (f#). Low f# causes a short depth of field (DOF). Only the portion of the laser light sheet within the camera's DOF will be in focus. It is possible to correct for this by rotating the camera's image plane with respect to the lens plane in the manner shown in Figure 5.11. This is known as the Scheimpflug condition.

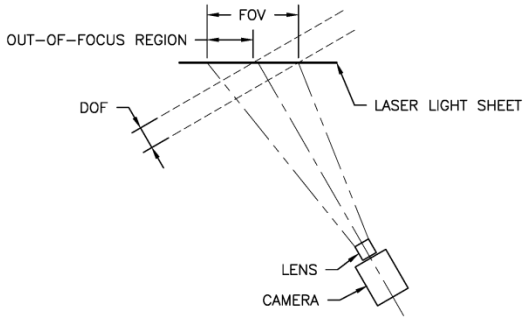

Figure 5.10 - Areas of the FOV outside the DOF will be out of focus

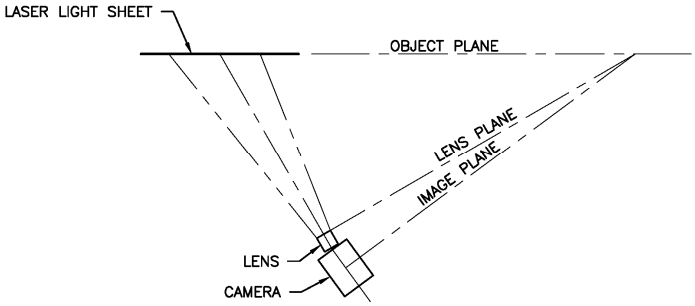

Figure 5.11 - Satisfying the Scheimpflug condition

5.1.5.3 *Image processing*

Another consideration caused by the cameras being separated at an angle is the intensity of scattered light. Small particles do not scatter light evenly in all directions. Light scattered forward of the particle is much greater than towards the back or to the side according to Mie scattering theory. The cameras will most likely receive different intensities of light based on their location in terms of the scattering profile of the tracer particles. Pre-processing of the images is necessary to correct for the variation in intensities to allow for correlation of particles between camera images.

Before the vector calculations can occur, image pre-processing is carried out in a similar fashion to Planar PIV. The images are filtered for background noise, corrected for light intensity variation and binarized to allow for particle images to be located in the pair of images.

The velocity vectors of the particles are then calculated for the image pairs. The process is similar to Planar PIV described above. The difference is that the out-of-plane velocity component can also be calculated. The out-of-plane velocity component is determined by the difference in the particle displacements as viewed by the two cameras. The geometry required to acquire the velocity components is shown in Willert (1997). The images are then presented as an image of 2D velocity vectors superimposed on a colour gradient plot representing the magnitude of the out-of-plane velocity component.

The size of the particle image should be at least 2 pixels in diameter. If the particle image is less than one pixel in diameter then regardless of where the particle is in the flow representing 1 pixel on the sensor, it will be registered at the same place by the correlation algorithm. This will result an error, known as pixel locking or peak locking, in the calculation of the velocity vector.

Stereo PIV requires about 15 particles per interrogation window to give accurate results (Melling 1997). Below this value lowers the signal-to-noise ratio (SNR) which can result in erroneous vectors being calculated. An erroneous vector (also known as spurious or wild vectors) is a vector that has a completely different magnitude or direction compared to its neighbouring vectors that is not due to actual fluid motion, as shown in Figure 5.12. Green, Doolan and Cannon (2000)and Cho, et al. (2005) discuss the post-processing required for the detection and correction of these erroneous vectors. It involves comparing the velocity variation between interrogation windows. If the variation is above a certain value then the vector is replaced with a new vector that is calculated by an interpolation of the neighbouring data. This technique is built into the commercial software package being used (LaVision, DaVis ver. 8.0).

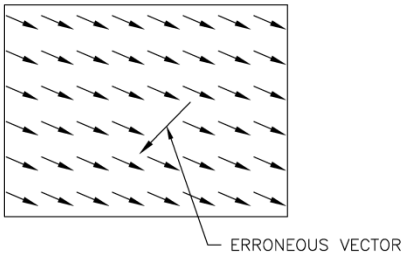

Figure 5.12 - Erroneous vector due to low signal-to-noise ratio

5.1.6 Stereo PIV as Applied to Wind Tunnel Experiments

Using Stereo PIV to measure velocity fields in wind tunnel flows has certain challenges which are addressed by Willert, Raffel, et al. (1996) and Willert (1997). These points are discussed in the sections that follow.

5.1.6.1 *Wind tunnel size*

Wind tunnel experiments tend to be large in size and the cameras are often required to be a long distance away from the measured flow. This requires lenses with long focal lengths. As well, the large volume of flow within a wind tunnel requires large volumes of tracer particles in order to achieve adequate particle density within the interrogation windows on the images. Achieving good particle density requires sophisticated seeding mechanisms that will dispense large volumes of tracer particles of constant size at homogeneous particle densities. Not achieving good particle density results in poor SNR.

5.1.6.2 *Tracer Particles*

The size of the tracer particles is important. For the particles to be assumed to follow the flow of air they should be 1 µm or less in diameter. (Hunter and Nichols 1985) (Melling 1997) However, the particles must be able to scatter enough light such that they will provide a good SNR for the cameras. Melling (1997) provides a table of particles used in gas flows, such as aluminum oxide, titanium oxide (which Mengel and Mørck (1993) rejects as unsuitable due to the large variation in particle diameter), oils and oil smoke, and discusses the advantages and disadvantages of liquid and solid particle use. For example, liquid particles are easier to produce at a steady rate but can coat viewing window surfaces that could cause the cameras to lose focus. Mørck (1993) also mentions that in order to achieve the desired 15 particles per interrogation window, a particle density of 10^8-10^{10} particles/m^3 is recommended.

More recent examples of flow seeding were found in the literature. Richard, et al. (2003) used olive oil drops of 1 µm diameter. Green, Doolan and Cannon (2000) used vaporized Shell Ondina E.L. oil at 2 µm diameter. Siddiqui, Hangan and Rasouli (2008) used Bis-(2-ethylhexyl) sebacate mist at 0.5 µm diameter. Grant, Smith and Infield, et al. (2005) used polycrystalline particles at 30 µm diameter. (These probably did not follow the flow well but were required in the experiment for their high light-scattering

properties.) McNiel, Pelteir and Reeder (2007) adds polystyrene, dioctylphathalate, and magnesium oxide as examples of solid tracer particles and glycol, water and silicone oil as examples of liquid tracer particles.

McNiel, Pelteir and Reeder (2007) proposes solid CO_2 particles as a new tracer particle for PIV systems. He lists the disadvantages of traditional tracer particles. Tracer particles can coat surfaces, cause abrasion and rust and make clean-up difficult. Polystyrene and glycol have flash points low enough that they could be a fire hazard when passing over the operating surfaces of compressors used in re-circulating wind tunnels. Solid CO_2 particles do not contaminate because they sublimate to gas but the paper admits that controlling the particle size was a challenge which was being worked on at the time of publishing. It would be worthwhile investigating the current progress of this technology.

Small particles will better follow the flow in a wind tunnel but they do not scatter very much light. Willert, Raffel, et al. (1996) advises that in order to maximize the scattered light, high energy-density lasers such as pulsed Nd:YAG lasers, should be used to generate the light sheet. In addition, the cameras should use low f# lenses to capture as much light as possible. Melling (1997) indicates that the intensity of scattered light from a particle is influenced by the particle's scattering cross-section and the intensity ratio of light scattered 90° to the light sheet to light scattered in the direction of the light sheet. Mengel and Mørck (1993) provide a method of predicting PIV performance based on the seed particle light scattering characteristics.

5.2 Experimental Setup

The Ampair 100 wind turbine was installed in the low-speed wind tunnel as previously described in Section 2.1. The wind tunnel ran at a constant wind speed while data were recorded. The experiment was repeated at nominal wind speeds of 5 m/s (11 mph), 7 m/s (16 mph), 9 m/s (20 mph), 11 m/s (25 mph) and 15 m/s (34 mph). The load bank was kept at 5.0 Ohms for all wind speeds. Wind speed was measured by the static-pitot tube mounted in the ceiling of the wind tunnel 4.29 m (169") upstream of the wind turbine mast and Dwyer manometers. Illumination, cameras and smoke generator were set up as shown in Figure 5.13 and described in the sections below.

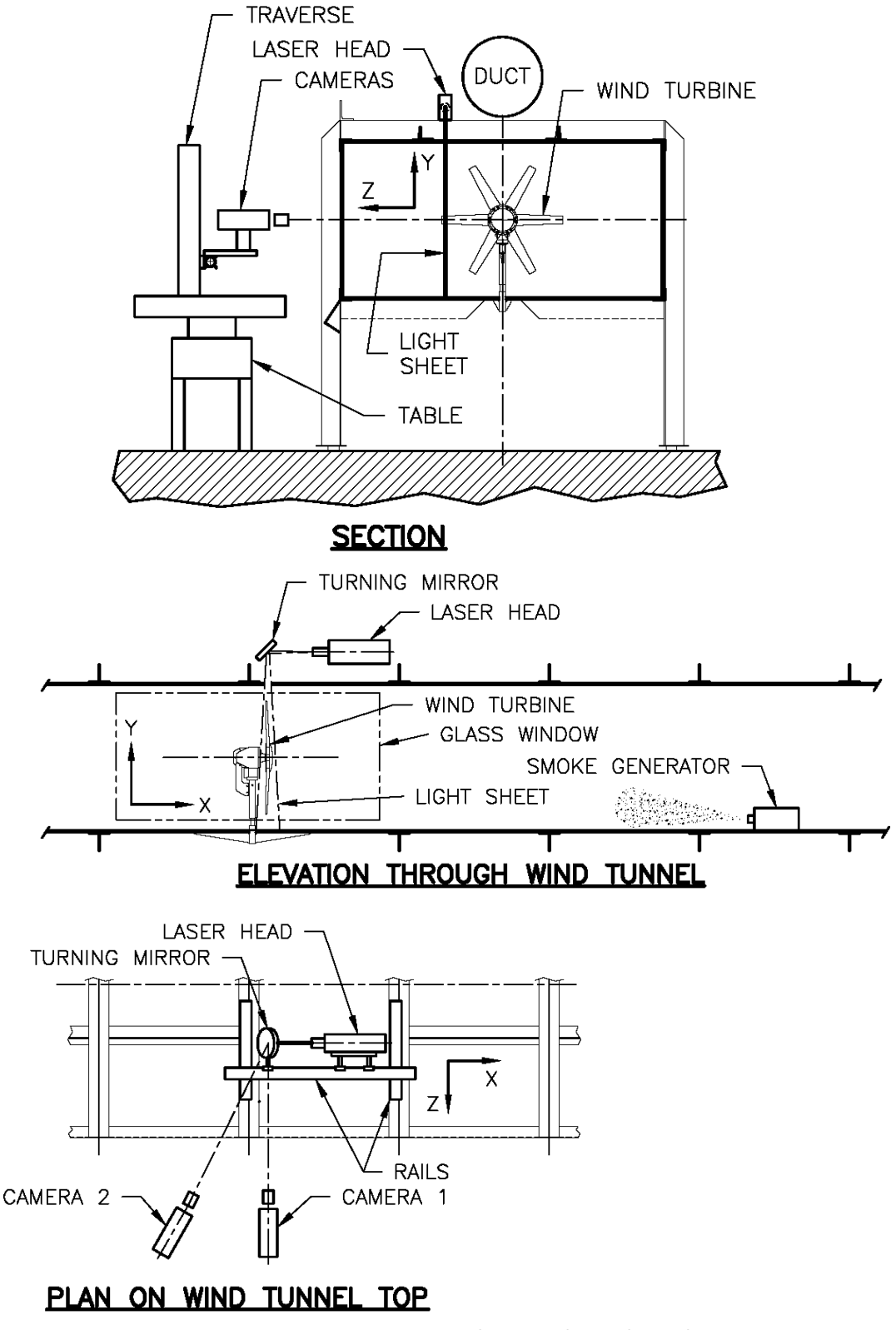

Figure 5.13 - Stereo PIV experimental setup in the wind tunnel

5.2.1 Illumination

The illumination of the tracer particles must be provided by high energy density lasers in order for the small particles to scatter enough light to be imaged onto the camera sensor. Illumination was provided by twin Nd:YAG double-pulsed and Q-switched lasers with an energy of 50 mJ each mounted together with a common emitter head. The lasers are frequency-doubled for an output beam at 532 nm. The laser pulses were formed into a light sheet of approximately 5 mm thick by a cylindrical lens optical system provided by the laser manufacturer. The main specifications of the lasers are presented in Table 5.1.

Table 5.1 - Q-switched Nd:YAG laser specifications

Specification	Value
Manufacturer	New Wave Research
Model	Solo-III-15
Temperature Range	10-30 °C
Relative Humidity Range	20-80% non-condensing
Voltage	95-240 V, 50/60 Hz
Power	800 W
Repitition rate	15 Hz
Energy @ 532 nm	50 mJ
Energy Stability	± 4%
Pulsewidth @ 532 nm	3-5 ns
Beam Diameter	4 mm
Divergence	< 4 mrad
Beam Pointing	< 100 µrad
Jitter	± 1 ns

It was necessary for the laser light sheet to be projected down from the top of the wind tunnel so that the leading edge of the wind turbine blades would be illuminated as they passed through the camera field of view. The laser emitter head was mounted horizontally on the roof of the wind tunnel (exterior to the test section) such that it fired at a mirror that reflected the light sheet down through a slot in the wind tunnel roof. The laser light sheet was oriented vertically in a plane parallel to the centerline of the wind turbine and wind tunnel such that the wind turbine blades would pass through the light sheet as they rotated. This orientation allowed for the major velocity vector of the air to be in plane with the light sheet.

The orientation of laser light sheet required the structure of the wind tunnel roof to be modified slightly to install the slot for the laser sheet to pass through. The slot was designed to allow for the light sheet's position to be adjusted along the length of the blade (though at less than 55% of rotor radius, the blade above would cast a shadow on

the blade in the cameras' field of view), however, this experiment would be carried out at a fixed position near the blade tip. The light sheet location was set at 436 mm (17.2") from wind turbine centerline such that the blades pass through the light sheet at 94% of rotor radius when they are parallel to the wind tunnel floor.

Alignment of the laser sheet was done with a measuring tape and checked by eye. If the light sheet was not perfectly aligned with the x-y plane it would induce an erroneous velocity component in the z-direction. For example, if the light sheet was out of alignment by 1° it would induce a z-component of velocity of 0.09 m/s (0.2 mph) at a freestream velocity of 5 m/s (11.2 mph) and 0.26 m/s (0.6 mph) at a freestream velocity of 15 m/s (33.5 mph). The light sheet could also rotate about the x-axis if the mirror shifted. The error in the z-component of velocity would then be caused by y-component velocity which is generally much smaller than the x-component.

The reflecting mirror was not 100% efficient and some of the laser sheet passed through it. This excess light reflected off the piping and ducting above the wind tunnel and presented a safety hazard. A laser trap was mounted to catch the excess laser light behind the mirror. The laser light sheet in the wind tunnel terminated at the floor of the wind tunnel and presented no dangerous reflections.

Drawings and photographs of the wind tunnel modifications, slot assembly, laser trap and mounting arrangements for the laser and mirror are available in Appendix L.

5.2.2 Seeding of Flow

It was decided to use a fog machine to generate smoke particles to seed the flow in the wind tunnel. A fog machine ("The Fog Machine" brand, approximately 250W) was already available in the Mechanical Engineering Department and the 'fog juice' was readily available and not expensive. The fog machine produces smoke by heating a mixture of deionized water, propylene glycol and triethylene glycol. The individual particle sizes are estimated to be from 1 to 60 microns mass median diameter (Pea Soup Ltd., UK 1997). The fog machine could not produce smoke continuously. The machine required intermittent pauses between jets of smoke to regain heat exchanger temperature.

Ideally, the fog machine would be mounted downstream of the wind turbine and the smoke allowed to circulate through the wind tunnel a few times to ensure a homogeneous particle density. This would also avoid affecting the velocity of the flow field with the jet produced by the fog machine. However, it was found that particle density rapidly decreased for wind speeds of 9 m/s (20 mph) and above when the fog machine was not actively producing smoke upstream of the wind turbine. The fog machine was located approximately 4 m (13'-1") upstream of the wind turbine rotor.

5.2.3 Cameras

The cameras selected for this experiment were PCO Imager Intense, Peltier-cooled, with charge-coupled device (CCD) sensors. They have the specifications listed in Table 5.2.

The cameras were fitted with 100mm Nikon lenses and Scheimpflug adapters. The field of view was 120.4 x 91.0 mm (4.74 x 3.58 in.). The orientation and shape of the blade caused a shadow on the upwind side of the blade where no data could be collected. The f# on both lenses were set at 2.8 (maximum aperture) to collect as much light scattered by the smoke particles as possible. The lights in the room were turned off during recording to reduce the background light intensity.

Table 5.2 - Camera specifications

Specification	Unit	Setpoint	Camera Value
Resolution (hor. X ver.)	Pixel		1376 x 1040
Pixel size (hor. X ver.)	μm		6.45 x 6.45
Sensor format	Inch		2/3
Quantum efficiency	%	@ 520 nm	>= 60
Full well capacity	e^-	per pixel	18,000
Scan rate	MHz		16
Readout noise @ 12.5 MHz	e^-rms	@ gain high @ gain low	4-5 5-6
Readout frequency, frame rate	fps	@ full frame @ binning 2x2	10.0 19.8
Spectral response	nm		280-1000
Exposure time	s		500 ns to 1000 s
Dark current	e^-/pixel-s	@ -12°C & standard light mode	<0.1

The cameras were mounted on a 3D traverse system to control the location of the field of view. Both cameras were mounted on a single rail. Camera 1 was arranged to view the wind turbine blade end-on, nearly perpendicular to the laser light sheet to allow planar PIV calculations to be made with this camera. Camera 2 was arranged to view the wind turbine blade from a downstream position. The angle between the two cameras was 25°. The cameras were 1156 mm (45.51”) from the laser light sheet.

5.2.4 Calibration

The cameras were calibrated using a commercially-produced stereo PIV calibration target (LaVision, Type 22) and a commercial software package (LaVision, DaVis ver. 8.0) prior to performing the experiment. The Scheimpflug adapters were used to ensure the entire field of view was in focus. After data were collected, a second calibration was

performed using the collected data itself. The software prompts the user to select up to 15 points that can be identified in images from both cameras. The software then calculates corrections and dewarps the images based on the selections.

5.2.5 Timing and Image Capture

It is important that the cameras are timed to capture an image at the exact moment that the laser fires its pulse. As well, the precise time separation between laser pulses is necessary for accurate velocity vector calculation. The timing mechanism was similar to that described in Grant et al. (1991). The once-per-revolution signal from the reflective IR detector described in Section 2.2.2 was sent to the programmable timing unit (PTU) installed in the PIV computer. The PTU requires a TTL input so the IR sensor output had to be adjusted to meet TTL voltage specifications with a circuit designed and built by Rick Conrad, Electronic Engineering Technician in the Mechanical Engineering Department. The PTU calculated the rotor rotation frequency and used that to calculate an appropriate delay before the first laser pulse and enabled the laser light sheet to catch the blade at exactly the same place each time. A phase angle delay was also chosen in the commercial software package to adjust where in the FOV the blade appeared. The PTU also calculated the triggers required for the second laser and both cameras.

The duration of the laser pulse allows the particles to be imaged at a moment in time. The shorter the pulse, the less the particles will move during the image capture and the less the particles will seem to be smeared. For no smear to occur, the laser pulse duration has to less than the time it would take a particle to move the distance represented by one pixel, i.e. 87.5 µm. At 15 m/s (34 mph) wind speed the rotor is turning at about 3150 rpm so it would take 31 ns for a particle near the rotor blade to travel across one pixel. The laser has a pulsewidth (duration) of 3-5 ns, therefore the particle image will have no smearing.

For good Stereo PIV results, the particles should travel about one-quarter the distance of the interrogation window (Mengel & Mørck, 1993). Assuming the interrogation windows are 16x16 pixels a particle should travel approximately 4 pixels. Equation 29 was used to determine the time between laser pulses, dt. The velocity used was the freestream velocity of the wind tunnel and 5 or 7 pixels were selected as the pixel shift.

$$dt\ (s) = \frac{pixel\ shift * field\ of\ view\ (mm) * number\ of\ kilopixels}{velocity\ (\frac{m}{s})} \qquad \text{(Eq. 29)}$$

The maximum repetition rate of the lasers is 20 Hz, which is one pulse every 0.05 seconds. To be able to produce two pulses at 15 µs apart, for example, there must be two lasers. As shown in Figure 5.14, the first laser's flashlamp is triggered by the LED emitter/detector via the PTU time delay generator. The laser pulses when the resonator

is charged and the Q-switch releases the beam (time Q1). The second flashlamp is triggered 15 µs after the first flashlamp to produce the time separation between the laser pulses.

The cameras operated in double-shutter mode in order to take two full resolution images in a very short amount of time. They were triggered by the IR sensor via the PTU at time Q1 less 5 µs. This gave time for the camera's phase-in period (0-40 ns) and the intrinsic time for the signal to travel the length of the signal cable (4.5 µs).

For each wind speed, the experiment was repeated three times with different phase angle delays to adjust the field of view. One field of view captured the entire blade airfoil, the second advanced the phase angle to capture the leading half of the blade and more of the flow field ahead of the leading edge, and the third retarded the phase angle to capture the trailing half of the blade and more of the flow field behind the trailing edge. Examples of the three fields of view are shown in Figure 5.15.

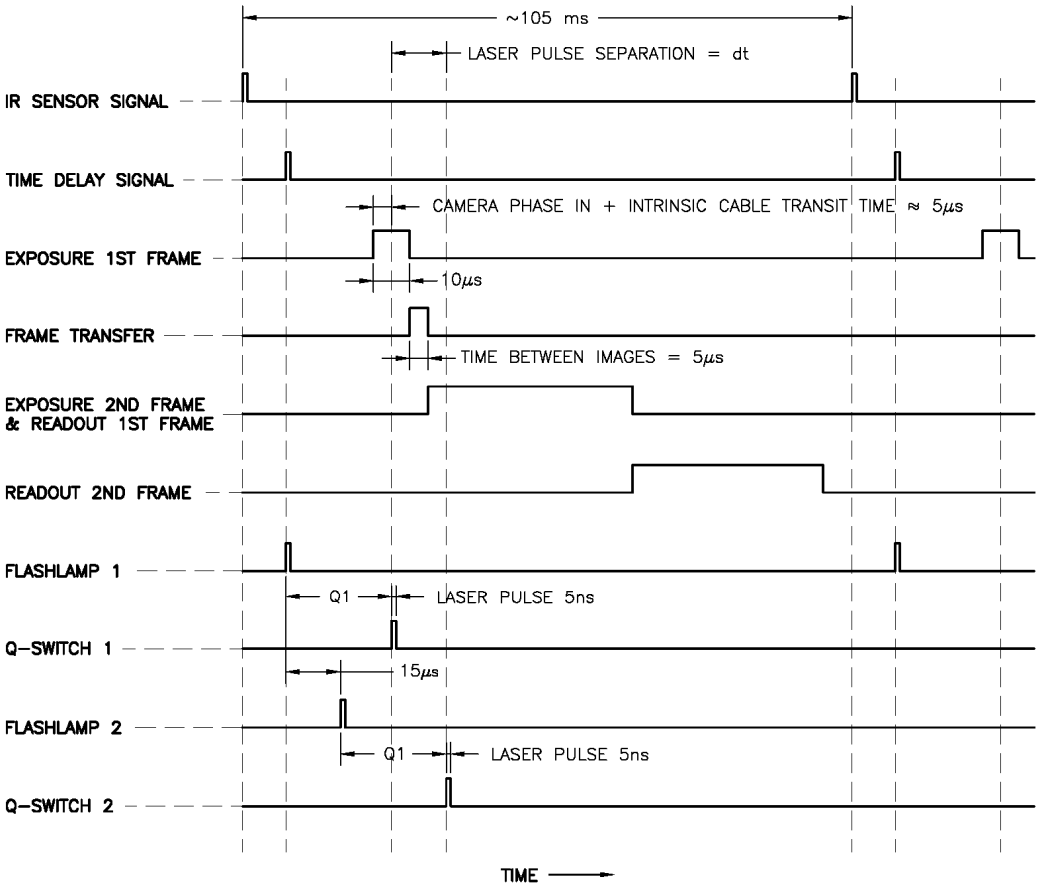

Figure 5.14 - PIV timing diagram

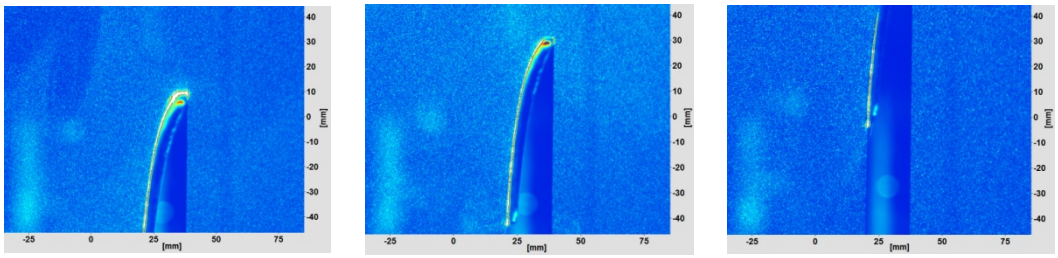

(a) lead (b) full (c) trail

Figure 5.15 - Examples of fields of view

5.3 Data Processing

5.3.1 Image recording

Each camera records a pair of images. This results in a total of four frames. Frame 0 and 1 are the image pair of camera 1 and frame 2 and frame 3 are the image pair of camera 2. These images were processed using the commercial software package to calculate a stereo vector field of the flow around the wind turbine blade. There were vector data lost on the upwind side of the blade because camera 2 was positioned downstream of the blade. The tip of the blade protruded through the laser light sheet and therefore the tip obscured a portion of the flow upstream of the blade. The image pair from camera 1 was also processed alone as planar PIV because it had a good view of both sides of the blade (though the shadow still obscured data).

Intensity values in each pixel represent the amount of light reflected from the smoke particles captured by the camera. The intensities range from 150 to 300 counts out of a maximum value of 4096. Background intensities were approximately 50 counts. These represent very low intensities for PIV data that could be lost in background noise. However, strong correlation peaks were calculated for the two image pairs with 64 x 64 pixel interrogation windows so good velocity data could be extracted.

An example of the four frames are shown in Figure 5.16. It can be seen in the images that the image pair of camera 1 contain strong laser reflections on the blade surface and this obscures regions ahead of the leading edge. On the suction side of the blade light reflecting off the blade surface behind the light sheet also obscures particle images.

For each wind speed a total of 250 image sets were recorded with each camera. PIV vector fields were calculated for each image set. The vectors were then averaged over the 250 image sets by the commercial software package to produce a final vector field. The rms velocity was also calculated to determine if there were large variations between the individual image sets and the final average.

For wind speeds of 9 m/s (20 mph) and above, there were problems with low seeding density when the smoke machine paused. During these low seeding events there were insufficient data with which to calculate vectors and many of those that were calculated

were wild vectors. An example of a vector field calculated during a low seeding event is shown in Figure 5.17. In order to improve the final average vector field, the image sets with low seeding density were removed and the set was re-processed. A list of the deleted images from each set is contained in Table 5.3.

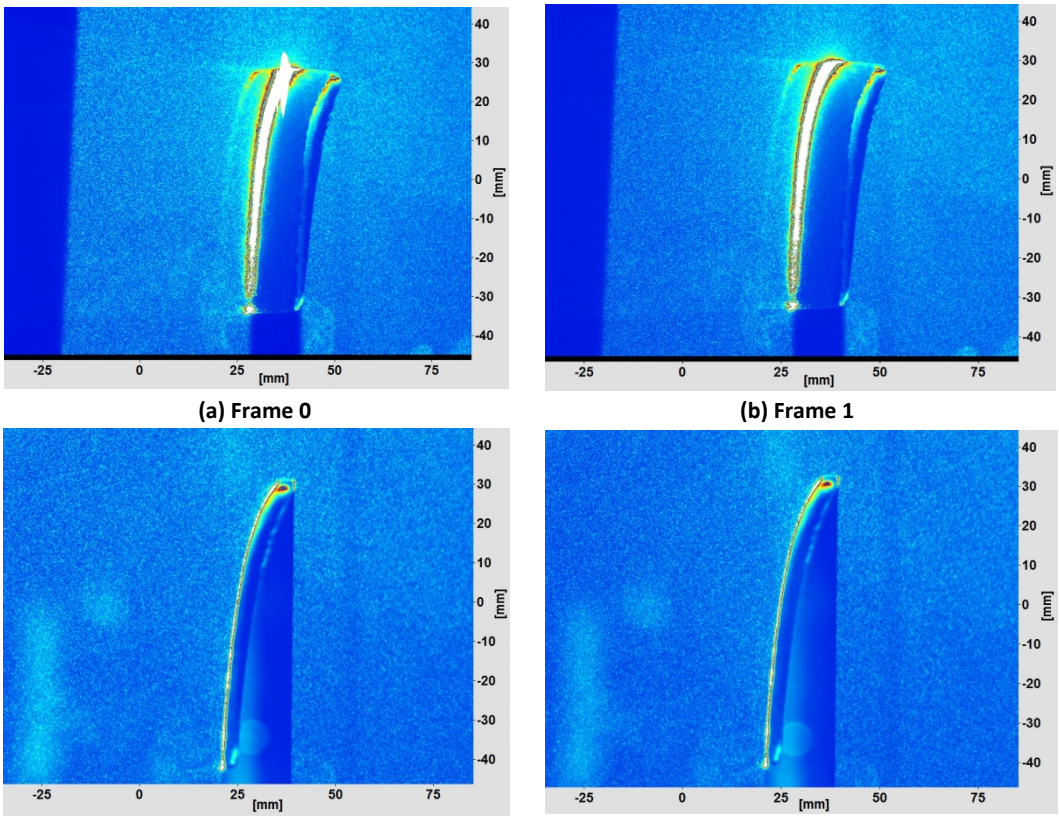

(a) Frame 0 **(b) Frame 1**

(c) Frame 2 **(d) Frame 3**

Figure 5.16 - Examples of image frames

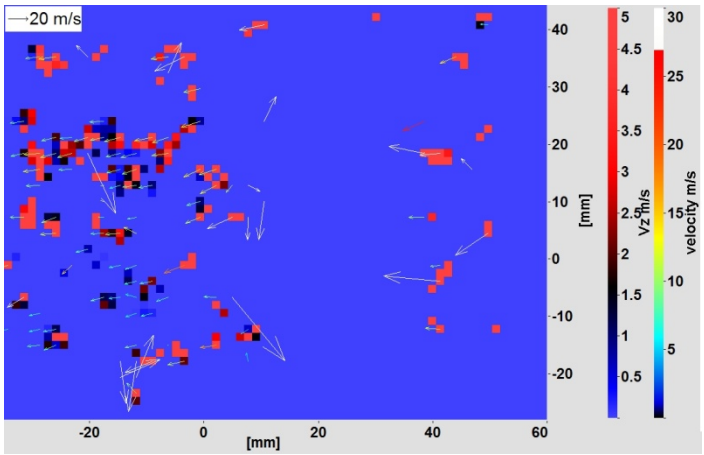

Figure 5.17 - Example of vector field calculated during a time of low seeding. 15 m/s nominal wind speed.

Table 5.3 - Images deleted from set due to lack of seeding

Data Set	Images Removed	Final Number of Images in Set
9 m/s full 3D	34-45, 92-111, 156-172, 217-234	183
9m/s lead 3D	46-63, 108-125, 170-188, 231-250	175
9 m/s trail 3D	11-22, 68-85, 135-140, 143-148, 194-209	191
11 m/s full 3D	1-7, 45-72, 109-116, 119-136, 174-201, 240-250	150
11 m/s lead 3D	1-8, 45-71, 107-133, 170-197, 232-250	141
11 m/s trail 3D	1-7, 45-70, 105-134, 170-198, 235-250	142
15 m/s full 3D	1-7, 32-43, 45-76, 102-143, 169-212, 237-250	99
15 m/s lead 3D	26-29, 32-70, 92-135, 159-202, 226-250	94
15 m/s trail 3D	1-7, 33-35, 37-75, 100-110, 112-135, 137-143, 169-185, 187-212, 237-240, 244-250	104

5.3.2 Image Preprocessing

All images were preprocessed in two ways. First, a geometric mask was applied. For each of the four frames of the first image in the data set, the airfoil and shadow were traced and the area within this geometric shape was removed from the data set. A new mask was created for each wind speed data set. The mask was applied to all 250 images in the data set. Due to variations in angular velocity of the rotor, the blade appeared in slightly different locations in each of the 250 images and therefore the mask was not completely effective. In some instances, the leading edge of the blade would be visible above the masked region and in other instances the leading edge would be below the edge of the mask and so a portion of the flow would be masked instead. This would result in errors in the final averaging of the vectors.

The second preprocessing step was to apply a high pass filter subtract a sliding background from the images. The filter length was set to 2 pixels. This improved the clarity of the smoke particles as shown in Figure 5.18.

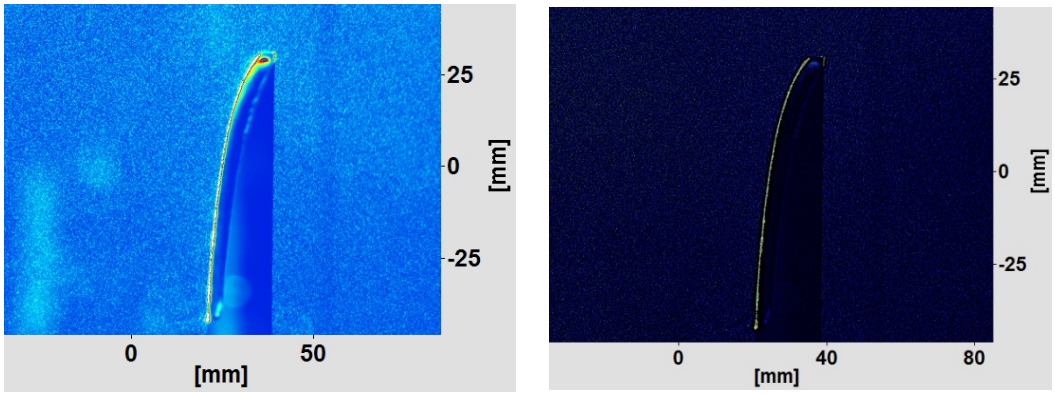

(a) raw image, 9 m/s nominal wind speed, 512k resolution

(b) preprocessed image, subtracted sliding background, filter length 2 pixels

Figure 5.18 - Example of image preprocessing

5.3.3 Vector Calculation

The vector calculation parameters were set to calculate a stereo PIV vector field. A stereo cross correlation was used to determine velocity vectors in three dimensions. Multi-pass iterations were done. First, a single pass was carried out on an interrogation window of 64x64 pixels, then two passes were carried out on interrogation windows of 32x32 pixels with 50% overlap.

5.3.4 Vector Postprocessing

The calculated vector field was postprocessed to remove wild vectors. Vectors were deleted if the peak ratio, Q, was < 1.1. Peak ratio Q is defined as

$$Q = \frac{Peak\ 1 - min}{Peak\ 2 - min} \qquad \text{(Eq. 30)}$$

where $Peak\ 1$ is the maximum peak in the correlation plane between the two frames, $Peak\ 2$ is the next highest peak, and min is the minimum value of the correlation plane (LaVision GmbH 2007).

In addition, the vector value was compared to the vector values in all bordering interrogation windows. If the vector deviates from the average of the neighbouring vectors by twice the rms, the vector is removed and replaced with the average value.

5.3.5 Peak locking

Peak locking errors were investigated by consulting the probability density functions (PDF) of the final vector fields. The commercial software package calculates a peak lock value according to Equation 31. The Vmod1 histogram displays the counts of the decimal portions of the velocity vectors. High pixel locking would not detect particles moving a fraction of a pixel and so would have high counts at the 0 and 1 ends of the scale. The Vmod0.5 histogram works in the same way but essentially mirrors the Vmod1 histogram about the 0.5 axis. Values near 1 are stacked on values near 0 and amplify any peak locking trend. The centre of mass of the Vmod0.5 histogram should be at 0.25 because all decimal places should have equal counts. Therefore, a peak lock value of 0 means there is no peak locking and a value of 1 means there is strong peak locking. The software documentation suggests that a peak lock value of less than 0.1 is acceptable (LaVision GmbH 2007). Peak lock values for the vector fields are listed in Table 5.4. "Full" refers to when the entire blade is within the field of view, "lead" refers to when the leading edge of the blade is in the field of view, and "trail" is when the trailing edge of the blade is in the field of view.

$$peak\ lock = 4 * (0.25 - Centre\ of\ Mass\ of\ Vmod0.5\ Histogram) \qquad \text{(Eq. 31)}$$

Peak lock values are generally close to 0.1. Peak locking errors are present in the data but the errors are relatively small. There will often be a trade-off between peak locking

errors due to small seeding particles and having small enough particles that they can be assumed to follow the air flow. The errors are deemed acceptable.

Table 5.4 - Peak lock values for recorded data sets

Set	Peak Lock	Set	Peak Lock	Set	Peak Lock
5 m/s full 3D	0.102	9 m/s full 3D	0.201	15 m/s full 3D	0.041
5 m/s full 2D	0.054	9 m/s full 2D	0.215	15 m/s full 2D	0.118
5m/s lead 3D	-0.022	9m/s lead 3D	0.115	15 m/s lead 3D	0.011
5 m/s lead 2D	-0.025	9 m/s lead 2D	0.160	15 m/s lead 2D	0.090
5 m/s trail 3D	0.097	9 m/s trail 3D	0.173	15 m/s trail 3D	0.116
5 m/s trail 2D	0.108	9 m/s trail 2D	0.101	15 m/s trail 2D	0.081
7 m/s full 3D	0.257	11 m/s full 3D	0.181		
7 m/s full 2D	0.129	11 m/s full 2D	0.129		
7 m/s lead 3D	0.202	11 m/s lead 3D	0.126		
7 m/s lead 2D	0.108	11 m/s lead 2D	0.082		
7 m/s trail 3D	0.113	11 m/s trail 3D	0.197		
7 m/s trail 2D	0.050	11 m/s trail 2D	0.054		

5.4 Results

The basic parameters of the experiment runs are listed in Table 5.5. The table values for wind speed were measured by the manometer (and corrected for static pressure rise to the location of the wind turbine mast). The wind speeds measured by the manometer were compared to the PIV results. Line plots of the x-component of the PIV calculated freestream wind speed (along the right edge of the field of view) for the "full" field of view are shown in Figure 5.19. It can be seen that the PIV results are close but slightly lower than the manometer measurements. This can be attributed to the slowing down of the freestream speed as it approaches the rotor. The PIV is therefore generating results that represent the flow field accurately.

Table 5.5 - Basic parameters of PIV experiments

Set	Wind Speed	RPM	dt	Set	Wind Speed	RPM	dt
	(m/s)		(µs)		(m/s)		(µs)
Full	5.03	585	58	Full	11.10	2140	26
Lead	5.02	585	58	Lead	11.11	2140	26
Trail	5.03	590	58	Trail	11.10	2143	26
Full	7.03	1095	41	Full	15.09	3135	20
Lead	7.05	1100	41	Lead	15.06	3135	20
Trail	7.05	1100	41	Trail	15.10	3145	20
Full	9.29	1690	32				
Lead	9.30	1690	32				
Trail	9.28	1690	32				

5.4.1 Stereo PIV

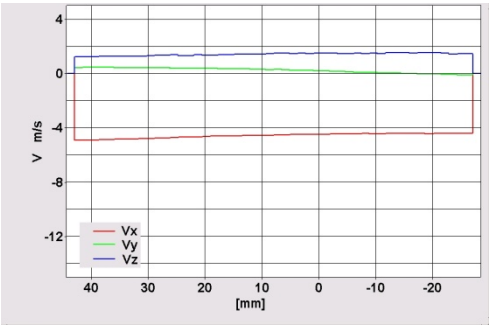

(a) 5 m/s nominal wind speed.
Average freestream wind speed, Vx = 4.59 m/s

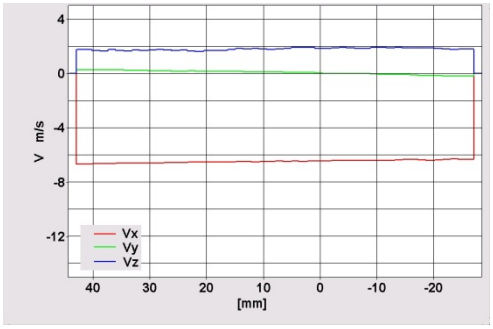

(b) 7 m/s nominal wind speed.
Average freestream wind speed, Vx = 6.50 m/s

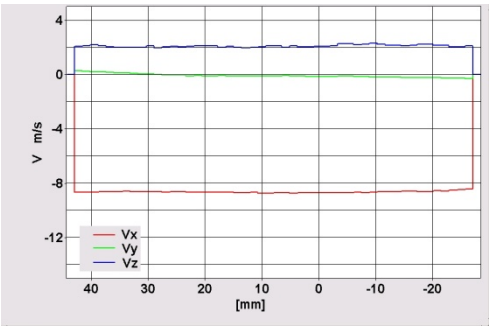

(c) 9 m/s nominal wind speed.
Average freestream wind speed, Vx = 8.70 m/s

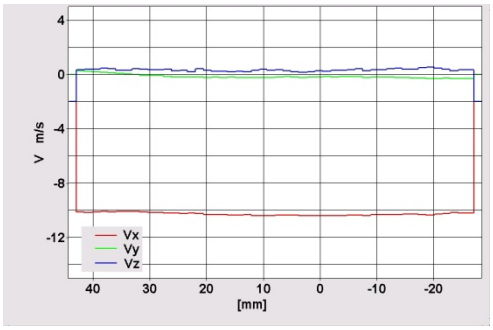

(d) 11 m/s nominal wind speed.
Average freestream wind speed, Vx = 10.27 m/s

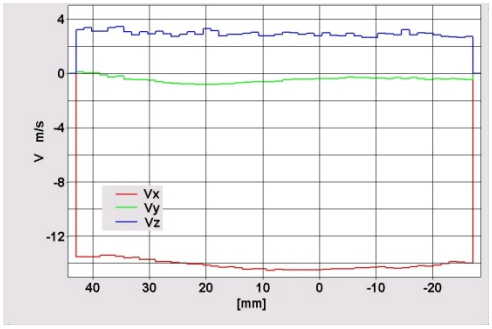

(e) 15 m/s nominal wind speed.
Average freestream wind speed, Vx = 14.04 m/s

NOMINAL WIND SPEED	CALCULATED WIND SPEED	
	Manometer	PIV
(m/s)	(m/s)	(m/s)
5	5.03	4.59
7	7.03	6.5
9	9.29	8.7
11	11.1	10.27
15	15.09	14.04

(f) Comparison of wind speed measurements in wind tunnel by manometer with wind speed measurements upstream of rotor (at right edge of field of view) by PIV

Figure 5.19 - Line plots of velocity vector lengths along inlet of camera field of view (set "full")

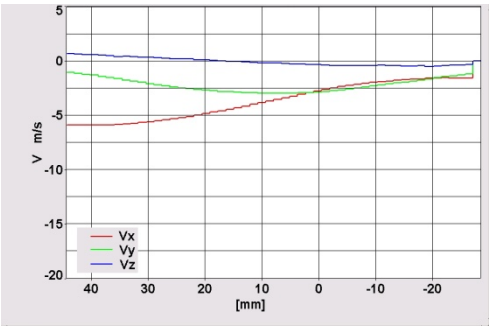

(a) 5 m/s nominal wind speed.

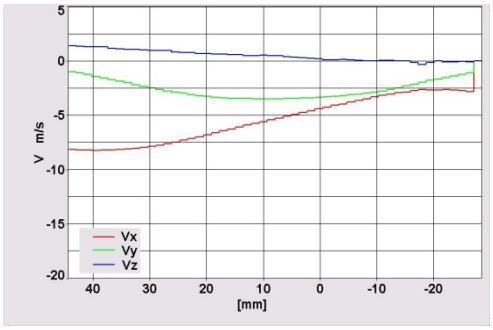

(b) 7 m/s nominal wind speed.

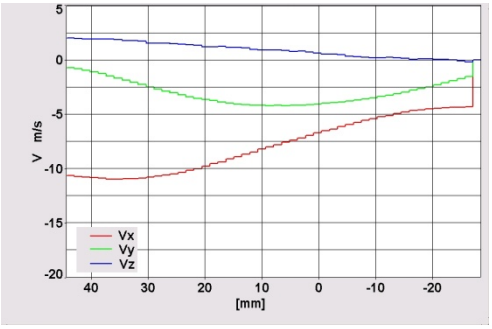

(c) 9 m/s nominal wind speed.

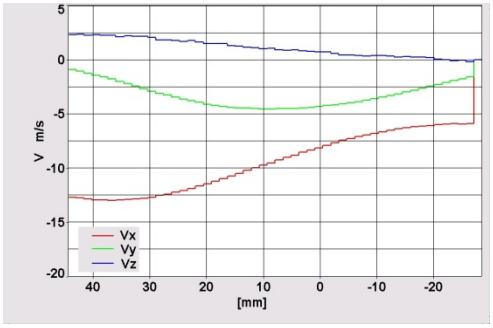

(d) 11 m/s nominal wind speed.

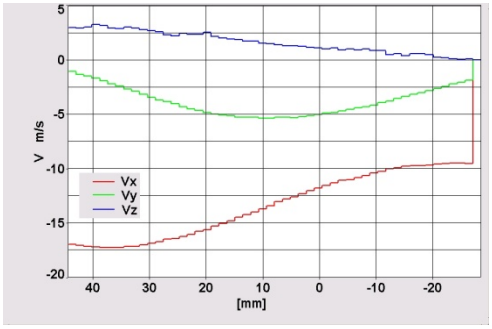

(e) 15 m/s nominal wind speed.

Figure 5.20 - Line plots of velocity vector lengths along a vertical line of camera field of view immediately downstream of blade (set "full")

Table 5.6 - Wake rotation with respect to wind speed

Wind Speed	Vx (m/s)	Vy (m/s)	Pitch Angle
5 m/s	-3.712	-1.17	17.5°
7 m/s	-5.343	-1.372	14.4°
9 m/s	-7.419	-1.683	12.8°
11 m/s	-8.89	-1.82	11.6°
15 m/s	-12.005	-2.003	9.5°

Figure 5.20 presents line plots of the x, y, and z-components of velocity extracted from the "full" blade sets of the Stereo PIV results. The line plots are taken along a vertical line in the camera field of view immediately downstream of the blade (at approximately -5 mm along horizontal axis in Figure 5.21 b, e, h, k, and n). The plots show the axial (Vx) velocity deficit behind the trailing edge of the blade. The y-component peaks as the air flows over the leading edge of the blade. The z-component is positive ahead of the leading edge and drops to zero after the trailing edge. It remains a small component of velocity regardless of freestream wind speed.

The final averaged 3D vector fields are shown in Figure 5.21. The vector fields clearly show that the flow field around the wind turbine blade is three dimensional. Upstream of the rotor there is a positive z-component of velocity (i.e. out of the page) and downstream of the rotor the z-component is negative. This is consistent with airfoil theory for wings with finite span. On the pressure side of a finite span airfoil the flow will be towards the tip while the suction side will flow towards the root. This is due to the pressure variation along the span of the blade. Where these two flows meet at the blade tip, they roll up into the tip vortex (Bertin and Smith 1979).

Also contributing to the flow upstream of the rotor is that the freestream wind is being slowed down by the rotor and the streamtube is diverging. In this field of view the divergence is seen as a positive z-component of velocity. In addition to this, the flat disc of the hub and rotor is a bluff body which will tend to force the flow around the rotor, adding to the positive z-component of velocity.

The wake of the rotor is rotating in an opposite direction to the rotor itself. If the full extent of the rotor were shown in the field of view, there would be positive z-component velocity at the top of the wake and negative z-component velocity at the bottom. At the centerline of the wind turbine, however, the wake rotation should have negative y-component velocity with a z-component close to zero. The laser light sheet is close to the blade tip, however, and there are concentrated tip vortices being shed from the blades which, as mentioned above, account for the z-component of velocity.

There is a strip of bad data visible in Figure 5.21 on the suction side of the blade. This is the result of reflections on the blade on the far side of the laser light sheet from the camera. The intensity of these reflections interferes with the intensities of the smoke particles in the plane of the laser light sheet. The result is poor data and no vector can be calculated.

One of the concerns of the Kiel probe experiment was that the rotating wake would result in a velocity vector that would fall outside the range of angles in which the Kiel probe was considered accurate. The Kiel probe was mounted one rotor diameter downstream of the rotor, which is outside the field of view of the cameras, but the vectors close to the rotor can be assumed to be a worst case. The wake slowly returns

to the freestream condition as it flows downstream. The wake velocity vectors at the downstream edge of the field of view and the rotation angle are shown in Table 5.6. It can be seen that all the angles are less than the Kiel probe's maximum pitch angle limit of 58°.

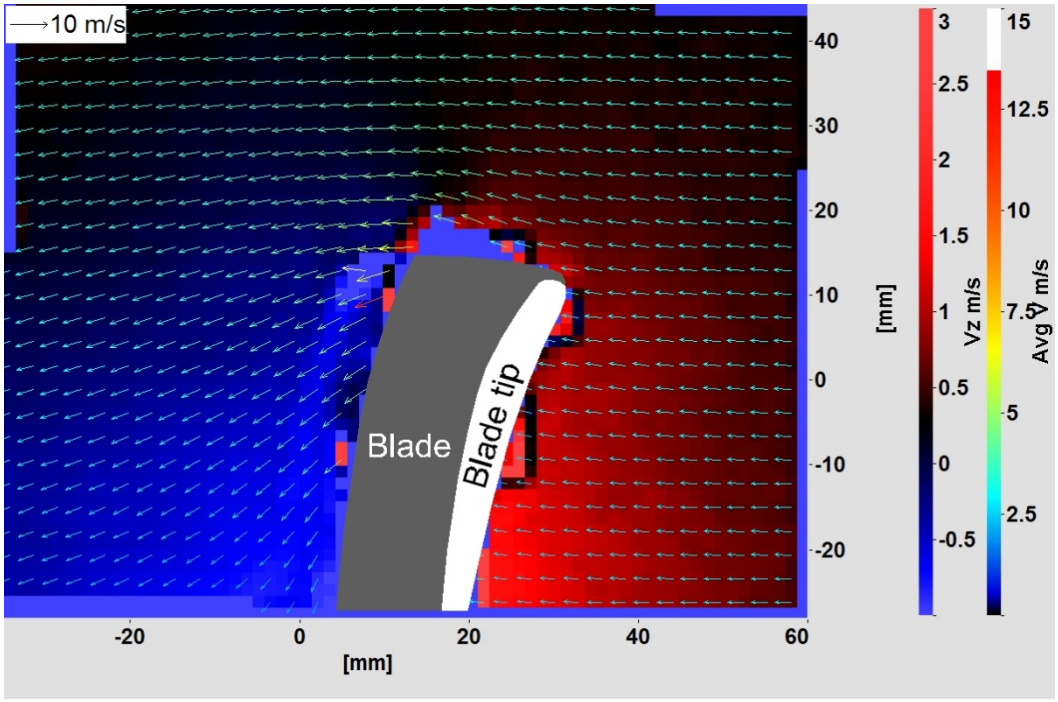

(a) 5 m/s nominal wind speed, "lead" field of view

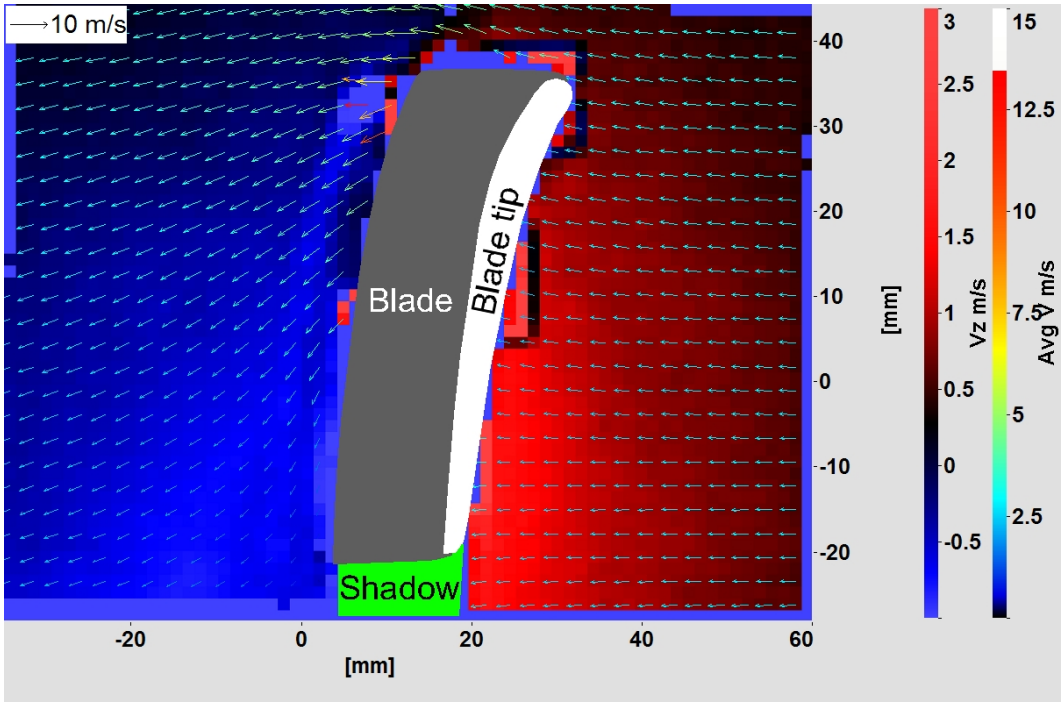

(b) 5 m/s nominal wind speed, "full" field of view

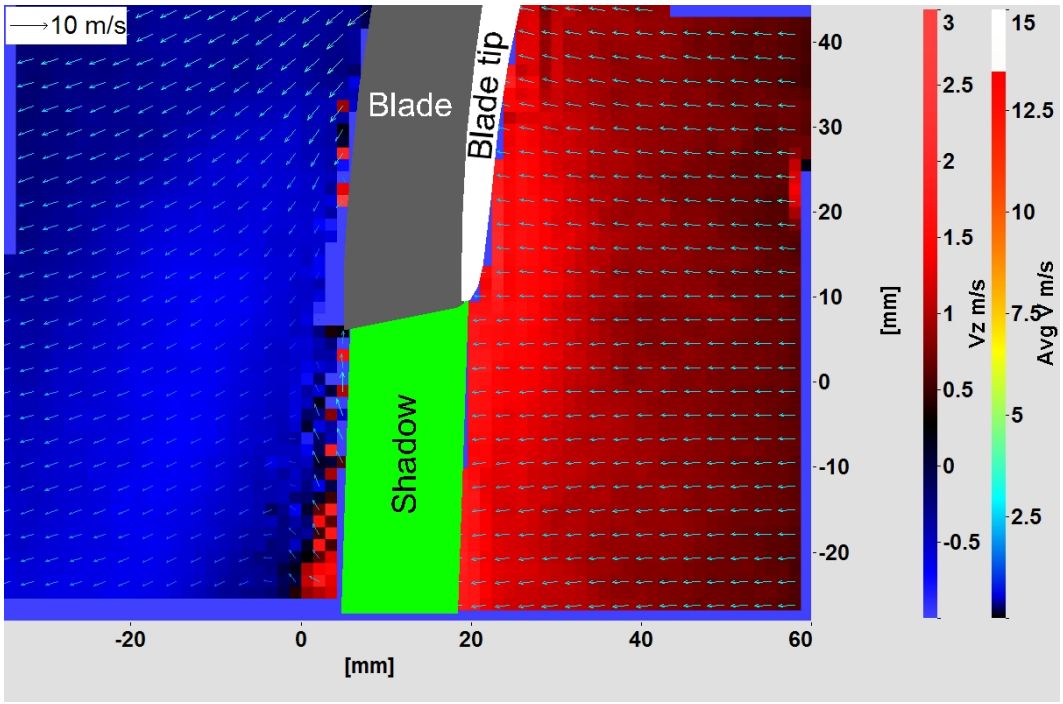

(c) 5 m/s nominal wind speed, "trail" field of view

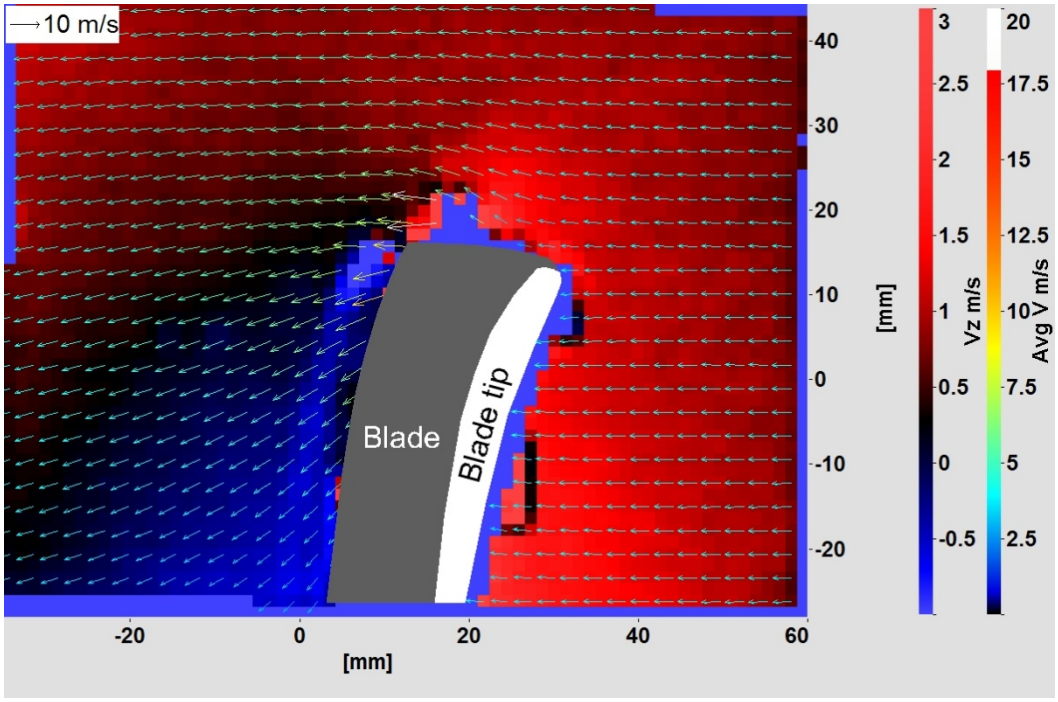

(d) 7 m/s nominal wind speed, "lead" field of view

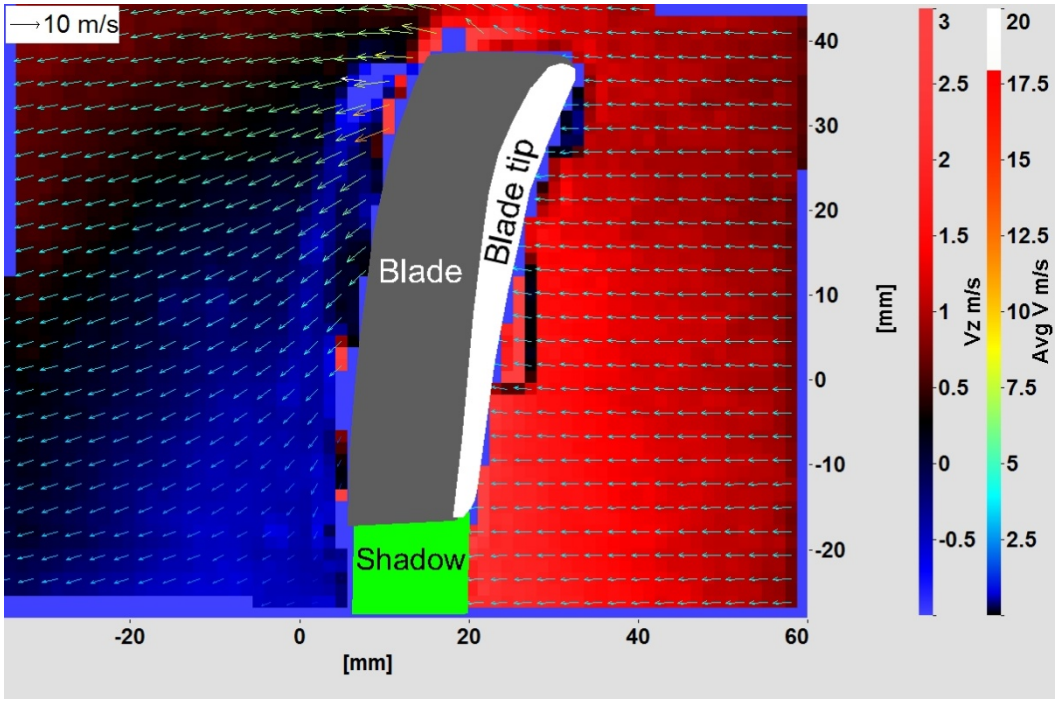

(e) 7 m/s nominal wind speed, "full" field of view

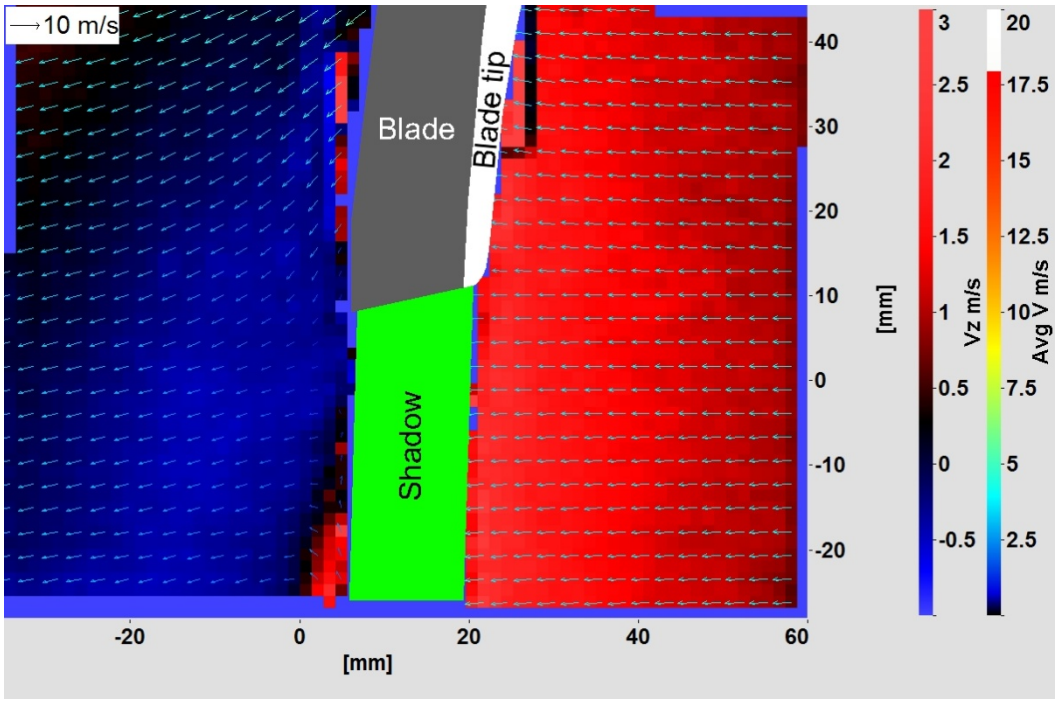

(f) 7 m/s nominal wind speed, "trail" field of view

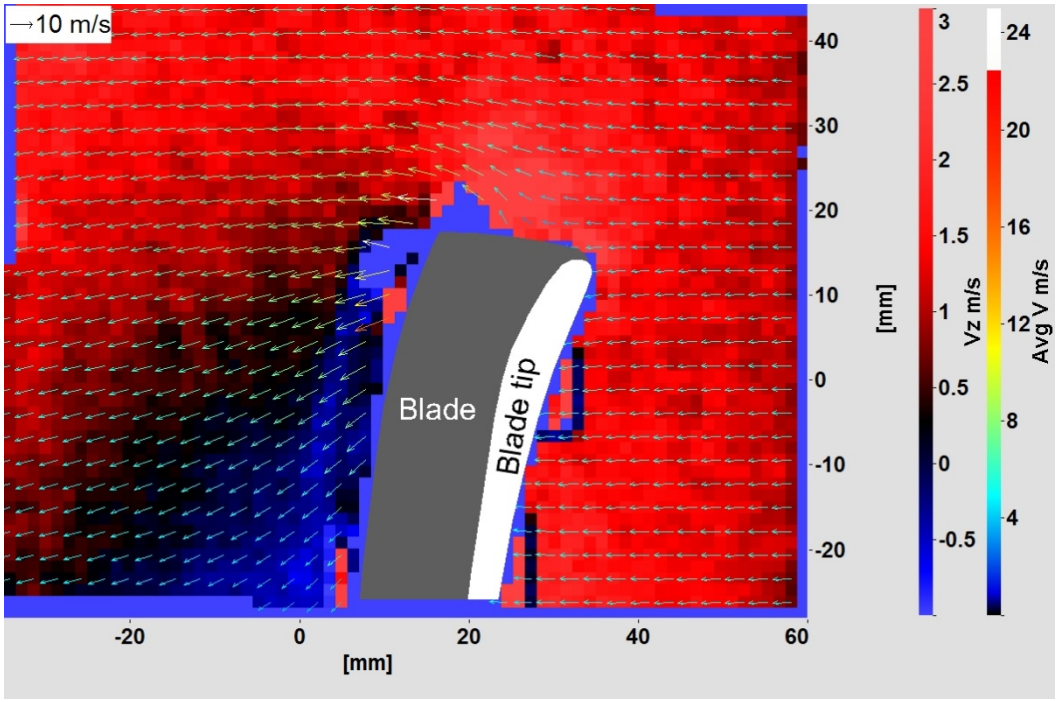

(g) 9 m/s nominal wind speed, "lead" field of view

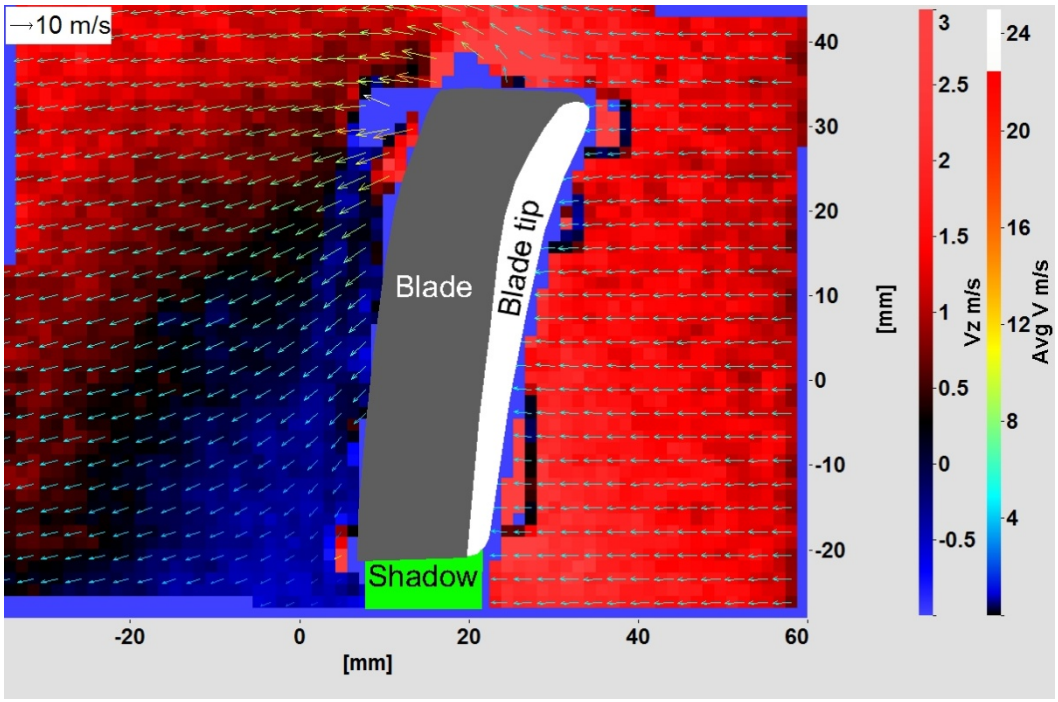

(h) 9 m/s nominal wind speed, "full" field of view

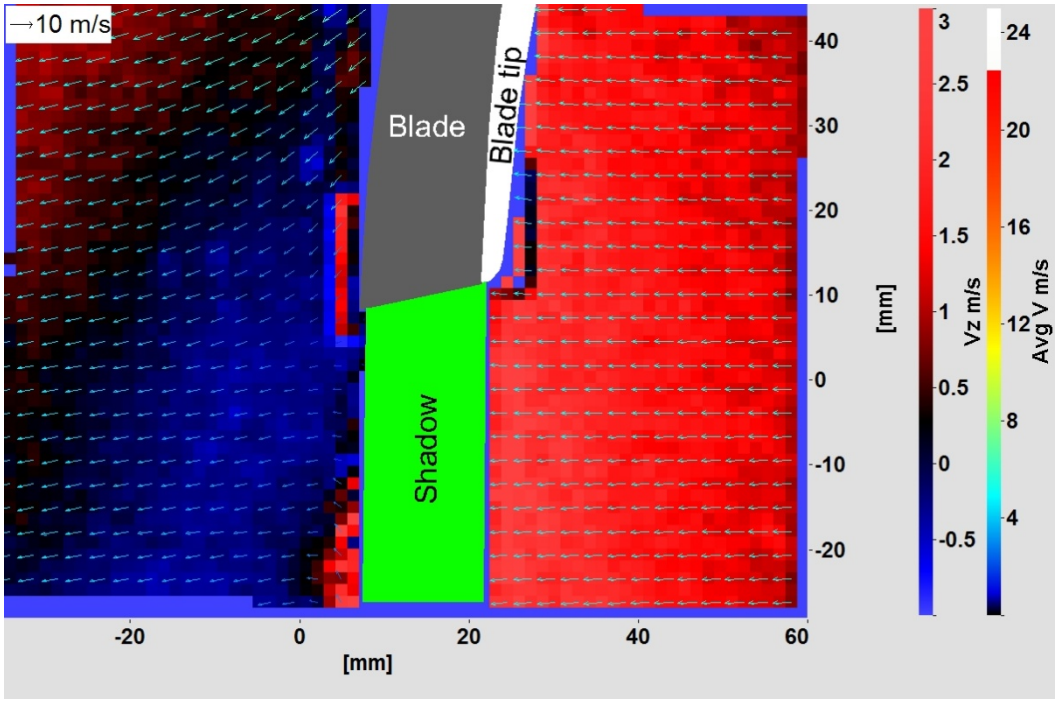

(i) 9 m/s nominal wind speed, "trail" field of view

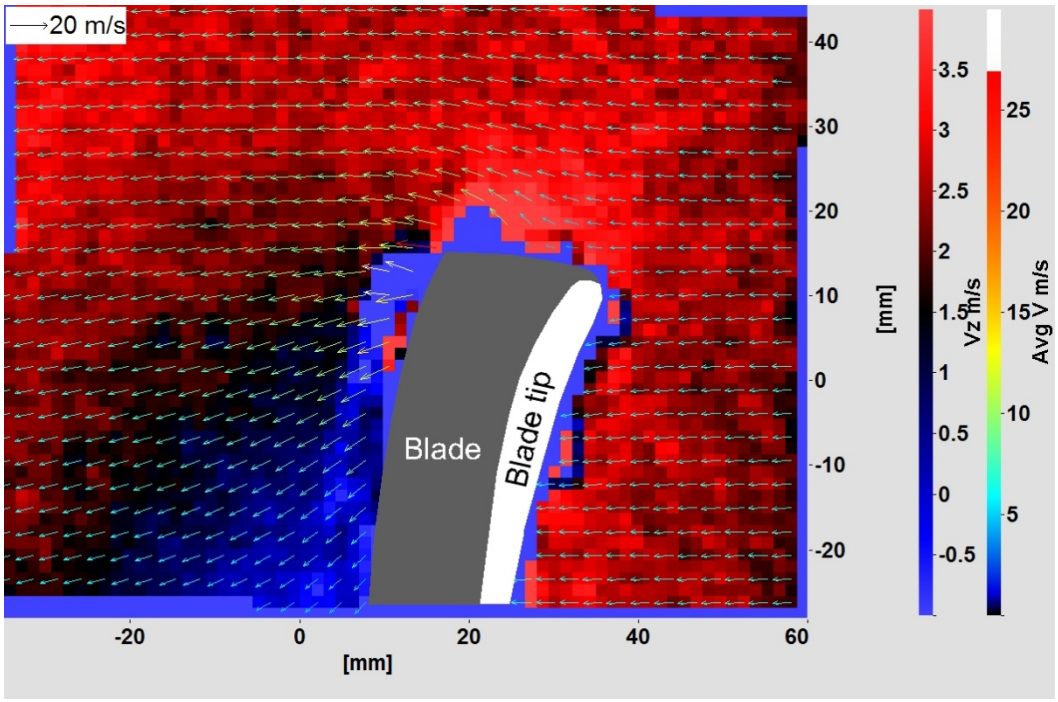

(j) 11 m/s nominal wind speed, "lead" field of view

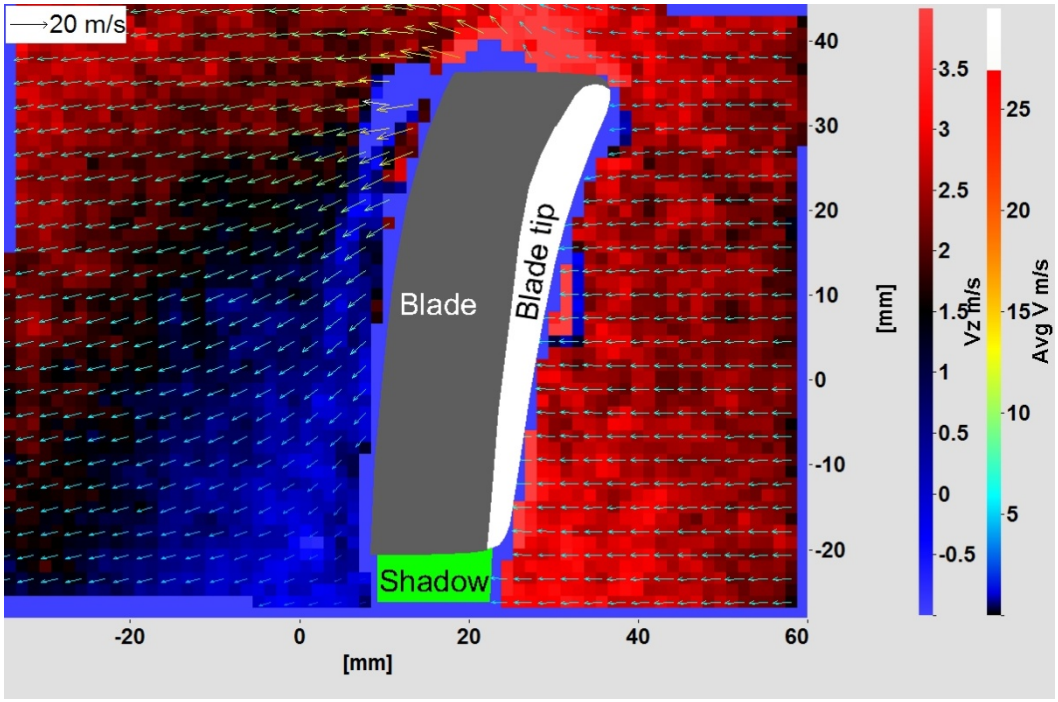

(k) 11 m/s nominal wind speed, "full" field of view

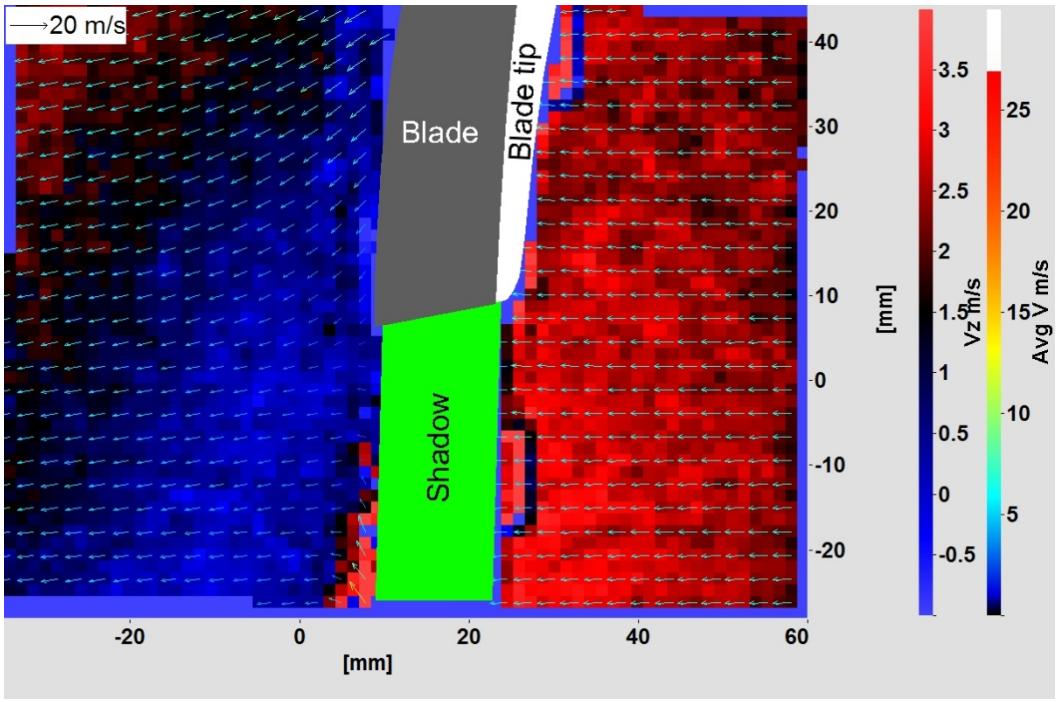

(l) 11 m/s nominal wind speed, "trail" field of view

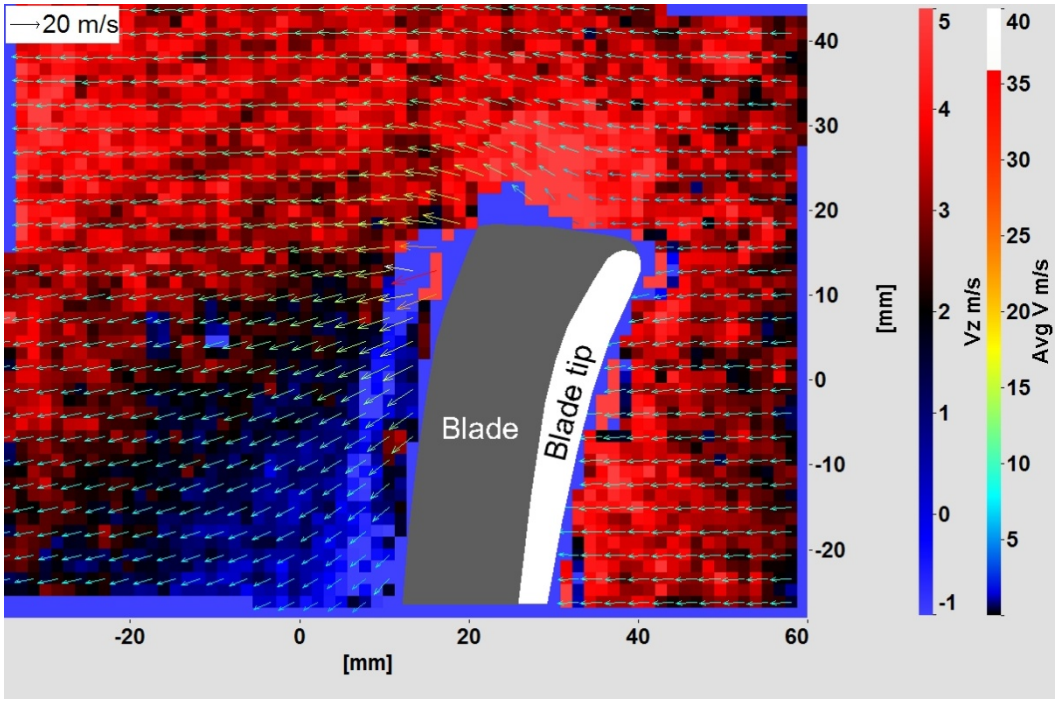

(m) 15 m/s nominal wind speed, "lead" field of view

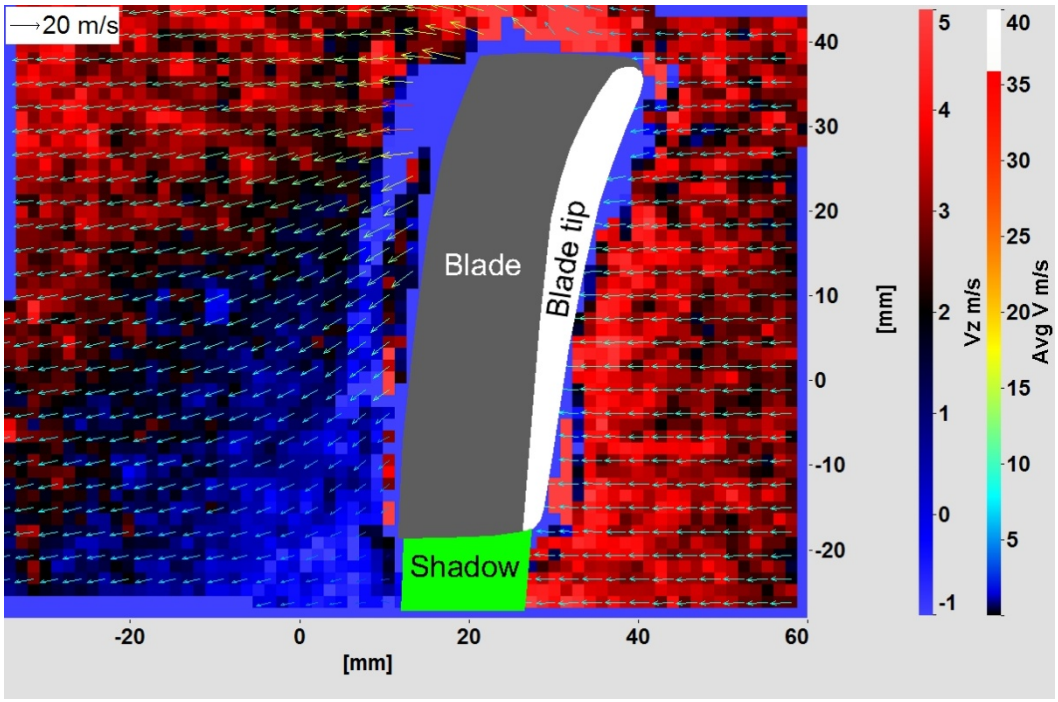

(n) 15 m/s nominal wind speed, "full" field of view

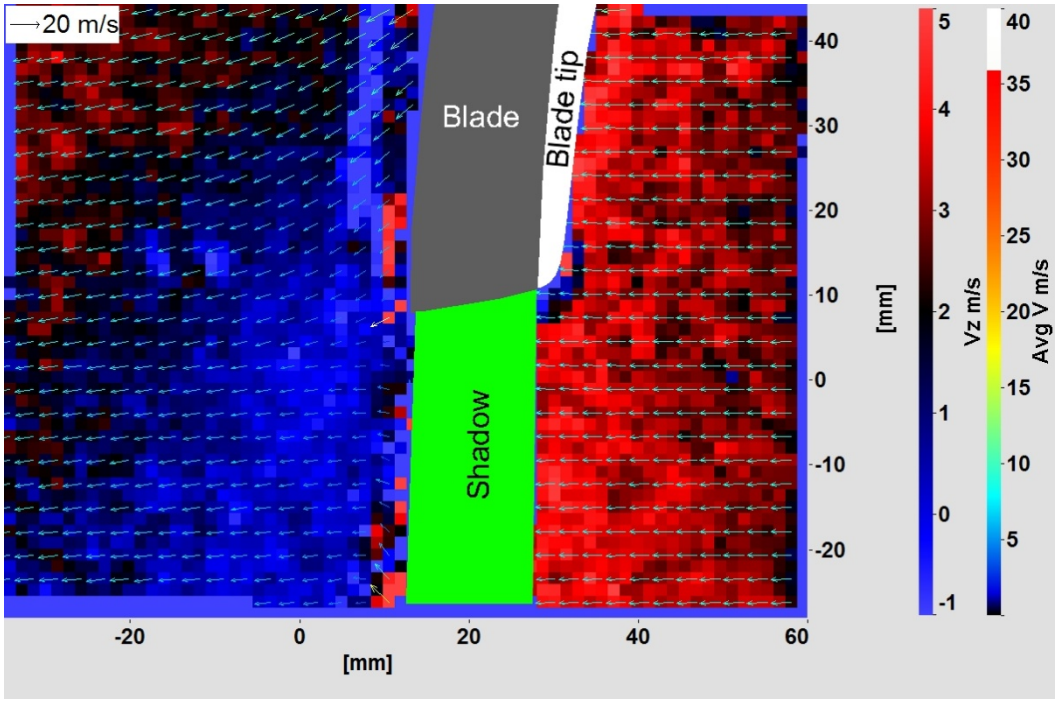

(o) 15 m/s nominal wind speed, "trail" field of view

Figure 5.21 - Stereo PIV average vector fields around Ampair 100 blade. Blade is moving up in the image. Axes are dimensions of field of view in millimeters. Left legend defines colour of magnitude of z-component of velocity. Right legend defines colour of magnitude of velocity vectors. Length of vectors also represent magnitude of velocity vectors.

5.4.2 Planar PIV

It can be seen in Figures 5.20 and 5.21 that the z-component velocities do not change significantly as freestream wind speed changes. At 5 m/s freestream wind speed the z-component of velocity ranges from -1 to 3 m/s. At 15 m/s freestream wind speed the z-component of velocity ranges from -1 to 5 m/s. At low wind speeds the 3D component of flow is significant but at higher wind speeds the 3D component is small. At higher wind speeds the 2D nature of the flow means that little is lost by presenting the 2D vector fields only. The 2D vector fields are able to better depict the flow field on the pressure side of the blade.

The 2D vector fields are shown in Figure 5.22. The flow can be seen to accelerate over the leading edge of the blade. In the wake of the blade, the velocity is seen to point down, indicating the rotation of the wake in the opposite direction of the rotor. A significant decrease in velocity in the wake is not seen. Haans, et al. (2005), who measured the near wake only 3.5 cm downstream of the rotor plane, plot the magnitude of wake velocity as a function of blade azimuth position. The wake velocity peaks at freestream wind speed immediately before the passage of the blade, drops suddenly as the blade passes, and climbs again to freestream wind speed as the next blade approaches. Therefore, the flow in the near wake of the blade as shown in the field of view does not contain a velocity deficit until the blade has past.

Figure 5.23 presents the rms velocity values. The rms values are greatest near the blade and masked regions. The blade is shifting up and down in the field of view due to variations in the speed of revolution of the rotor. When the individual vector fields are averaged to produce the final averaged vector field, the vectors in the blade shifting regions have the highest rms.

The 2D vector fields are presented again in Figure 5.24 in which the vectors are shown relative to the blade. Streamlines of the flow are also shown. The blade rotates very quickly and the very strong positive y-component obscures the subtleties of the other components in the flow field. The streamlines around the blade look similar to the flow fields of the NACA 6308 airfoil presented in Appendix B.

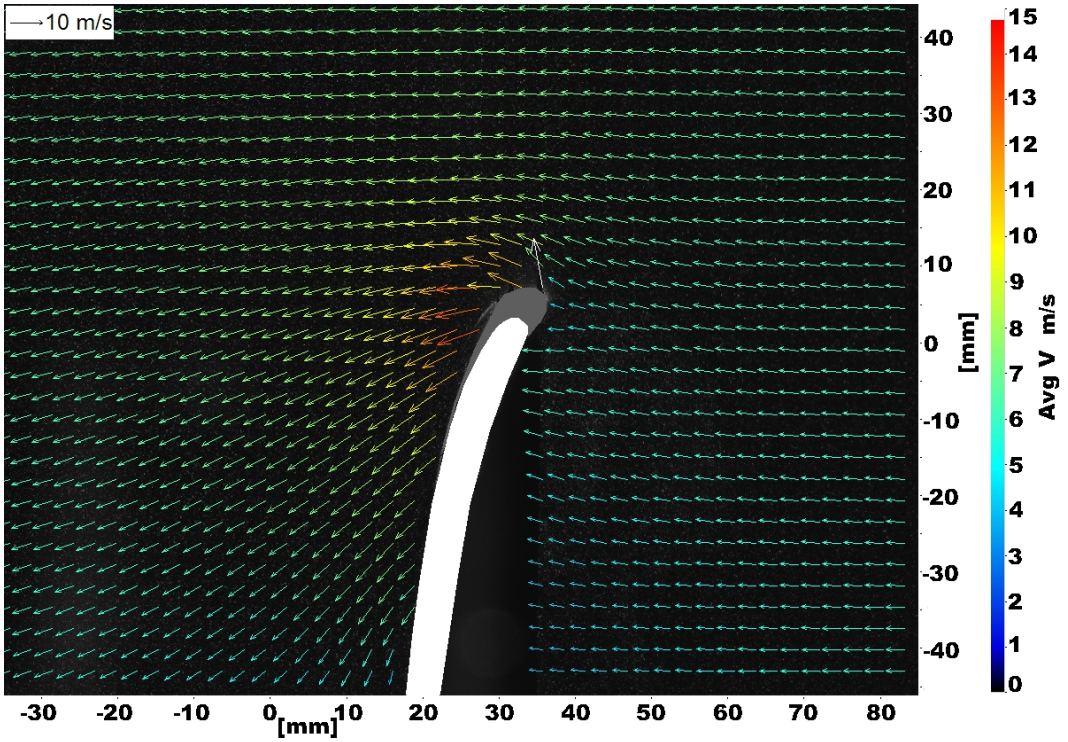

(a) 5 m/s nominal wind speed, “lead” field of view

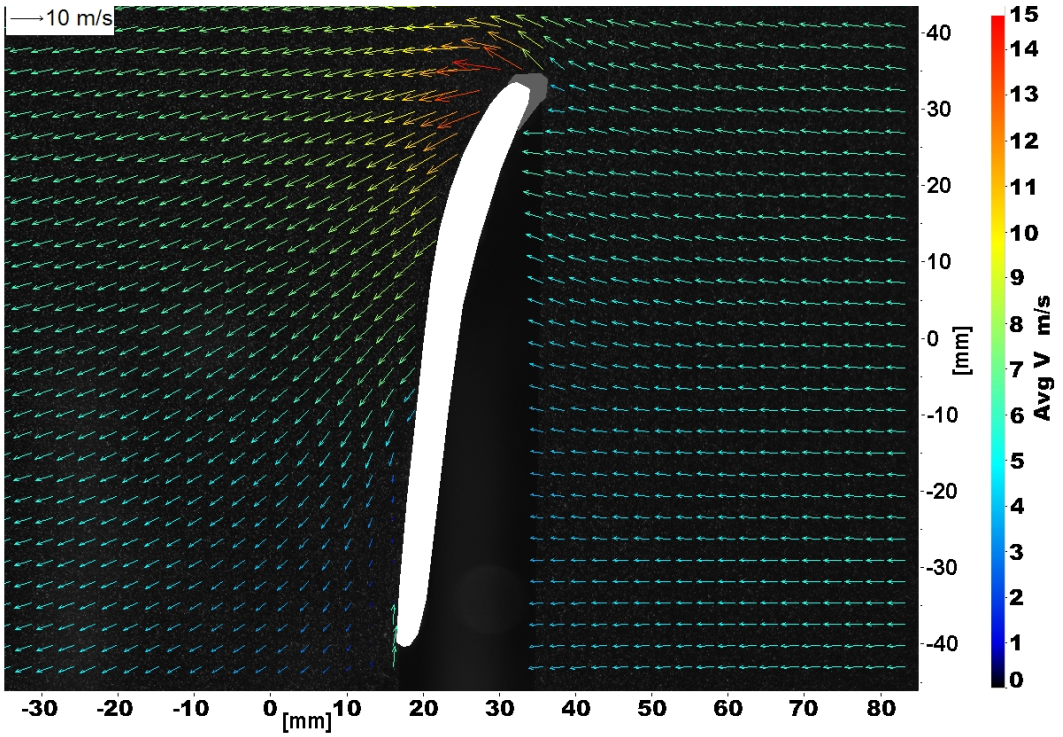

(b) 5 m/s nominal wind speed, “full” field of view

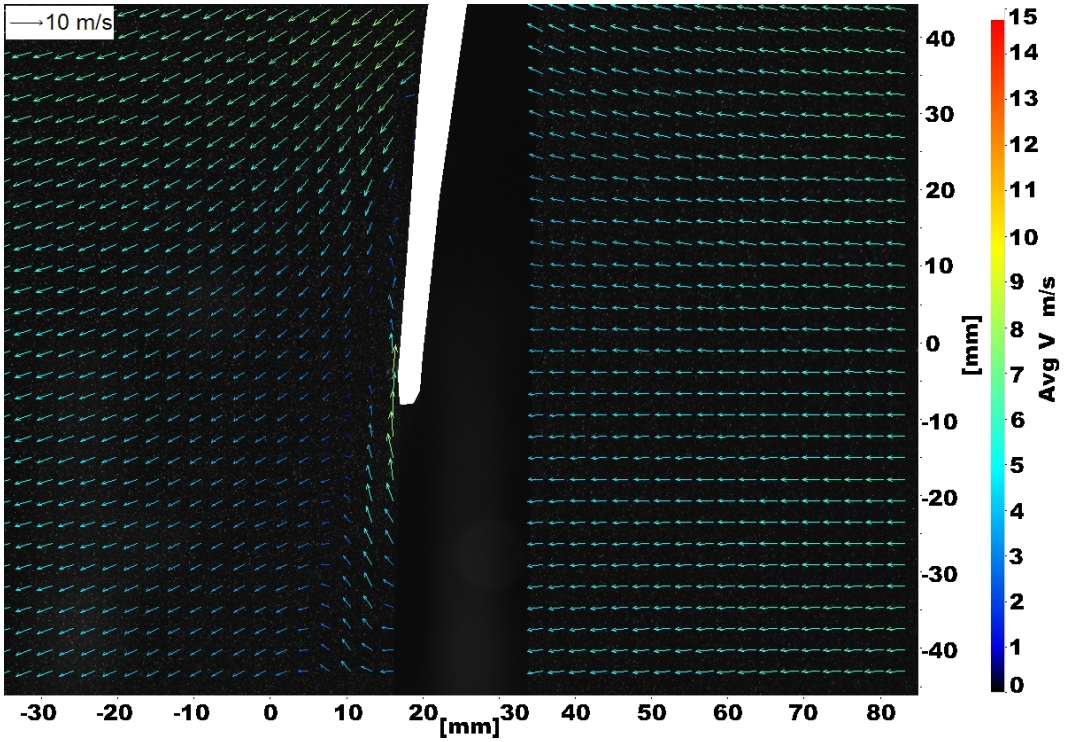

(c) 5 m/s nominal wind speed, "trail" field of view

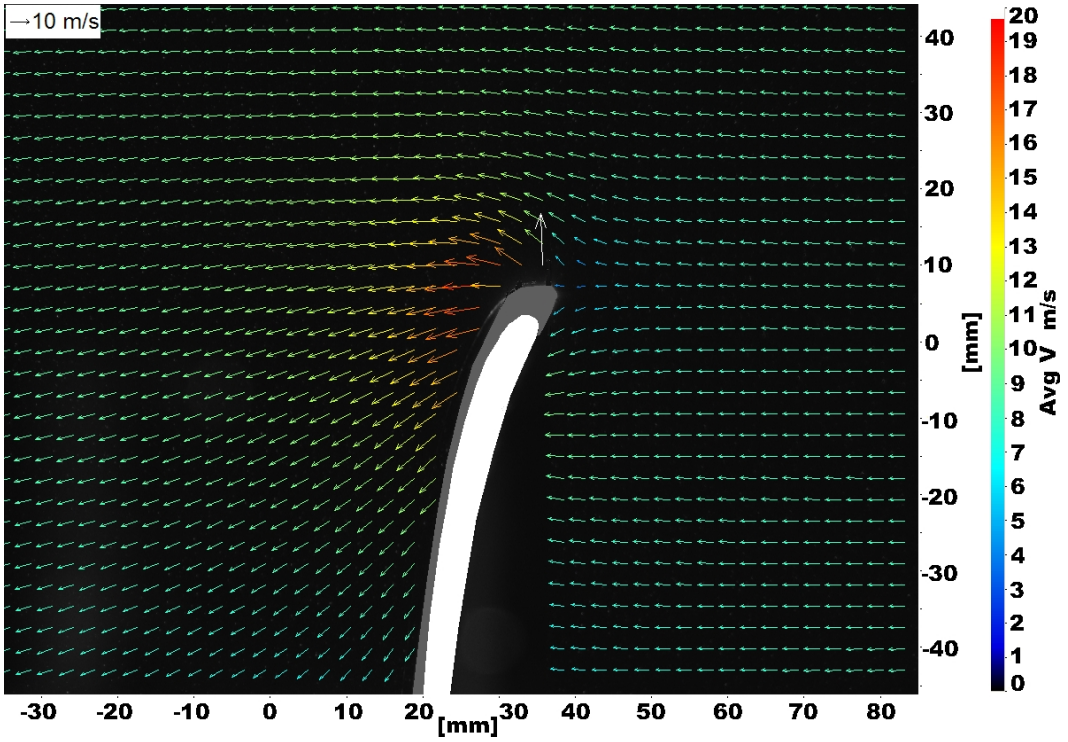

(d) 7 m/s nominal wind speed, "lead" field of view

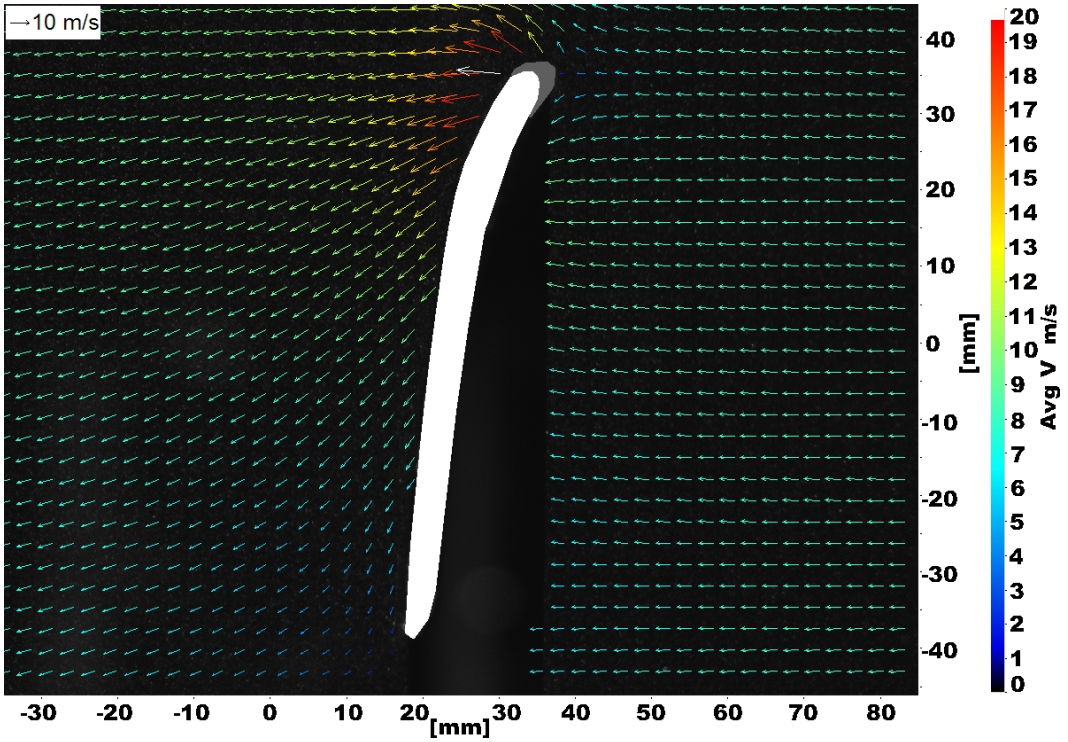

(e) 7 m/s nominal wind speed, "full" field of view

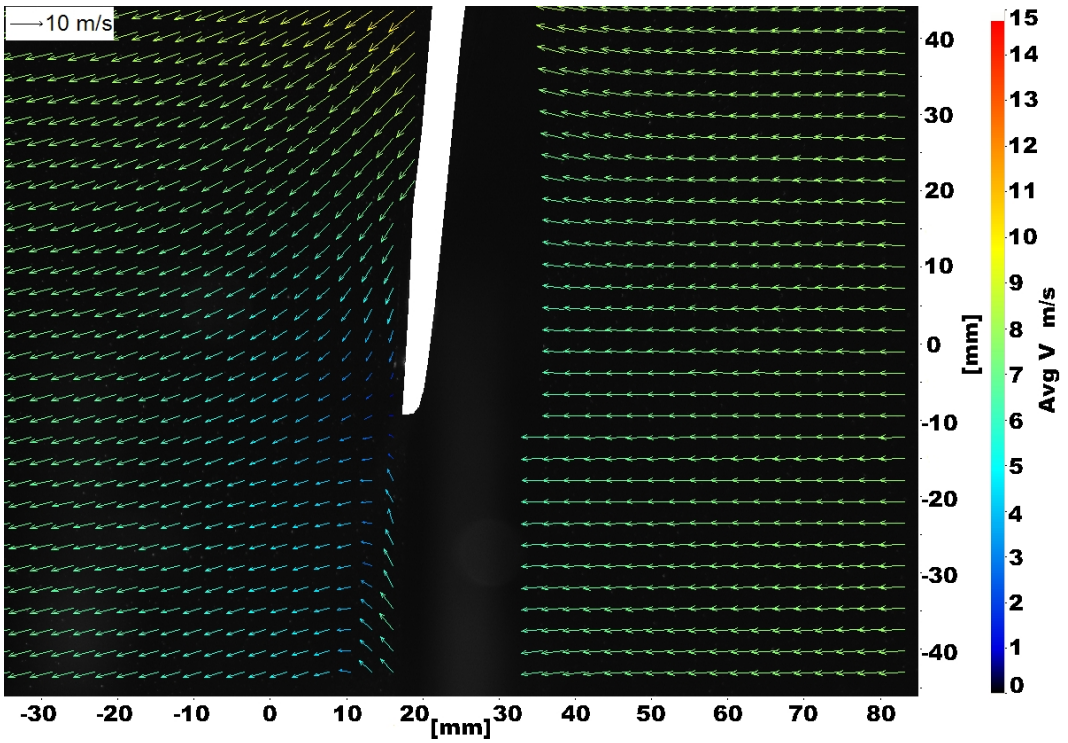

(f) 7 m/s nominal wind speed, "trail" field of view

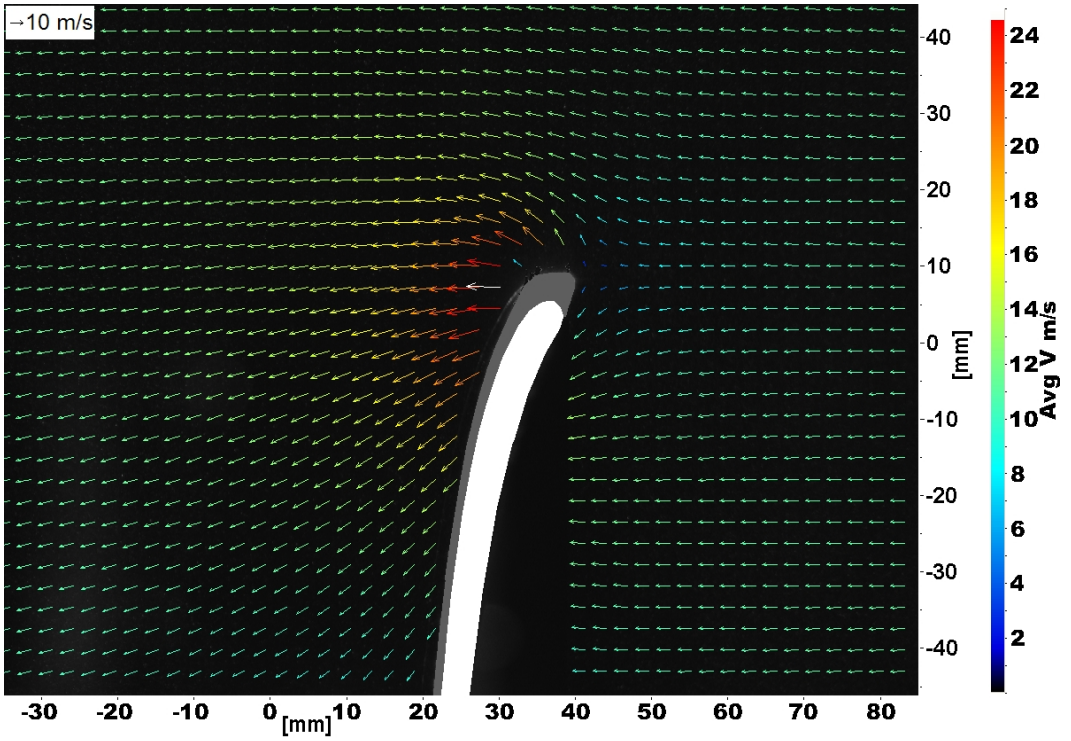

(g) 9 m/s nominal wind speed, "lead" field of view

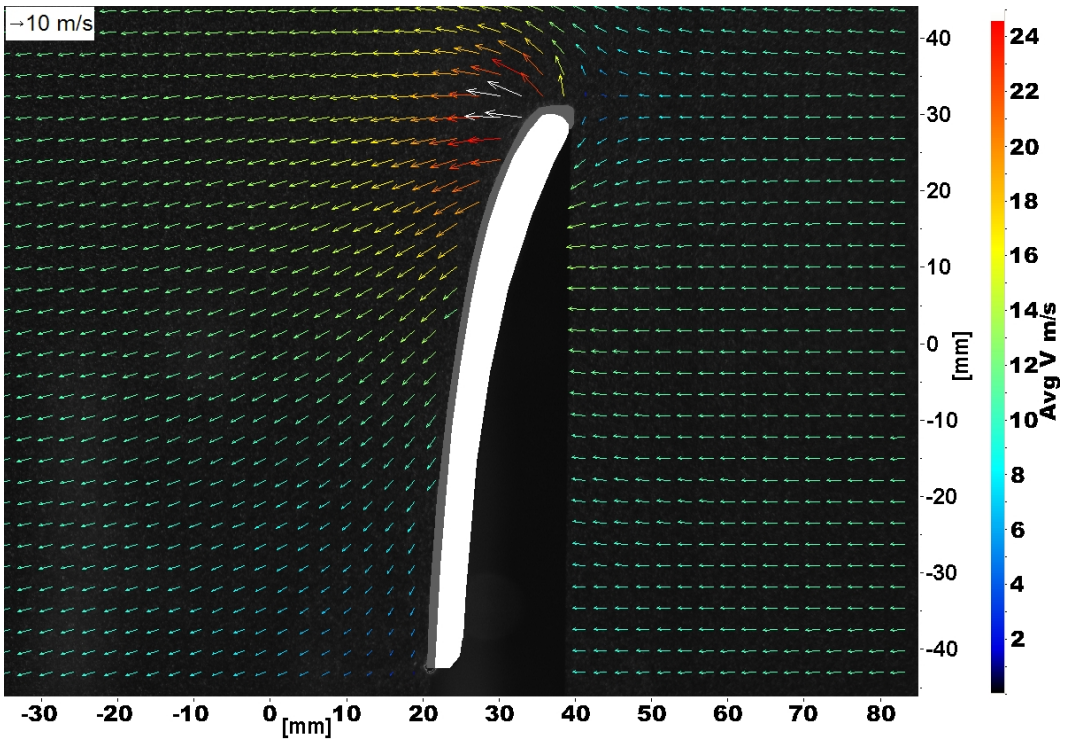

(h) 9 m/s nominal wind speed, "full" field of view

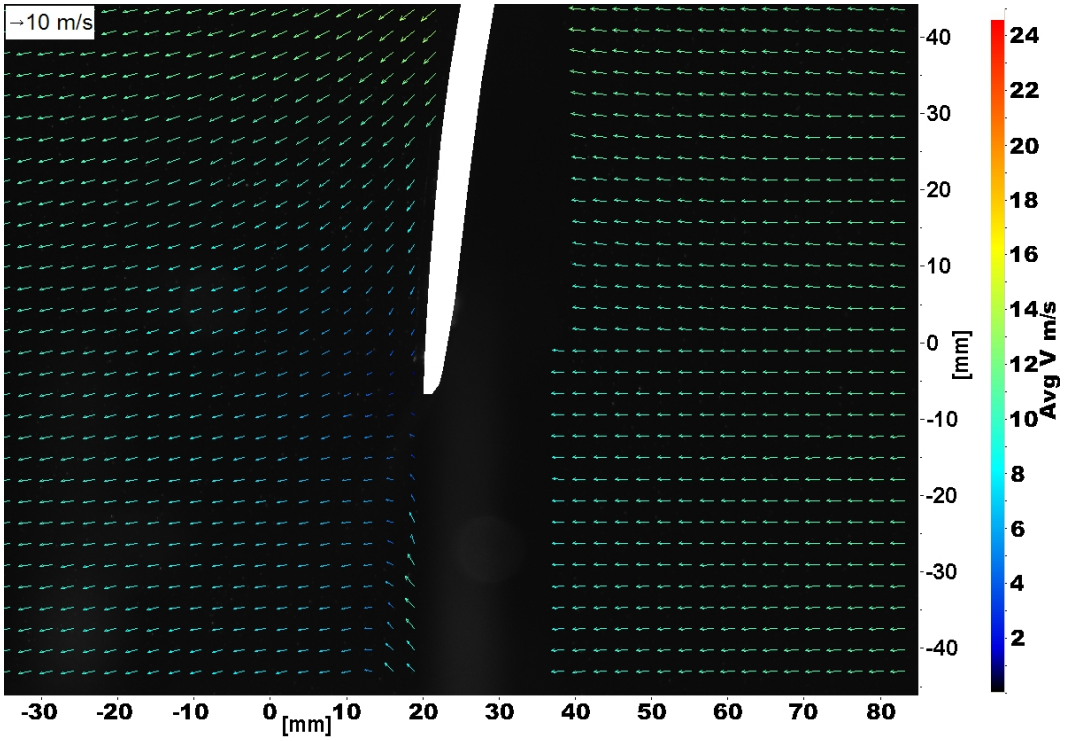

(i) 9 m/s nominal wind speed, "trail" field of view

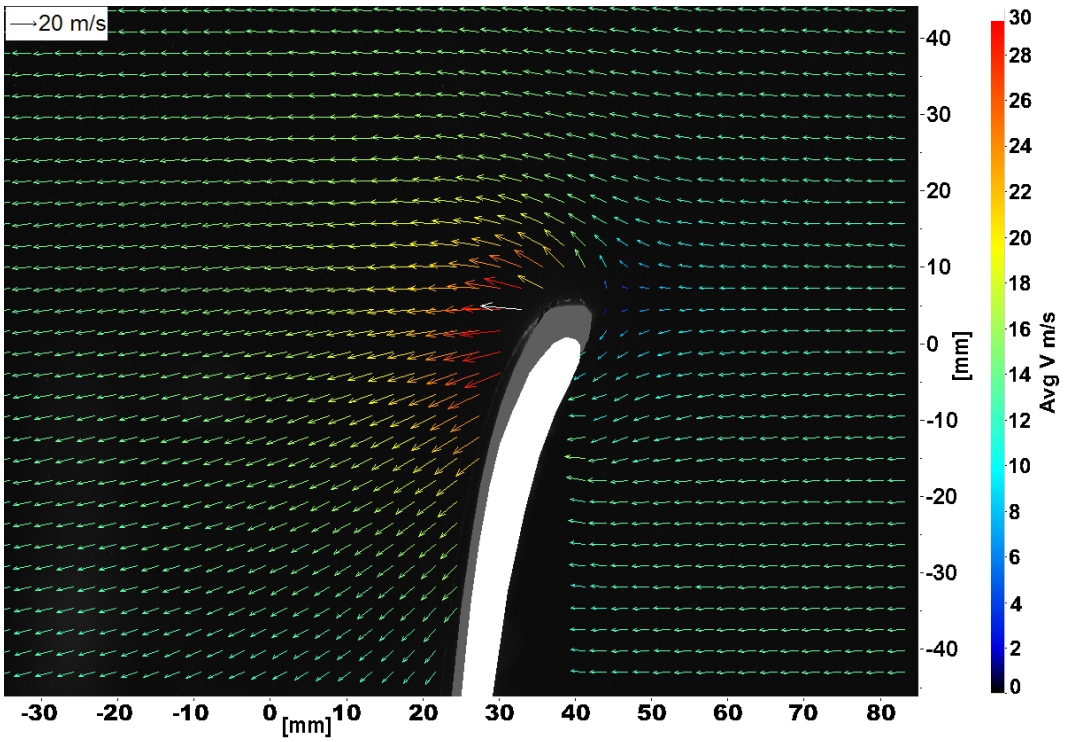

(j) 11 m/s nominal wind speed, "lead" field of view

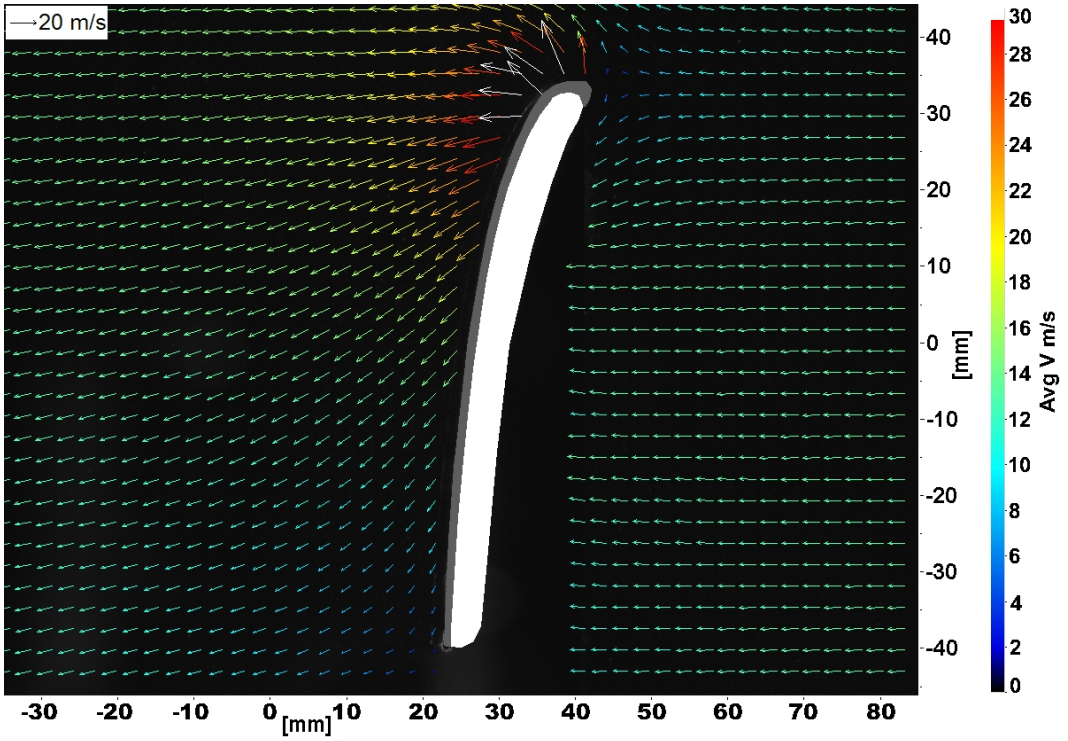

(k) 11 m/s nominal wind speed, “full” field of view

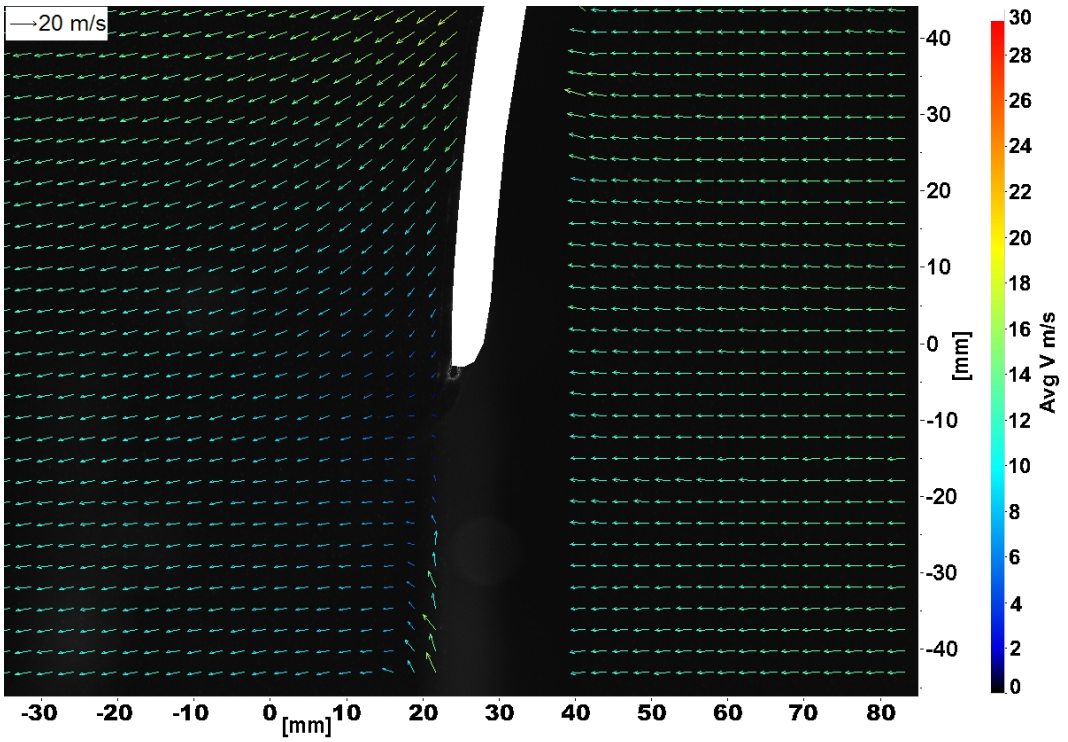

(l) 11 m/s nominal wind speed, “trail” field of view

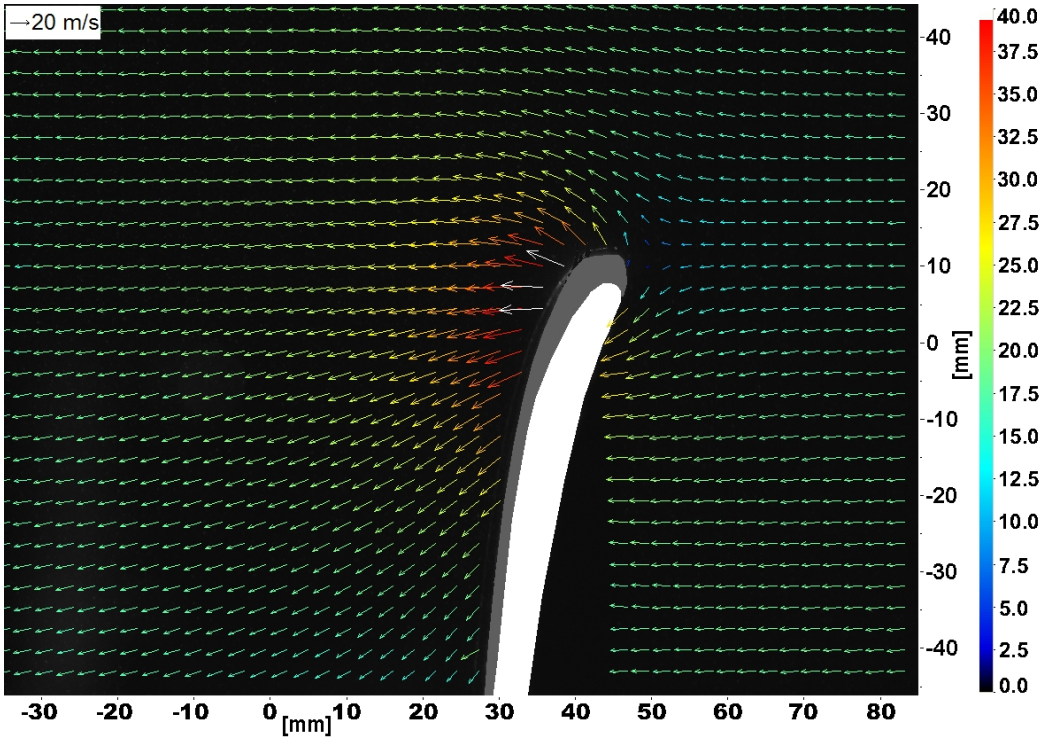

(m) 15 m/s nominal wind speed, "lead" field of view

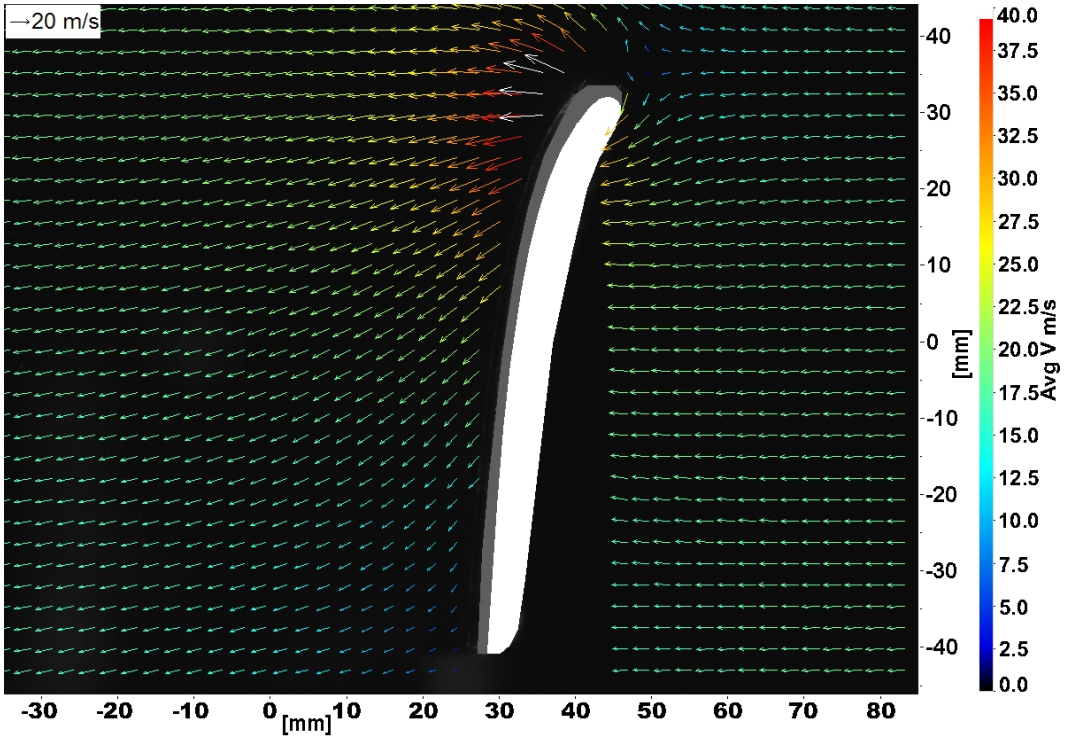

(n) 15 m/s nominal wind speed, "full" field of view

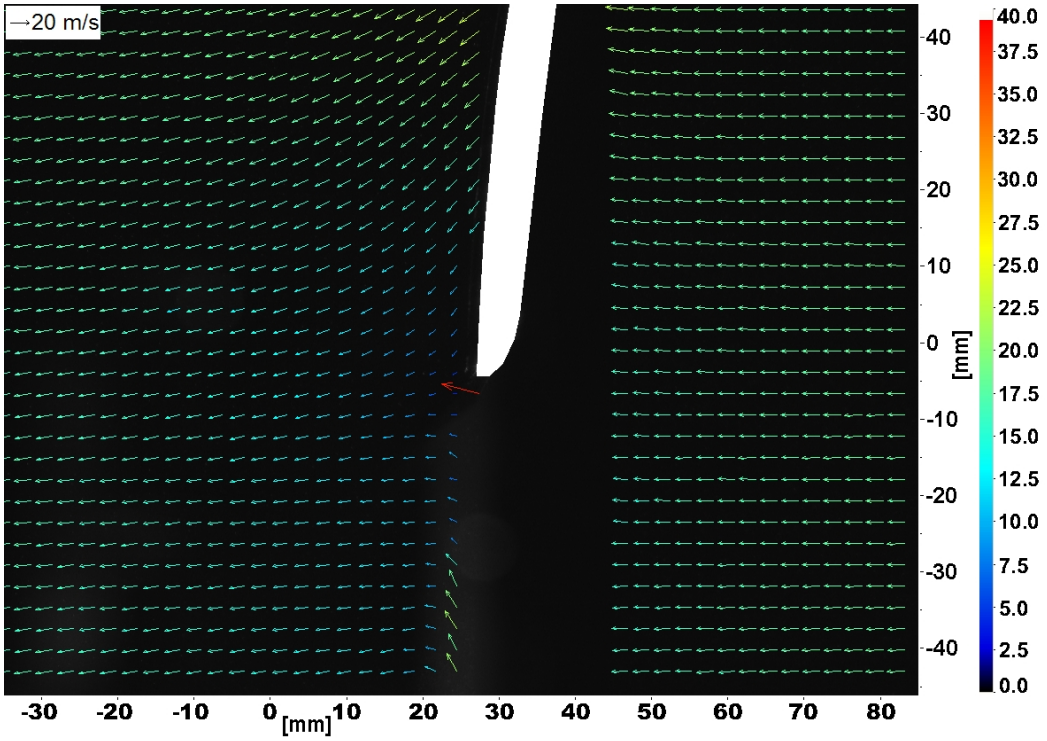

(o) nominal wind speed, "trail" field of view

Figure 5.22 - Planar PIV average vector fields around Ampair 100 blade. Blade is moving up in the image. Axes are dimensions of field of view in millimeters. Legend defines colour of magnitude of velocity vectors. Length of vectors also represent magnitude of velocity vectors.

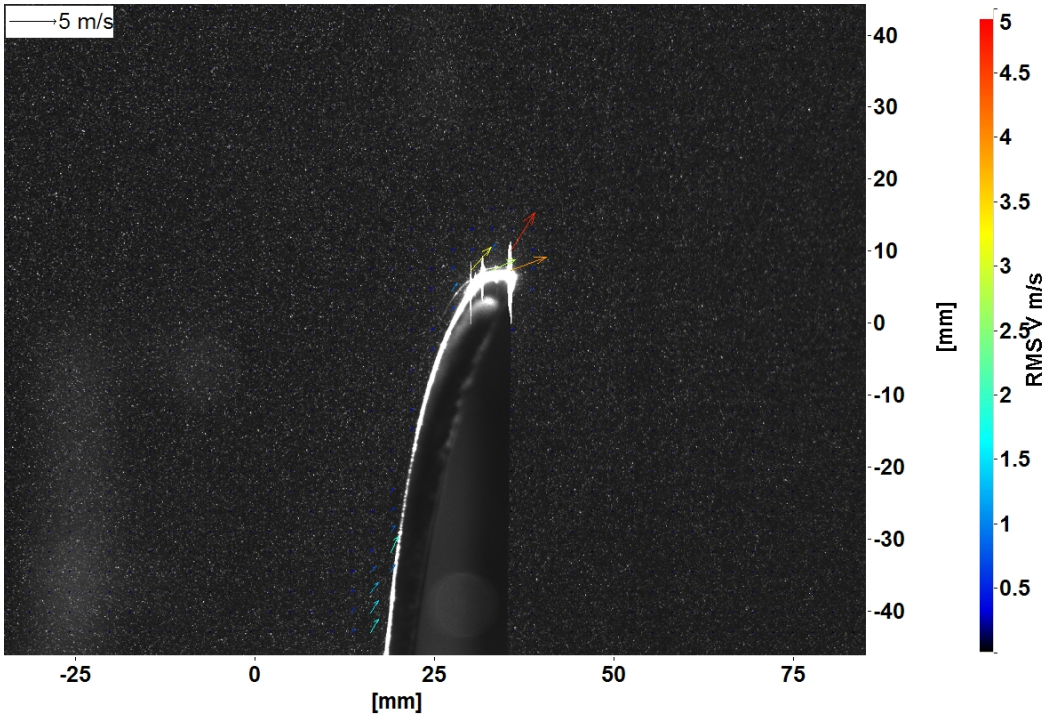

(a) 5 m/s nominal wind speed, “lead” field of view

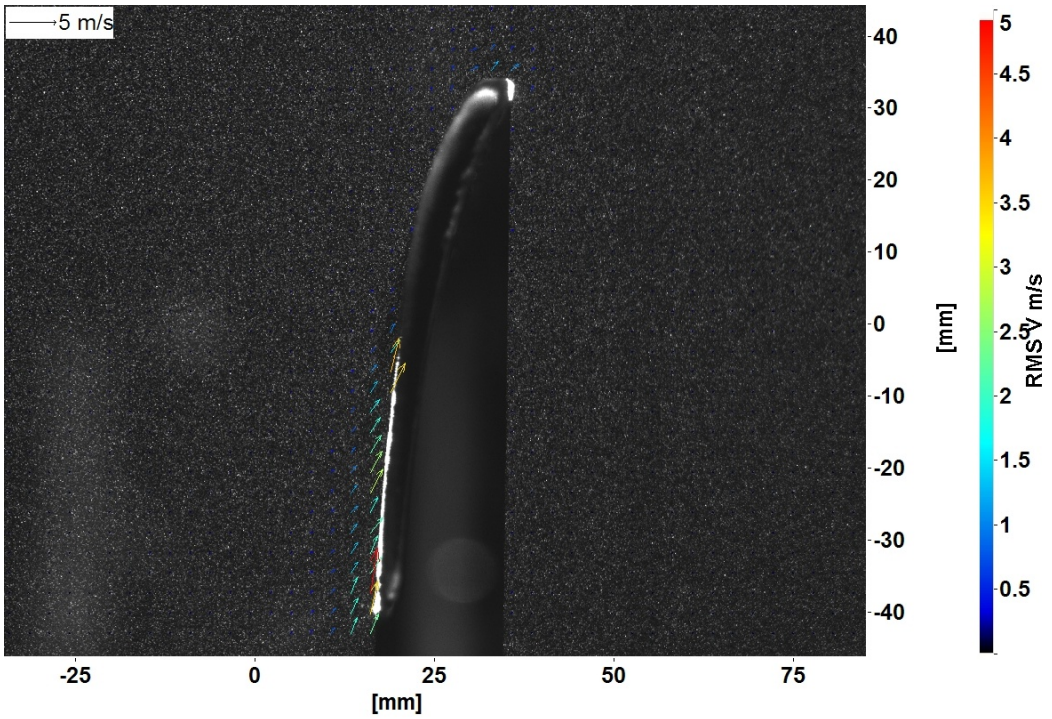

(b) 5 m/s nominal wind speed, “full” field of view

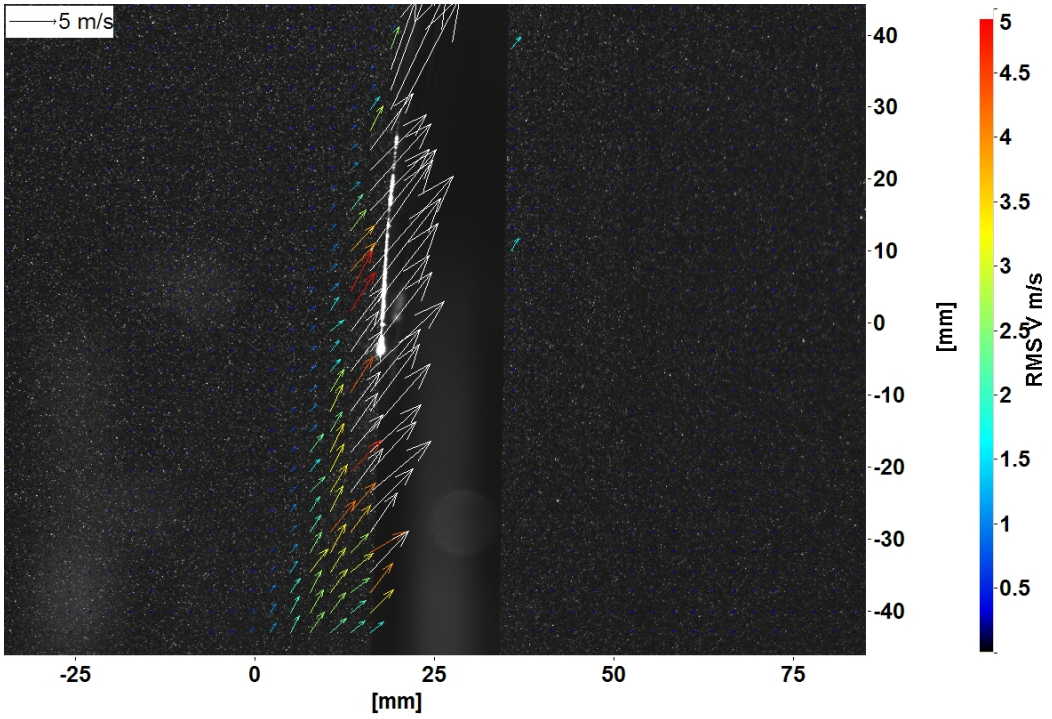

(c) 5 m/s nominal wind speed, "trail" field of view

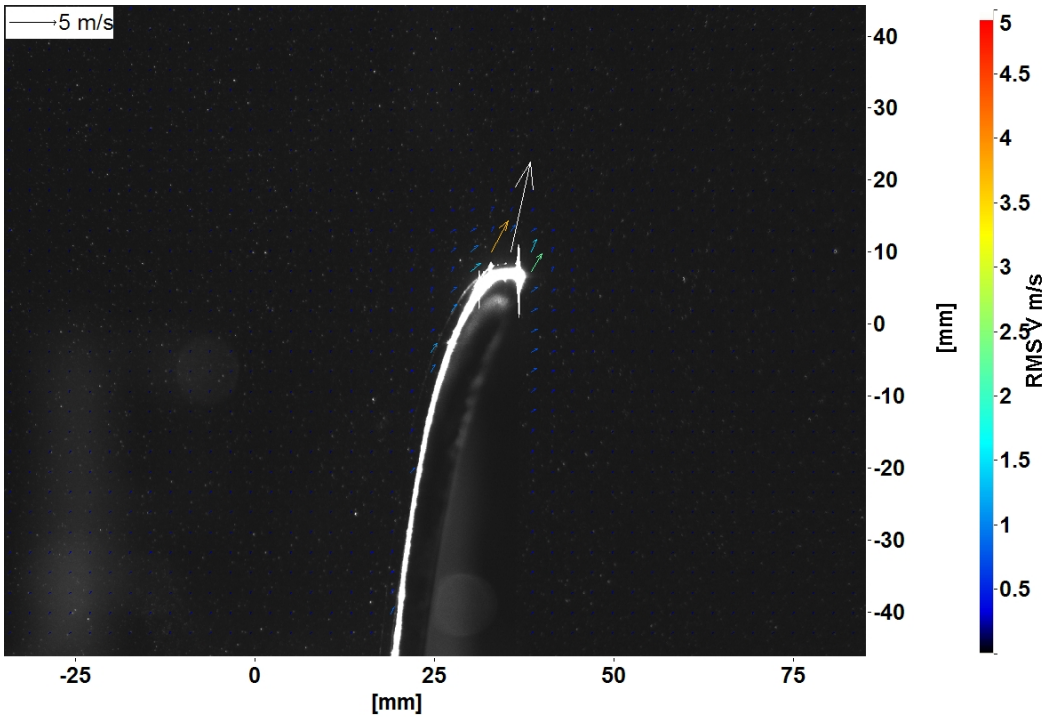

(d) 7 m/s nominal wind speed, "lead" field of view

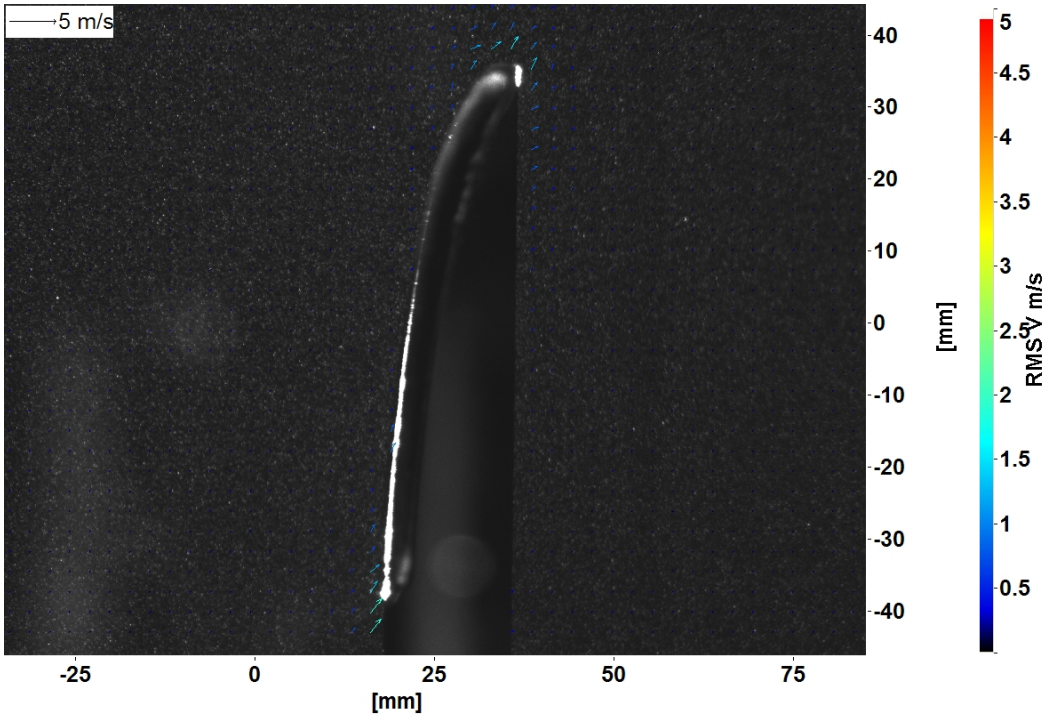

(e) 7 m/s nominal wind speed, “full” field of view

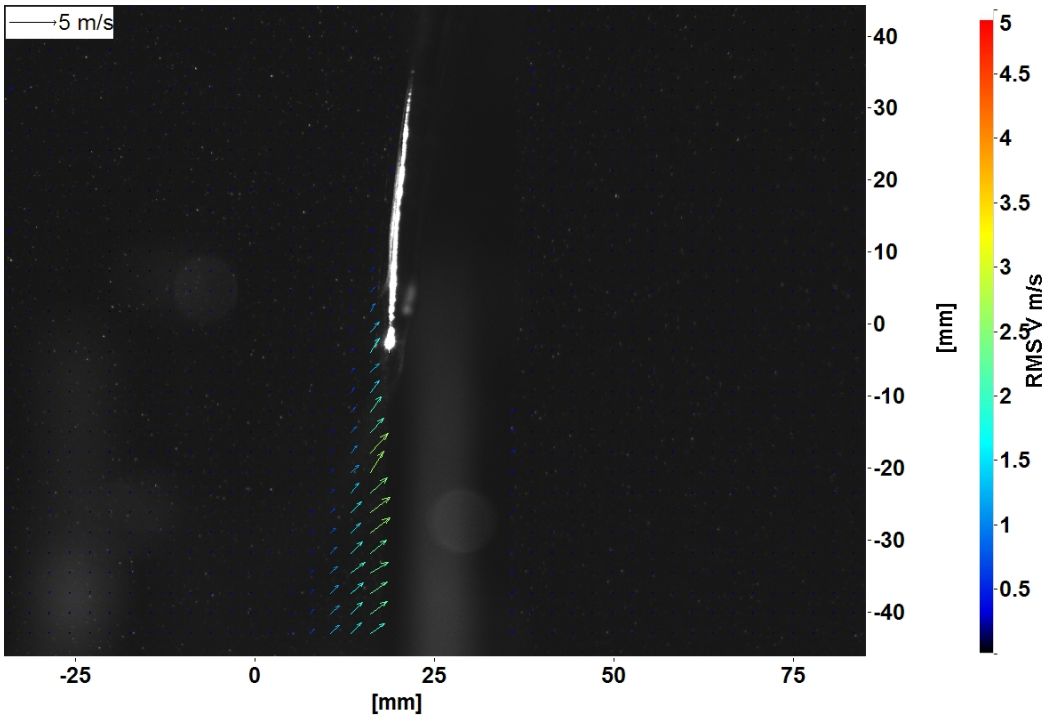

(f) 7 m/s nominal wind speed, “trail” field of view

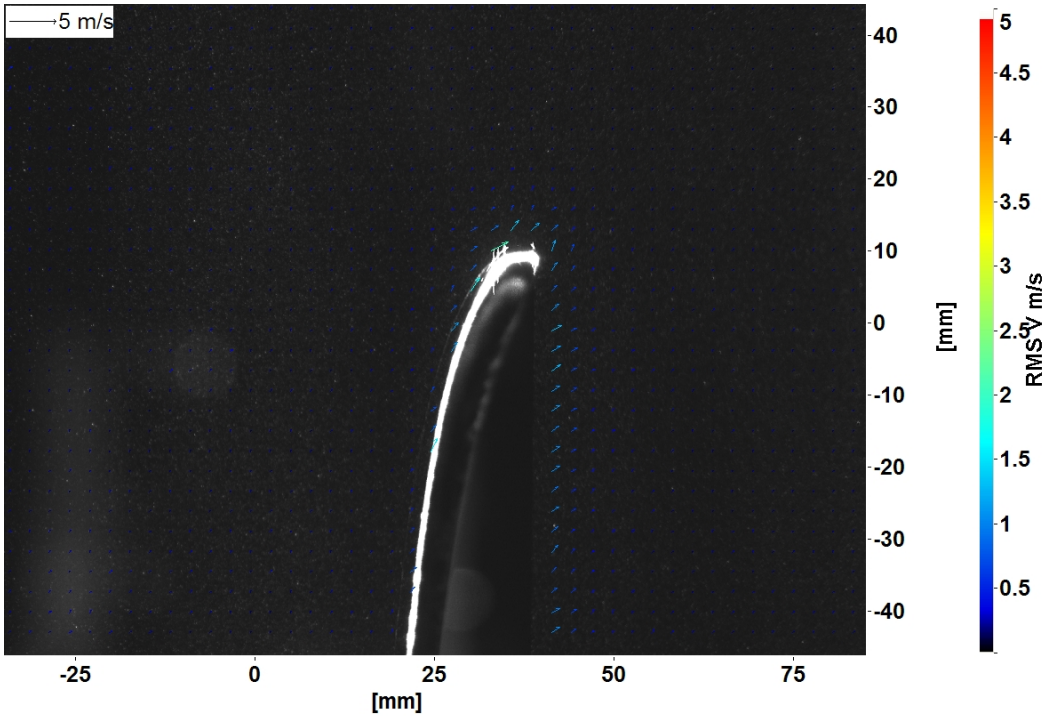

(g) 9 m/s nominal wind speed, "lead" field of view

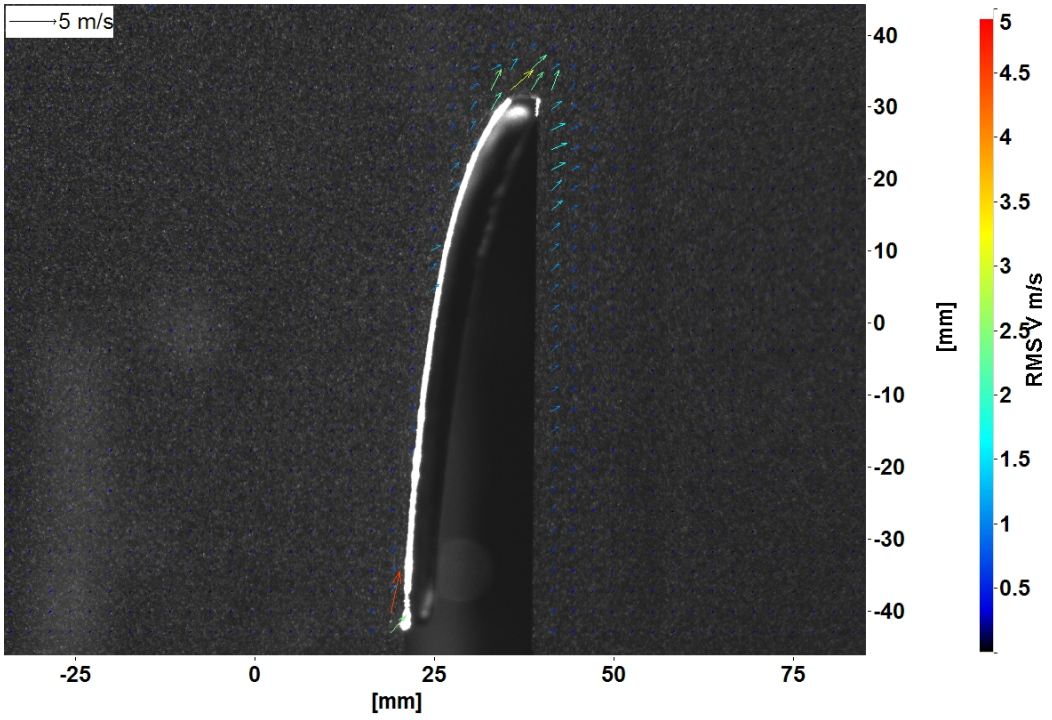

(h) 9 m/s nominal wind speed, "full" field of view

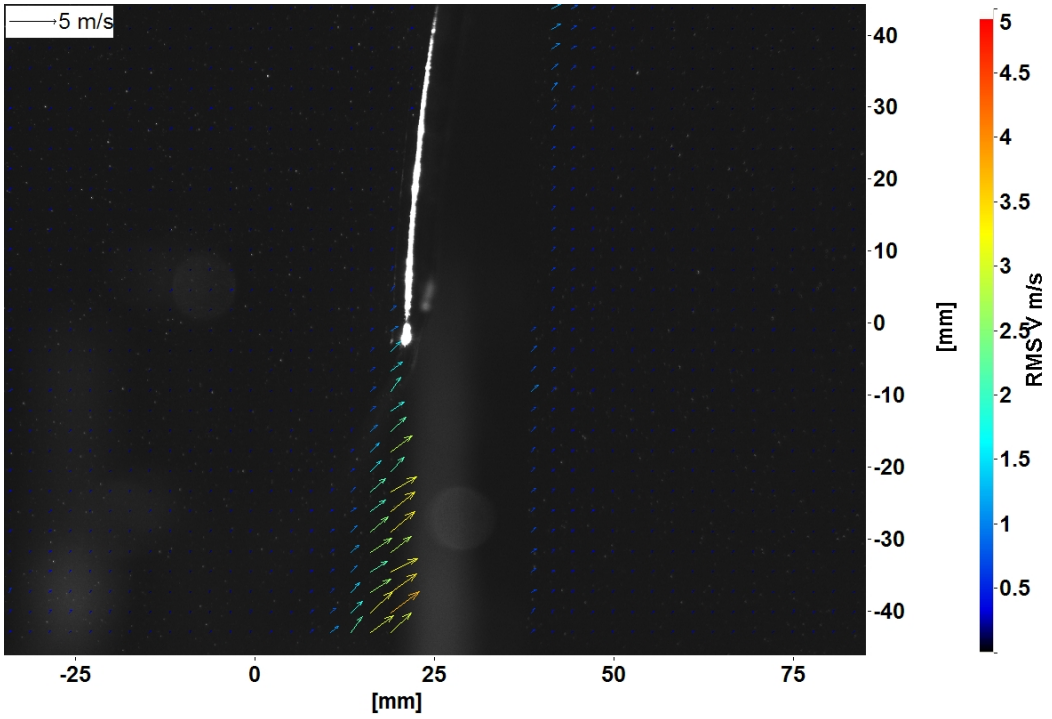

(i) 9 m/s nominal wind speed, "trail" field of view

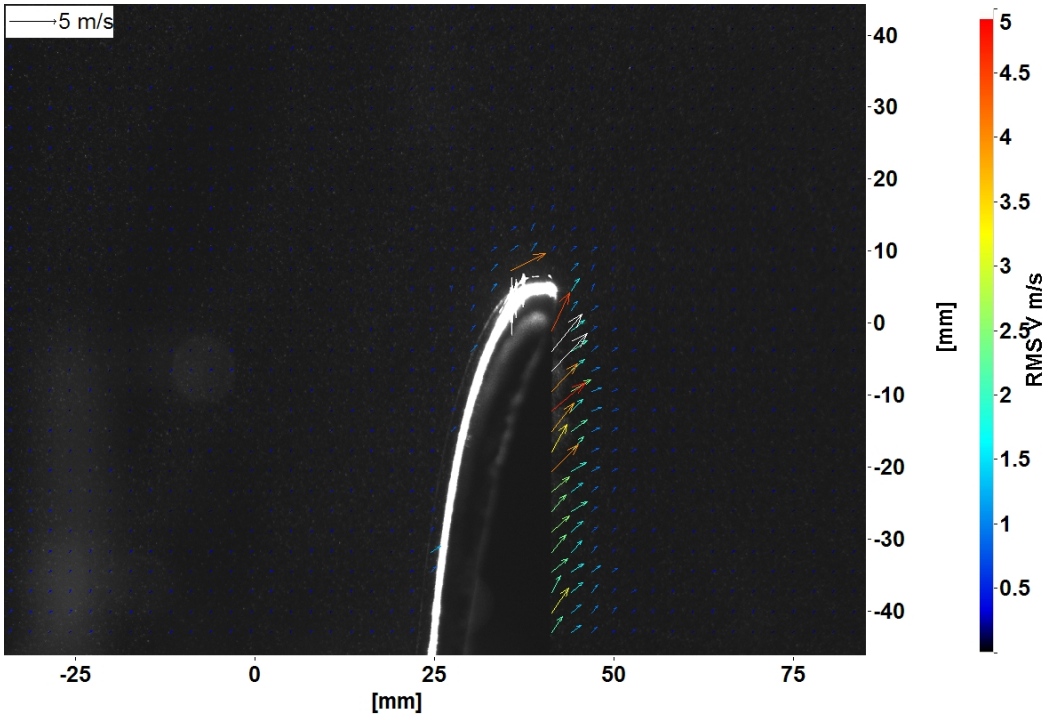

(j) 11 m/s nominal wind speed, "lead" field of view

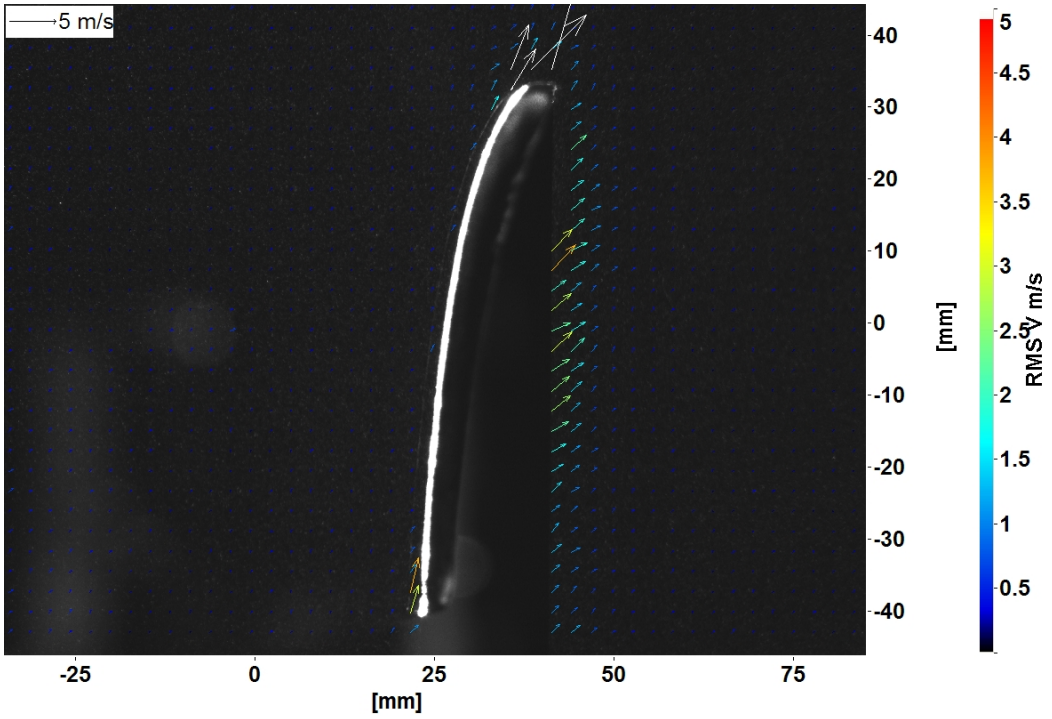

(k) 11 m/s nominal wind speed, “full” field of view

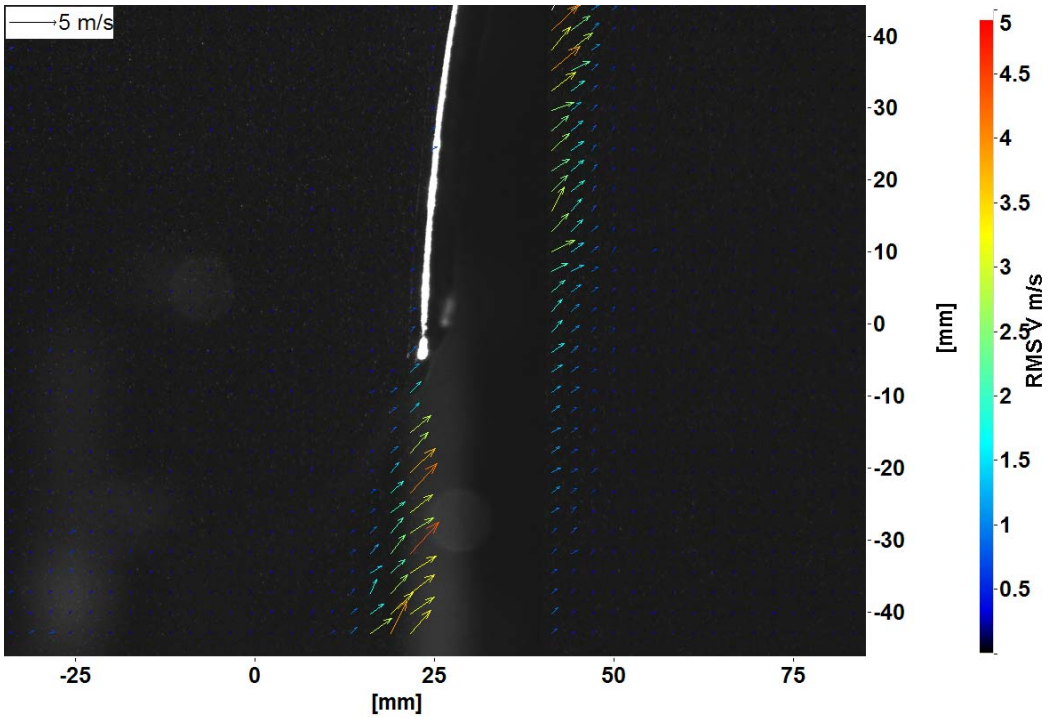

(l) 11 m/s nominal wind speed, “trail” field of view

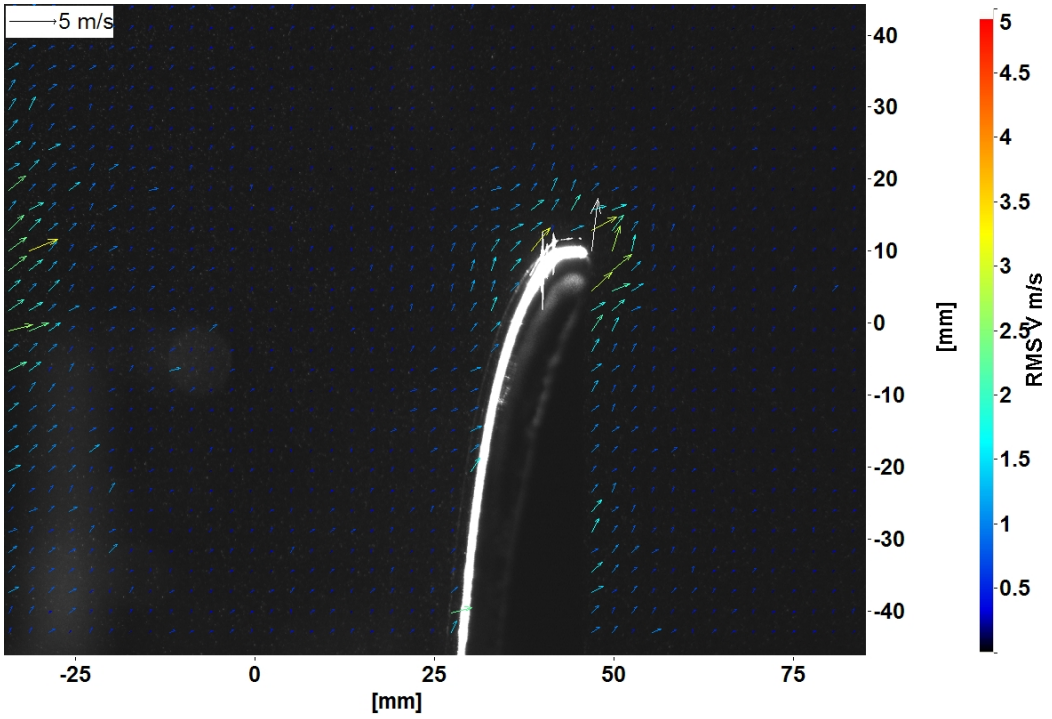

(m) 15 m/s nominal wind speed, “lead” field of view

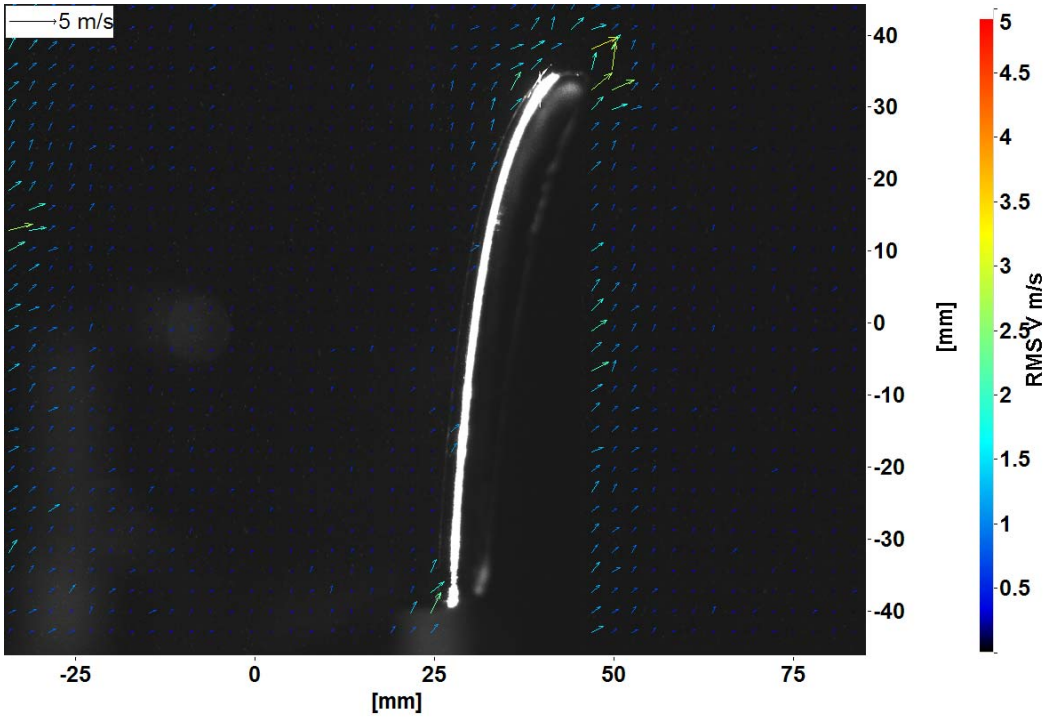

(n) 15 m/s nominal wind speed, “full” field of view

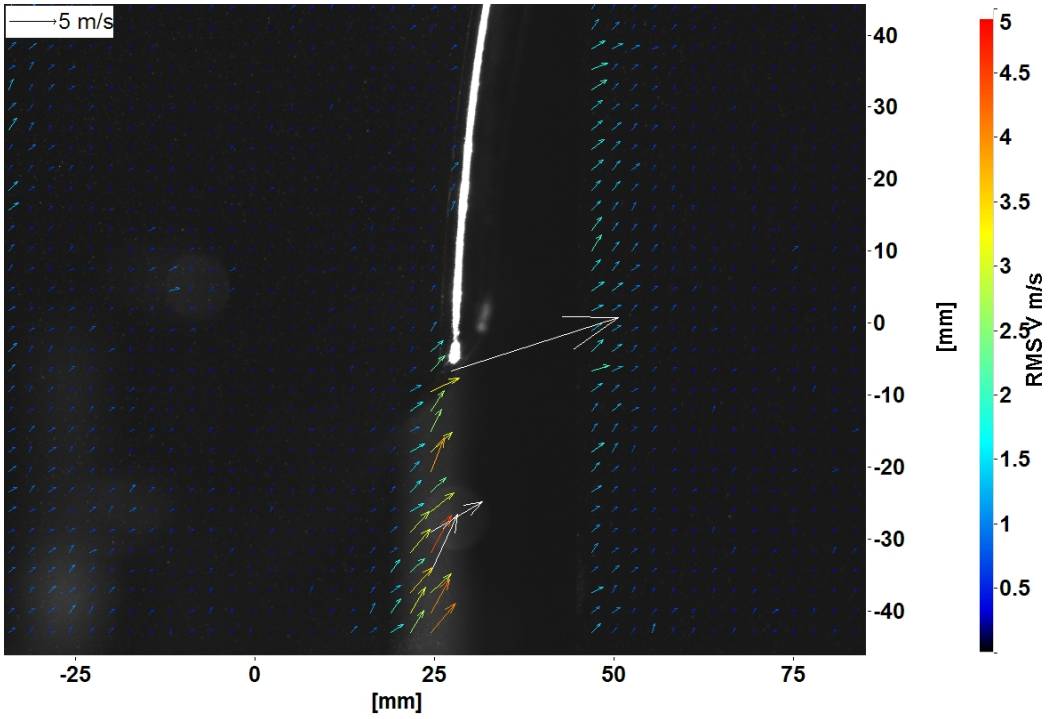

(o) 15 m/s nominal wind speed, "trail" field of view

Figure 5.23 - Planar PIV RMS velocity values

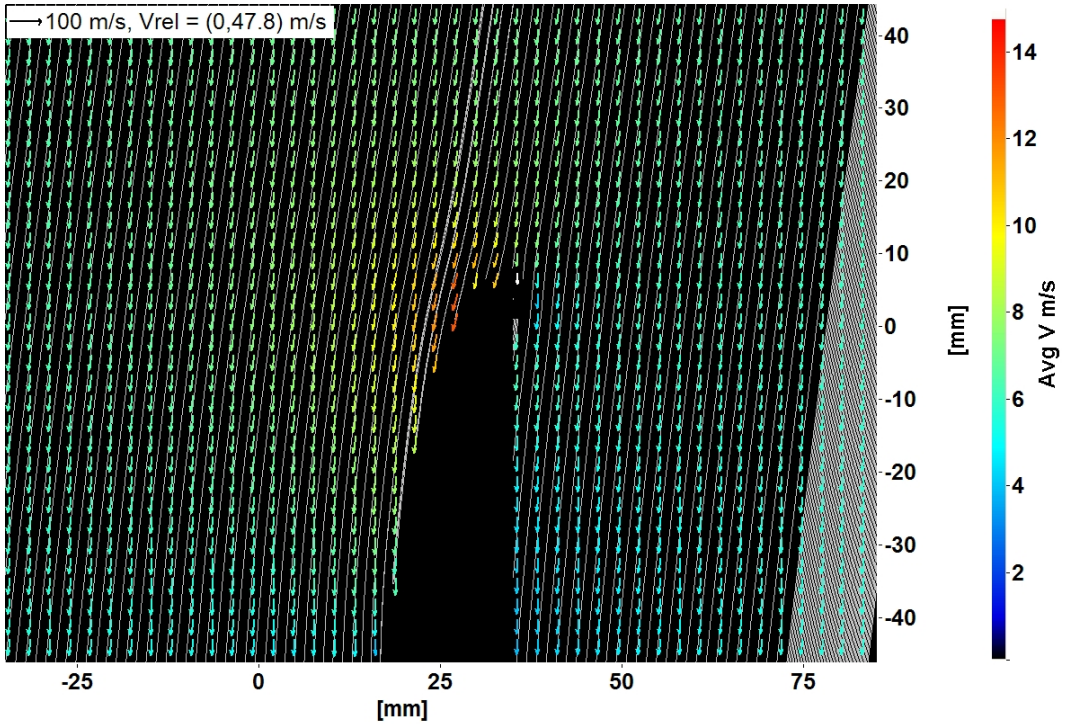

(a) 5 m/s nominal wind speed, "lead" field of view

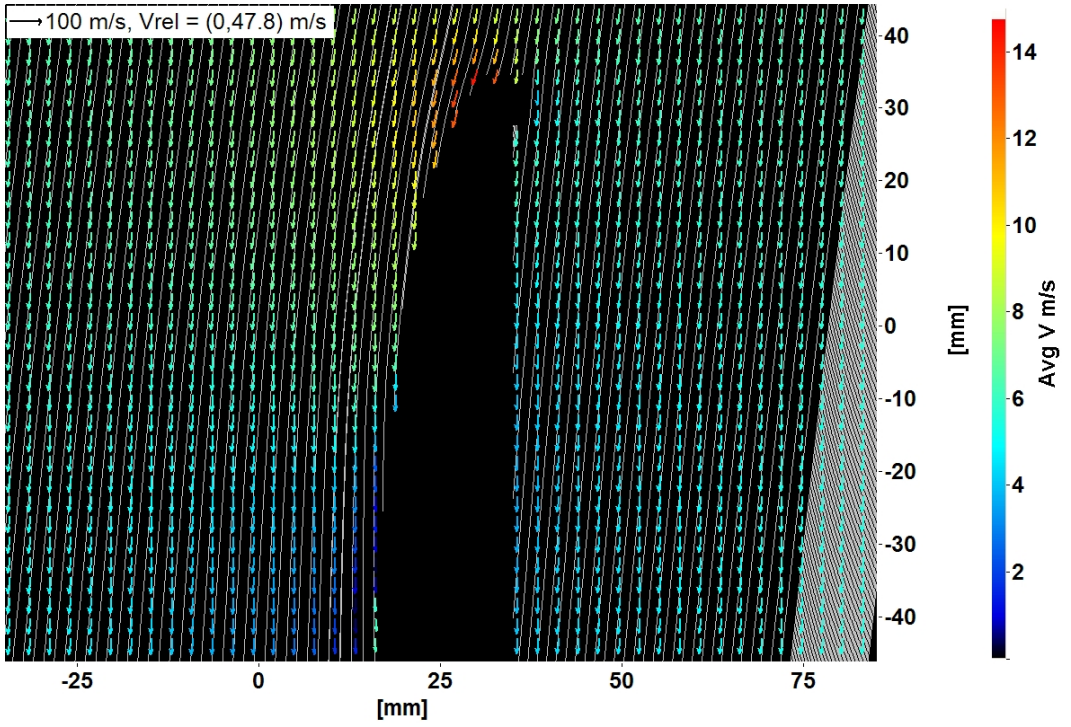

(b) 5 m/s nominal wind speed, "full" field of view

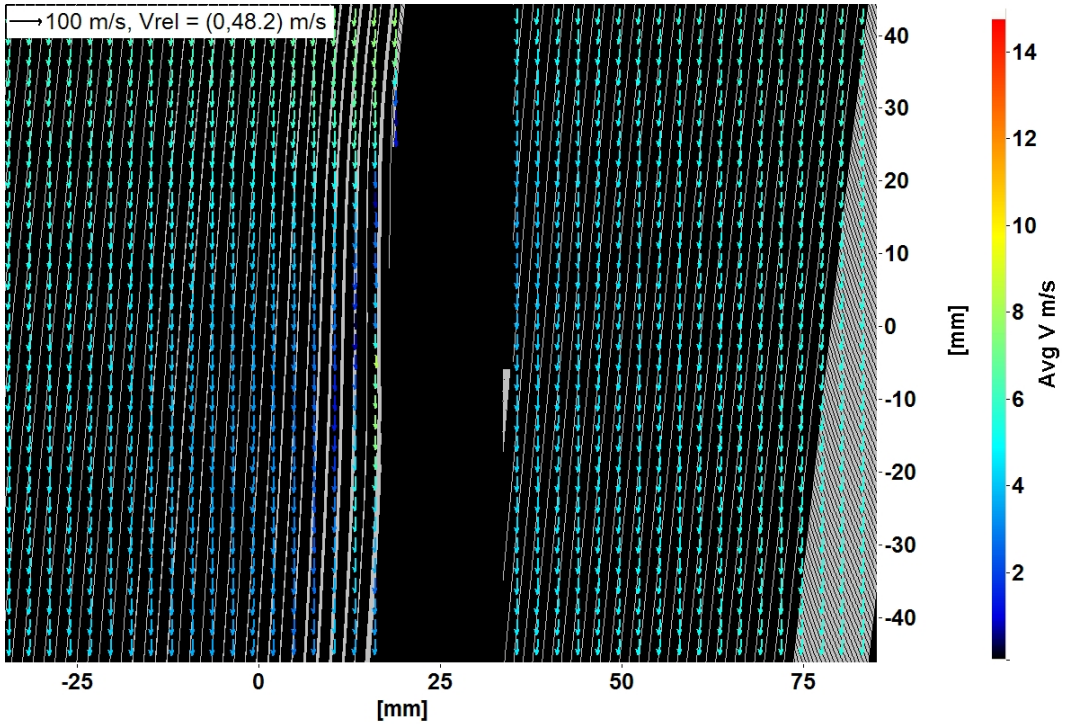

(c) 5 m/s nominal wind speed, "trail" field of view

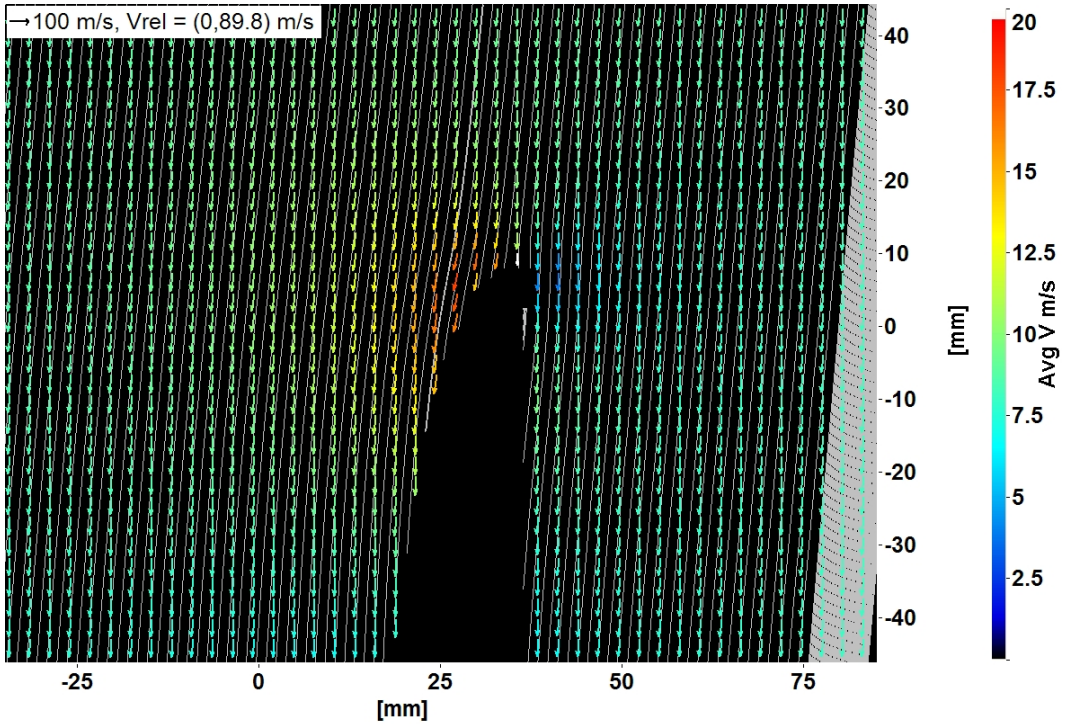

(d) 7 m/s nominal wind speed, "lead" field of view

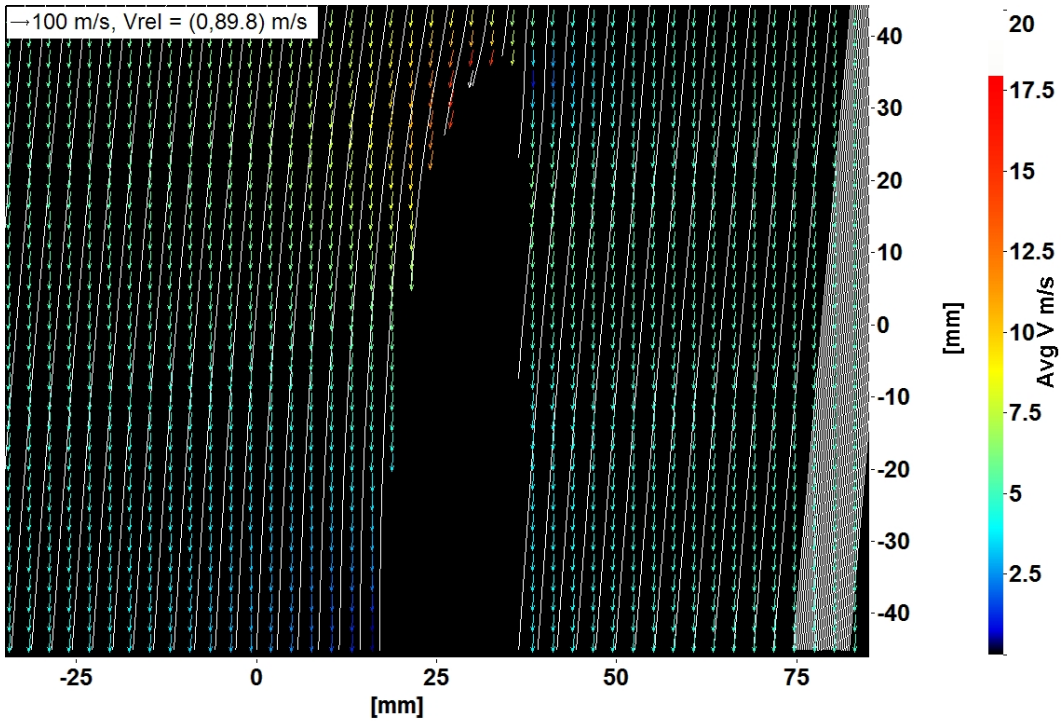

(e) 7 m/s nominal wind speed, "full" field of view

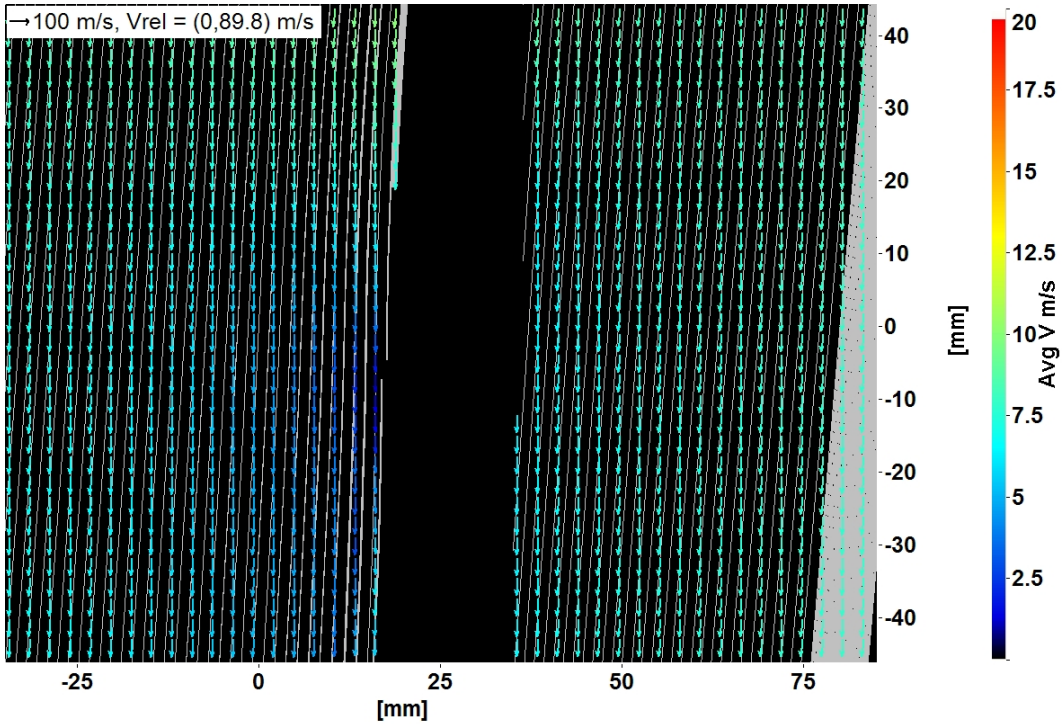

(f) 7 m/s nominal wind speed, "trail" field of view

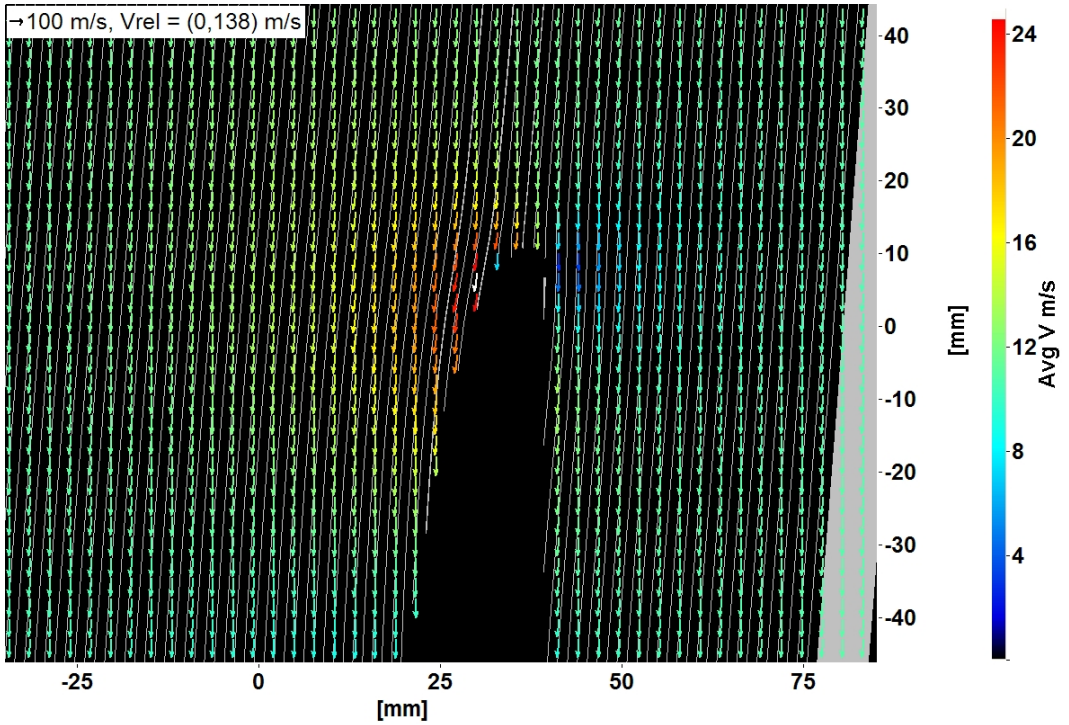

(g) 9 m/s nominal wind speed, "lead" field of view

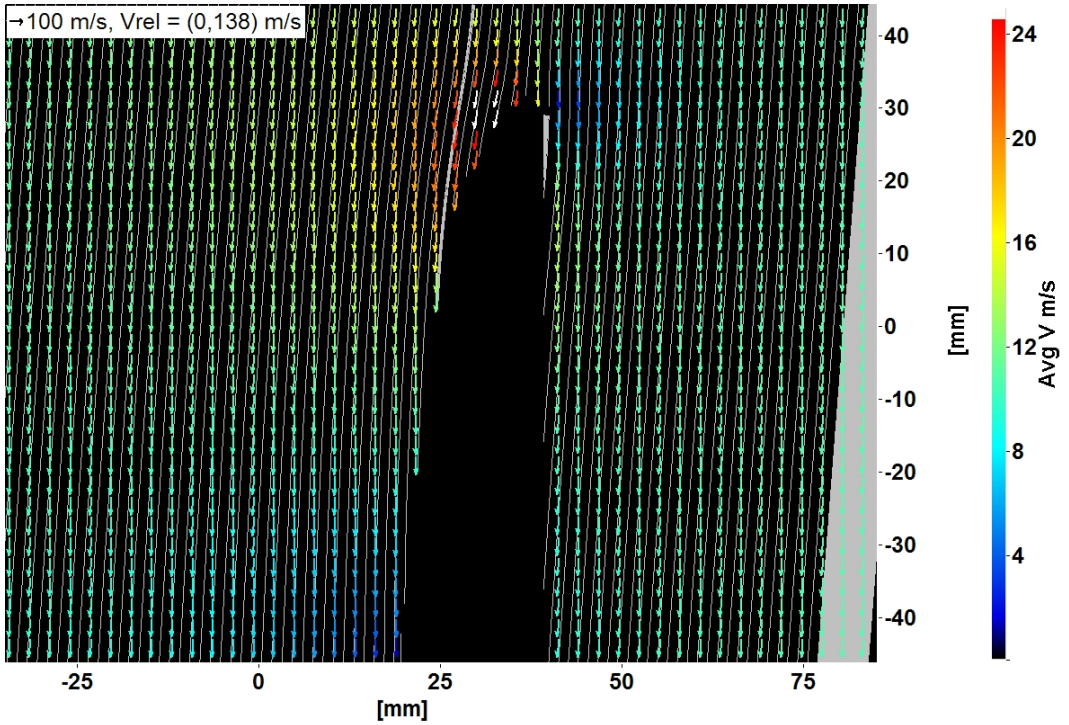

(h) 9 m/s nominal wind speed, "full" field of view

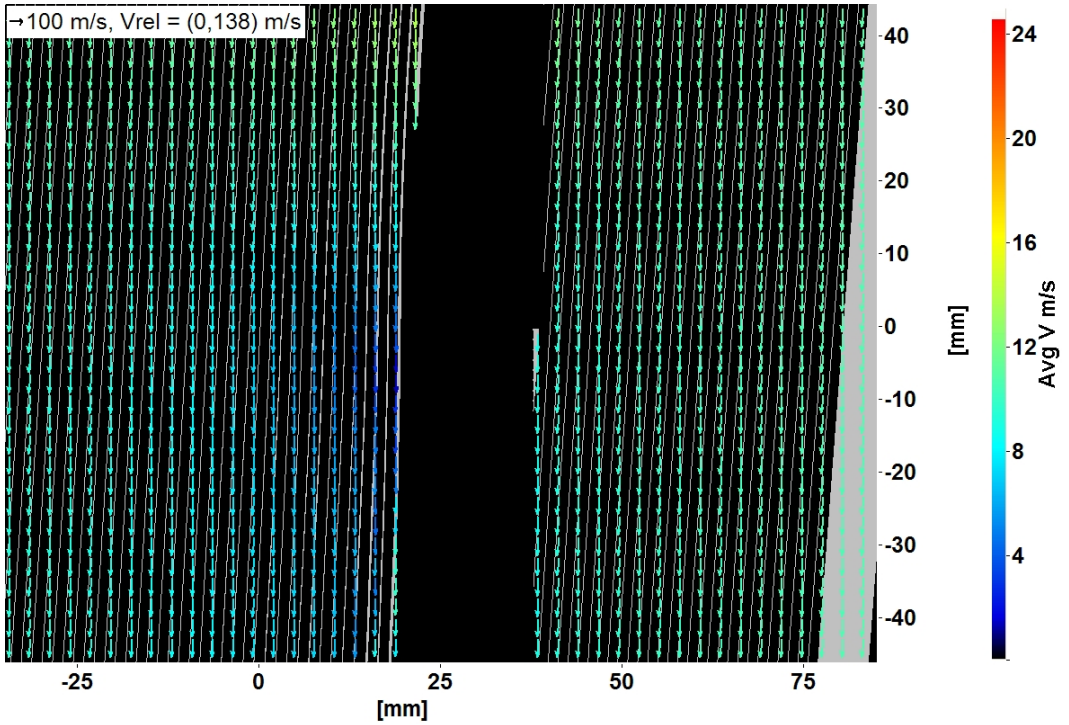

(i) 9 m/s nominal wind speed, "trail" field of view

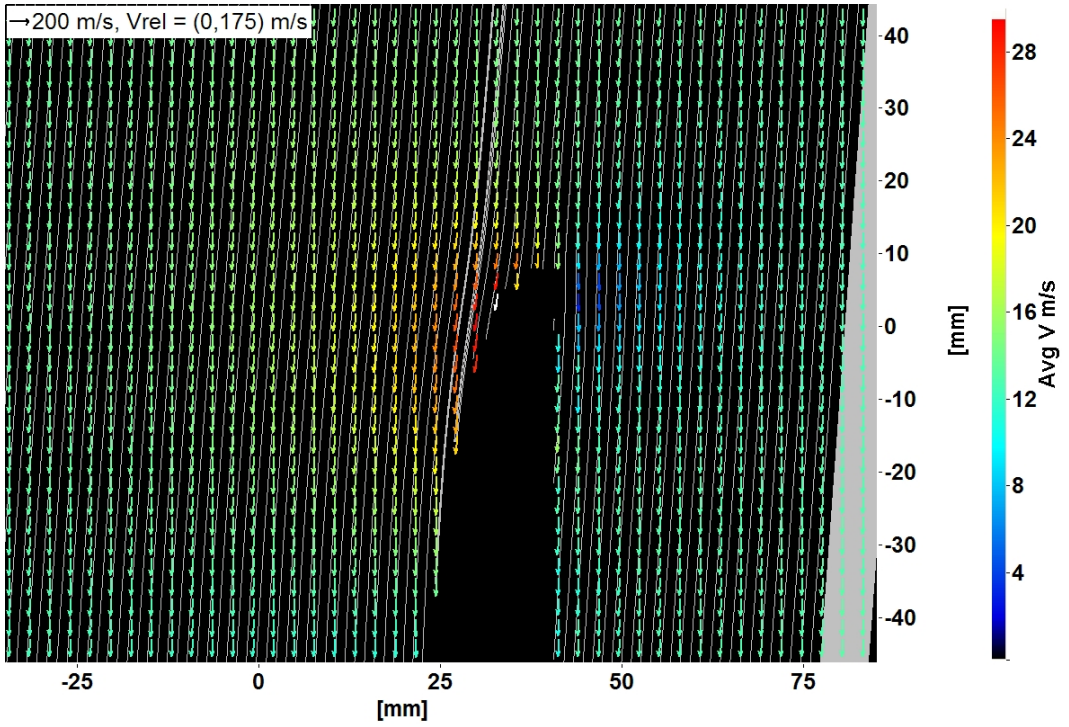

(j) 11 m/s nominal wind speed, "lead" field of view

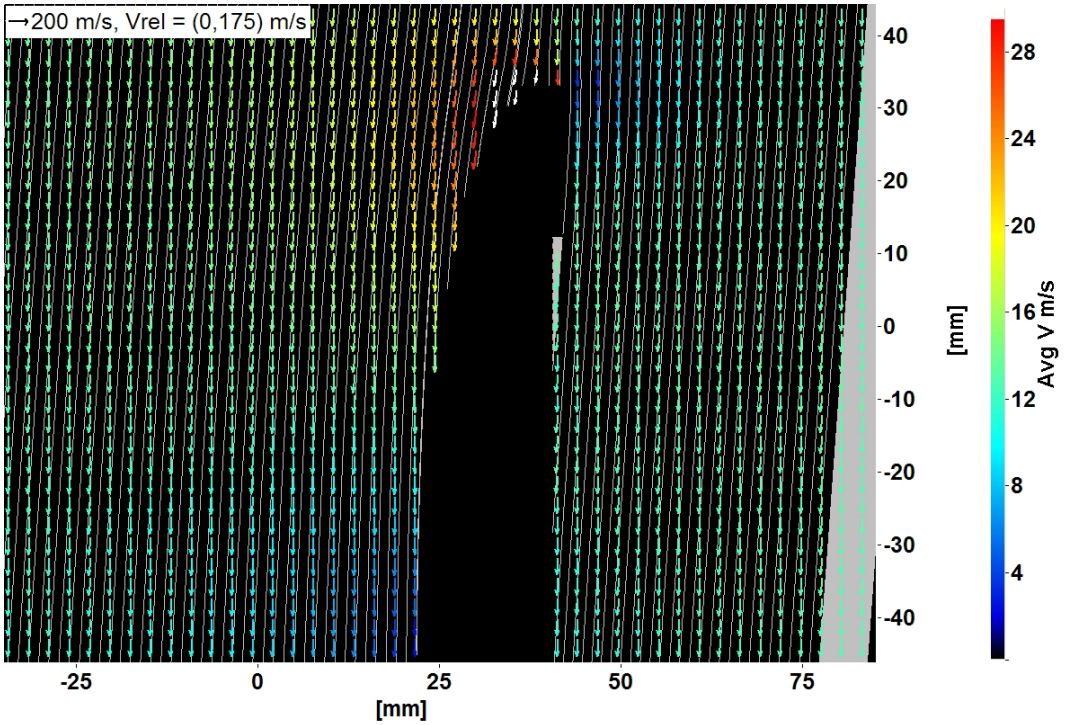

(k) 11 m/s nominal wind speed, "full" field of view

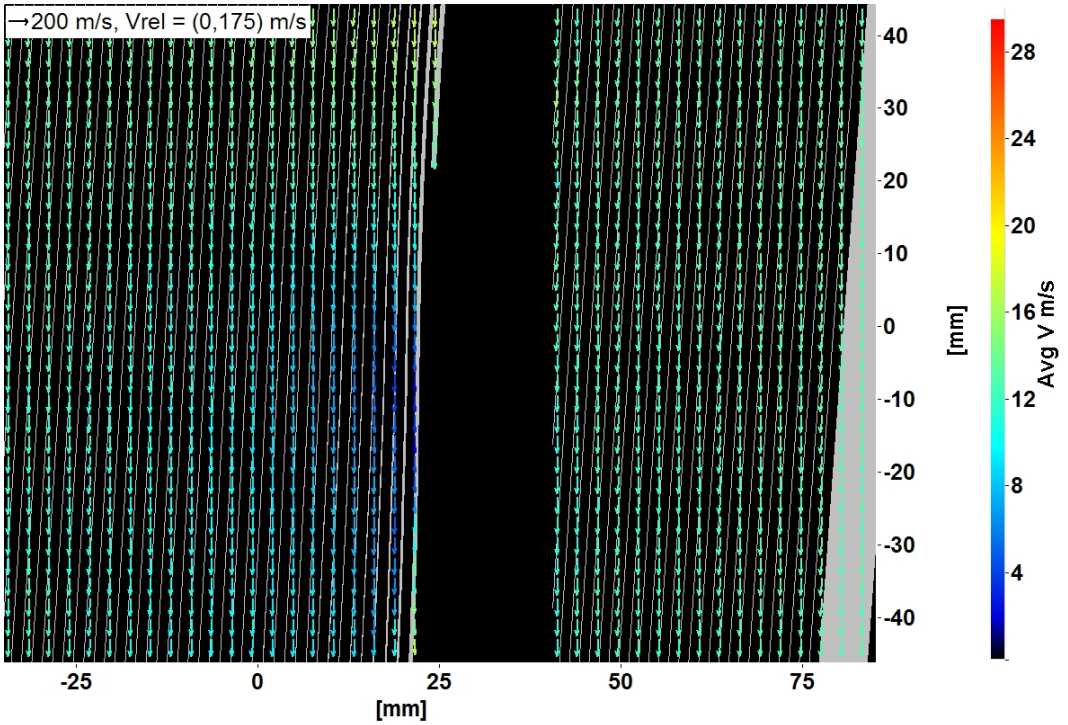

(l) 11 m/s nominal wind speed, "trail" field of view

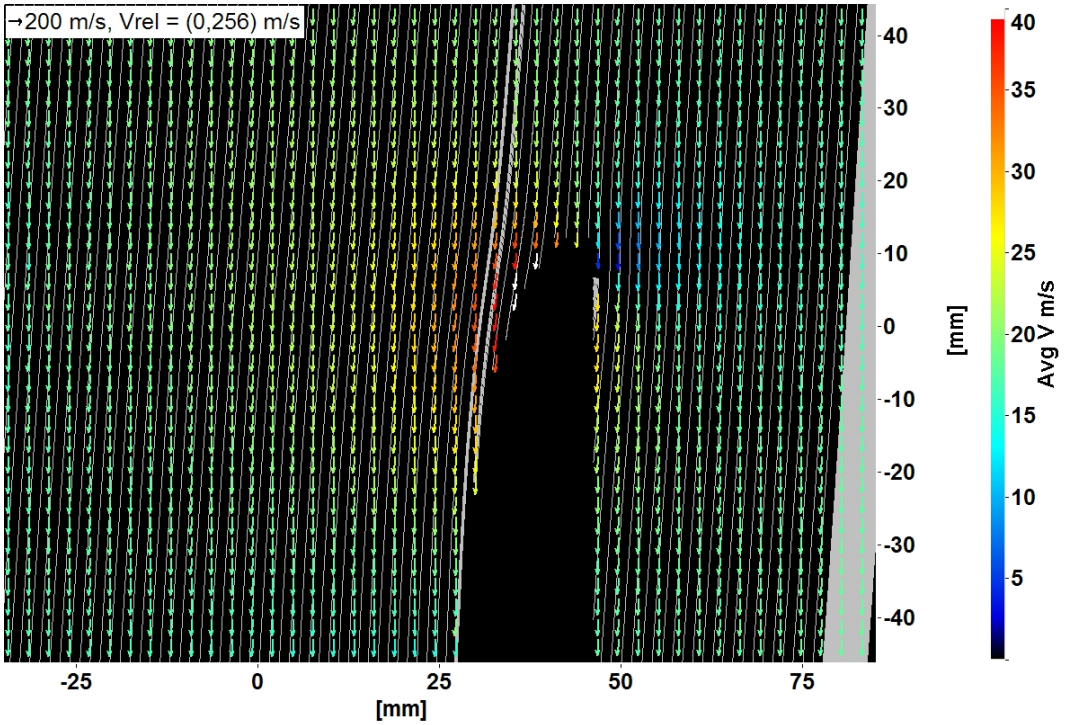

(m) 15 m/s nominal wind speed, "lead" field of view

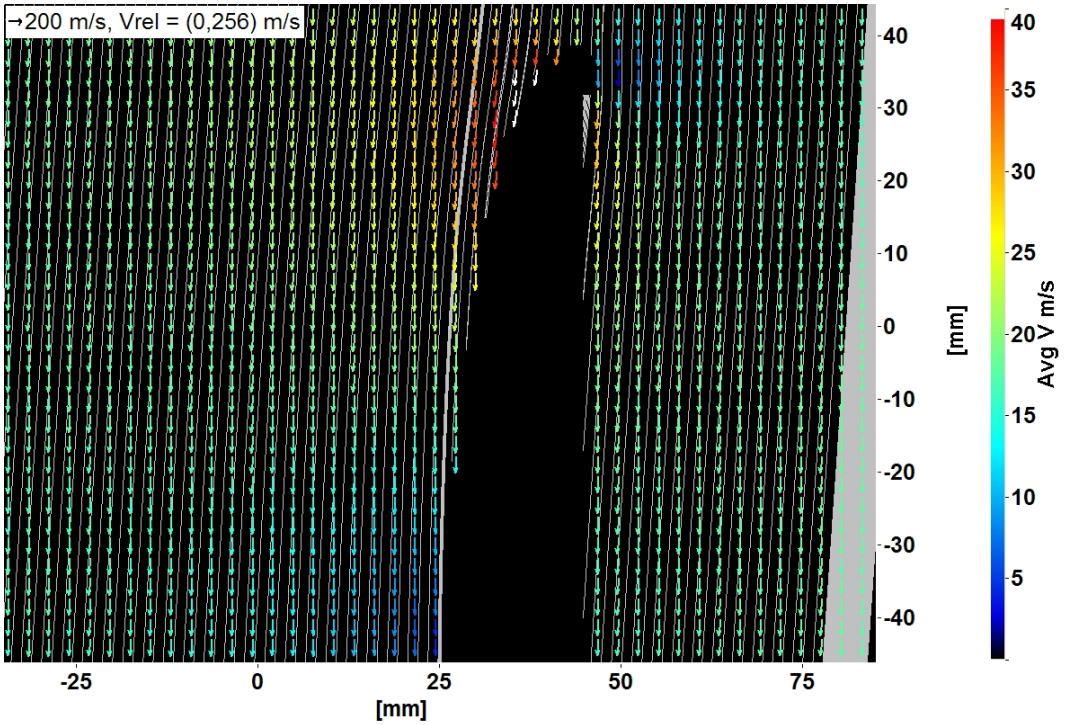

(n) 15 m/s nominal wind speed, "full" field of view

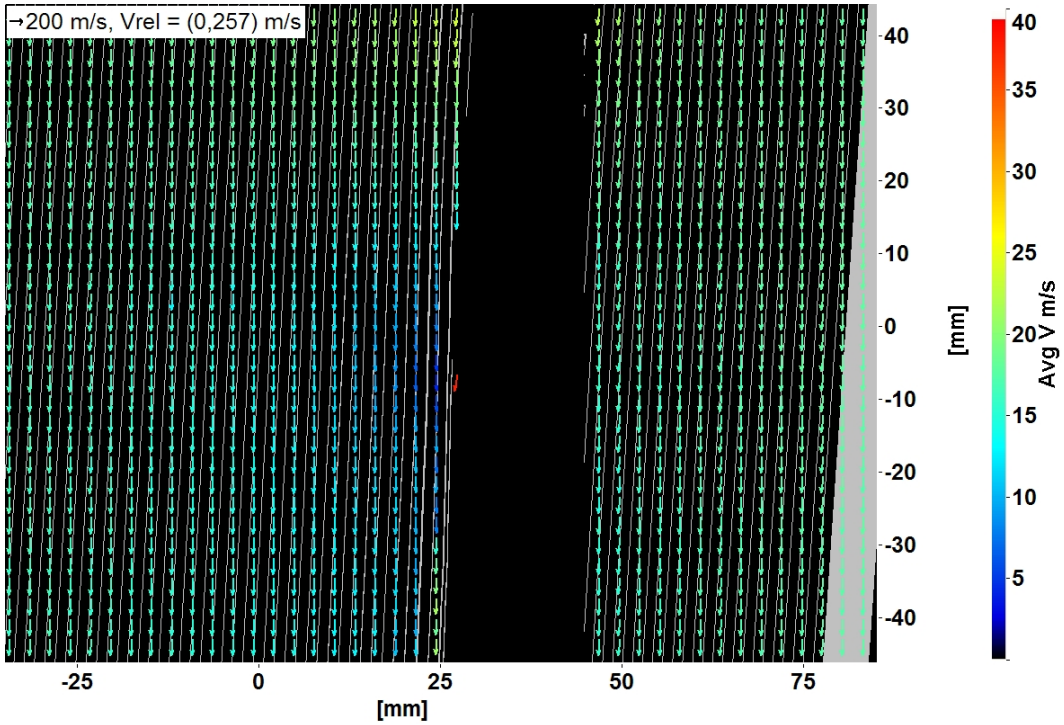

(o) 15 m/s nominal wind speed, "trail" field of view

Figure 5.24 - Planar PIV average vector field around Ampair 100 blade. Vectors are relative to blade speed. Blade is moving up in the image. Axes are dimensions of field of view in millimeters. Legend defines colour of magnitude of velocity vectors. Length of vectors also represent magnitude of velocity vectors.

5.5 Conclusions

The arrangement described resulted in a process that was capable of collecting PIV data and producing vector fields. Fog machine particles are adequate for seeding the flow but are not ideal. The particle size is not well documented and the reflected light being detected by the cameras can be very low. The resulting vector fields from Stereo PIV agree with manometer readings of wind tunnel wind speeds and agree with the general expectations of 3D flow by airfoil theory.

The arrangement described needs improvement. Stereo PIV around wind turbine blades is not effective close to the blade. Even if the shadow could be eliminated with elaborate arrangements of lasers and cameras, the high intensity laser light required for good reflection off the seeding particles will cause reflections off the blade that obscures data at the blade surface. In addition, different camera lenses would be required to zoom in on a smaller field of view to visualize detailed flow information close to the blade.

The PIV arrangement described is capable of demonstrating the 3D flow around the wind turbine blades. At higher wind speeds the z-component of velocity does not increase proportionally with freestream wind speed. At higher wind speeds the flow around the blade can be approximated by 2D flow.

6 Flow Visualization of Water Droplets in Air around a Rotating Wind Turbine Blade using PIV and Particle Tracking

This experiment was set up to capture PIV images of water droplets in the flow around a rotating wind turbine blade and of water droplets impacting on the blade itself. The optics available for the experiment was unable to resolve droplets in the typical icing range (20-40 μm) and even the category of large droplet ice accretion (40-400 μm) would be difficult to see. However, the droplets size that were possible to generate with inexpensive nozzles and resolvable by the optics (0.5-3.0 mm) could still be classified as drizzle or rain (Ice Accretion Simulation December 1997).

The goal of the experiment was to determine the feasibility of tracking the water droplets in comparison to the flow field of the air around a rotating wind turbine blade. Capturing images of droplet impacts on the blade was of great interest for future blade icing experiments.

In addition, wind turbine blades follow one another in the air flow. One of the questions this experiment would like to answer is whether water from splashed droplets on one blade is carried away by the air flow, or if some impinge on the following blade. This would have implications on how numerical blade icing simulations dealt with mass transfer of water droplets.

6.1 Experimental Setup

The experiment was set up exactly as for the previous PIV experiments described in Chapter 5 except a nozzle was introduced upstream of the wind turbine to spray water at the rotor. The wind tunnel ran at a constant wind speed while data were recorded. The experiment was repeated at wind speeds of 5 m/s (11 mph), 6 m/s (13 mph),8 m/s (18 mph), 10 m/s (22 mph) and 15 m/s (34 mph). Two trials at each speed (A & B) were done for redundancy. The load bank was adjusted for the wind speeds as described in Section 2.2.3. Wind speed was measured by the static-pitot tube mounted in the ceiling of the wind tunnel 4.29 m (169”) upstream of the wind turbine mast and Dwyer manometers. Illumination, cameras, smoke generator, and spray nozzle were set up as shown in Figure 6.1 and described in the sections below.

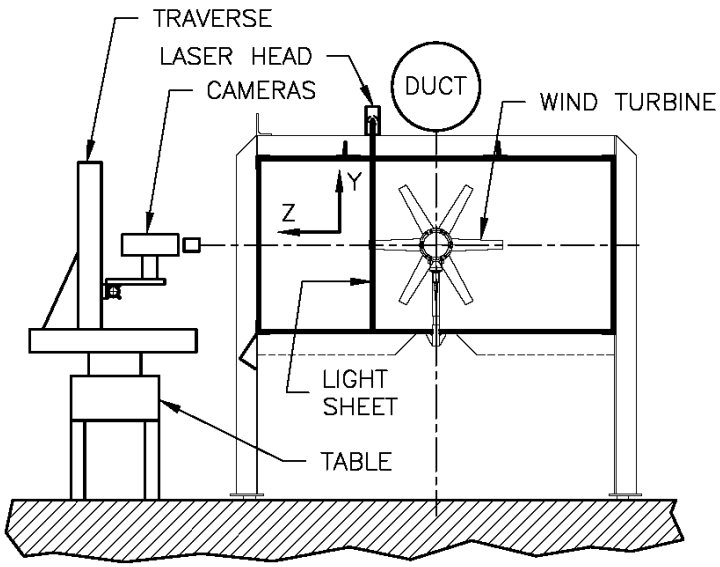

SECTION THROUGH WIND TUNNEL

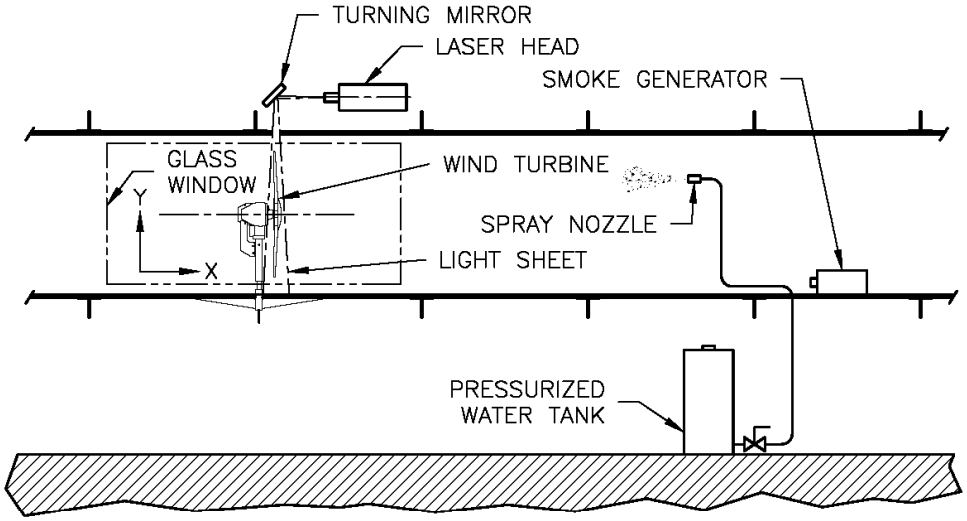

ELEVATION THROUGH WIND TUNNEL

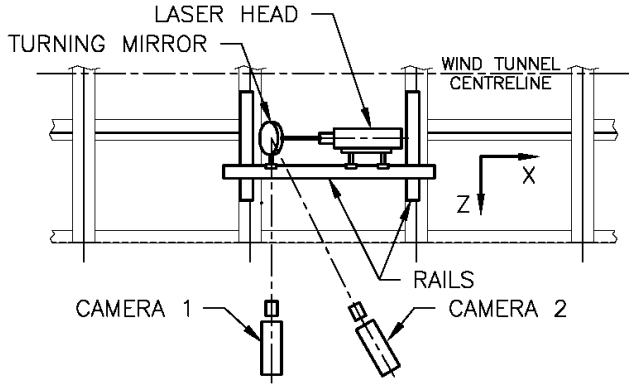

PLAN ON WIND TUNNEL TOP

Figure 6.1 - PIV experiment and water spray in wind tunnel

6.1.1 Illumination

Illumination in this experiment was provided by the laser light sheet described in Section 5.2.1.

6.1.2 Seeding of Flow

Seeding of the flow was accomplished in the same manner as described in Section 5.2.2. However, the previous fog machine broke down so a Fun-Lites FX-8, 700 W machine was used instead. It was found during the experiment that this model was much more effective at providing adequate particle density even at high wind speeds.

6.1.3 Cameras

The cameras used were the same as described in Section 5.2.3. The field of view was selected to view the leading half of the blade with more of the flow field visible as shown in Figure 6.3(a). The orientation and shape of the blade caused a shadow on the upwind side of the blade where no data could be collected. The f# on both lenses were set at 2.8 (maximum aperture) to collect as much light scattered by the smoke particles as possible. The lights in the room were turned off during recording to reduce the background light intensity.

The cameras were mounted on a 3D traverse system to control the location of the field of view. Both cameras were mounted on a single rail. Camera 1 was arranged to view the wind turbine blade end-on, nearly perpendicular to the laser light sheet to allow planar PIV calculations to be made with this camera. Camera 2 was arranged to view the wind turbine blade from an upstream position. The angle between the two cameras was 14°. Camera 1 was 1250 mm (49.21”) from the laser light sheet. Camera 2 was 1152 mm (45.35”) from the laser light sheet.

6.1.4 Calibration

The cameras were calibrated in the same manner as described in Section 5.2.4.

6.1.5 Timing and Image Capture

The timing of the laser and cameras was arranged in the same manner as described in Section 5.2.5.

6.1.6 Water Spray

The system for producing the water spray is illustrated in Figure 6.2. The existing compressed air system in the wind tunnel room is fitted with a pressure regulator valve, pressure gauge and quick-connect fitting. An existing 20 US gallon (17 Imp. gal., 76 L) pressure vessel was filled with fresh water and pressurized with the compressed air. The spray nozzle was connected to the tank by 15 m (50’) of J-flex hose which passed through a hole in the floor of the wind tunnel. The hose was mounted horizontally to a retort stand assembly upstream of the wind turbine so that the nozzle sprayed at the rotor.

The spray nozzle used was a brass BETE nozzle, model GJB16MX, with ½" NPT female thread that produced a full cone spray. Water flow rate was 4.7 Litres/min. (1.0 Imp. GPM) at 70 kPa (10 psi) air pressure. The full cone shape of this nozzle made it easy to ensure that droplets were being directed to the field of view.

The nozzle was mounted upstream of the wind turbine such that the majority of the spray fell short of the rotor in still air but passed through the rotor (and camera field view) when the wind tunnel was brought up to speed. The locations of the nozzles with respect to wind speed are listed in Table 6.1.

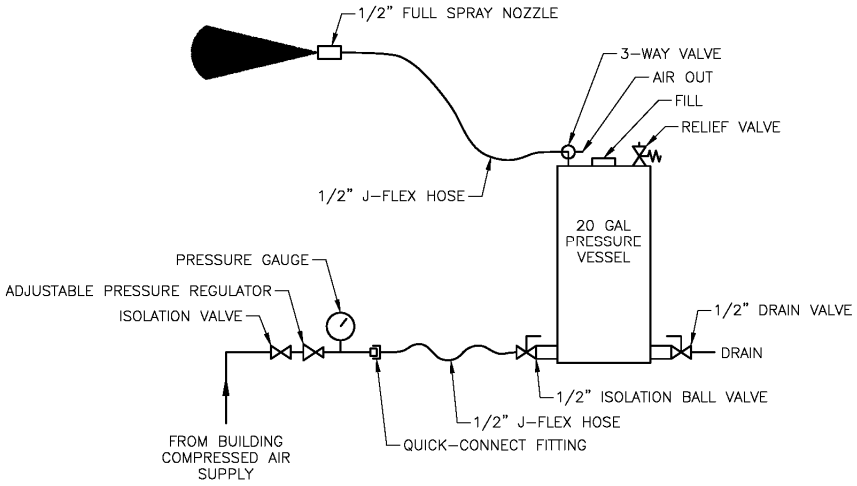

Figure 6.2 - System to produce water spray in wind tunnel

Table 6.1 - Location of water spray nozzle upstream of wind turbine for different wind speeds

Wind Speed		Upstream Distance from Wind Turbine Mast to Nozzle	
(m/s)	(mph)	(m)	(in.)
5	11	3.0	120
6	13	2.3	91
8	18	3.6	142
10	22	3.6	142
15	34	3.9	152

6.2 Data Processing

6.2.1 Image recording

For each wind speed a total of 250 image sets were recorded with each camera. PIV vector fields of the smoke-seeded air flow were calculated for each image set. The vectors were then averaged over the 250 image sets by the commercial software package (LaVision, DaVis ver. 8.0) to produce a final vector field. The rms velocity was also calculated to determine if there were large variations between the individual image sets and the final average.

For each wind speed of the experiment a total of 250 image sets were recorded with each camera. This number was determined by the time it took the pressurized water tank to run out of water. The two cameras allowed stereo PIV to be performed but as it was shown in the previous experiment that the flow field was nearly 2D in nature, the data recorded by camera 1 was chiefly of interest.

The data sets were processed two times. First, to produce a 2D PIV vector field of the air flow around the blades using the smoke seeding particles. Second, to use particle tracking features in the commercial software package to produce a 2D vector field of the water droplets.

The 2D vector fields required only the two frames of camera 1. The original data set was preprocessed to remove the two frames of camera 2. The individual vector fields for each image pair were averaged over the 250 image sets by the commercial software package to produce a final vector field. The rms velocity was also calculated to determine if there were large variations between the individual image sets and the final average.

For particle tracking, individual water droplets were detected in each image pair and vectors drawn for their velocity. The individual vector fields for each image pair were then merged into one final vector field of all the detected water droplets.

6.2.2 2D Air Flow

6.2.2.1 *Image Preprocessing*

The introduction of the water spray significantly affected the speed of the rotor. It was typical for the position of the blade to drop 5 mm or more in the field of view (decreased phase angle, decreasing rotor speed) in the first 70 images or so, especially at wind speeds of 8 m/s (18 mph) and above. After the initial large change, the rotor speed decreased at a slower rate. In addition, uneven rotation, probably due to the mass of the water spray impinging mostly on one side of the rotor, was noticed. The position of the blade in the field of view jumped up and down much more than in the trials without water. In some cases, the IR sensor was fouled by water causing a random

signal to be temporarily sent to the PTU. This caused the blade to move entirely out of the field of view.

The shifting blade in the field of view reduced the accuracy of the final average of the image set. Images that did not contain the wind turbine blade were removed from the data set. Images that were 4 mm above or below the average position of the blade were also removed from the data set. The method of determining the average position of the blade and which images were removed from the data sets can be found in Appendix M.

To calculate the planar PIV vector field of the air flow, the images were preprocessed in three steps: Intensities above a certain value were set to zero, a geometric mask was applied, and a sliding background filter was applied. The seeding particles that were assumed to follow the air flow was the smoke. The smoke particles did not reflect as well as the water droplets. The smoke particles had intensities from 50 to 250 counts so to separate the smoke data intensities above 300 counts were set to zero as shown in Figure 6.3(b).

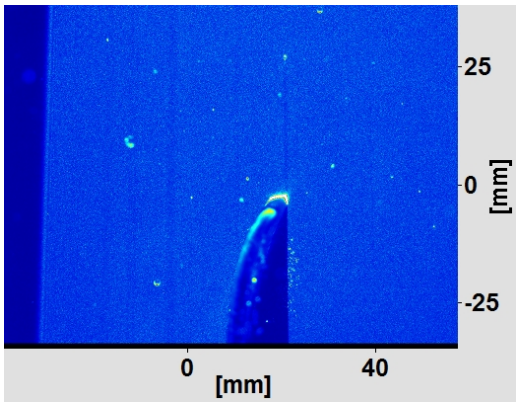

(a) raw image, 8 m/s nominal wind speed, 1k resolution

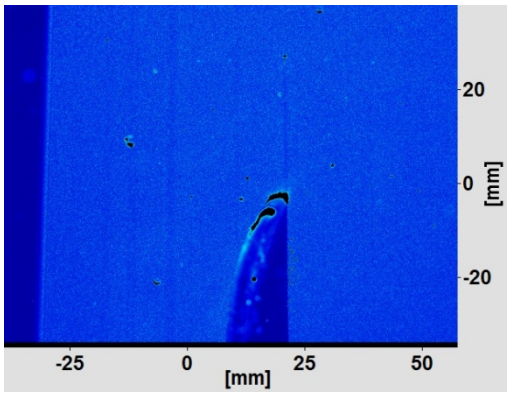

(b) preprocessed image, set intensity counts above 300 to 0, 1k resolution

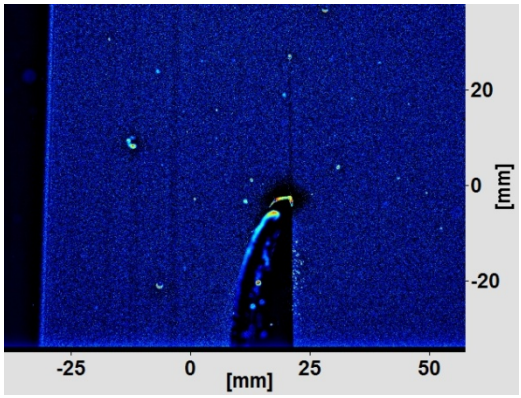

(c) preprocessed image, subtract sliding background, filter length 16 pixels, 512 resolution

Figure 6.3 - Example of image preprocessing

A geometric mask was applied to remove the area taken up by the rotor blade and its shadow. Due to the shifting of the blade in the field of view, it was more difficult to choose where to place the masking shape. An average of all the images was taken to determine the most common position of the blade, which is shown in Appendix M. The errors in the flow vectors near the blade are greater than in the trials without water. A separate mask was applied to each frame of the image pair and applied to all image pairs in the data set.

The third preprocessing step was to apply a high pass filter subtract a sliding background from the images. The filter length was set to 16 pixels. This improved the clarity of the smoke particles as shown in Figure 6.3(c).

6.2.2.2 *Vector Calculation*

The vector calculation parameters were set to calculate a planar PIV vector field. A cross correlation between the two frames of camera 1 was used to determine a 2D velocity vector field. Multi-pass iterations were done. First, a single pass was carried out on an interrogation window of 64x64 pixels, then two passes were carried out on interrogation windows of 16x16 pixels with 50% overlap.

6.2.2.3 *Vector Postprocessing*

The calculated vector field was postprocessed to remove wild vectors. Vectors were deleted if the peak ratio, Q, was < 1.1. In addition, the vector value was compared to the vector values in all bordering interrogation windows. If the vector deviated from the average of the neighbouring vectors by twice the rms, the vector was removed and replaced with the average value.

6.2.2.4 *Peak locking*

Peak locking errors were investigated by consulting the probability density functions (PDF) of the final vector fields as described in Section 5.3.5 above. Peak lock values for the vector fields are listed in Table 6.2. The errors due to peak locking are all acceptable.

Table 6.2 - Peak lock values for recorded data sets

Set	Peak Lock	Set	Peak Lock	Set	Peak Lock
5 m/s A	0.050	8 m/s A	0.125	15 m/s A	-0.022
5 m/s B	0.040	8 m/s B	0.094	15 m/s B	-0.028
6 m/s A	0.096	10 m/s A	0.062		
6 m/s B	0.073	10 m/s B	0.058		

6.2.3 2D Particle Tracking

6.2.3.1 *Particle Detection*

To calculate the 2D particle tracking of the water droplets, the images were preprocessed for particle detection. First a bandwidth filter was applied that detected particles in a size range between 5-60 pixels. Of those particles only those with an intensity of at least 300 counts were accepted. Particle fit mode was set to Gaussian 3x3.

6.2.3.2 *Particle Tracking*

The software settings for processing the particle tracking vectors are shown in Table 6.3. A final vector field was produced by merging all the individual vector fields of each image pair.

Table 6.3- Settings for particle tracking

Allowed Vector Range	
X-direction	0 ± 100 m/s
Y-direction	0 ± 100 m/s
To check special coherence of vector field	
Number of neighbours used	10
Max. search range	50 pixels
Max. gradient of vector field	0.4 pixel/pixel
Median Filter	
Passes	2x
Remove vector if RMS >	2
Insert vector if RMS <	3
Epsilon	0.2 pixel

6.2.3.3 *Vector post-processing*

The final merged vector field was cluttered around the blade. There were some erroneous vectors detected from laser reflections off the blade itself. In addition, droplet splash off the blade leading edge resulted in many droplets upstream and downstream of the blade. Due to the high reflections off these droplets many erroneous vectors were produced in this area, usually of high velocity. To remove some of the excess vectors, a filter of allowable vector range was applied. The filter values applied are listed in Table 6.4.

Table 6.4 - Vector postprocessing filter values

Wind Speed	Vector Range		
(m/s)	Vx	Vy	Vz
5	0 ± 14 pixels	0 ± 20 pixels	0 ± 0 pixels
6	0 ± 10 pixels	0 ± 20 pixels	0 ± 0 pixels
8	0 ± 10 pixels	0 ± 20 pixels	0 ± 0 pixels
10	0 ± 8 pixels	0 ± 20 pixels	0 ± 0 pixels
15	0 ± 7 pixels	0 ± 20 pixels	0 ± 0 pixels

6.2.3.4 *Particle Size*

The shadowgraphy particle sizing module of the commercial software package (LaVision, DaVis ver. 7.2) was used to size the water droplets in the images. The images first had to have the intensity counts inverted before the shadowgraphy process could be applied. The settings for the shadography are listed in Table 6.5.

Table 6.5 - Shadowgraphy particle sizing settings

Multiframe selection		
	# 1st frame:	0
	# 2nd frame:	1
Preprocessing		
	No smoothing	
	Calculate reference image for each source image	
	Reference Calculation	
	Strict sliding max filter	Filter length 16 pixels
Particle Recognition		
	Normalize images by reference images	
	Global threshold:	15%
	Low Level threshold:	15%
	High level threshold:	15%
	AOI expansion:	500%
	Fill particles	
Recognition Filter		
	Maximal low level area:	100% of high level area
	Minimal area:	9 pixel
	Remove particles touching border	
Velocity Parameter		
	Initial window size:	2x2 mm
	Final window size:	1x1 mm
	Passes:	2
	Decrease size:	2 times each pass
	Diameter deviation:	± 100%

6.3 Results

The basic parameters of the experiment runs are listed in Table 6.6.

Table 6.6 - Basic parameters of PIV experiments

Set	Wind Speed (m/s)	RPM	dt (μs)
5 m/s A	5.01	718	58
5 m/s B	5.08	741	58
6 m/s A	6.31	986	46
6 m/s B	6.12	929	48
8 m/s A	8.03	1331	36
8 m/s B	8.07	1336	36
10 m/s A	10.00	1776	29
10 m/s B	10.18	1829	29
15 m/s A	15.02	3040	20
15 m/s B	15.11	3052	20

6.3.1 Particle Size

The average diameter of droplets for each experiment as determined by the shadowgraphy particle sizing process are shown in Table 6.7. These results tended to give diameters that were smaller than the actual droplets because the computer process could detect only the high intensity highlight point of the droplet.

Table 6.7 - Average droplet size as detected by computer process

Set	No. Particles Detected	Average Diameter (mm)
5 m/s A	1904	0.536
5 m/s B	1980	0.575
6 m/s A	3400	0.544
6 m/s B	3370	0.536
8 m/s A	3822	0.582
8 m/s B	3187	0.649
10 m/s A	5149	0.494
10 m/s B	8937	0.556
15 m/s A	15568	0.639
15 m/s B	14933	0.611

Droplets in a single image from the 8 m/s nominal wind speed (Trial B) experiment were manually sized using the software package. The full diameter of the droplets could be seen in the images but the contrast between the droplet edge and the background was not enough for the software to detect. The droplets were sized manually by picking two

points for the maximum diameter and two points for the minimum diameter. The software package used these points to calculate the average diameter.

The particle detection results are compared in Figure 6.4 and Table 6.8. The computer process had 5 erroneous detections caused by reflections from the blade and failed to detect 8 droplets that were identified manually. The average diameter of computer detected droplets was 0.729 mm while the average diameter of the manually detected droplets was 0.935 mm. Using a masking function on the images would reduce some errors in false detections when the blade did not shift beyond the extents of the mask. However, the average size of the particles calculated by the computer would still be smaller than the actual droplet size. To correct this, the experiment would have to be modified to be true shadowgraphy. Backlit droplets would be more likely to be detected as a full droplet and not just a bright highlight.

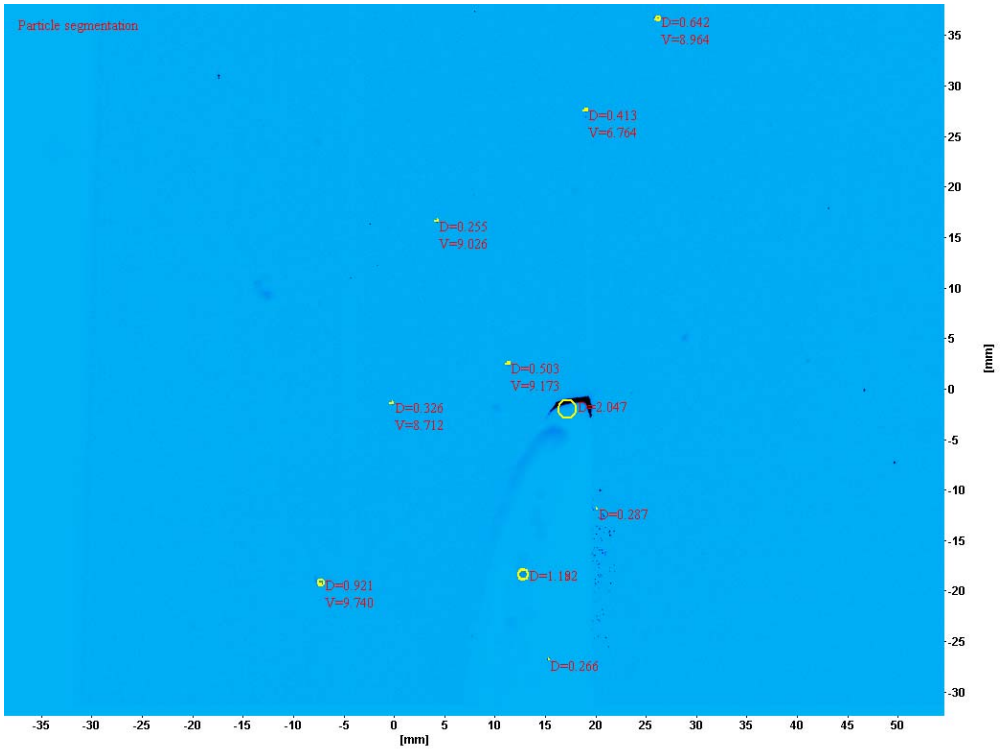

(a) Particle detection by computer process

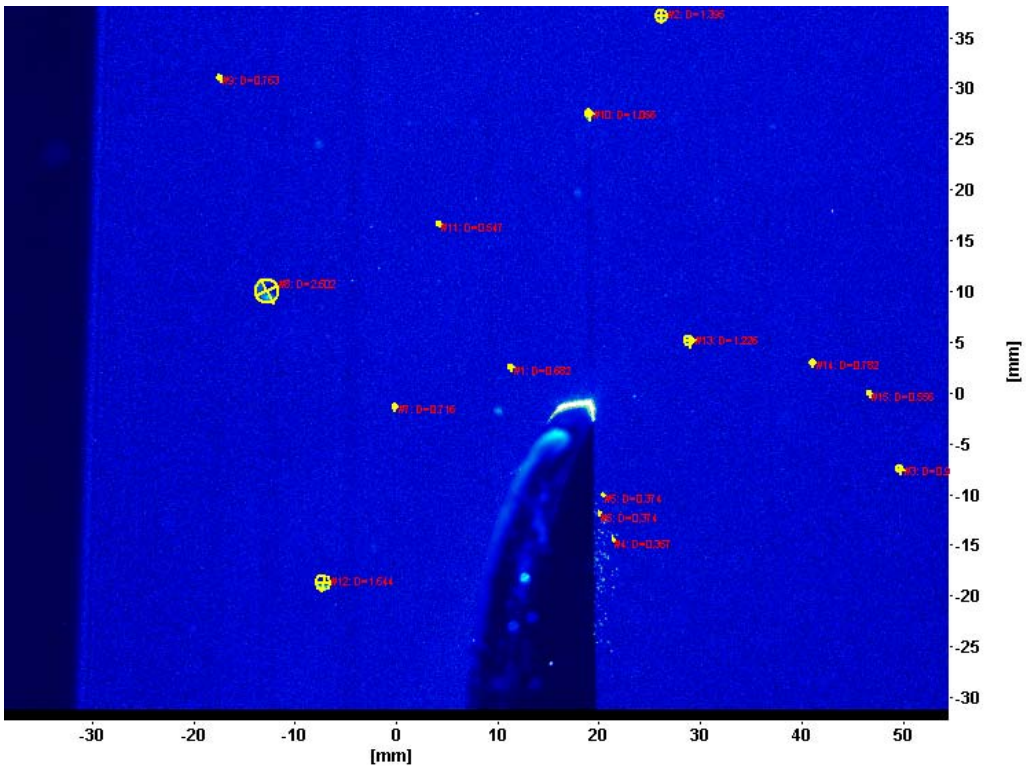

(b) Particle detection by manual process

Figure 6.4 - Comparison of particle detection between computer process and manual process. Wind speed = 8.07 m/s.

Table 6.8 - Droplet size comparison between computer process and manual process

Particle	Location (x,y)	Diameter (computer process)	Diameter (manual sizing)	% larger
1	11.43,2.39	0.503	0.682	35
2	26.35,37.15	0.642	1.395	117
3	49.94,-7.69	Not detected	0.955	-
4	21.58,-14.63	Not detected	0.357	-
5	20.58,-10.19	Not detected	0.374	-
6	20.22,-12.01	0.287	0.374	30
7	-0.02,-1.50	0.326	0.716	20
8	-12.73,9.95	Not detected	2.602	-
9	-17.36,30.99	Not detected	0.763	-
10	19.20,27.42	0.413	1.056	155
11	4.37,16.59	0.255	0.547	115
12	-7.15,-18.92	0.921	1.644	78
13	29.10,5.00	Not detected	1.226	-
14	41.26,2.88	Not detected	0.782	-
15	46.94,-0.22	Not detected	0.556	-
16	17.25,-2.08	2.047	Erroneous	-
17	12.76,-18.48	1.182	Erroneous	-
18	12.76,-18.48	1.182	Erroneous	-
19	15.42,-26.85	0.266	Erroneous	-
Average		0.729	0.935	

6.3.2 Particle Tracking

An example of particle tracking vectors for a single image pair is shown in Figure 6.5. It shows the vectors overlaid on the raw image and shows that the vectors actually correspond to detected water droplets.

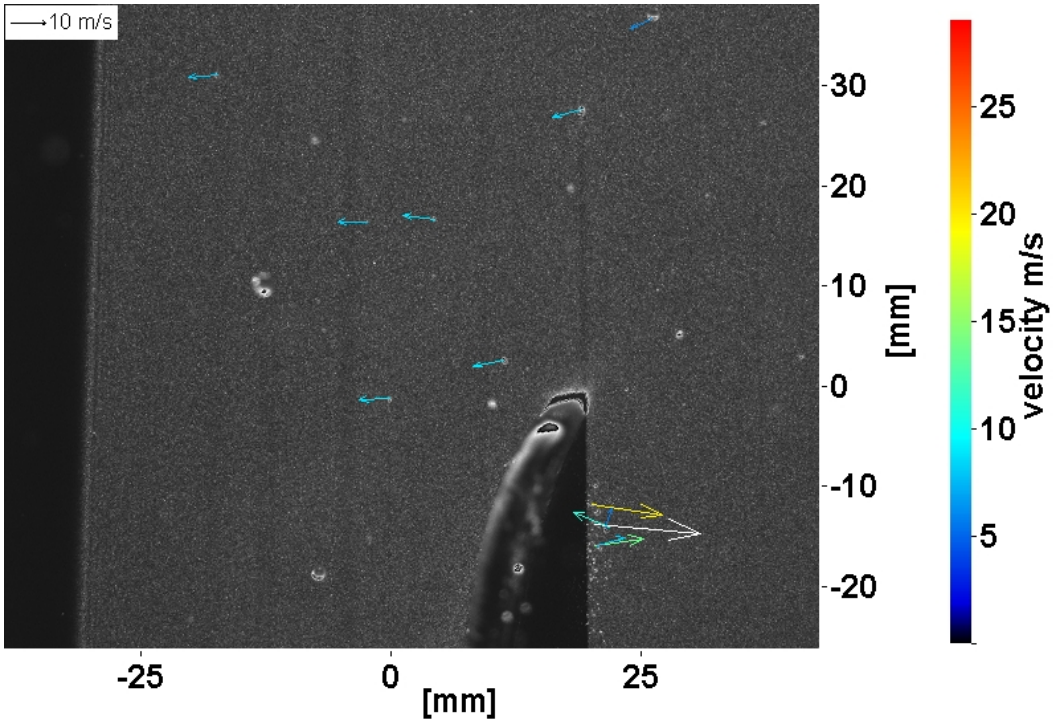

Figure 6.5 - Velocity vectors of detected water droplets. Nominal wind speed 8 m/s, trial A.

Water droplet velocity vector fields merged from all image pairs displayed over the 2D streamlines for trial A of each wind speed are shown in Figure 6.6. The droplets upstream of the rotor can be seen to be affected by gravity and are falling down compared the air streamlines. An average of the particle velocity vectors in the upper right corner of the field of view was calculated by the commercial software package. The average velocity of the particles is compared with the speed of the blade in the vertical direction in Table 6.9 to highlight the difference in relative speeds between them. It is clear that this is the reason that the droplets are more likely to impact the projected area of the blade in the rotor plane than with the upstream-facing pressure side of the blade.

Table 6.9 - Average water droplet velocity in freestream flow compared with blade speed

Set	Blade Speed	Average Droplet Velocity
	(m/s)	(V_x, V_y)
5 m/s A	32.8	-5.04,-0.82
5 m/s B	33.8	-5.06,-0.75
6 m/s A	45.0	-6.45,-0.51
6 m/s B	42.4	-6.22,-0.88
8 m/s A	60.8	-7.92,-0.65
8 m/s B	61.0	-8.05,-0.63
10 m/s A	81.1	-9.45,-0.21
10 m/s B	83.5	-9.50,-0.41
15 m/s A	138.8	-13.37,-0.40
15 m/s B	139.3	-12.56,-0.30

Droplets being hit by the rotor splash into many smaller droplets that have momentum imparted to them by the moving blade. Immediately downstream of the blade the vectors of these splash droplets can be seen to be moving up compared to the air streamlines. Splashed droplets are also knocked upstream of the rotor. They can be seen as vectors moving up and down against the freestream flow immediately upstream of the blade.

Re-impingement of splashed droplets back onto the blade cannot be reliably determined. The shadow upstream of the blade hides any data that might be there. On the suction side of the blade the intensity of the laser on the blade itself, and the reflections from the many splashed droplets, make wild vectors common.

At wind speeds of 8 m/s and greater there are some vectors in the upper right quadrant of the field of view that are oriented up compared to the streamlines. Visual inspection of the raw images that produced these vectors indicate that they are not just wild vectors and they are indeed following a water droplet. It may be that these water droplets were given their upward momentum by the previous blade. These particles would represent splashed droplet particles that were ejected into the air flow upstream of the rotor and may re-impinge on the following blade.

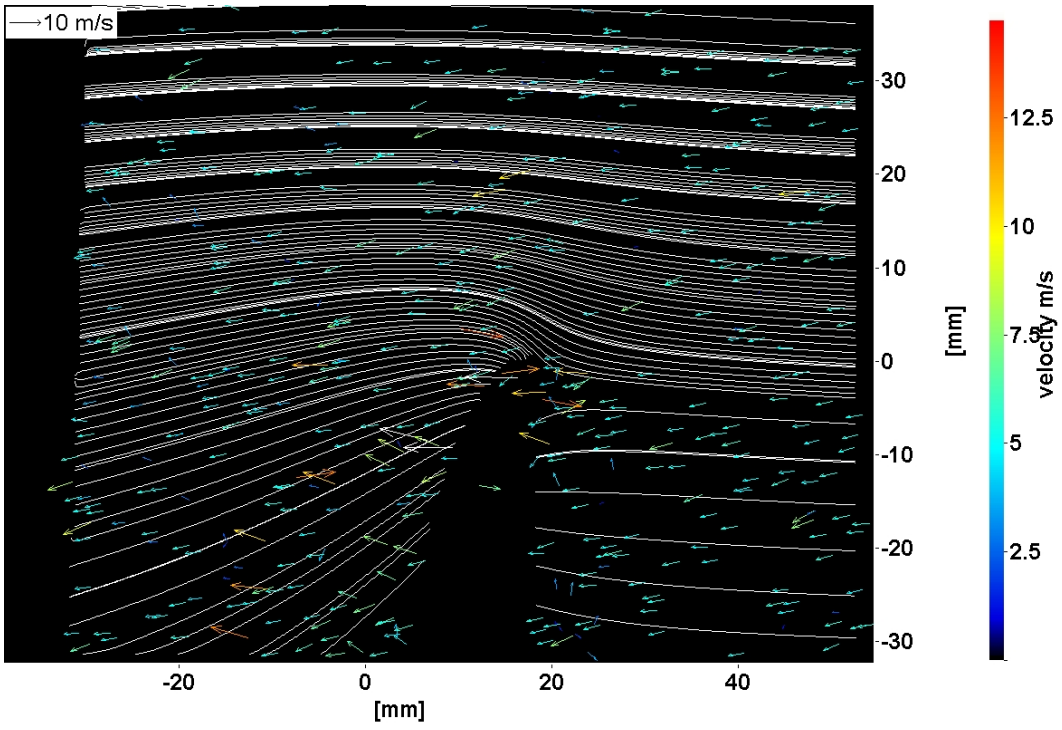

(a) 5 m/s nominal wind speed

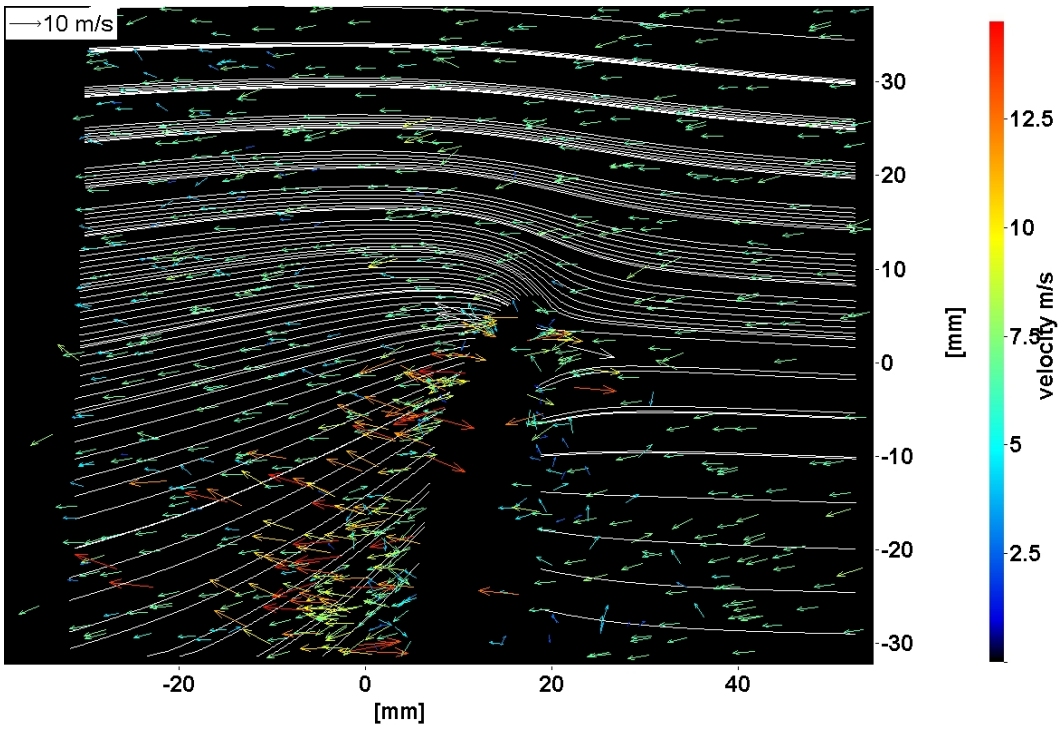

(b) 6 m/s nominal wind speed

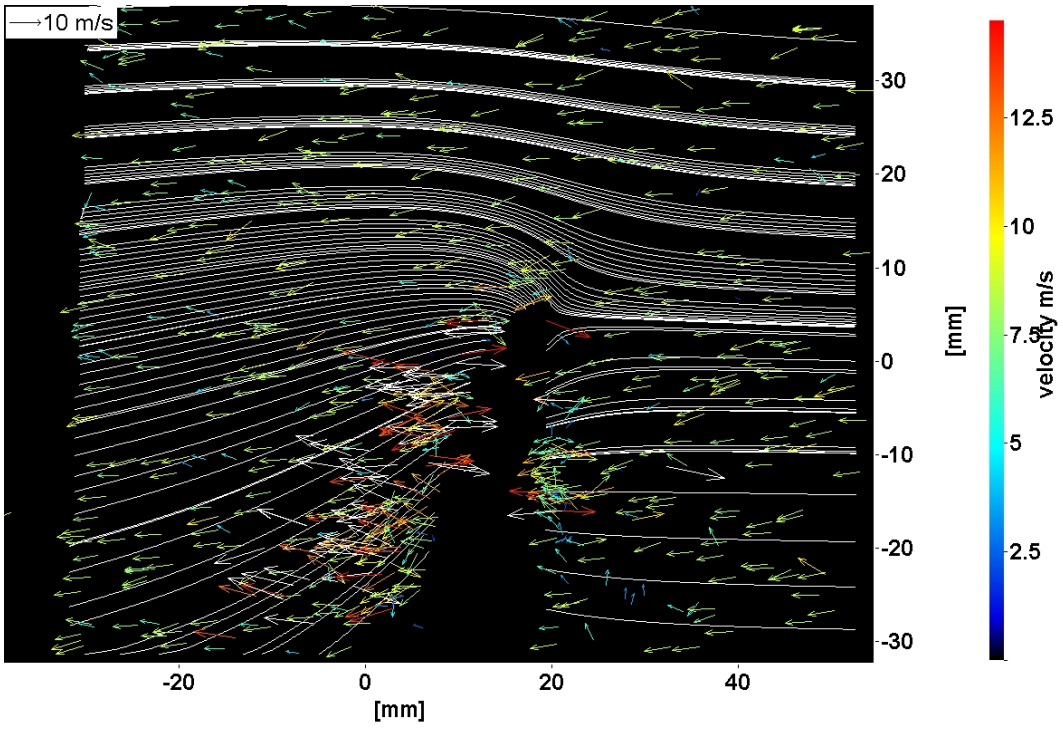

(c) 8 m/s nominal wind speed

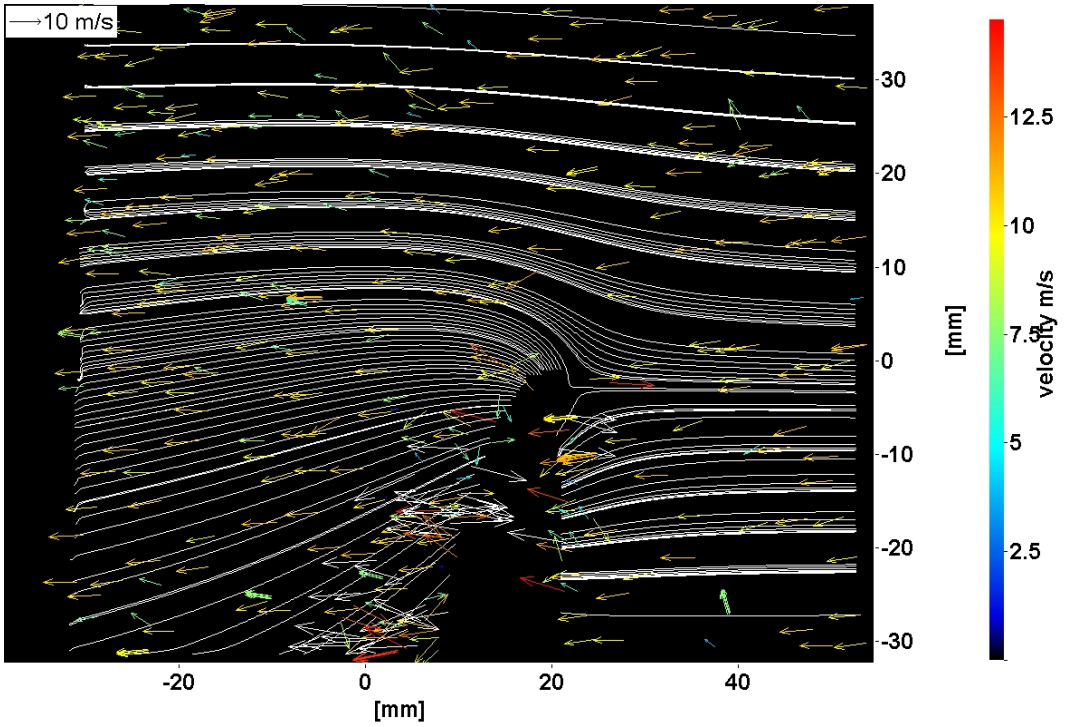

(d) 10 m/s nominal wind speed

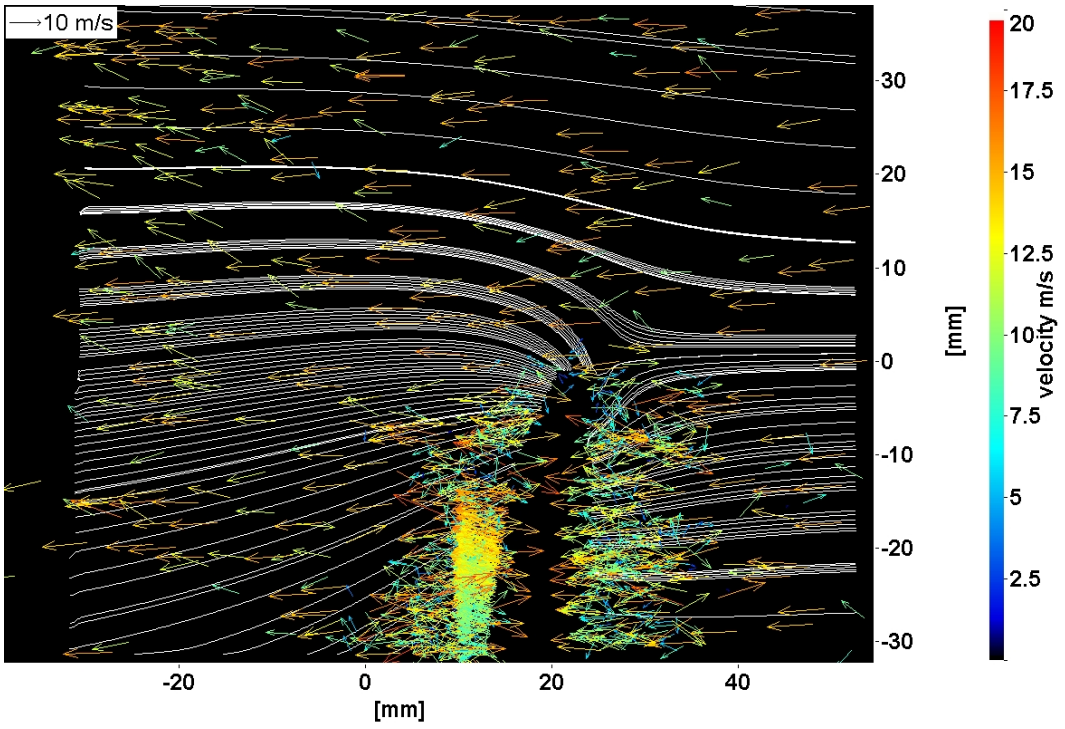

(e) 15 m/s nominal wind speed

Figure 6.6 - Particle tracking vectors of water droplets overlaid on air streamlines

6.4 Conclusions

It was determined that fog machines with a minimum power of 700 W greatly enhance the seeding density in the wind tunnel for PIV experiments.

The experiment should be redesigned in several ways to improve results. The illumination should be arranged to back-light droplets for shadowgraphy. This would allow a more accurate particle size measurement. In order for the experiment to more accurately simulate icing events, the droplet size should be reduced to 40-400 µm for large droplet icing, or 20-40 µm for more typical icing events. The cameras should remain external to the wind tunnel so a long focal length microscope would be required to zoom in on a smaller field of view to resolve smaller water droplets accurately.

The deceleration and irregular rotation speed of the rotor was a problem for averaging the vector fields. Improvements on the rotary encoder that would prevent them being fouled by water droplets would improve the stability of the blade in the field of view. The rotor probably would reach an equilibrium rotation speed after a certain amount of time. A constant supply of water instead of a finite volume tank would allow for the rotor to reach this equilibrium before the experiment began. In addition, ensuring the rotor had an even spray on its entire area may reduce the irregular rotation frequency. These procedures would most likely not entirely eliminate the shifting of the blade position in the field of view. Pre-processing of the images may be necessary to reposition the images so that the leading edge of the blade occurred at the same place for all images.

The blade is moving approximately 7 to 10 times the speed of the droplets. The large droplets being used in the experiment (0.729 mm diameter on average) do not follow the air streamlines as well as would typical icing event droplets of 20-40 µm. As a result, the droplets impact the blade on the projected area of the blade in the direction of rotation – the leading edge and suction side – instead of impacting in the vicinity of the stagnation point on the pressure side of the blade.

The existence of droplets with positive y-component (vertical) velocity upstream of the rotor at freestream wind speeds of 8 m/s (18 mph) and greater suggests that they have previously interacted with the rotor blades. Numerical simulations of large droplet icing for wind turbine blades may require mass transfer of water from one blade to the following blade due to splash particles being ejected upstream into the air flow.

7 Conclusions and Future Work

7.1 Summary

The aim of this study was to accomplish some groundwork towards a greater understanding of small horizontal axis wind turbines within the Mechanical Engineering Department at the University of Alberta. Along these lines, a micro wind turbine was installed, instrumented and tested in the low speed wind tunnel. The wind speed in the wake was measured with a Kiel probe and fundamental models of turbine theory were applied to determine the theoretical power extracted in comparison to the measured output power.

The following conclusions can be made from the performance evaluation and wake study of the micro wind turbine:

- The manufacturer (Ampair) published accurate performance characteristics for the Ampair 100.
- The wind turbine is in good working condition and performs well for such a small turbine. The Ampair 100 was optimized for a wind speed of approximately 10 m/s (22 mph).
- The testing arrangement in the wind tunnel used for this study results in highly blocked flow. Blocking correction factors based on the ratio of bypass wind speed to freestream wind speed must be applied in order to get results that represent operation in a field setting. Testing of full-sized wind turbines should be done in a much larger wind tunnel or in field conditions.
- Fundamental models based on axial momentum theory and ideal rotors can provide the general trend of power absorbed by the rotor but will over-predict power by as much as 50%. The difference between power predicted using measurements of thrust on the rotor and measurements of average wake speed is small.
- The low speed wind tunnel in the Mechanical Engineering Department at the University of Alberta does not provide good results at wind speeds close to 20 m/s (45 mph) for the arrangement used in this experiment.

Another goal of this study was to develop a system to use Stereo PIV to visualize the 3D air flow around an operating small wind turbine in the wind tunnel. The system developed used a laser light sheet directed through the roof of the wind tunnel. The laser light sheet was aligned with the freestream flow of the wind tunnel and the wind turbine blades passed through the light sheet as they rotated. Cameras mounted external to the wind tunnel watched a field of view of 120.4 x 91.0 mm through a glass window in the side wall of the wind tunnel. Seeding of flow was accomplished with a commercially available fog machine. An infrared reflective sensor sent rotation speed information to a computer that controlled the timing of laser and cameras using a

commercial software package. This timing control allowed for the capture of the wind turbine blade at the same place in the field of view so that an average flow field could be calculated around the blade.

The following conclusions can be made from the results of this experiment:

- Stereo PIV can provide accurate results of a 3D flow field in a wind tunnel provided a fog machine with a minimum power of 700 W is used to provide adequate seeding density.
- Consistent with airfoil theory, the flow around an upwind-facing horizontal axis wind turbine blade near the blade tip is toward the tip upstream of the rotor and toward the root downstream of the rotor. The 3D component of velocity does not increase proportionally with freestream wind speed so at high wind speeds the flow around the turbine blade can be approximated by 2D flow.
- The arrangement used in this study cannot provide 3D flow data in all locations around the blade airfoil. One side of the airfoil will be hidden from one camera and the blade casts a shadow in the light sheet.
- The arrangement used in this study cannot provide accurate flow data close to the blade. The reflection of the laser from the surface of the blade obscured reflections from the tracer particles. The optic lenses on the cameras could not zoom in to a small enough field of view to give information about the boundary layer around the airfoil.

The final goal of this study was to investigate the process of blade icing by visualizing the interaction of water droplets in the air flow with the blade. Droplet generators were placed upstream of the wind turbine in the wind tunnel and produced water droplets that ranged in size from 0.5 mm to 3.0 mm average diameter. This is much larger than the supercooled water droplets that typically produce icing on wind turbine blades which are 20-40 μm MVD. It is also much larger than supercooled large droplet ice accretion on aircraft wings which are 40-400 μm MVD. The droplets produced are categorized as drizzle or rain in the aircraft industry. High-speed still photography, PIV and particle tracking techniques were used to investigate the impingement process on the blade and calculate the velocity vectors of the droplets in the air flow.

The following conclusions can be made from the results of this experiment:

- The wind turbine blades are moving much faster in the plane of rotation than the droplets are moving across the plane of rotation. Water droplets are much more likely to hit the leading edge or the projected area of the suction side of the blade in the plane of rotation than the pressure side of the blade facing the freestream flow.
- Water droplets impinging on the wind turbine rotor caused the rotation speed of the rotor to decrease. The rotation frequency became much more uneven,

possibly due to the fact that the water spray was unevenly distributed on the rotor area.

- The arrangement used in this study could only resolve droplet sizes of 0.25 mm average diameter and larger.
- The arrangement used in this study cannot provide detailed information about the impingement of individual droplets on the blade for two reasons. First, the camera lenses could not zoom in to a small enough field of view to visualize details. Second, the splash created by the large droplets caused intense reflections that obscured velocity data.
- Numerical simulations of large droplet icing for wind turbine blades may require mass transfer of water from one blade to the following blade due to splash particles being ejected upstream in the air flow.

7.2 Future Work

This study revealed many areas of possible future study. Possible lines of investigation are listed below:

- In this study the axial profile of the wake speed was taken in one direction only. The cross-section of the wind tunnel test section is much shorter than it is wide so the measured profile did not give a complete picture of the wake blockage. Installing a 2D traverse system or using a PIV system could give a much clearer picture of the actual wake.
- Different blade shapes could be designed and tested on the existing mast and hub.
- A blade element momentum analysis method should be developed to improve upon the ability to predict output power from a specific blade design.
- By developing the PIV system further to visualize detailed flow fields around the blade at varying span locations could be used to assist and/or verify new blade designs or BEM models. It is known from Raffel, et al. (2006) that it is technically possible to extract detailed PIV data close to a stationary airfoil, so this technique could be adapted for a rotating blade.
- Correction factors for C_T and λ were developed by Whelan, Graham and Peiro (2009). They did not provide a correction factor for C_P. The axial momentum theory indicates that the thrust on the rotor is related to the difference in the freestream and wake wind speeds. The axial momentum theory indicates that the power of the turbine is related to the difference in the squares of the freestream and wake wind speeds. Power is also related to the rotational speed of the rotor and the tangential component of velocity of the wake through Euler's turbine equation (Hansen 2008). Garrett and Cummins (2007) show that rotor thrust and power are both related to bypass flow in a blocked condition. It is therefore probable that a blockage factor can be developed for C_P based on freestream, bypass and wake wind speeds.

- The shifting position of the blade in the field of view due to irregularities in the rotation frequency reduced the accuracy of the averaged vector fields. A method of pre-processing the images such that the leading edge was always in the same position would improve accuracy. In addition, a method of transmitting the rotation frequency information to the timing unit that does not get fouled by water would increase the number of useable images.
- A system to produce water droplets in the range of 20-400 µm should be developed for further blade icing studies. Camera lenses capable of zooming in on small fields of view at long focal lengths would be required. Illumination methods to silhouette the water droplets for shadowgraphy would improve the accuracy of particle sizing.
- This study focused solely on a rotor orientation facing directly into the wind. Effects of yaw could be examined.
- According to the manufacturer of the wind turbine, a major problem is the effect of rain drops on the start-up speed of wind turbines. This problem could be investigated further and a solution developed.

References

Addy Jr., Harold E., Dean R. Miller, and Robert F. Ide. "A Study of Large Droplet Ice Accretion in the NASA Lewis IRT at Near-Freezing Conditons; Part 2." *Prepared for the International Conference on Aircraft In-flight Icing sponsored by the Federal Aviation Administration.* Springfield, VA. May 6-8: NASA Technical Memorandum 10724, 1996.

Aguilera, Carlos A. V. "EXTREMA.M." *MATLAB Central File Exchange.* April 11, 2007.

Ampair. "Ampair 100 operation installation & maintenance manual." 2008.

Anschau, P., and K. Mach. "Application of a stereo PIV system for investigations of flow fields in towing tank and cavitation tunnel." *Archives of Civil and Mechanical Engineering* 7, no. 3 (2007).

Avallone, Eugene A., and Theodore Baumeister III, . *Marks' Standard Handbook for Mechanical Engineers.* Tenth Edition. New York: McGraw-Hill, 1997.

Baker, R. W., S. N. Walker, and P. C. Katen. "Wake measurements around operating wind turbines." *Journal of Solar Energy Engineering* 107 (1985): 183-185.

Baring-Gould, I., and D. Corbus. *Status of wind-diesel applications in arctic climates.* NREL/CP-500-42401, 2007.

Battisti, L., and R. Fedrizzi. "2D Numerical Simulation of a Wind Turbine De-icing System, Using Cycled Heating." *Wind Engineering* 31, no. 1 (2007): 33-42.

Becker, W., J. Zhai, R. Rebstock, and S. Loose. "Propeller testing in the cryogenic wind tunnel Cologne DNW-KKK." *21st Insternational Congress on Instrumentation in Aerospace Simulation Facilities.* 2005.

Bertin, John J., and Michael L. Smith. *Aerodynamics for Engineers.* Englewood Cliffs, N.J.: Prentice-Hall, Inc., 1979.

Bose, Neil. "Icing on a small horizontal-axis wind turbine - Part 1: Glaze ice profiles." *Journal of Wind Engineering and Industrial Aerodynamics* 45 (1992): 75-85.

Bose, Neil. "Icing on a small horizontal-axis wind turbine - Part 2: Three dimensional ice and wet snow formations." *Journal of Wind Engineering and Industrial Aerodynamics* 45 (1992): 87-96.

British Wind Energy Association. "BWEA small wind turbine performance and safety standard." 2008.

Cao, Y., Q. Zhang, and J. Sheridan. "Numerical simulation of rime ice accretions on an aerofoil using an Eulerian method." *The Aeronautical Journal*, May 2008: 243-249.

Cho, G., M. Kawahash, H. Hirahara, and M. Kitadume. "Application of stereoscopic particle image velocimetry to experimental analysis of flow through multiblade fan." *JSME International Journal Series B* 48, no. 1 (2005): 25-33.

Dalili, N., A. Edrisy, and R. Carriveau. "A review of surface engineering issues critical to wind turbine performance." *Renewable and Sustainable Energy Reviews* 13 (2009): 428-438.

eFormative Options, LLC & Entegrity Wind Systems, Inc. *Small wind siting and zoning study, development of siting guidelines and a model zoning by-law for small wind turbines (under 300 kW).* submitted to CanWEA, 2006.

Environment Canada. *Canadian Wind Atlas.* 2003. http://www.windatlas.ca/en/index.php (accessed February 20, 2010).

Faulkner, Bernie, interview by Graeme Comyn. *Specialist Technician* (June 2009).

Fei, R., and W. Merzkirch. "Investigations of the measurement accuracy of stereo particle image velocimetry." *Experiments in Fluids* 37 (2004): 559-565.

Feo, A. "Effect of Heavy Rainfall on Aircraft Performance." *Lecture presented at the von Karman Insitute for Fluid Dynamics.* 1997.

Garrett, C., and P. Cummins. "The efficiency of a turbine in a tidal channel." *Journal of Fluid Mechanics* 588 (2007): 243-251.

Gipe, Paul. *Wind Power: renewable energy for home, farm, and business. Completely revised and expanded edition.* White River Junction, VT: Chelsea Green Publishing Company, 2004.

—. "Wulf Test Field." *Wind-Works.org.* 2007. http://www.wind-works.org/wulf/index.html (accessed March 20, 2010).

Grant, I., et al. "Laboratory and field experiences in the application of particle image velocimetry to wind turbines." *SPIE*, 2005: 467-477.

Grant, I., G. H. Smith, A. Liu, D. Infield, and T. Eich. "Particle image velocimetry measurements of the aerodynamics of a wind turbine." *International Congress on Instrumentation in Aerospace Simulation Facilities.* 1991. 314-320.

Green, R., C. Doolan, and R. Cannon. "Measurements of the orthogonal blade-vortex interaction using a particle image velocimetry technique." *Experiments in Fluids* 29 (2000): 369-379.

Haans, W., T. Sant, G. A.M. van Kuik, and G. J.W. van Bussel. "Velocity measurements in the near wake of a horizontal axis wind turbine." *31st European Rotorcraft Forum.* 2005.

Hansen, Martin O. L. *Aerodynamics of Wind Turbines.* Second. Sterling, VA: Earthscan, 2008.

Hau, Erich. *Wind Turbines - Fundamentals, Technologies, Application, Ecomonics (2nd Edition).* Springer, 2006.

Hepperle, Martin. *JavaFoil.* January 27, 2007. http://www.mh-aerotools.de/airfoils/javafoil.htm (accessed July 17, 2009).

Hochart, Clement, Guy Fortin, and Jean Perron. "Wind Turbine Performance under Icing Conditions." *Wind Energy* 11 (2008): 319-333.

Hunter, William W. (Jr.), and Cecil E. (Jr.) Nichols. "Wind tunnel seeding systems for laser velocimeters." *NASA Conference Publication 2393, March 19-20.* 1985. 264.

Huot, Marc D. *Environmental and performance evaluation of a roof-mounted small wind turbine.* MSc Thesis, Edmonton: University of Alberta, 2009.

Ice Accretion Simulation. AGARD Advisory Report 344, Fluid Dynamics Panel Working Group 20, Advisory Group for Aerospace Research & Development, North Atlantic Treaty Organization, December 1997.

Johnson, M. R. "Wake-stabilized diffusion flames in crossflow: application to the efficiencies of gas flares." PhD Dissertation, Department of Mechanical Engineering, University of Alberta, Edmonton, 2001.

LaVision GmbH. *FlowMaster.* Product Manual for DaVis 7.2, Göttingen: LaVision, 2007.

Magnusson, M. "Near-wake behavior of wind turbines." *Journal of Wind Engineering and Industrial Aerodynamics* 80 (1999): 147-167.

Magnusson, M., and A.-S. Smedman. "Air flow behind wind turbines." *Journal of Wind Engineering and Industrial Aerodynamics* 80 (1999): 169-189.

Makkonen, Lasse, Timo Laakso, and Karen J. Finstad. "Modelling and prevention of ice accretion on wind turbines." *Wind Engineering* 25, no. 1 (January 2001): 3-21.

Marbek Resource consultants Ltd. & GPCo Inc. *Survey of the small (300 W to 300 kW) wind turbine market in Canada.* submitted to NRCan, 2005.

Maskell, E. "A theory of the blockage effects on bluff bodies and stalled wings in a closed wind tunnel." *ARC R&M 3400*, 1963.

McNiel, C., D. Peltier, and M. Reeder. "Clean seeding for particle image velocimetry." *22nd International Congress on Instrumentation in Aerospace Simulation Facilities.* ICIASF Record, 2007. 66-71.

Melling, A. "Tracer particles and seeding for particle image velocimetry." *Measurement Science and Technology* 8 (1997): 1406-1416.

Mengel, F., and T. Mørck. "Prediction of PIV recording performance." *SPIE Vol. 2052 Laser Anemometry Advances and Applications*, 1993: 331-338.

Miller, Dean R., Christopher J. Lynch, and Peter A. Tate. "Overview of High Speed Close-Up Imaging in an Icing Environment." *NASA/TM-2004-212926, AIAA-2004-0407.* Prepared for the 42nd Aerospace Sciences Meeting and Exhibit sponsored by the American Institute of Aeronautics and Astronautics, Reno, NV, January 5-8, 2004.

Morency, François, Fatih Tezok, and Ion Paraschivoiu. "Anti-Icing System Simulation Using CANICE." *Journal of Aircraft* 36, no. 6 (November-December 1999): 999-1005.

National Renewable Energy Laboratory. "Small Wind Turbine Independent Testing." *Wind Research.* 2007. http://www.nrel.gov/wind/smallwind/independent_testing.html (accessed February 20, 2010).

Okulov, V. L., and J. N. Sørensen. "Refined Betz limit for rotors with a finite number of blades." *Wind Energy* 11 (2008): 415-426.

Özgen, S., and M. Canibek. "Ice accretion simulation on multi-element airfoils using extended Messinger model." *Heat Mass Transfer* 45 (2009): 305-322.

Papadakis, Michael, and Colin S. Bidwell. "Overview of Experimental Water Droplet Impingement Research and Future Aviation Community Requirements, Including SLD Experimental Data." *Proceedings of the FAA International Conference on Aircreaft In-flight Icing Volume II - Working Group Papers. DOT/FAA/AR-96/81,II.* 1996. 257-273.

Pea Soup Ltd., UK. *Smoke Particle Size - Why Smaller is Better!* 1997. http://www.smokemachines.net/smoke-particle-size.shtml (accessed September 16, 2010).

Pope, Alan, and John J. Harper. *Low-Speed Wind Tunnel Testing.* New York, NY: John Wiley & Sons, Inc., 1966.

Prasad, A. "Stereo particle image velocimetry." *Experiments in Fluids* 29 (2000): 103-116.

Raffel, M., D. Favier, E. Berton, C. Rondot, M. Nsimba, and W. Geissler. "Micro-PIV and ELDV wind tunnel investigations of the laminar separation bubble above a helicopter blade tip." *Measurement Science and Technology* 17 (2006): 1652-1658.

Richard, H., W. Becker, S. Loose, M. Thimm, J. Bosbach, and M. Raffel. "Application of Particle Image Velocimetry under Cryongenic Conditions." *International Congress on Instrumentation in Aerospace Simulation.* ICIASF Record, 2003. 393-398.

Sharman, David, interview by Graeme Comyn. *Personal email* (May 14, 2009).

Sharman, David, interview by Graeme Comyn. *Personal email* (April 24, 2010).

Siddiqui, K., H. Hangan, and A. Rasouli. "PIV technique impementation for wind mapping in complex topographies." *Measurement Science and Technology* 19, no. 065403 (2008): 11pp.

Soloff, S., R. Adrian, and Z.-C. Liu. "Distortion compensation for generalized stereoscopic particle image velocimetry." *Measurement Science and Technology* 8 (1997): 1441-1454.

The Cadmus Group, Inc. "Progress report on small wind energy development projects receiving funds from the Massachusetts Technology Colaborative (MTC)." 2008.

United Sensor Corp. *Kiel Probes.* 1995. http://www.unitedsensorcorp.com/kiel.html (accessed February 15, 2010).

—. *Static-Pitot Pressure Probes.* 1995. http://www.unitedsensorcorp.com/pitot.html (accessed February 15, 2010).

Vermeer, L. J., J. N. Sørensen, and A. Crespo. "Wind turbine wake aerodynamics." *Progress in Aerospace Sciences* 39 (2003): 467-510.

Wang, Xin, Eric L. Bibeau, and Greg F. Naterer. "Experimental Investigation of Energy Losses due to Icing of a Wind Turbine." *International Conference on Power Engineering-2007, October 23-27, 2007, Hangzhou, China.* 2007. 1143-1147.

Whale, J., and C. Anderson. "The application of particle image velocimetry to wind turbine wakes." *SPIE Vol. 2052 Laser Anemometry Advances and Applications*, 1993: 667-674.

Whale, J., and C. Anderson. "The application of particle image velocimetry to wind turbine wakes." *SPIE Vol. 2052 Laser Anemometry Advances and Applications*, 1993: 667-674.

Whale, J., C. Anderson, R. Bareiss, and S. Wagner. "An experimental and numerical study of the vortex structure in the wake of a wind turbine." *Journal of Wind Engineering and Industrial Aerodynamics* 84 (2000): 1-21.

Whelan, J. I., J. M. R. Graham, and J. Peiro. "A free-surface and blockage correction for tidal turbines." *J. Fluid Mech* 624 (2009): 281-291.

Wieneke, B. "Stereo-PIV using self-calibration on particle images." *Experiments in Fluids* 39 (2005): 267-280.

Willert, C. "Stereoscopic digital particle image velocimetry for application in wind tunnel flows." *Measurement Science and Technology* 8 (1997): 1465-1479.

Willert, C., and M. Gharib. "Digital particle image velocimetry." *Experiments in Fluids* 10 (1991): 181-193.

Willert, C., M. Raffel, J. Kompenhans, B. Stasicki, and C. Kähler. "Recent applications of particle image velocimetry in aerodynamic research." *Flow. Meas. Instrum.* 7, no. 3/4 (1996): 247-256.

Wood, D. H. "Including swirl in the actuator disk analysis of wind turbines." *Wind Engineering* 31, no. 5 (2007): 317-323.

Woods, J. A.R. "Effects fo Crossflow on Burning Rates of Rectangular Methanol Pool Fires." MSc Thesis, Department of Mechanical Engineering, University of Alberta, Edmonton, 2005.

Wright, William B., and Mark G. Potapczuk. "Computational Simulation of Large Droplet Icing." *Paper presented at the FAA Phase III International Conference on Aircraft In-flight Icing in Springfield, VA on May 5-8.* 1996.

Appendix A: Wind Turbine Blade Shape

A.1 Coordinate Measurement Machine

The Ampair wind turbine blade was measured with the Brown & Sharpe MicroVal coordinate measurement machine (CMM) using a 4.0 mm diameter spherical tip on the measurement probe. The blade was measured in order to determine the airfoil shapes and root connection dimensions. The root connection dimensions would be useful when designing new blades to fit with the existing Ampair assembly. A mould of the upper surface of the blade was taken with Bondo so that both the upper (low pressure) and lower (high pressure) surfaces of the blade could be measured without moving the blade once it was mounted in the CMM. The lower surface was oriented up (facing the CMM probe). With the blade sitting in the mould the lower surface of the blade was measured with the CMM, then the blade was removed and the upper surface was measured from the mould surface. Figure A.1 shows the blade being measured by the CMM.

Figure A.1 - Brown & Sharpe MicroVal coordinate measuring machine with Ampair 100 blade and Bondo blade mould

Since the CMM registers the point at the centre of the probe tip, both the lower surface and the upper surface had to be offset “outward” in order to achieve the actual surface

of the blade, as shown in Figure A.2. The 4.0 mm diameter probe tip was not ideal for measuring the blade shape. In areas where the surface slope was high (i.e. at the blade root) or when trying to trace the hard corner at the leading or trailing edges, it was difficult to determine where on the sphere the surface had touched. It was therefore difficult to know which direction the point should be offset. Point data in these areas had many apparent inaccuracies when they were input into the 3D modeling software.

Fifty-two point files were taken with the CMM to define the shape of the blade. Table A.1 describes the blade part being measured in each file and Figure A.3 illustrates the locations of the files.

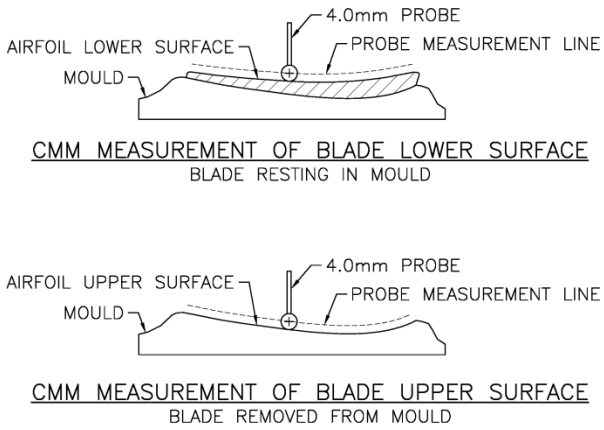

Figure A.2 - Measurement of the Ampair 100 blade and offset required for CMM probe tip

Table A.1 - CMM point file locations

Point File	Description	Point File	Description
WIND1	Leading edge	WIND27	Airfoil section
WIND2	Tip shape	WIND28	Airfoil section
WIND3	Trailing edge	WIND29	Airfoil section
WIND4	Root connection side plane, trailing	WIND30	Airfoil section
WIND5	Root connection radius, trailing	WIND31	Airfoil section
WIND6	Root connection bottom	WIND32	Airfoil section
WIND7	Root connection radius, leading	WIND33	Airfoil section
WIND8	Root connection side plane, leading	WIND34	Airfoil section
WIND9	Root connection face plane, lower	WIND35	Root connection bolt hole, trailing
WIND10	Airfoil section	WIND36	Root connection bolt hole, leading
WIND11	Airfoil section	WIND37	Airfoil span section
WIND12	Airfoil section	WIND38	Airfoil span section
WIND13	Airfoil section	WIND39	Root connection face plane, Trailing edge lower surface corner using bottom of probe tip, Outline of root connection, Trailing edge lower surface corner using side of probe tip
WIND14	Airfoil section	WIND40	Airfoil span section (lower surface only)
WIND15	Airfoil section	WIND41	Airfoil span section
WIND16	Airfoil section	WIND42	Airfoil span section
WIND17	Airfoil section	WIND43	Airfoil span section
WIND18	Airfoil section	WIND44	Airfoil span section
WIND19	Airfoil section	WIND45	Airfoil span section
WIND20	Airfoil section	WIND46	Airfoil span section
WIND21	Airfoil section	WIND47	Airfoil span section
WIND22	Airfoil section	WIND48	Airfoil span section
WIND23	Airfoil section	WIND49	Airfoil span section
WIND24	Airfoil section	WIND50	Airfoil span section
WIND25	Airfoil section	WIND51	Airfoil span section
WIND26	Airfoil section	WIND52	Airfoil span section

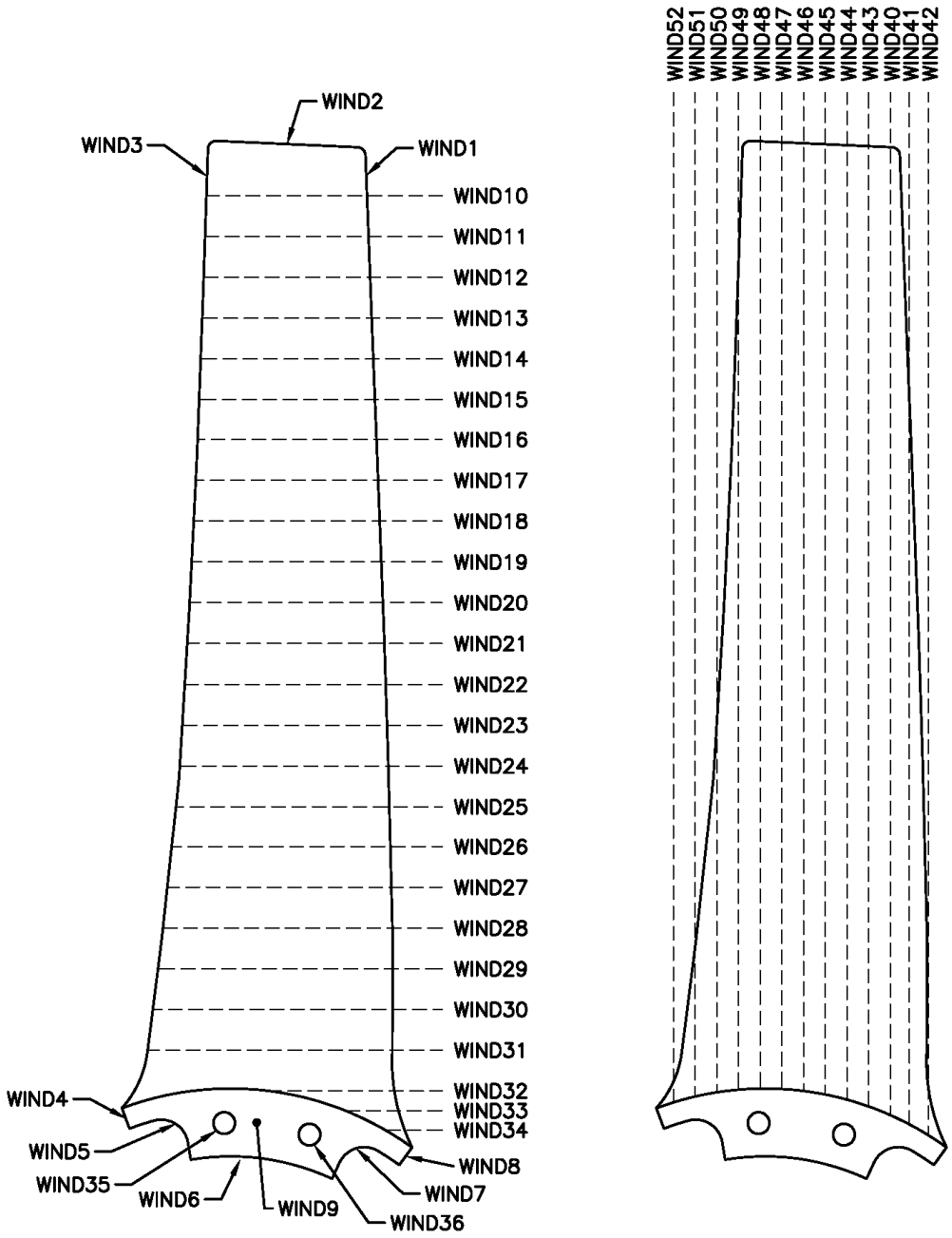

Figure A.3 - CMM point file locations

A.2 Blade Root

A drawing of the blade root connection is shown in Figure A.4. A solid model created from this drawing was used to create a resin prototype of the blade root connection. By installing this prototype in the Ampair wind turbine, it was confirmed that the dimensions are correct.

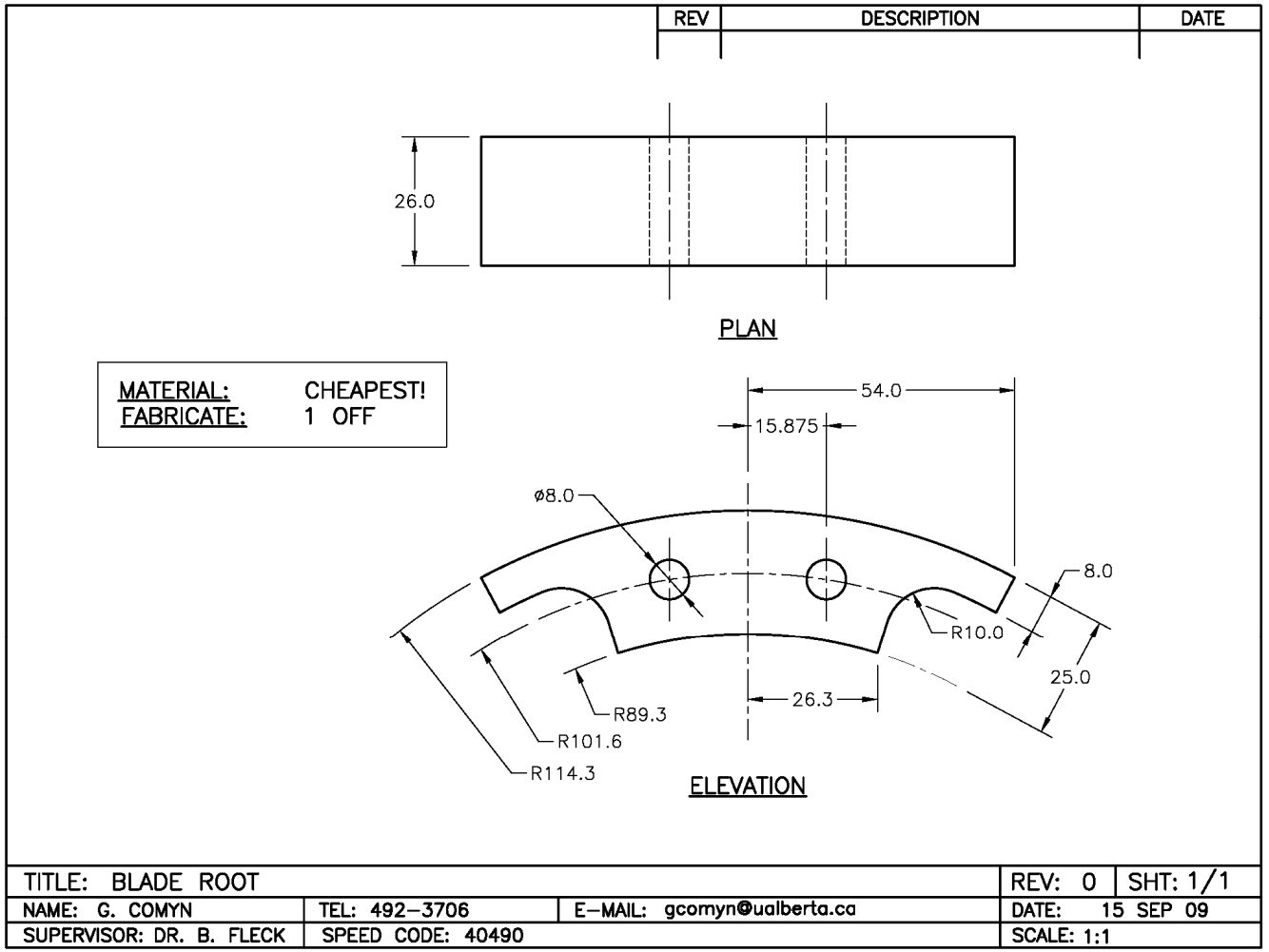

Figure A.4 - Drawing of blade root connection

Appendix B: NACA 6308 Airfoil Parameters

Figures B.1 to B.5 are airfoil parameters of the Ampair 100 blade tip as measured by the Mechanical Engineering department CMM (see Table 2.2). The parameters were calculated by JavaFoil (Hepperle 2007) using the calculation options listed in Table B.1.

Table B.1 - JavaFoil Options

Density	1.05 kg/m^3
Kinematic viscosity	1.983x10^{-5} kg/m s
Speed of sound	340.29 m/s

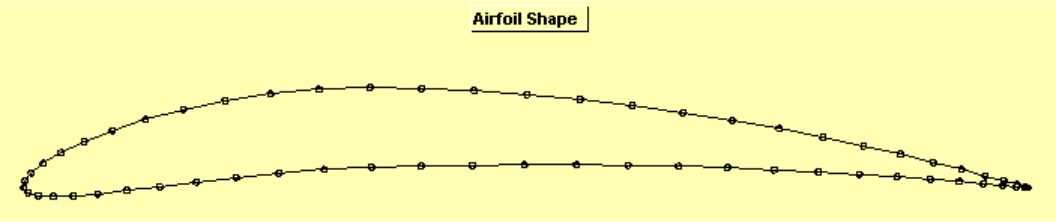

Figure B.1 - NACA 6308 geometry using 61 points

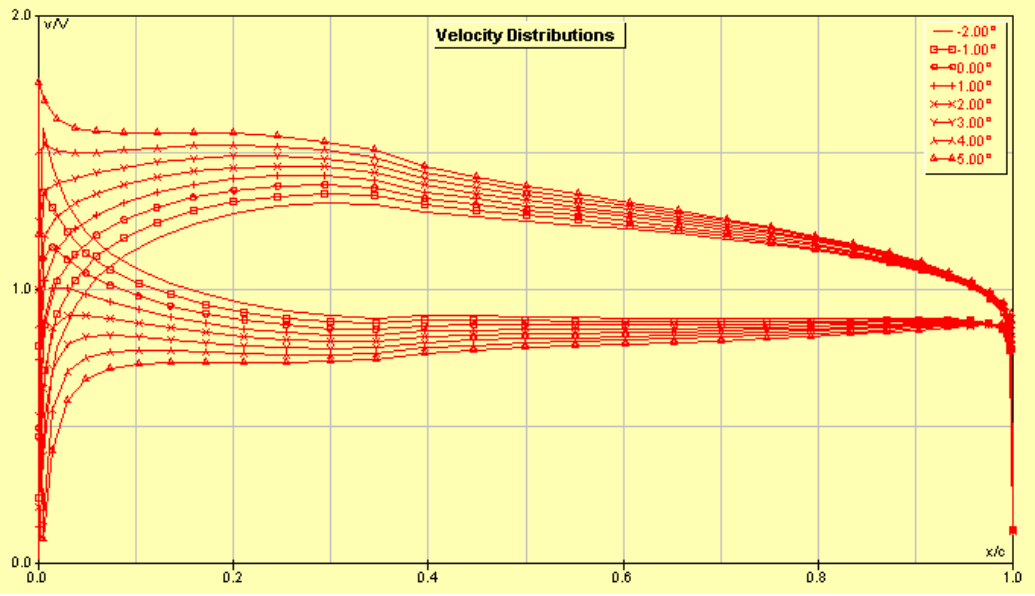

Figure B.2 - NACA 6308 airfoil velocity distributions at angles of attack from -2° to 5°

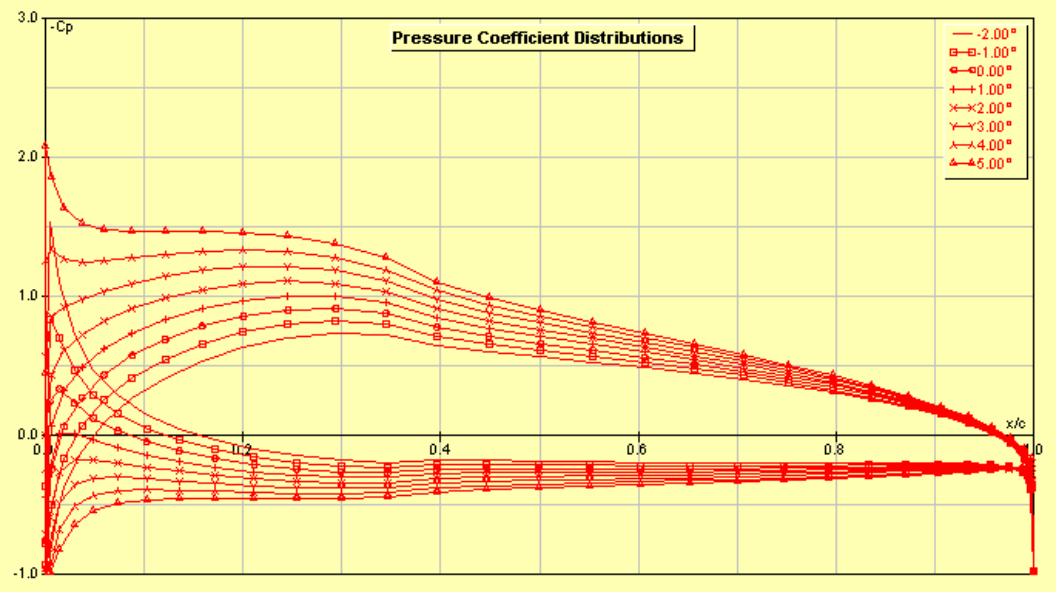

Figure B.3 – NACA 6308 airfoil pressure coefficient distributions at angles of attack from -2° to 5°

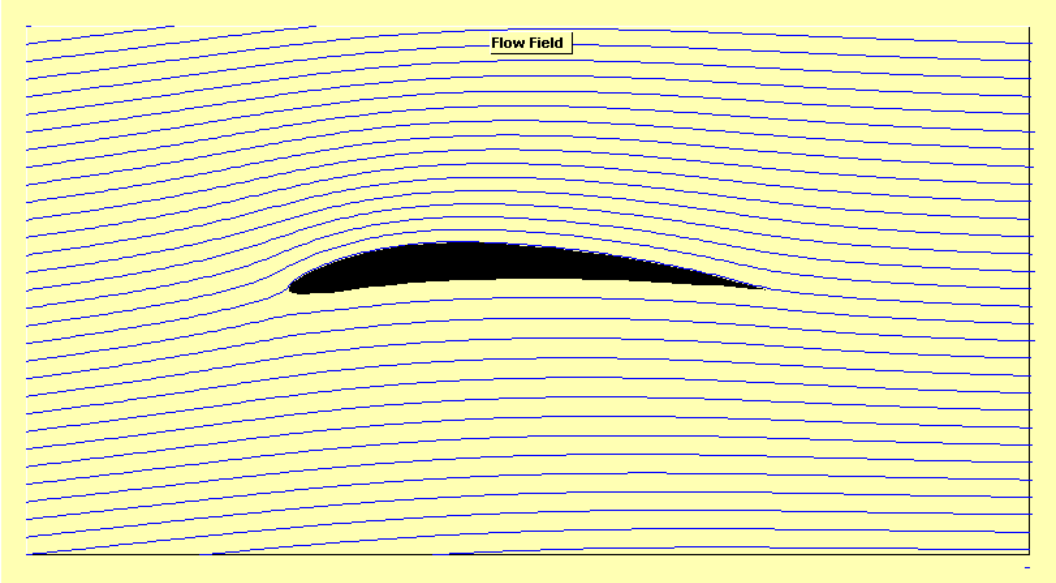

(a) 5 m/s nominal wind speed, Re = 58,000, γ = 2.50

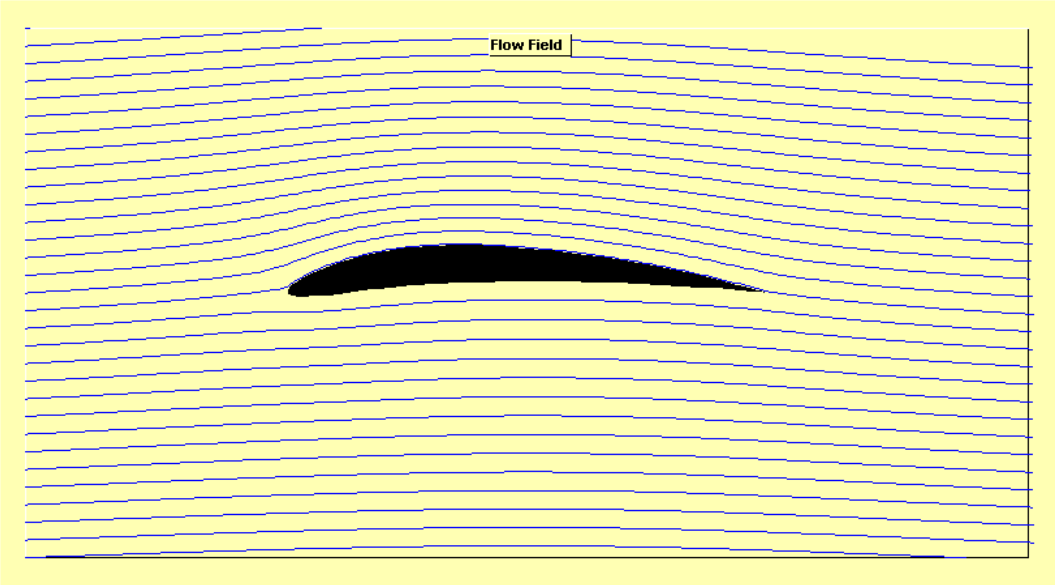

(b) 10 m/s nominal wind speed, Re = 140,000, γ = -0.10

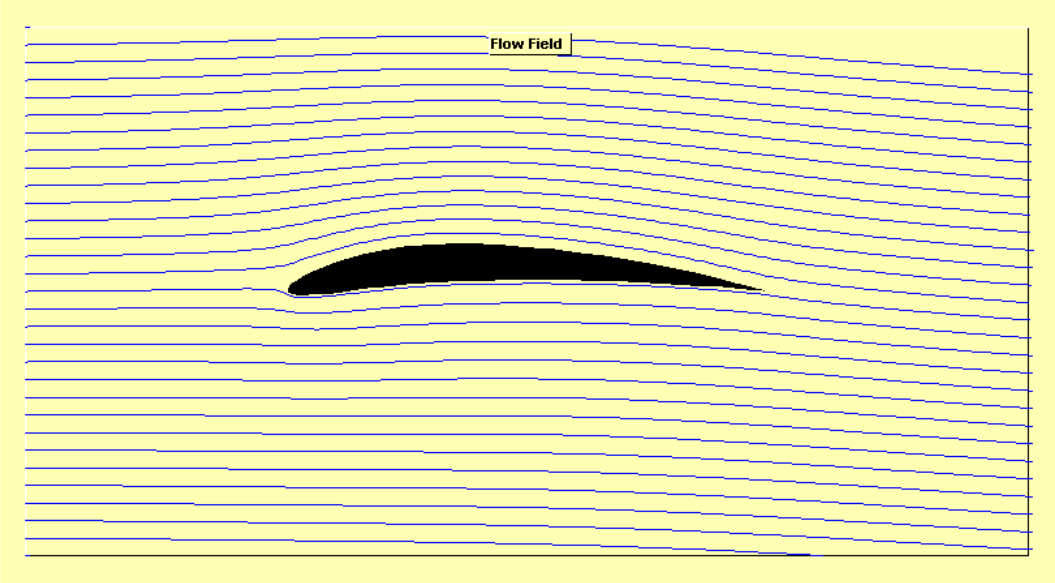

(c) 15 m/s nominal wind speed, Re = 240,000, γ = -1.75

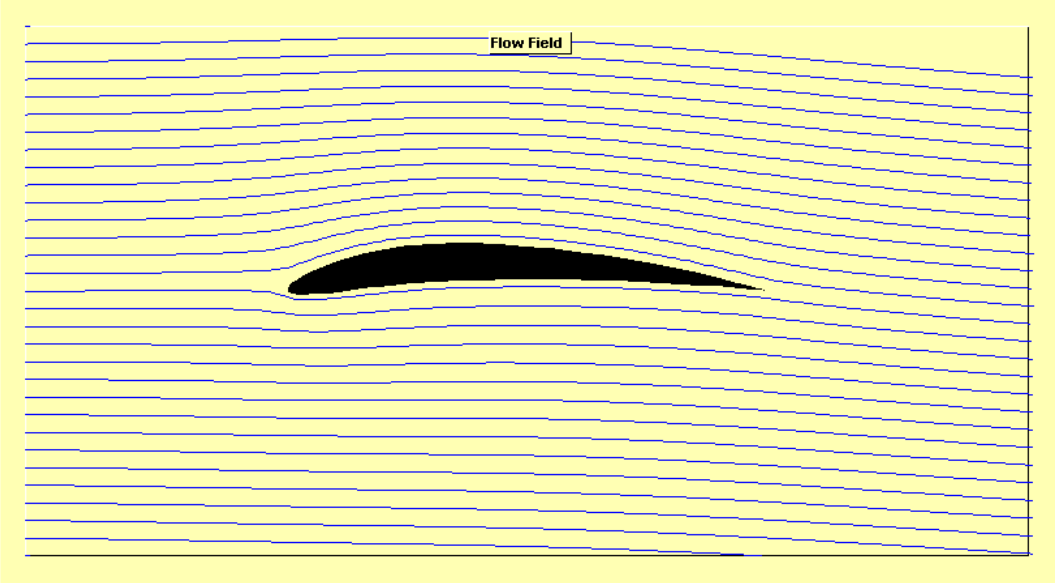

(d) 20 m/s nominal wind speed, Re = 330,000, γ = -2.00

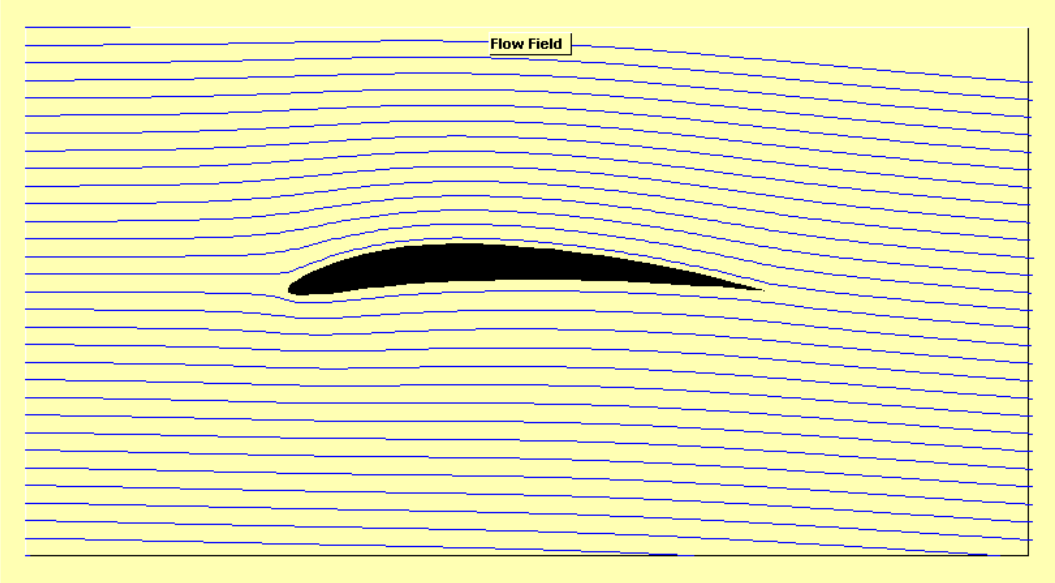

(e) 25 m/s nominal wind speed, Re = 410,000, γ = -2.25

Figure B.4 – NACA 6308 airfoil flow fields

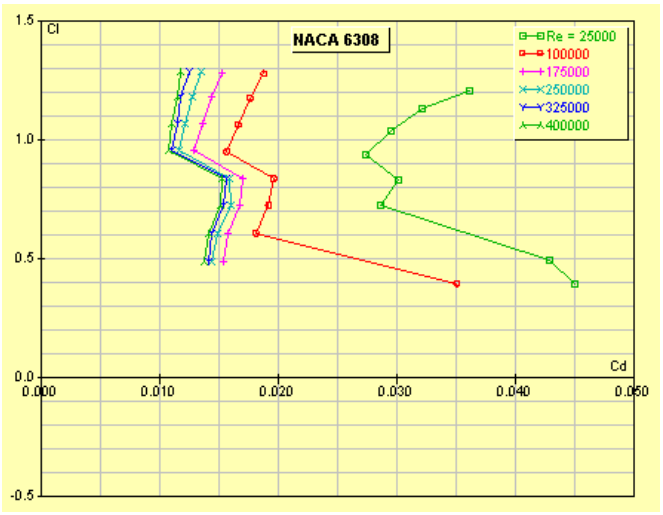

(a) Coefficient of lift (Cl) vs. Coefficient of drag (Cd) curve

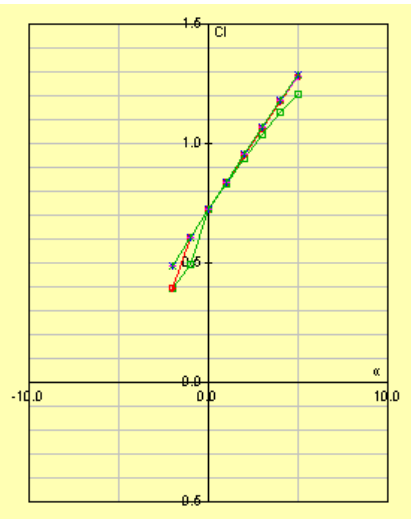

(b) Coefficient of Lift (Cl) vs. angle of attack curve

Figure B.5 – NACA 6308 airfoil lift and drag curves

Appendix C: Wind Turbine Support Structure Calculations

C.1 Mast

The Ampair 100 wind turbine was designed to fit inside a standard 1-1/2” (38 mm) diameter Schedule 40 steel pipe mast. The manufacturer’s documentation specifies that the drag due to the wind turbine is about 22 kg (50 lbs) at 50 knots (25 m/s). The drag force is assumed to act through the centerline of the turbine which is at 0.610 m (24”) above the floor of the wind tunnel as shown in Figure C.1.

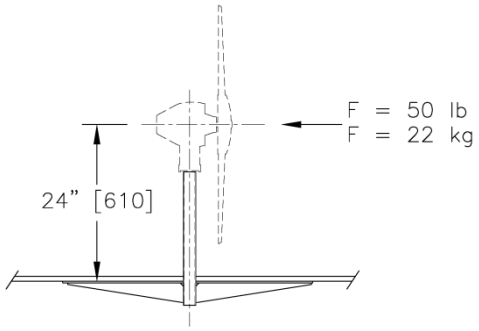

Figure C.1 - Mast arrangement

Table C.1 - Properties of 1-1/2" (38mm) Sch. 40 steel pipe

Nominal Pipe size	Sch.	Outside Diameter	Wall Thickness	Inside Diameter	Cross-section Area	Section Modulus
1-1/2”	40	1.900 in	0.145 in	1.610 in	0.799 in^2	0.326 in^3
38 mm	40	48.26 mm	3.68 mm	40.89 mm	515 mm^2	5342 mm^3

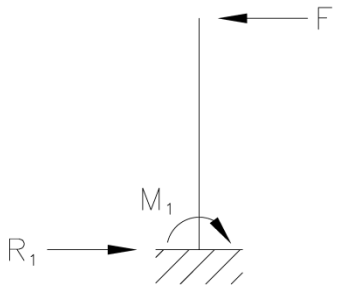

Figure C.2 - Mast free body diagram

The mast is a cantilever as shown in the free body diagram in Figure C.2. Properties of 1-1/2” (38 mm) Sch. 40 steel pipe are shown in Table C.1. The balance of static forces and moments is shown below.

Imperial Units	SI Units
$\Sigma F_X = 0$	$\Sigma F_X = 0$
$R_1 = 50\ \text{lb}$	$R_1 = (22\ \text{kg})\left(9.81\frac{\text{m}}{\text{s}^2}\right) = 215.8\ \text{N}$
$\Sigma M_1 = 0$	$\Sigma M_1 = 0$
$M_1 - F(24\ \text{in}) = 0$	$M_1 - F(0.61\ \text{m}) = 0$
$M_1 = 1200\ \text{in} - \text{lb}$	$M_1 = 131.7\ \text{N} - \text{m}$

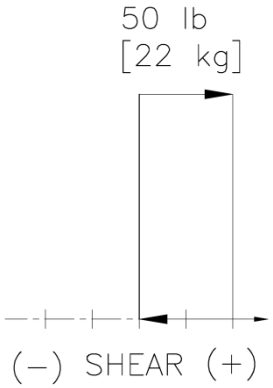

Figure C.3 - Mast shear diagram

The shear diagram of the mast is shown in Figure C.3. The shear stress in the pipe is calculated below and it is shown to have ample cross sectional area.

	Imperial Units	SI Units
Shear Stress	$\sigma_S = \frac{F}{A}$	$\sigma_S = \frac{F}{A}$
Required mast cross-sectional area	$A_{Reqd} = \frac{F}{(0.4)\sigma_Y}$	$A_{Reqd} = \frac{F}{(0.4)\sigma_Y}$
	$A_{Reqd} = \frac{50\ \text{lb}}{(0.4)(36000\ \text{psi})}$	$A_{Reqd} = \frac{215.8\ \text{N}}{(0.4)(248\ \text{MPa})}$
	$A_{Reqd} = 0.0035\ \text{in}^2$	$A_{Reqd} = 2.2\ \text{mm}^2$
Actual mast cross-sectional area	$A_{pipe} = 0.799\ \text{in}^2$	$A_{pipe} = 515\ \text{mm}^2$

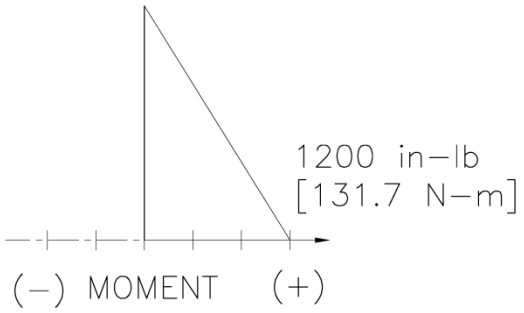

Figure C.4 - Mast moment diagram

The mast moment diagram is shown in Figure C.4. The bending stress is calculated below and it is shown that the mast has adequate section modulus.

	Imperial Units	SI Units
Bending Stress	$\sigma_B = \frac{My}{I_M} = \frac{M}{Z}$	$\sigma_B = \frac{My}{I_M} = \frac{M}{Z}$
Required mast section modulus	$Z_{Reqd} = \frac{M}{(0.6)\sigma_Y}$	$Z_{Reqd} = \frac{M}{(0.6)\sigma_Y}$
	$Z_{Reqd} = \frac{1200\ \text{in} - \text{lb}}{(0.6)(36000\ \text{psi})}$	$Z_{Reqd} = \frac{131.7\ \text{N} - \text{m}}{(0.6)(248\ \text{MPa})}$
	$Z_{Reqd} = 0.0555\ \text{in}^3$	$Z_{Reqd} = 885\ \text{mm}^3$
Actual mast section modulus	$Z_{pipe} = 0.326\ \text{in}^3$	$Z_{pipe} = 5342\ \text{mm}^3$
Safety Factor	$\text{S. F.} = \frac{Z_{pipe}}{Z_{Reqd}} = \frac{0.326}{0.0555} = 5.8$	$\text{S. F.} = \frac{Z_{pipe}}{Z_{Reqd}} = \frac{5342}{885} = 6.0$

C.2 Base Plate

The baseplate is attached to the bottom of the wind tunnel floor with a series of 3/16" (5 mm) cap screws as shown in Figure C.5. The moment from the mast wants to lift the baseplate. It is assumed for the purposes of this calculation that the cap screws are the sole material resisting this bending moment. The arrangement of the screws are shown in Figure C.6 for the purposes of calculating the moment of inertia of the bolting pattern and the results are shown in Table C.2. The minimum cross sectional area through the threads of the cap screws is used for the calculation.

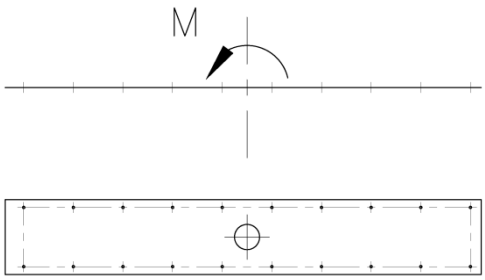

Figure C.5 - Mast bending moment applied to baseplate above. Plan of baseplate below.

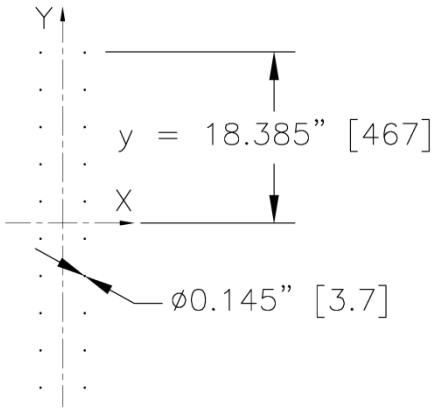

Figure C.6 - Baseplate bolting arrangement on bending axis to calculate moment of inertia.

Table C.2 - Properties of bolt pattern

	Imperial Units	SI Units
Area	0.3303 in^2	213 mm^2
Centroid X	0.0000 in	0 mm^2
Centroid Y	0.3125 in	8 mm
Moment of Inertia X	43.627 in^4	18,158,928 mm^4
Moment of Inertia Y	1.8633 in^4	775,564 mm^4
Radius of Gyration X	11.4935 in	292 mm
Radius of Gyration Y	2.3755 in	60.3 mm

The bending stress through the cap screws is calculated below. It is shown that the stress in the cap screws is acceptable.

	Imperial Units	SI Units
Bending Stress	$\sigma_B = \frac{My}{I}$	$\sigma_B = \frac{My}{I}$
	$\sigma_B = \frac{(1200\ \text{in} - \text{lb})(18.385\ \text{in})}{43.627\ \text{in}^4}$	$\sigma_B = \frac{(131.7\ \text{N} - \text{m})(0.467\ \text{m})}{18{,}158{,}928\ \text{mm}^4}$
	$\sigma_B = 505.70\ \text{psi}$	$\sigma_B = 3.387\ \text{MPa}$
Allowable bending stress	$\sigma_{Ba} = 0.6\sigma_Y$	$\sigma_{Ba} = 0.6\sigma_Y$
	$\sigma_{Ba} = 0.6(36{,}000\ \text{psi})$	$\sigma_{Ba} = 0.6(248\ \text{MPa})$
	$\sigma_{Ba} = 21{,}600\ \text{psi}$	$\sigma_{Ba} = 148.8\ \text{MPa}$

C.3 Drawings

Construction drawings for the wind turbine mast structure and its installation into the wind tunnel are shown in Figure C.7.

(a)

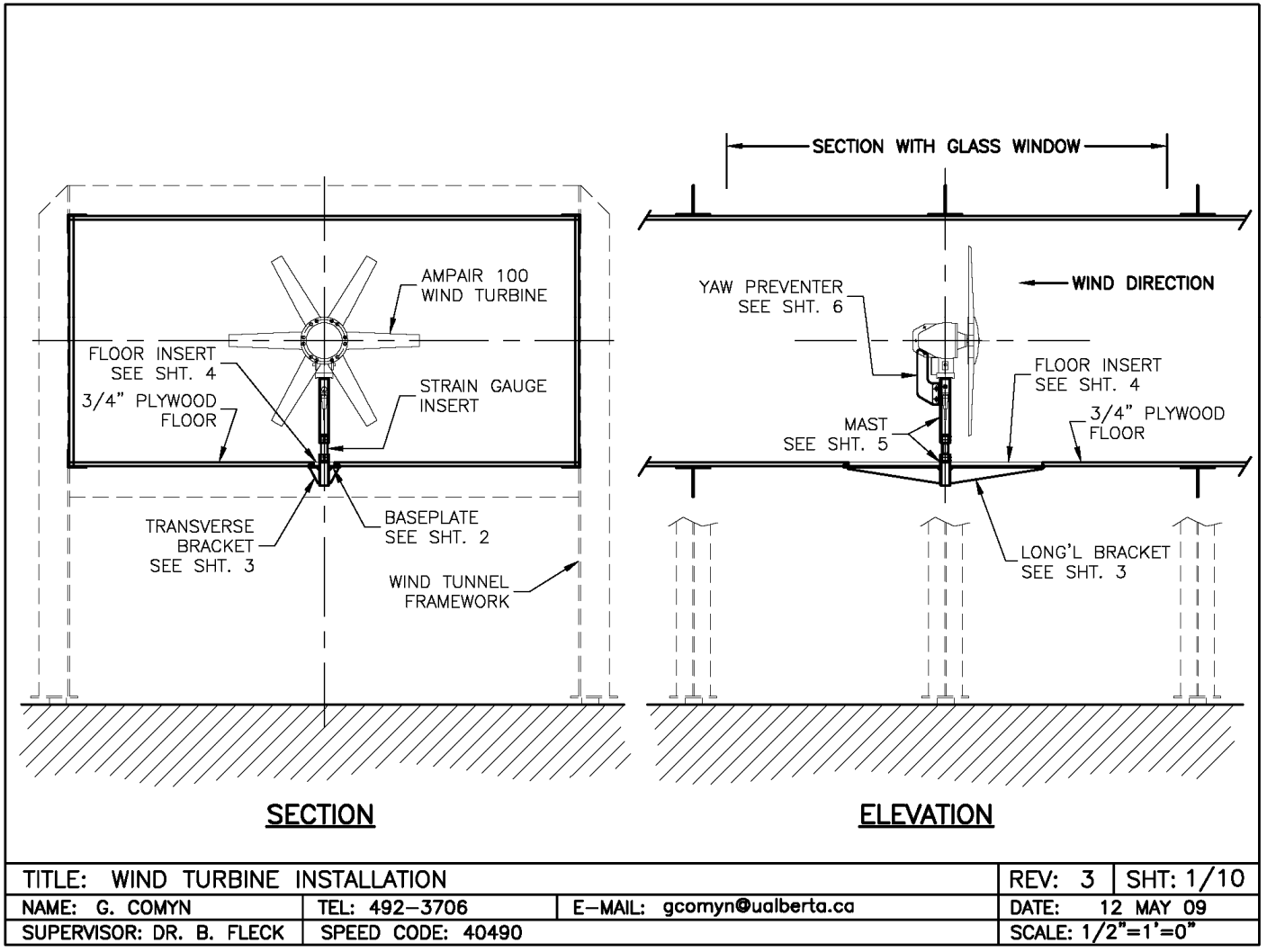

TITLE: WIND TURBINE INSTALLATION			REV: 3 | SHT: 1/10
NAME: G. COMYN	TEL: 492–3706	E–MAIL: gcomyn@ualberta.ca	DATE: 12 MAY 09
SUPERVISOR: DR. B. FLECK	SPEED CODE: 40490		SCALE: 1/2"=1'=0"

(b)

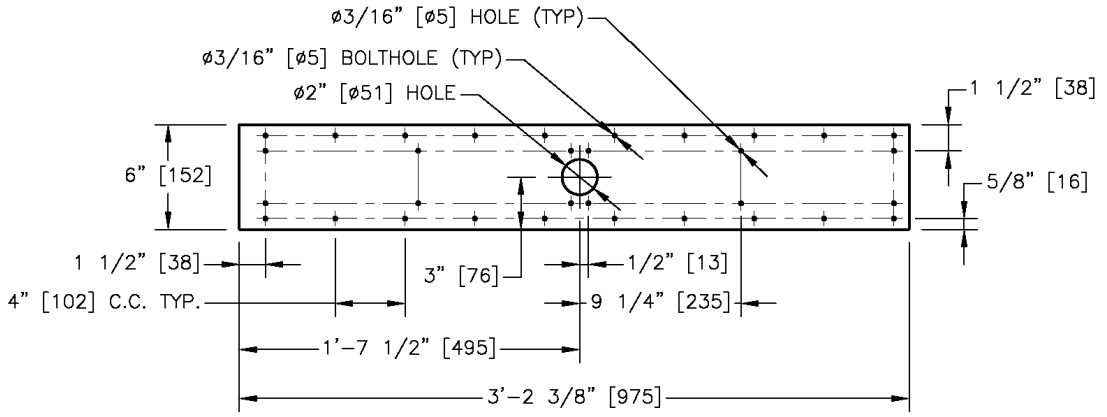

BASEPLATE

MATERIAL: 1/4" STEEL PL.
FABRICATE: 1 OFF

TITLE: WIND TURBINE INSTALLATION – BASEPLATE			REV: 3 / SHT: 2/10
NAME: G. COMYN	TEL: 492-3706	E-MAIL: gcomyn@ualberta.ca	DATE: 12 MAY 09
SUPERVISOR: DR. B. FLECK	SPEED CODE: 40490		SCALE: 1-1/2"=1'=0"

(c)

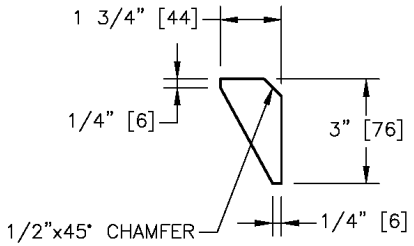

TRANSVERSE BRACKET

MATERIAL: 1/8" STEEL PL.
FABRICATE: 2 OFF

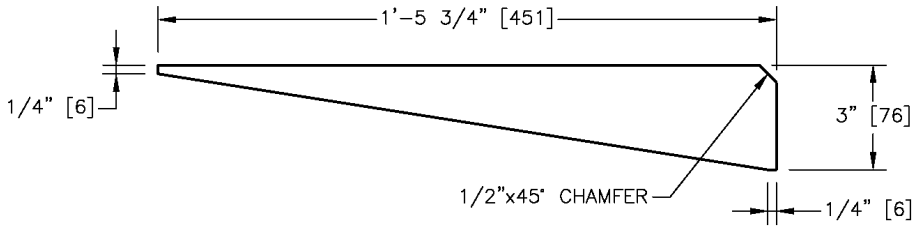

LONGITUDINAL BRACKET

MATERIAL: 1/8" STEEL PL.
FABRICATE: 2 OFF

TITLE: WIND TURBINE INSTALLATION – BRACKETS			REV: 3	SHT: 3/10
NAME: G. COMYN	TEL: 492-3706	E-MAIL: gcomyn@ualberta.ca	DATE: 12 MAY 09	
SUPERVISOR: DR. B. FLECK	SPEED CODE: 40490		SCALE: 3"=1'=0"	

(d)

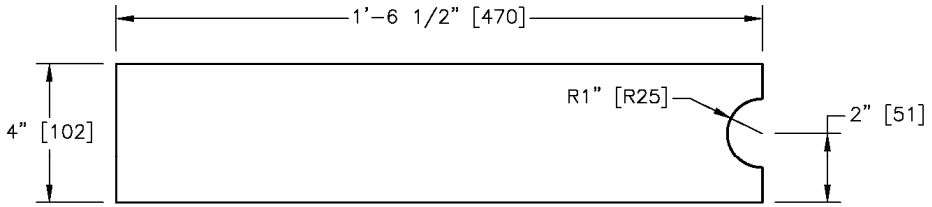

FLOOR INSERT

MATERIAL: 3/4" PLYWOOD
FABRICATE: 2 OFF

TITLE: WIND TURBINE INSTALLATION – FLOOR INSERT			REV: 3	SHT: 4/10
NAME: G. COMYN	TEL: 492-3706	E-MAIL: gcomyn@ualberta.ca	DATE: 12 MAY 09	
SUPERVISOR: DR. B. FLECK	SPEED CODE: 40490		SCALE: 3"=1'=0"	

(e)

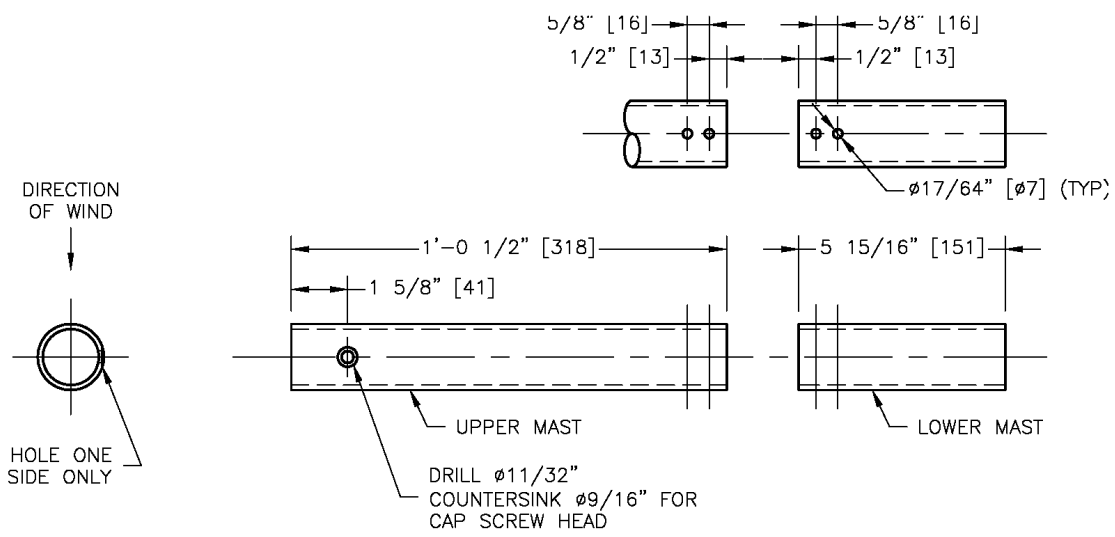

MAST

MATERIAL: 1–1/2" SCH. 40 STEEL PIPE
FABRICATE: 1 OFF EACH

TITLE: WIND TURBINE INSTALLATION – MAST			REV: 3	SHT: 5/10
NAME: G. COMYN	TEL: 492–3706	E–MAIL: gcomyn@ualberta.ca	DATE: 12 MAY 09	
SUPERVISOR: DR. B. FLECK	SPEED CODE: 40490		SCALE: 3"=1'=0"	

(f)

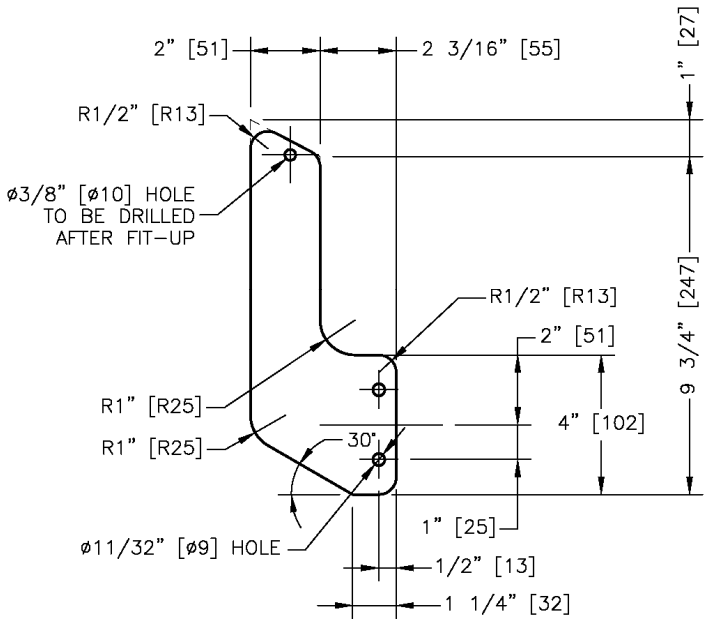

YAW PREVENTER
MATERIAL: 1/8" STEEL PL.
FABRICATE: 1 OFF

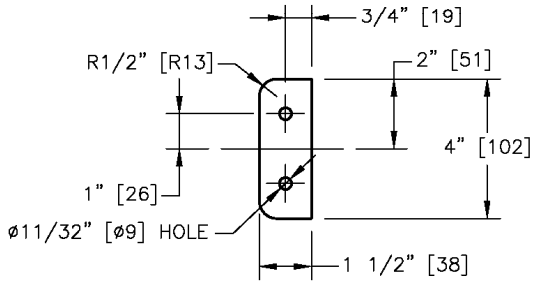

YAW PREVENTER LUG
MATERIAL: 1/4" STEEL PL.
FABRICATE: 1 OFF

TITLE: WIND TURBINE INSTALLATION – YAW PREVENTER			REV: 3	SHT: 6/10
NAME: G. COMYN	TEL: 492-3706	E-MAIL: gcomyn@ualberta.ca	DATE: 12 MAY 09	
SUPERVISOR: DR. B. FLECK	SPEED CODE: 40490		SCALE: 3"=1'=0"	

(g)

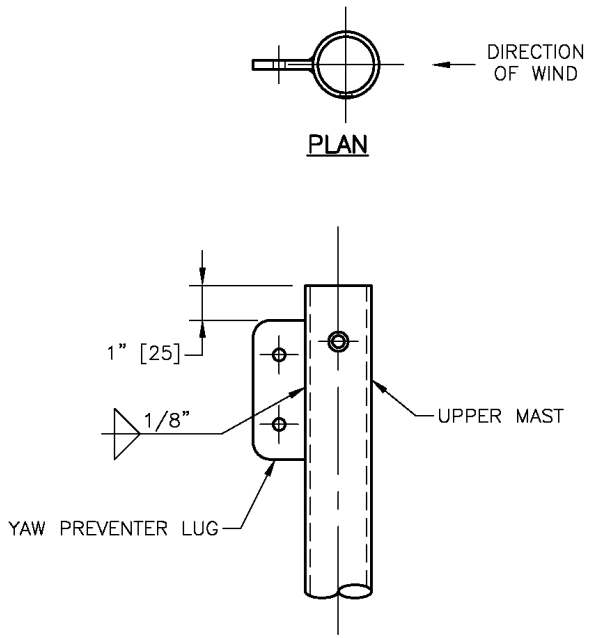

ASSEMBLY 1

TITLE: WIND TURBINE INSTALLATION – ASSEMBLY DRAWING 1			REV: 3 | SHT: 7/10
NAME: G. COMYN	TEL: 492–3706	E–MAIL: gcomyn@ualberta.ca	DATE: 12 MAY 09
SUPERVISOR: DR. B. FLECK	SPEED CODE: 40490		SCALE: 3"=1'=0"

(h)

FASTENERS REQUIRED:

No.	ITEM
21	3/16" CAP SCREW
21	3/16" HEX NUT
12	8x3/4" ROUND HEAD WOOD SCREW
3	5/16" x 1" HEX BOLT
3	5/16" PLAIN WASHER
3	5/16" NYLOC HEX NUT

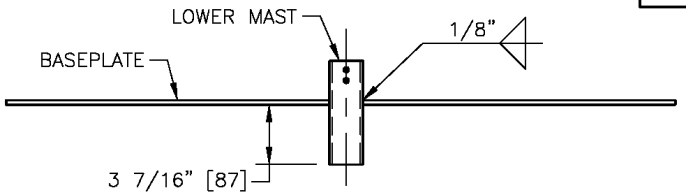

ELEVATION

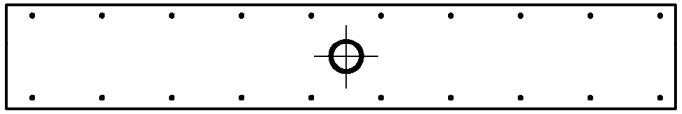

PLAN

ASSEMBLY 2

TITLE: WIND TURBINE INSTALLATION – ASSEMBLY DRAWING 2			REV: 3 / SHT: 8/10
NAME: G. COMYN	TEL: 492–3706	E–MAIL: gcomyn@ualberta.ca	DATE: 12 MAY 09
SUPERVISOR: DR. B. FLECK	SPEED CODE: 40490		SCALE: 1–1/2"=1'=0"

(i)

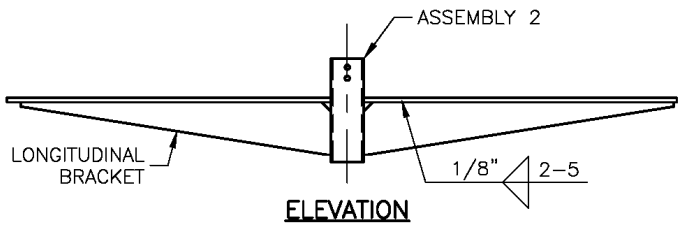

ELEVATION

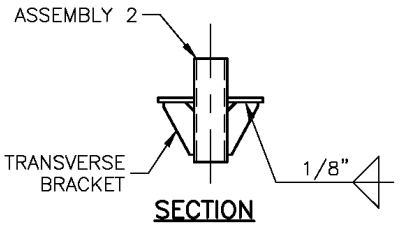

SECTION

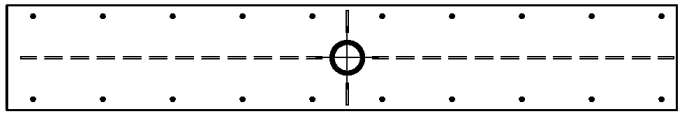

PLAN

ASSEMBLY 3

TITLE: WIND TURBINE INSTALLATION – ASSEMBLY DRAWING 3			REV: 3 / SHT: 9/10
NAME: G. COMYN	TEL: 492-3706	E-MAIL: gcomyn@ualberta.ca	DATE: 12 MAY 09
SUPERVISOR: DR. B. FLECK	SPEED CODE: 40490		SCALE: 1-1/2"=1'=0"

(j)

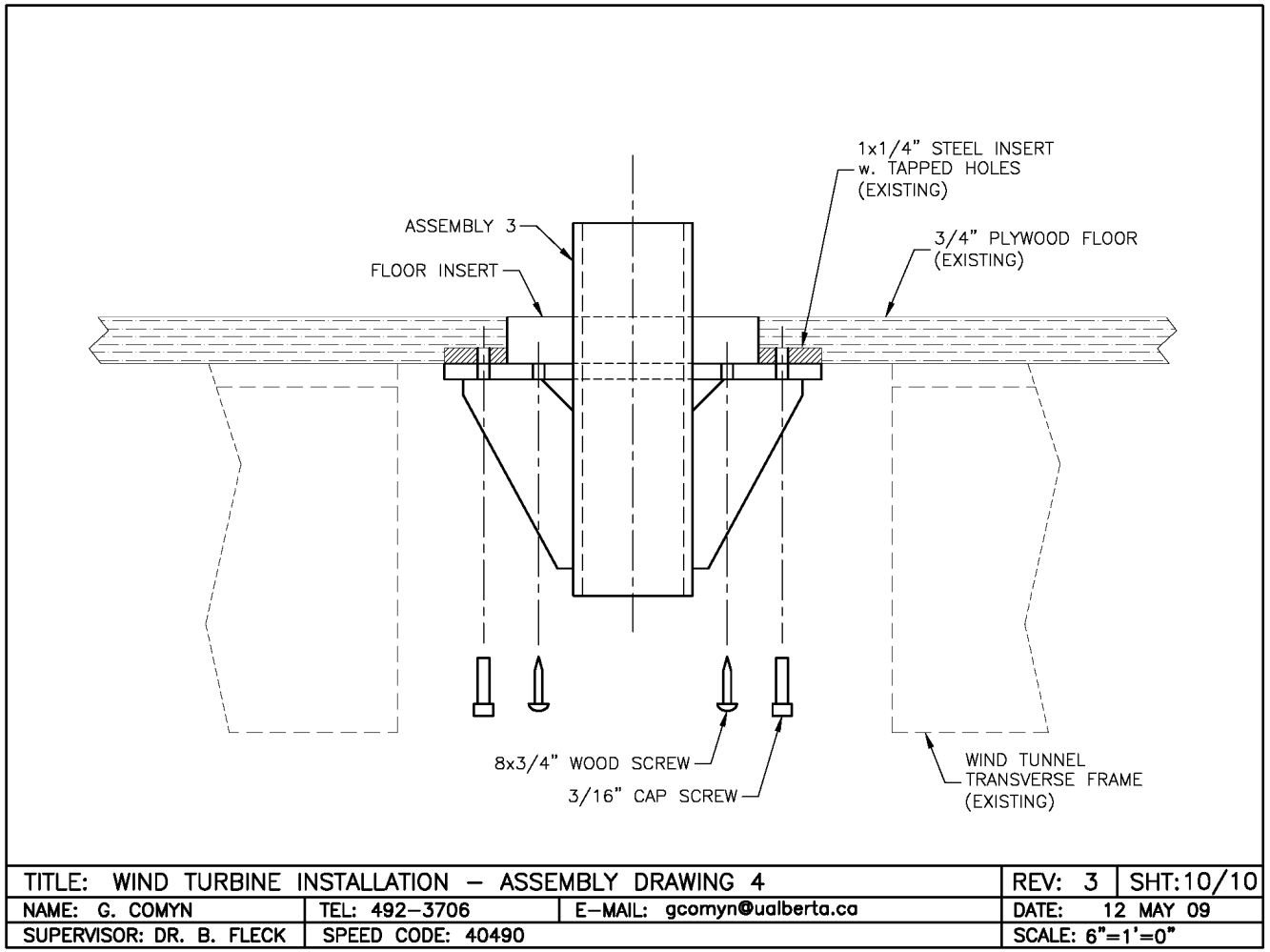

Figure C.7 - Construction drawings for wind turbine mast structure

Appendix D: Strain Gauge Insert

D.1 Design Calculations

In order for strain gauges to function there has to be enough deflection in the material that the gauges are mounted on to give a clear signal. It is common practice that to get a good signal the gauges should see about 1000 μstrain (Faulkner 2009). The strain gauges will be mounted on an insert piece in the steel pipe mast near the base. This insert piece will be designed to have about 1000 μstrain at maximum drag force of the wind turbine at the top of the mast.

The insert piece will be mounted in the mast near the base. The mast is a cantilever as shown in Figure D.1, where W is the drag force of the wind turbine, 50 lb (22 kg), and L is the length of the mast. For the purposes of this calculation, it is assumed that the strain gauges are mounted at the very bottom of the mast. Therefore L is assumed to be 24" (0.61 m).

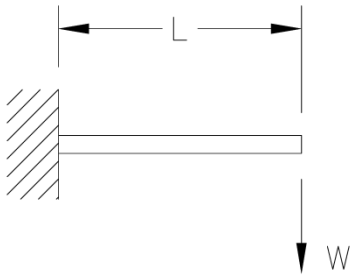

Figure D.1 - Cantilever free body diagram

Stress at the base of the cantilever is defined as

$$\sigma = \frac{M}{Z} = \frac{WL}{Z} \qquad \text{(Eq. C.1)}$$

where M is the moment, and Z is the section modulus of the beam.

Strain at the base of the cantilever is defined as

$$\varepsilon = \frac{WL}{ZE} \qquad \text{(Eq. C.2)}$$

where E is the modulus of elasticity.

The material of the insert piece will be aluminum 6061-T6 because it is readily available and has a lower modulus of elasticity that steel. Properties of aluminum 6061-T6 can be found in Table D.1.

Table D.1 - Properties of aluminum alloy 6061-T6

Density	Tensile, Yield Strength	Tensile Strength	Modulus of Elasticity
0.098 lb/in^3	40,000 psi	45,000 psi	10x10^6 psi
2.70 g/cm^3	275.8 MPa	310.3 MPa	68,947 MPa

The insert piece will fit inside the steel pipe mast and must be open in the centre to allow for the wind turbine generator output cable to pass through. Full drawings of the insert piece can be found in Figure D.3. The cross section in way of the strain gauges is shown in Figure D.2 and the properties of this shape are given in Table D.2.

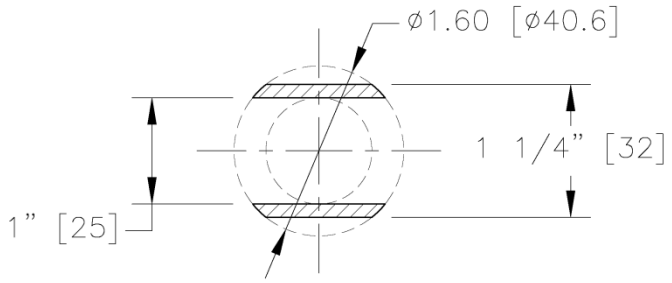

Figure D.2 - Cross-section of strain gauge insert

Table D.2 - Properties of strain gauge insert cross-section

	Imperial Units	SI Units
Area	0.2833 in^2	182 mm^2
Centroid X	0.0000 in	0 mm
Centroid Y	0.0000 in	0 mm
Moment of Inertia X	0.0893 in^4	37,169 mm^4
Moment of Inertia Y	0.0307 in^4	12,78 mm^4
Radius of Gyration X	0.5614 in	14.26 mm
Radius of Gyration Y	0.3291 in	8.36 mm
Section Modulus X	0.1428 in^3	2,340 mm^3
Section Modulus Y	0.0491 in^3	804 mm^3

Stress and strain in the strain gauge insert piece are calculated below. The maximum strain does not reach 1000 µstrain but 840 µstrain will provide a strong enough signal for measurement purposes. The maximum stress is acceptable for aluminum alloy 6061-T6.

	Imperial Units	SI Units
Stress	$\sigma = \frac{(50\ lb)(24\ in)}{0.1428\ in^3} = 8403\ psi$	$\sigma = \frac{(215.8\ N)(0.61\ m)}{2340\ mm^3} = 57.9\ MPa$
Strain	$\varepsilon = \frac{(50\ lb)(24\ in)}{(0.1428\ in^3)(10x10^6\ psi)} = 840.3\ \mu strain$	$\varepsilon = \frac{(215.8\ N)(0.61\ m)}{(2340\ mm^3)(6.89x10^4\ MPa)} = 816.2\ \mu strain$

(a)

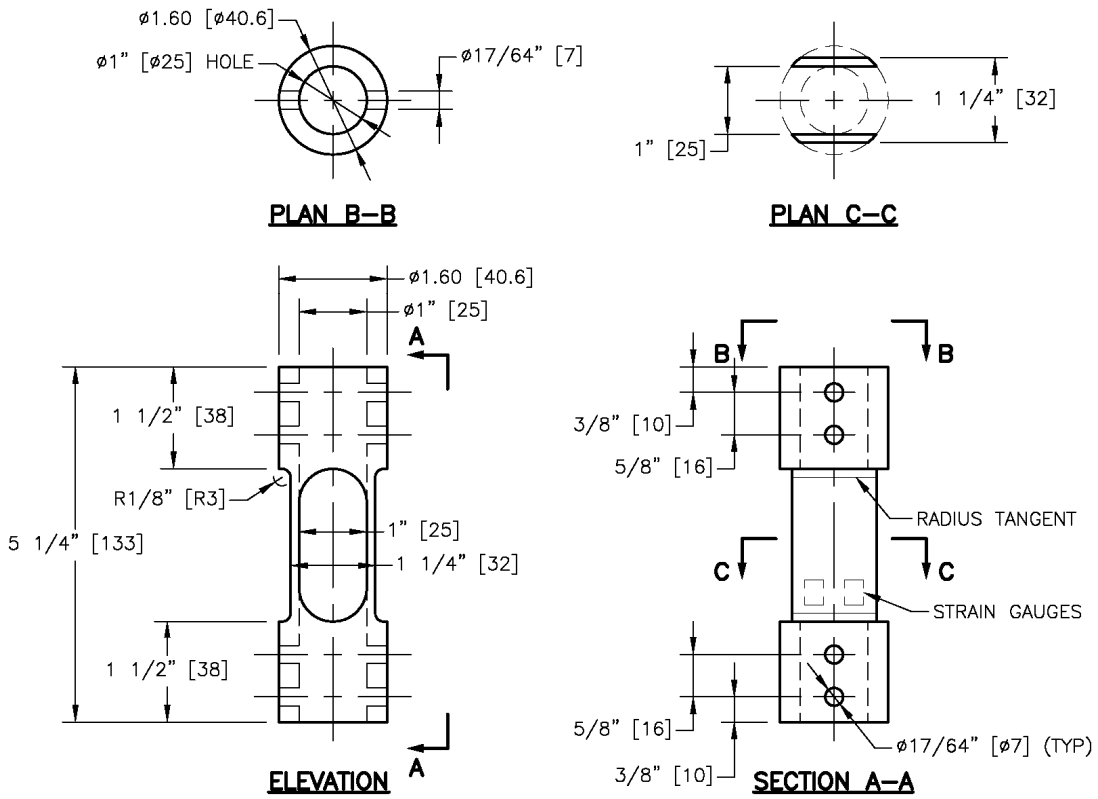

TITLE: STRAIN GAUGE INSERT			REV: 1	SHT: 1/2
NAME: G. COMYN	TEL: 492–3706	E–MAIL: gcomyn@ualberta.ca	DATE: 19 JUN 09	
SUPERVISOR: DR. B. FLECK	SPEED CODE: 40490		SCALE: 6" = 1'–0"	

(b)

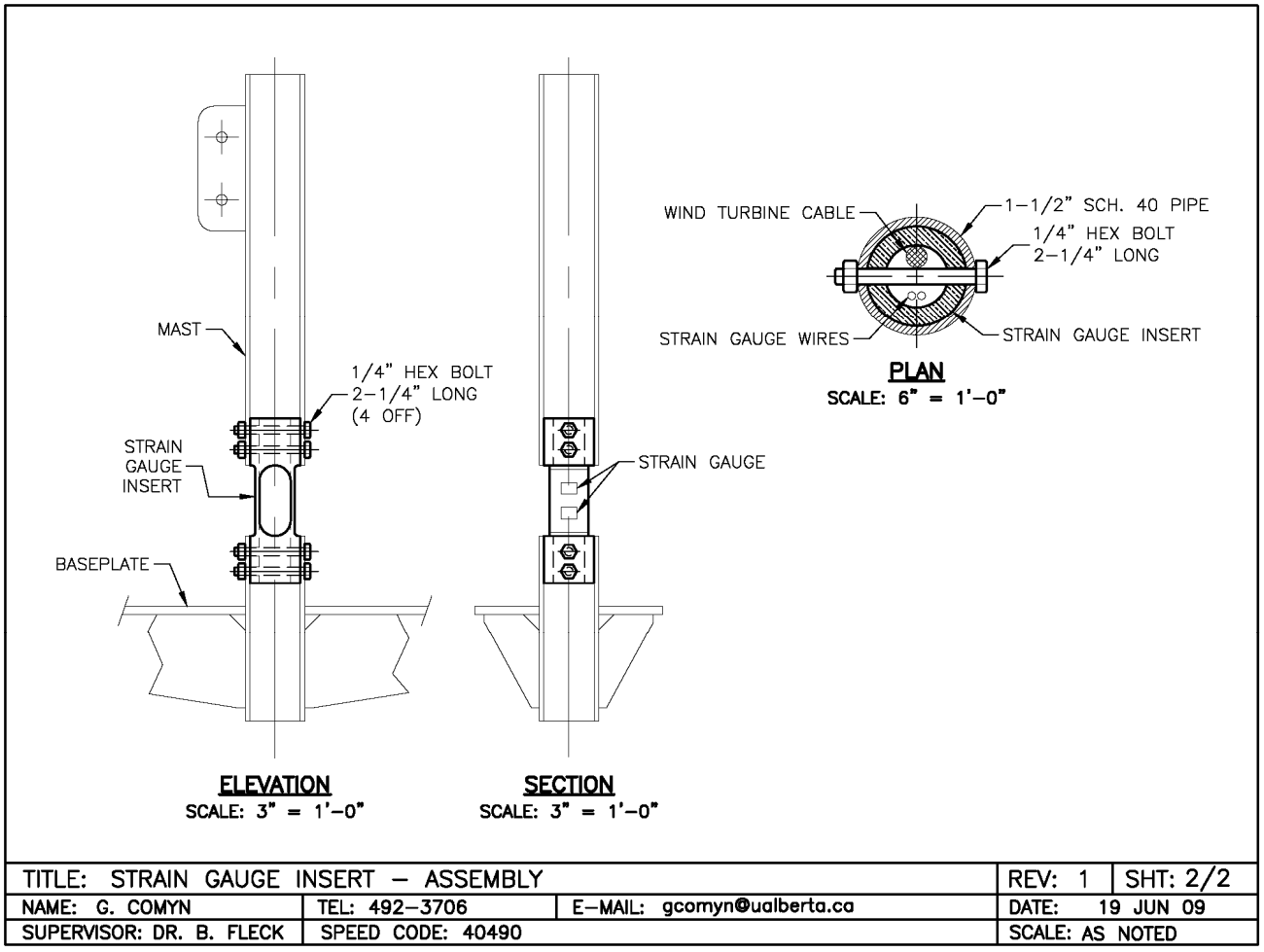

Figure D.3 - Drawing of strain gauge insert

D.2 Strain gauges

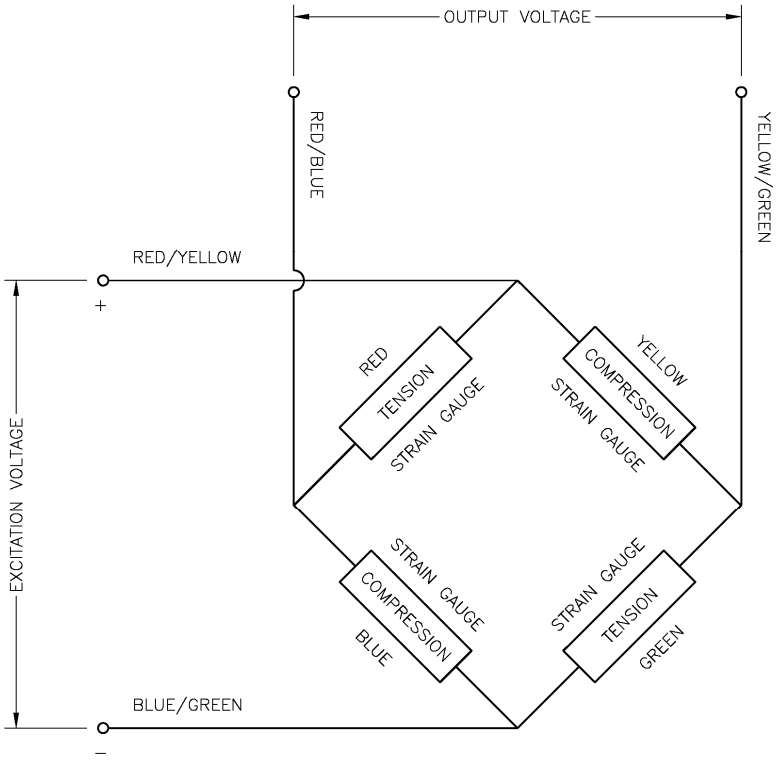

Figure D.4 - Strain gauge wiring diagram

Four strain gauges were used, two in tension on the upwind face of the insert piece and two in compression on the downwind face. These strain gauges were wired in a Wheatstone bridge configuration as shown in Figure D.4.

D.3 Calibration Apparatus

A simple gantry was constructed from wooden 2x4s and a sheave as shown in Figure D.5. 1/8" (3 mm) diameter wire rope with thimble eyes on each end was run over the sheave to convert dead weight force into a horizontal force pulling on the wind turbine. The steel flat bar had a hole drilled through it to fit over the shaft of the carriage bolt and acted as a platform to carry the weights. The carriage bolt threaded into the body of the turnbuckle which allowed the base to be disengaged from the system when changing weights.

The strain gauges were calibrated in the following manner. As shown in Figures D.6 and D.7, the gantry was screwed to the floor of the wind tunnel downwind of the turbine. Weights were hung vertically on a wire rope that passed over a sheave on the gantry. The wire rope then connected horizontally to the centre of the wind turbine. The force of the weights would pull on the wind turbine in the direction of the wind. Known weights were added and subtracted from the gantry system and the output voltage from the strain gauge bridge was recorded.

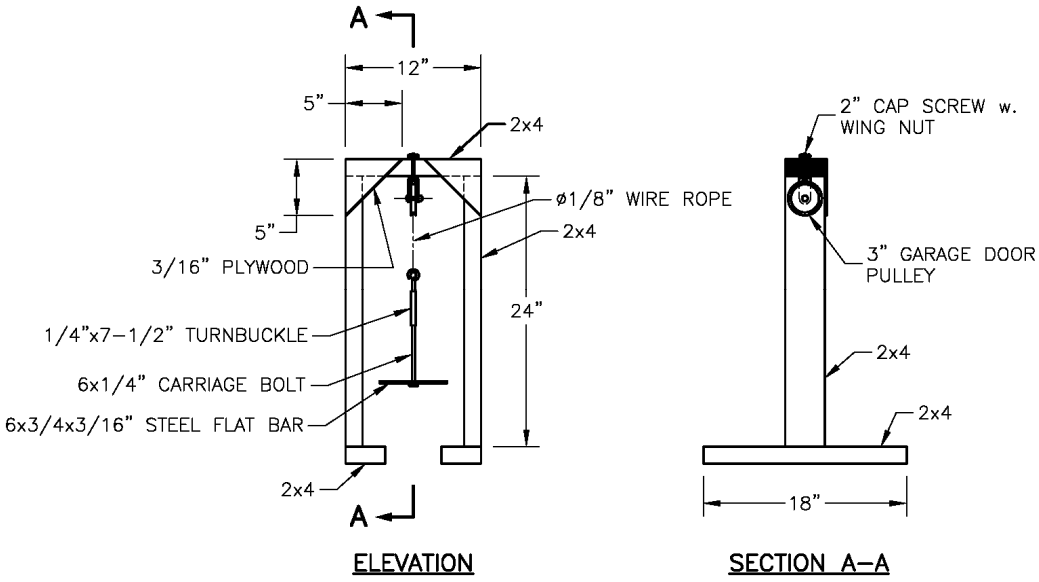

Figure D.5 - Gantry construction drawing

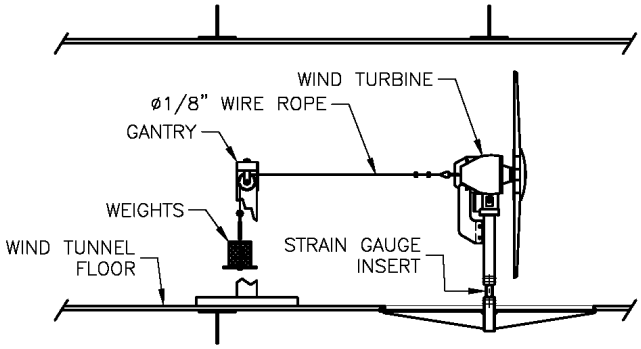

Figure D.6 – Strain gauge calibration procedure

Figure D.7 - Photograph of the strain gauge calibration process

D.4 Calibration curves

The results of the calibration are shown in Figures D.8, D.9, D.10 and D.11. The initial calibration of 20 August 2009 was done without the rotor but all subsequent calibrations included the rotor. The strain gauges were recalibrated after the wind tunnel was used by another user but the calibration curves remained very consistent.

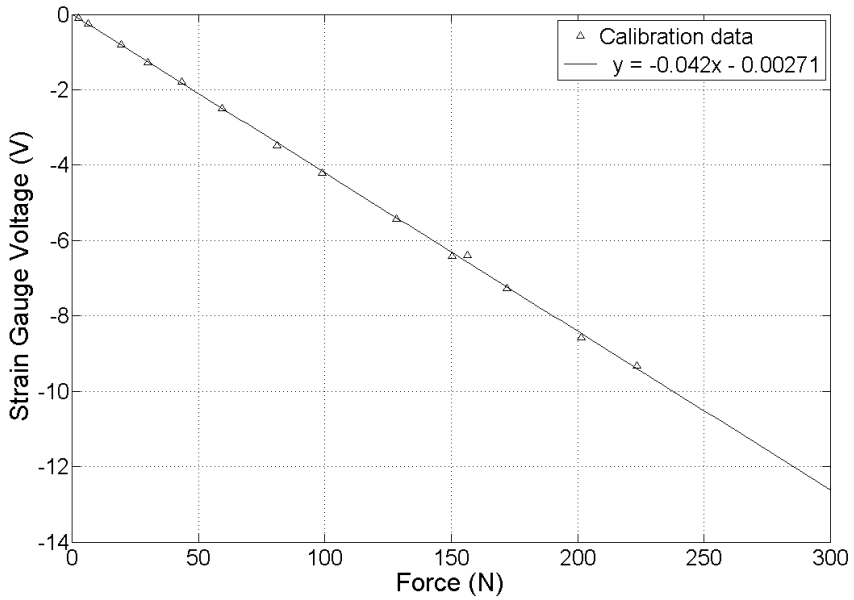

Figure D.8 - Strain gauge calibration curve 20 August 2009, with rotor removed

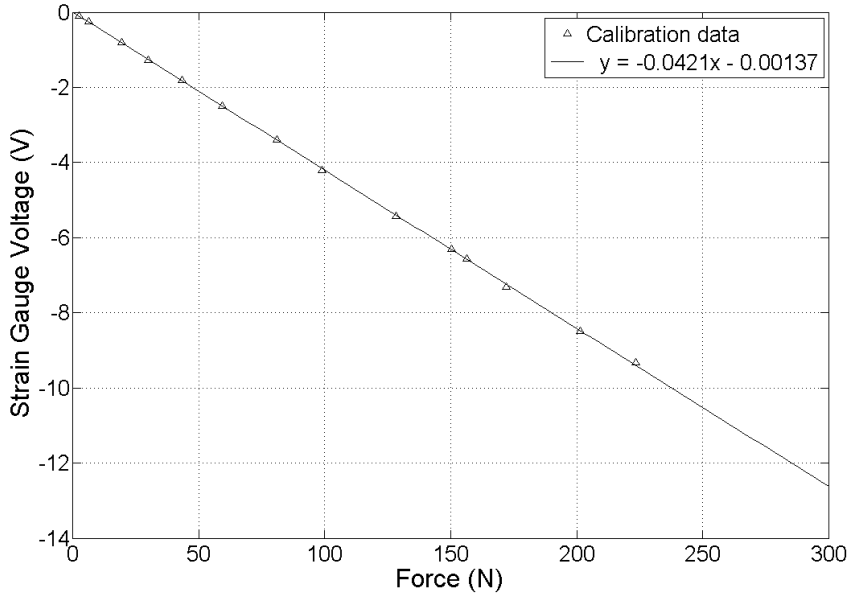

Figure D.9 - Strain gauge calibration curve 10 September 2009, with rotor installed

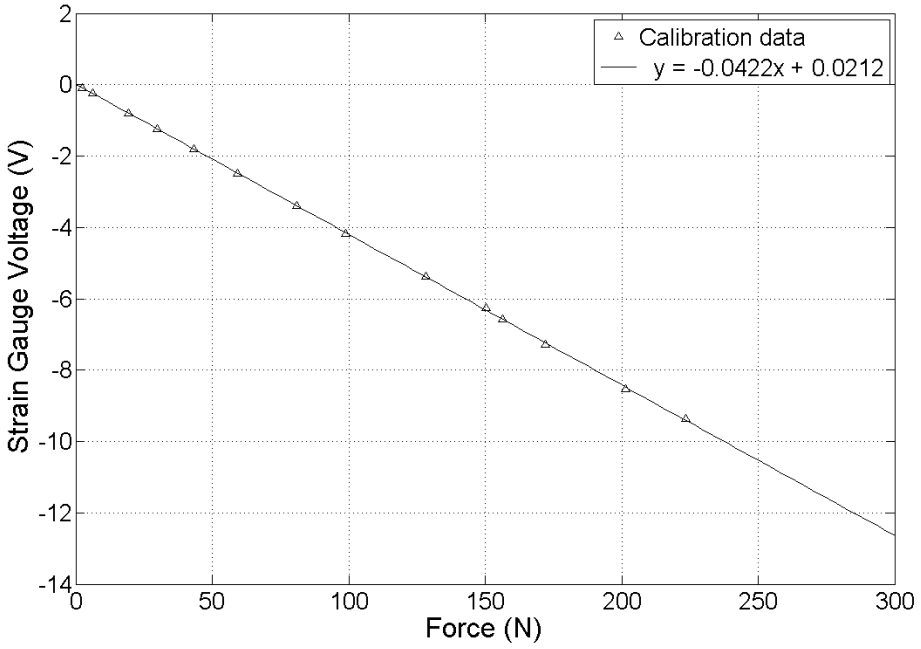

Figure D.10 - Strain gauge calibration curve 24 September 2009, with rotor installed

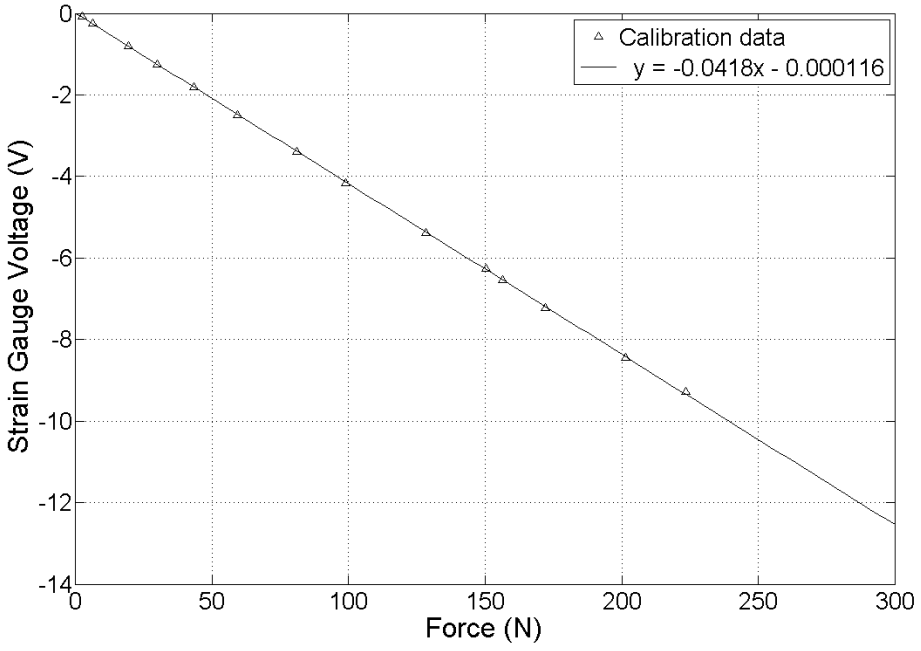

Figure D.11 - Strain gauge calibration curve 27 November 2009, with rotor installed

Appendix E: Absolute Position Rotary Encoder

E.1 Arrangement of sensors

The rotational speed of the rotor was determined with the use of an absolute position rotary encoder fabricated from two infrared (IR) reflective sensors. Two Honeywell HOA 1180 reflective sensors, shown in Figure E.1, were affixed to the forward face of the turbine casing as shown in Figure E.2. The sensors consist of an infrared emitting diode and photodarlington detector and their specifications can be found in Table E.1. The rear side of the rotor was etched with two sets of markings, as shown in Figure E.2. They were painted with reflective silver paint. One set of markings were located at the midpoint of each blade radially around the rotor. The other set was a single mark that indicated the passage of a full revolution of the rotor. This latter mark was used to determine the rotational speed of the rotor and the former set divided one revolution into individual blade passes.

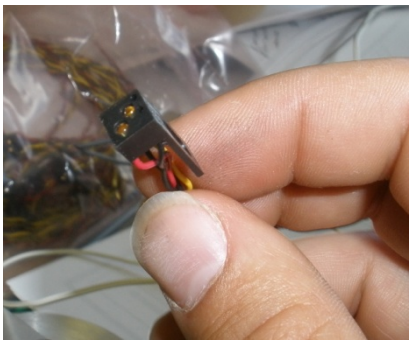

Figure E.1 - Honeywell HOA 1180 infrared reflective sensor

Table E.1 - Infrared sensor specifications

Manufacturer	Honeywell				
Model	HOA1180				
Parameter	**Symbol**	**Min**	**Max**	**Units**	**Test Conditions**
Operating Temperature Range		-55	100	°C	
IR Emitter					
Forward Voltage	V_F		1.6	V	I_F = 20 mA
Continuous Forward Current	I_F		50	mA	
Reverse Voltage	V_R		3	V	
Reverse Leakage Current	I_R		10	µA	V_R = 3 V
Power Dissipation			75	mW	
Detector					
Collector-Emitter voltage	V_{CE}		15	V	
Emitter-Collector voltage	V_{EC}		5	V	
Power dissipation			75	mW	
Collector DC Current			30	mA	
Collector-Emitter Breakdown Voltage	$V_{(BR)CEO}$	15		V	I_C = 100 µA
Emitter-Collector Breakdown Voltage	$V_{(BR)ECO}$	5.0		V	I_E = 100 µA
Collector Dark Current	I_{CEO}		250	nA	V_{CE} = 10 V I_F = 0
Coupled Characteristics					
On-State Collector Current	$I_{C(ON)}$	2.0		mA	V_{CE} = 5 V I_F = 30 mA
Collector-Emitter Saturation Voltage	$V_{CE(SAT)}$		1.1	V	I_F = 30 mA I_C = 250 µA
Rise and Fall Time	t_r, t_f		75	µs	V_{CC} = 5V, I_C = 1 mA R_L = 100 Ω

(a)

REV	DESCRIPTION	DATE

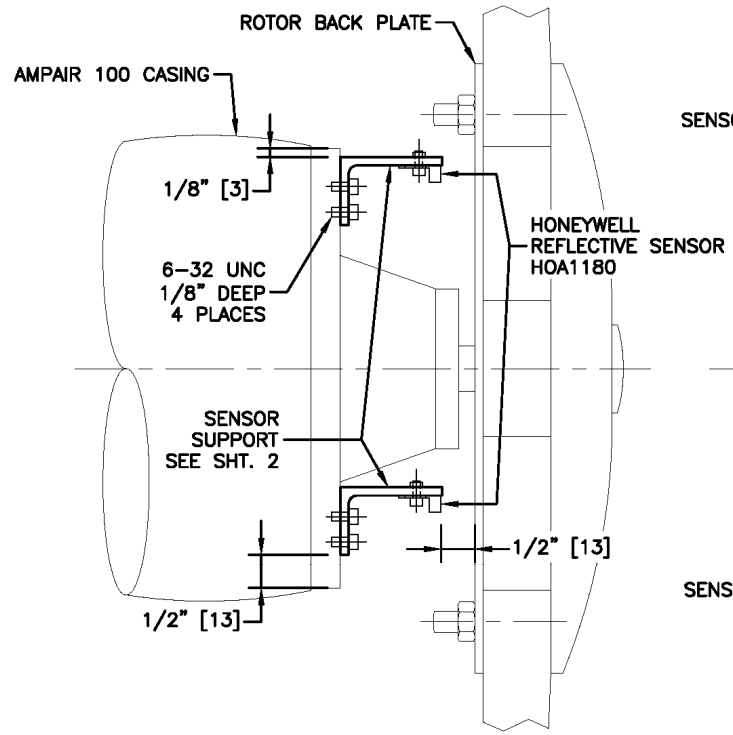

ELEVATION ON AMPAIR 100 WIND TURBINE

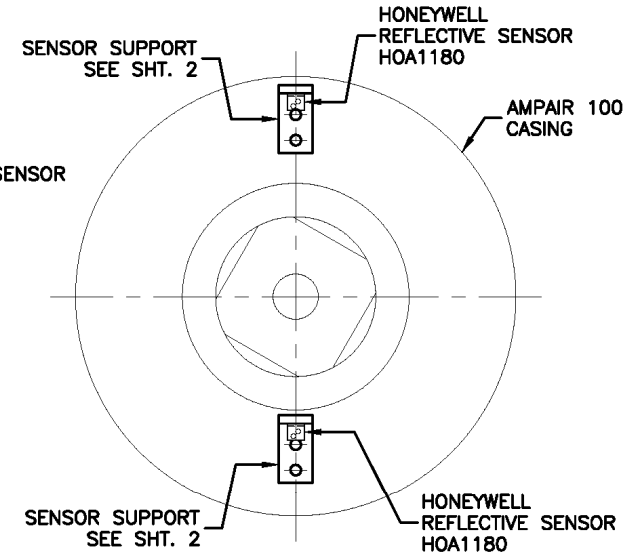

VIEW ONTO CASING

TITLE: WIND TURBINE TACHOMETER INSTALLATION			REV: 1 / SHT: 1/3
NAME: G. COMYN	TEL: 492-3706	E-MAIL: gcomyn@ualberta.ca	DATE: 15 JUN 09
SUPERVISOR: DR. B. FLECK	SPEED CODE: 40490		SCALE: 6" = 1'-0"

(b)

REV	DESCRIPTION	DATE

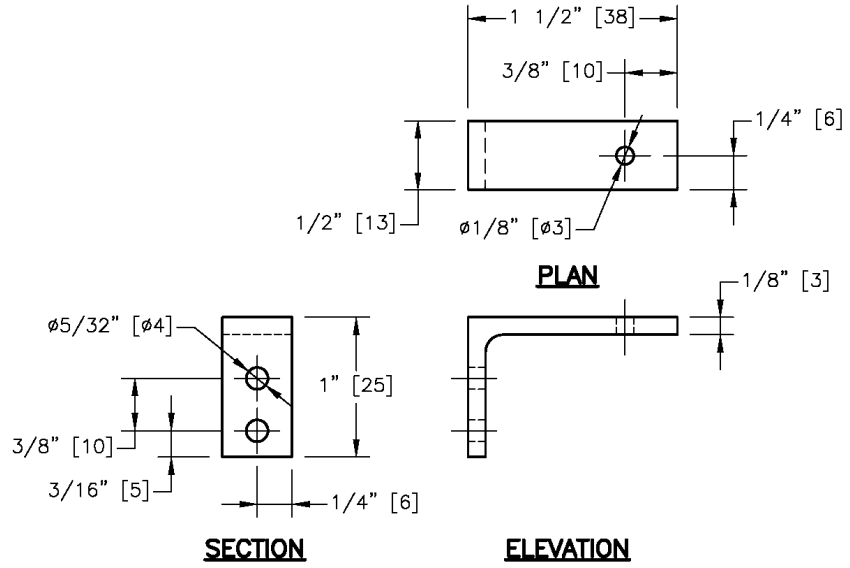

SENSOR SUPPORT

MATERIAL: 1"x1–1/2"x1/8" ANGLE BAR OR BENT 1/8" PLATE
FABRICATE: 2 OFF
FASTENERS: 6–32 UNC x 1/4" LONG CAP SCREW (4 OFF)
4–40 UNC x 1/4" LONG CAP SCREW & NUT (2 OFF)

TITLE: WIND TURBINE TACHOMETER – SENSOR SUPPORT			REV: 1	SHT: 2/3
NAME: G. COMYN	TEL: 492–3706	E–MAIL: gcomyn@ualberta.ca	DATE: 15 JUN 09	
SUPERVISOR: DR. B. FLECK	SPEED CODE: 40490		SCALE: 1:1	

(c)

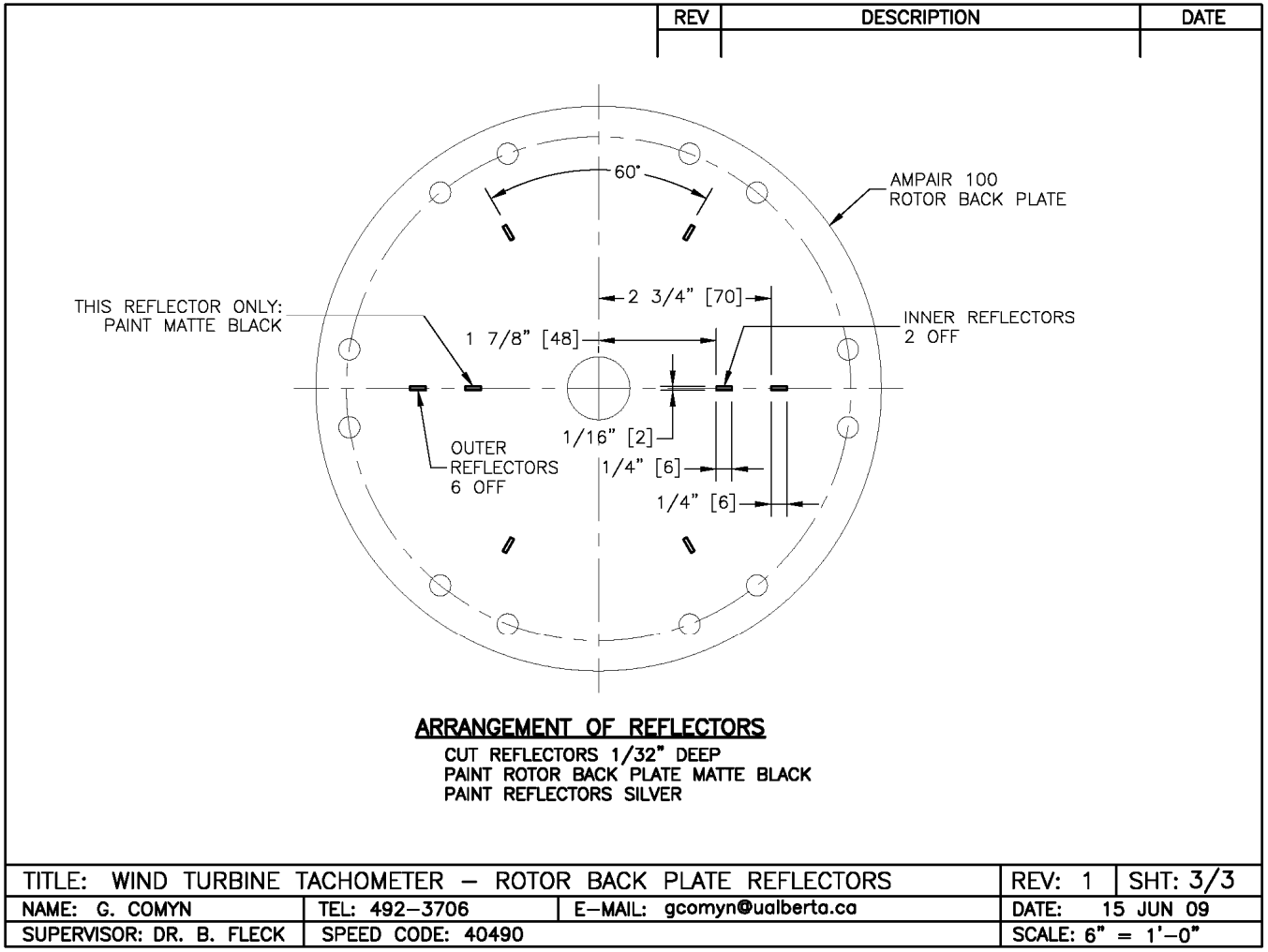

Figure E.2 - Infrared sensor installation for absolute rotary encoder

E.2 Wiring details

The IR sensors were supplied with a single 5 V power supply. The emitter was wired in series with a 510 Ω resistor to limit the current through the diode. The detector was wired in series with a 10 kΩ resistor so that when the photodarlington closed the 5V power source would not be shorted directly to ground. The cathodes of both were connected to ground and the output voltage, V_0, was measured between ground and the input to the detector as shown in Figure E.3. The output from both IR sensors was about 4.85 V unless they detected IR radiation within its field of view (due to reflection). When radiation struck the detector, the darlington opened and the output voltage dropped. These negative spikes recorded the passage of the reflective marks.

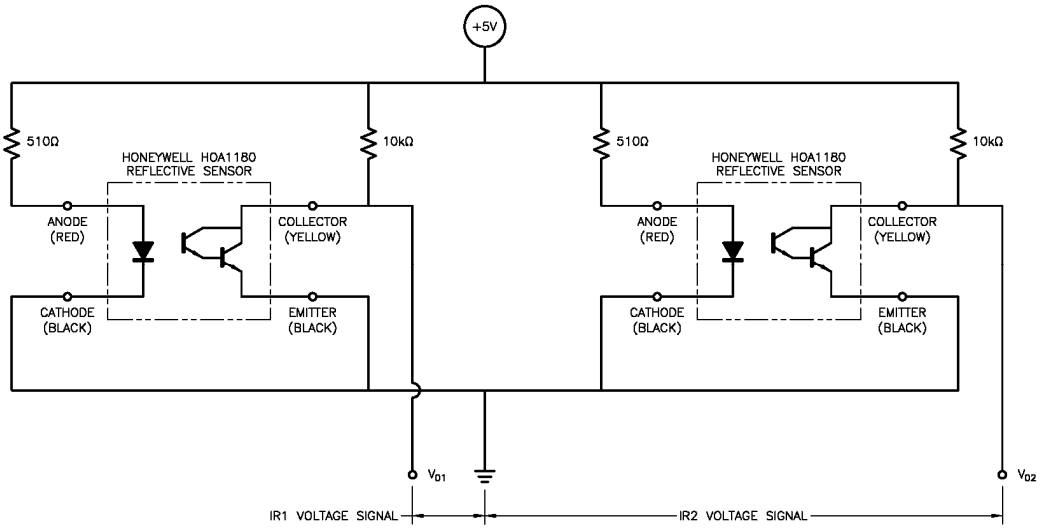

Figure E.3 - Infrared sensor wiring diagram

Appendix F: Kiel Probe Specifications

The specifications of the Kiel probe used for measuring the wake velocity are shown in Table F.1. A drawing of the Kiel probe from the manufacturer is shown in Figure F.1.

Table F.1 - Kiel probe specifications

Brand	United Sensor
Type	E
Diameter of stem	3 mm (1/8”)
Length of stem	305 mm (12”)
Diameter of head	9 mm (3/8”)
Length of head	19 mm (3/4”)
Yaw	+/- 63°
Pitch	+/- 58°

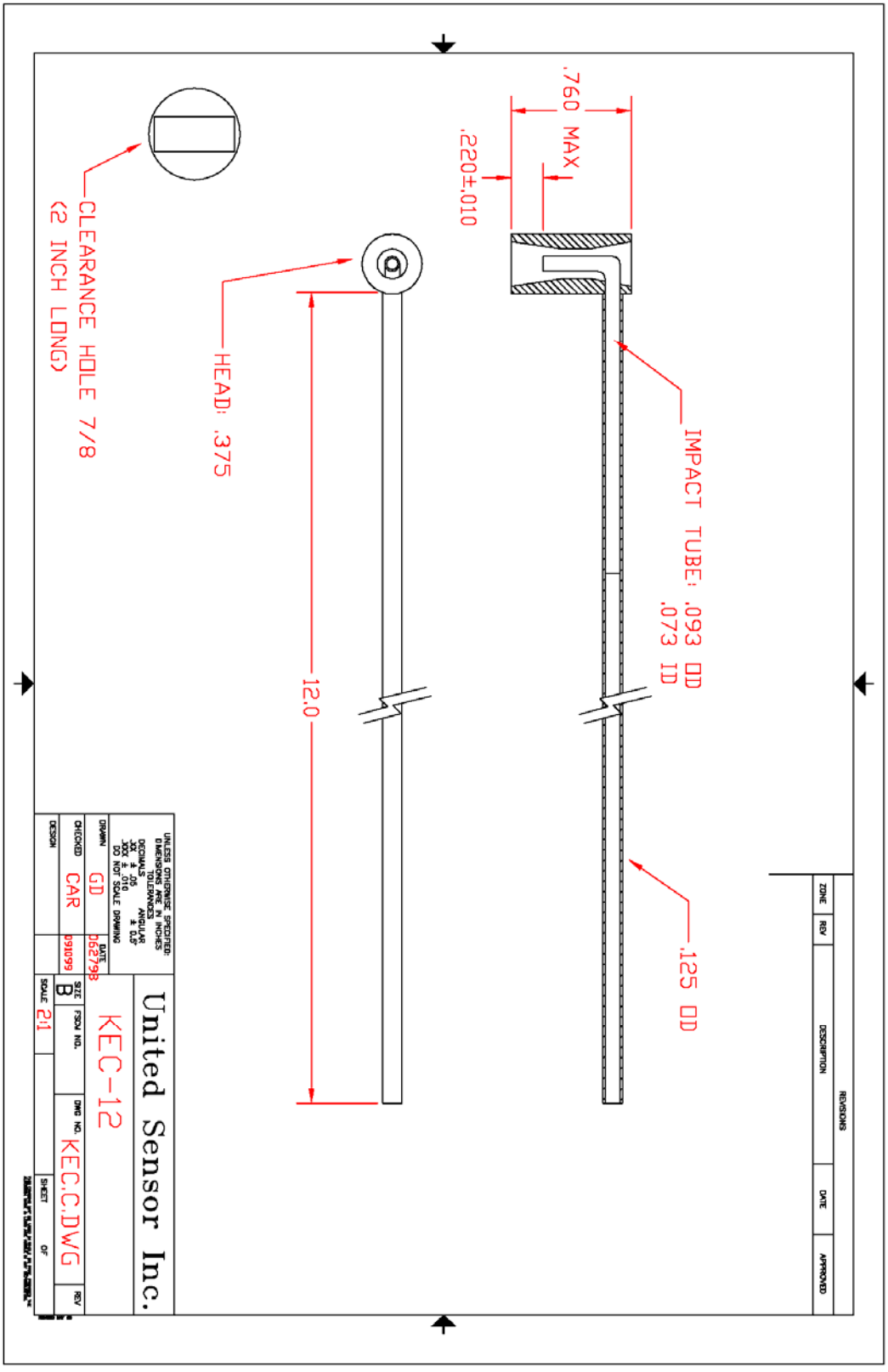

Figure F.1 - Manufacturer's drawing of the Kiel probe

Appendix G: Kiel Probe Data Sampling Locations

G.1 Calibration Apparatus

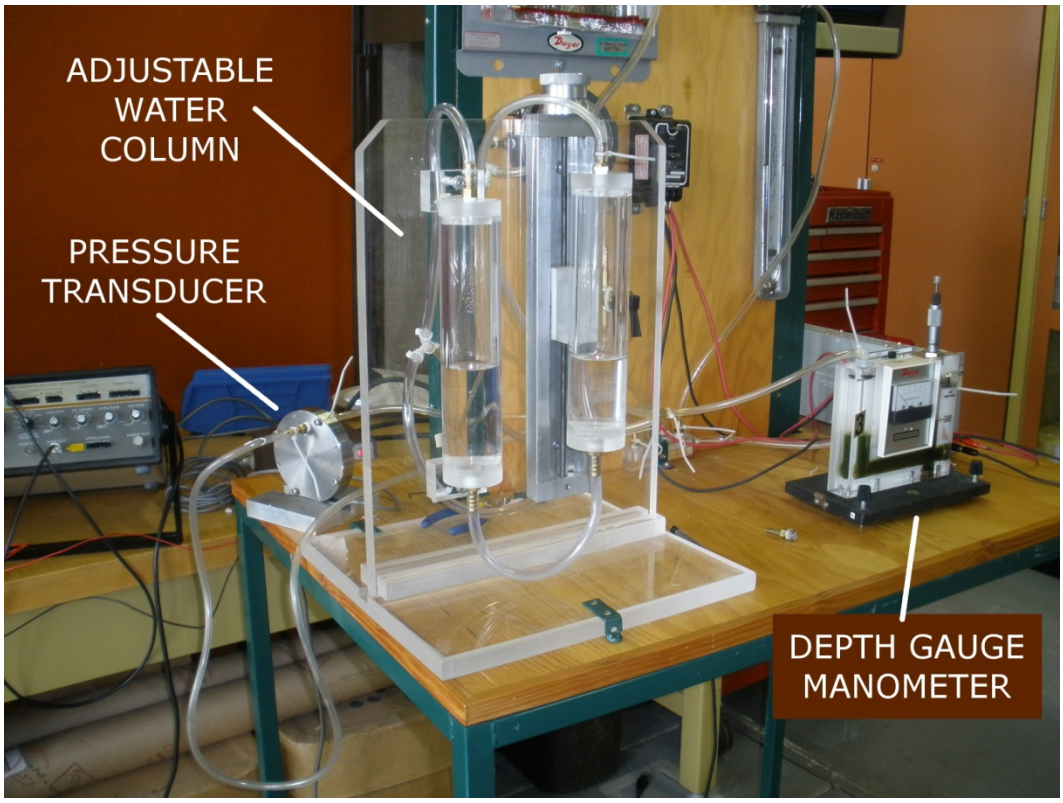

Figure G.1 - Apparatus for calibration of pressure transducers

The pressure transducers were calibrated using the apparatus shown in Figure G.1. The pressure transducer was connected to an adjustable water column and a Dwyer "Microtector" (a manometer with a depth gauge micrometer). A specific column height was set on the micrometer and the water column adjusted until it reached the micrometer. The measured displacement of a single column is half the total differential pressure. Output voltage of the pressure transducer was recorded for this pressure. This process was repeated a number of times up to the limit of the diaphragm. The results of the calibrations are shown in the Sections G.2.1 – G.2.3. The pressure transducers were calibrated each time the ports or diaphragms were adjusted, or if the control box settings were changed.

G.2 Calibration curves

G.2.1 Validyne DP103-08

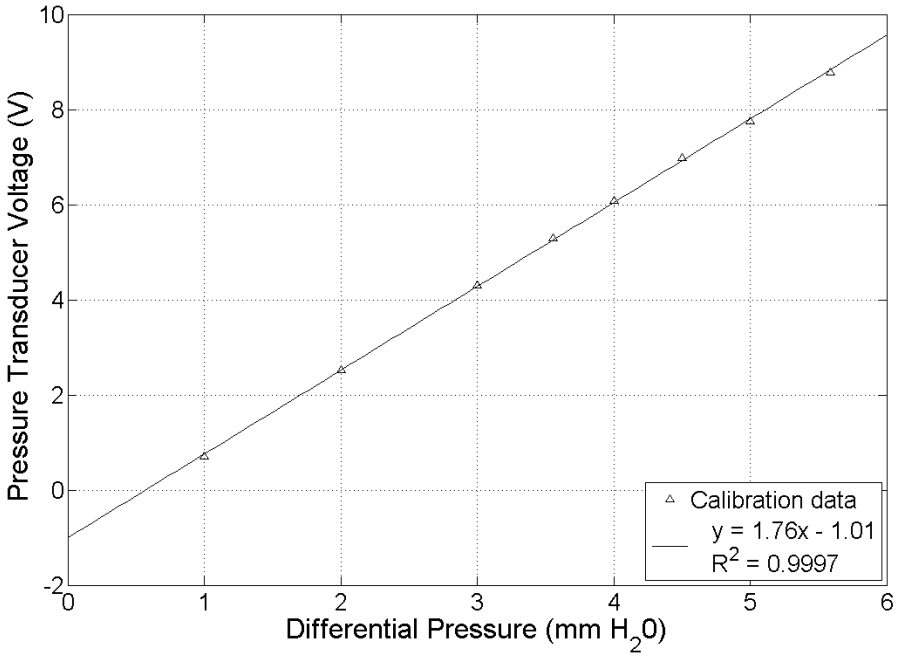

Figure G.2 - Validyne DP103-08 calibration curve, 14 July 2009

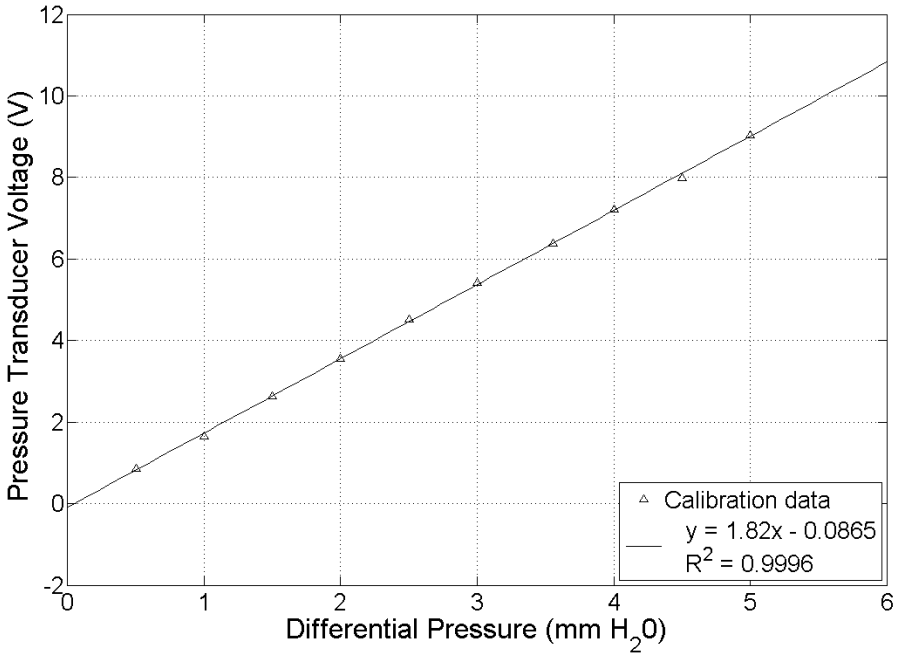

Figure G.3 - Validyne DP103-08 calibration curve, 11 September 2009

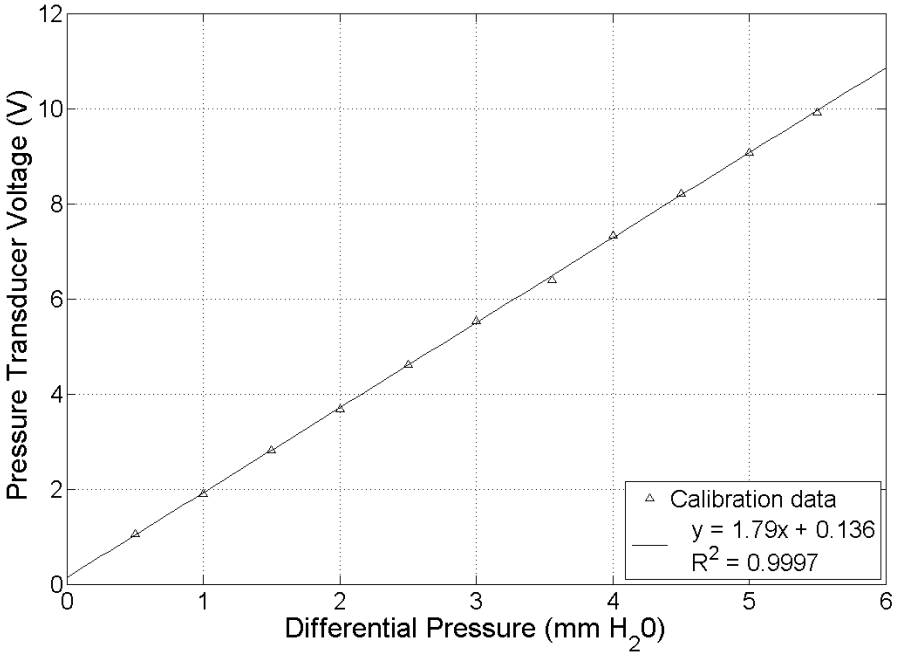

Figure G.4 - Validyne DP103-08 calibration curve, 10 November 2009

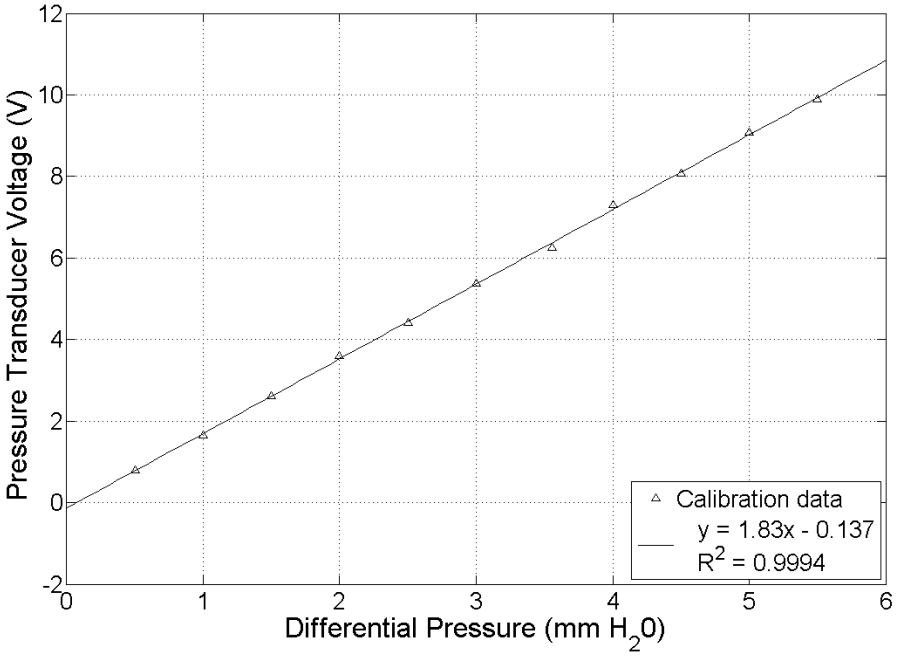

Figure G.5 - Validyne DP103-08 calibration curve, 07 December 2009

G.2.2 Validyne DP45-14

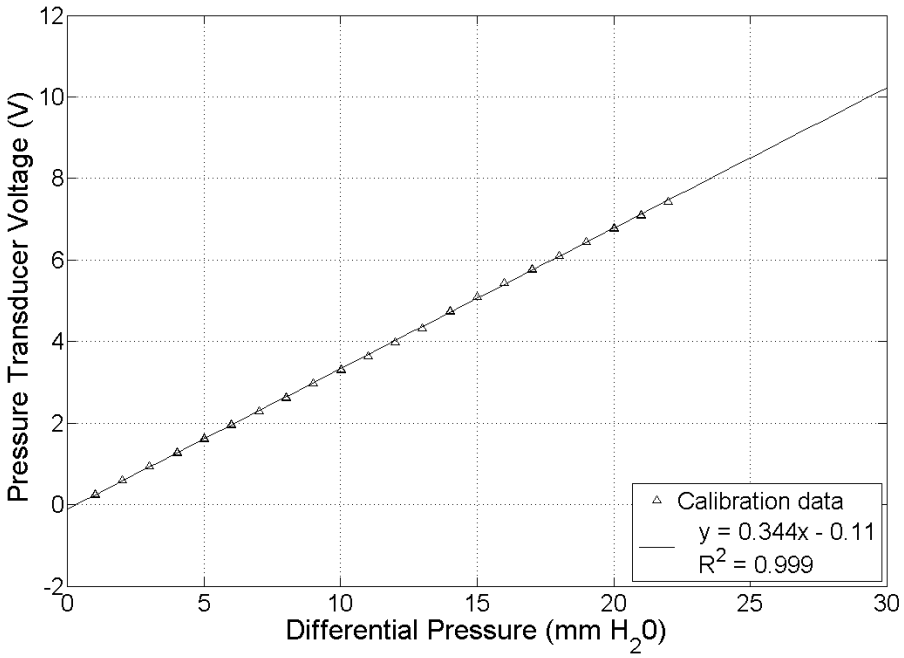

Figure G.6 - Validyne DP45-14 calibration curve, 03 June 2009

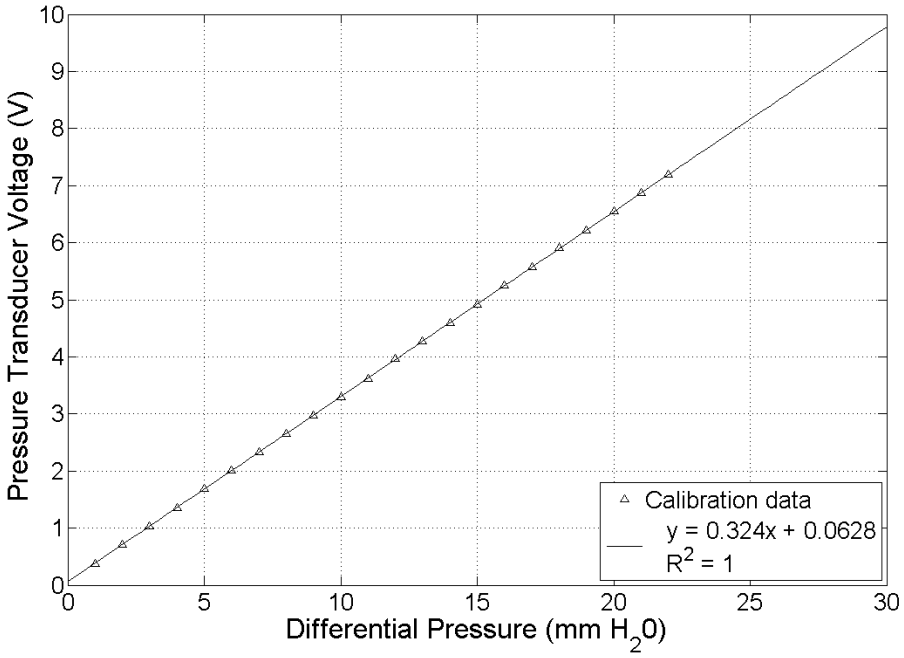

Figure G.7 - Validyne DP45-14 calibration curve, 28 September 2009

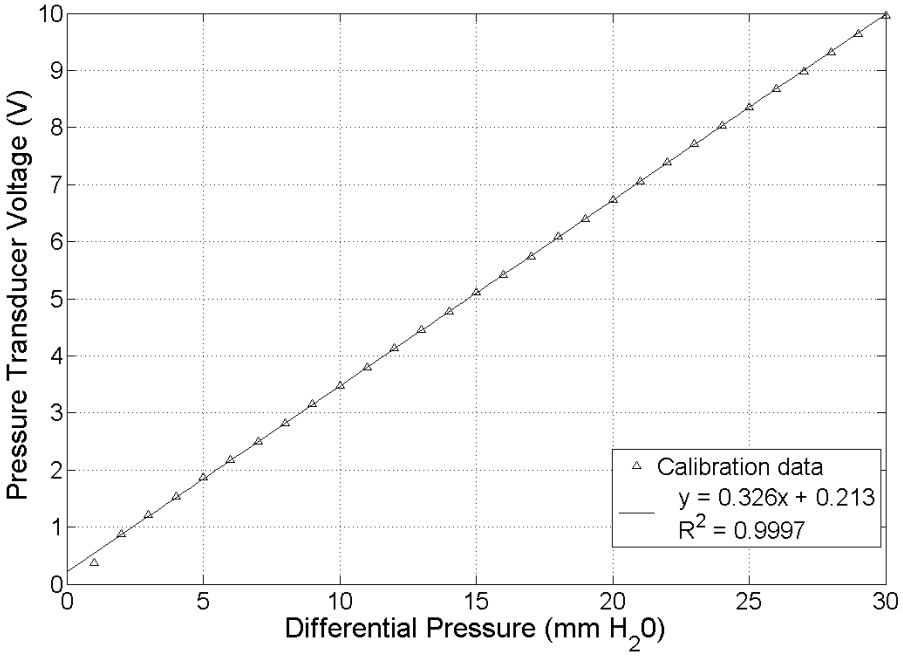

Figure G.8 - Validyne DP45-14 calibration curve, 11 November 2009

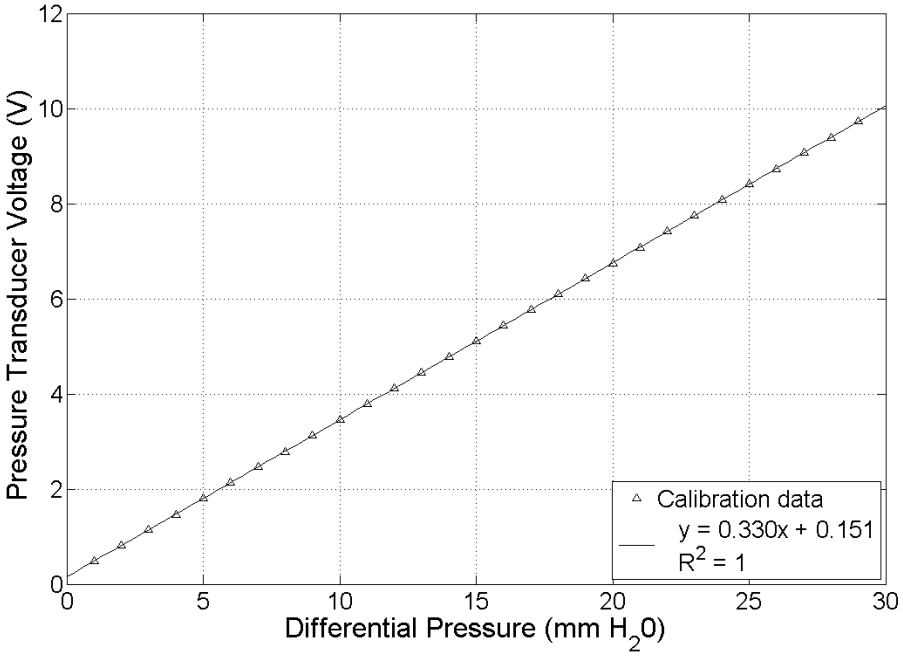

Figure G.9 - Validyne DP45-14 calibration curve, 09 December 2009

G.2.3 Validyne DP45-16

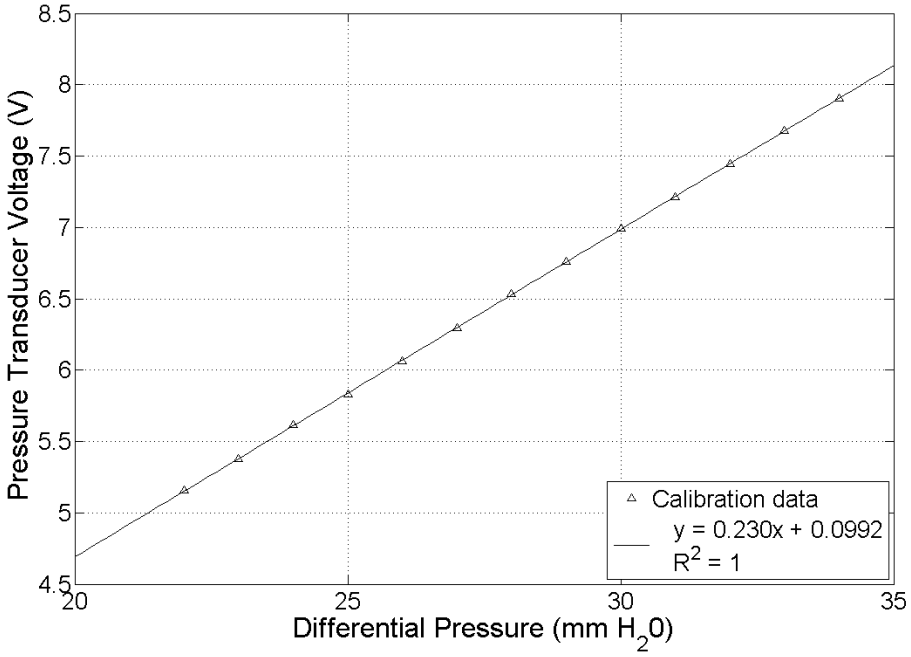

Figure G.10 - Validyne DP45-16 calibration curve, 13 July 2009

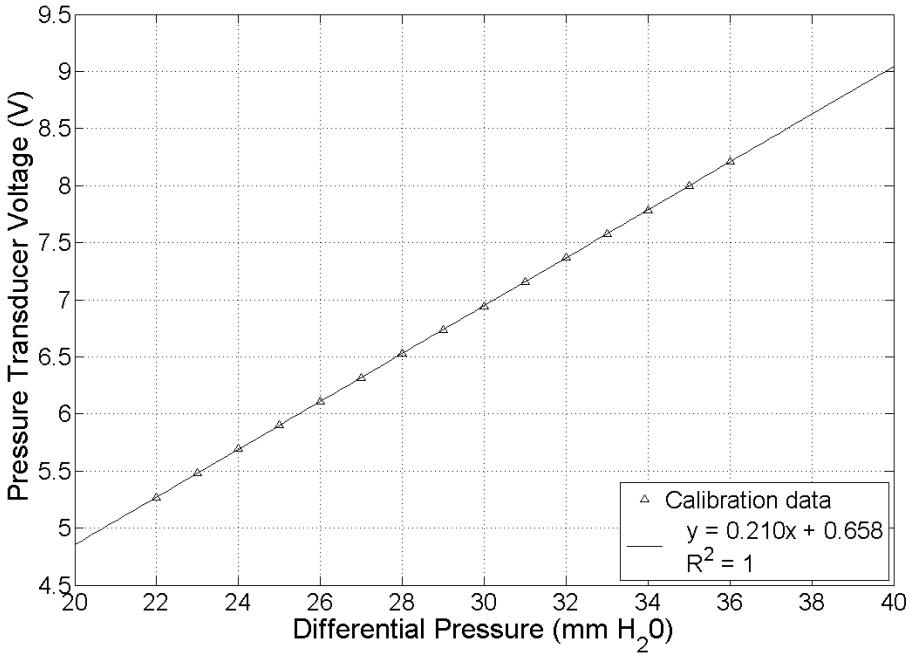

Figure G.11 - Validyne DP45-16 calibration curve, 08 October 2009

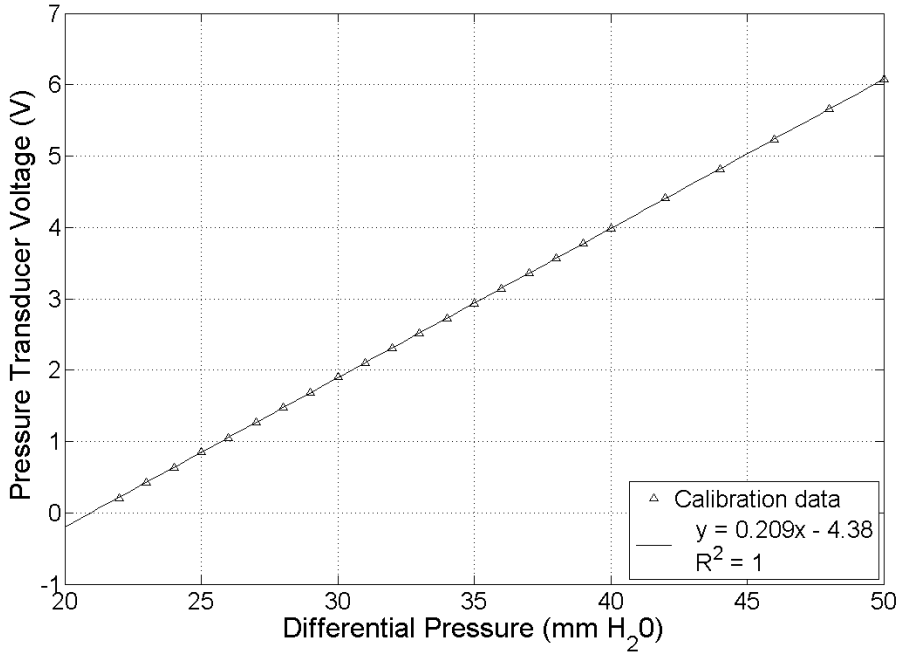

Figure G.12 - Validyne DP45-16 calibration curve, 12 October 2009

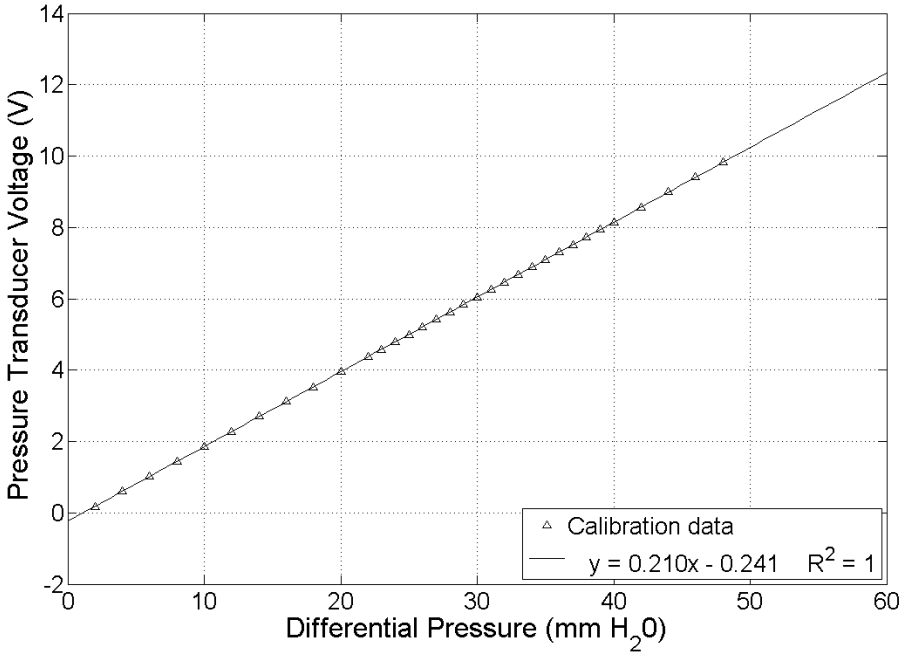

Figure G.13 - Validyne DP45-16 calibration curve, 12 November 2009

Appendix H: Traverse Path

Table H.1 - Traverse path of the Kiel probe

Path No.	inches	millimeters	Path No.	inches	millimeters	Path No.	inches	millimeters
1	0.000	0.000	38	18.000	457.20	75	36.000	914.40
2	1.500	38.10	39	18.250	463.55	76	37.500	952.50
3	3.340	84.84	40	18.500	469.90	77	39.000	990.60
4	4.490	114.1	41	18.760	476.50	78	40.500	1028.7
5	5.390	136.9	42	19.020	483.11	79	42.000	1066.8
6	6.160	156.5	43	19.290	489.97	80	43.500	1104.9
7	6.850	174.0	44	19.560	496.82	81	45.000	1143.0
8	7.470	189.7	45	19.830	503.68	82	46.500	1181.1
9	8.050	204.5	46	20.110	510.79			
10	8.590	218.2	47	20.390	517.91			
11	9.090	230.9	48	20.680	525.27			
12	9.570	243.1	49	20.980	532.89			
13	10.030	254.76	50	21.280	540.51			
14	10.460	265.68	51	21.580	548.13			
15	10.880	276.35	52	21.900	556.26			
16	11.290	286.77	53	22.220	564.39			
17	11.680	296.67	54	22.550	572.77			
18	12.050	306.07	55	22.880	581.15			
19	12.420	315.47	56	23.230	590.04			
20	12.770	324.36	57	23.580	598.93			
21	13.120	333.25	58	23.950	608.33			
22	13.450	341.63	59	24.320	617.73			
23	13.780	350.01	60	24.710	627.63			
24	14.100	358.14	61	25.120	638.05			
25	14.420	366.27	62	25.540	648.72			
26	14.720	373.89	63	25.970	659.64			
27	15.020	381.51	64	26.430	671.32			
28	15.320	389.13	65	26.910	683.51			
29	15.610	396.49	66	27.410	696.21			
30	15.890	403.61	67	27.950	709.93			
31	16.170	410.72	68	28.530	724.66			
32	16.440	417.58	69	29.150	740.41			
33	16.710	424.43	70	29.840	757.94			
34	16.980	431.29	71	30.610	777.49			
35	17.240	437.90	72	31.510	800.35			
36	17.500	444.50	73	32.660	829.56			
37	17.750	450.85	74	34.500	876.30			

Appendix I: Matlab Scripts

I.1 General

Separate Matlab variables were used for the different sampling rates (1,000 samples @ 1,000 Hz, 10,000 samples @ 5,000 Hz, and 20,000 samples @ 10,000 Hz) and for each wind speed in those sampling rate sets. For example, to calculate the rotor RPM for 10 m/s wind speed at 1,000 Hz, the variable would be RPM_1000_1000_10 and for 10,000 Hz the variable would be RPM_20000_10000_10. As a result, there are many repetitive Matlab scripts. For the sake of space, the Matlab scripts that follow have been edited down to show the calculations performed for 10 m/s nominal wind speed in the 20,000 samples @ 10,000 Hz data set.

I.2 Run_Ampair_20000_1000.m

```
%Execute data analysis for Ampair blade 20000 samples at 10000 hz by running all the other scripts

%%
%%
read_data_20000_10000_10
save Ampair_20000_10000_10.mat
clear

%%
Rotor_Radius = 0.464; %meters

%%
Calc_Force_20000_10000

%%
Calc_Power_20000_10000

%%
Calc_Current_20000_10000

%%
Calc_WT_windspeed_20000_10000

%%
Calc_RPM_20000_10000_10
save Ampair_20000_10000_RPM
clear
clc

%%
Calc_Velocity_20000_10000

%%
Calc_mean_vel_def2_20000_10000
Calc_mean_vel_def3_20000_10000

%%
Calc_Phase_averages_20000_10000_10
save Ampair_20000_10000_PHAVE_10.mat
```

```
clear

%%
Calc_Ub

%% Write Output file
load Ampair_20000_10000_10 WT_Temp* Atmos_press* Air_den* Resistance*
load Ampair_20000_10000_RPM Wind_vel_WT_mast* Force* Current* Voltage* Power* RPM* TSR*
load Ampair_20000_10000_PHAVE_10 most*
load Ampair_20000_10000_mean_vel_linear Vel_Def_mean2*
load Ampair_20000_10000_mean_vel_area Vel_Def_mean3*

% Run 1
A = {'Wind Tunnel Wind Speed','Wind Tunnel Temp.','Air Density','Atmos.
Press.','Force','Resistance','Current','Voltage','Power','RPM','TSR','Points per Blade Pass','Linear Mean Wake
Velocity','Area Mean Wake Velocity'; Wind_vel_WT_mast_10 WT_Temp_10 Air_den_10 Atmos_press_10
Force_10 Resistance_10 Current_10 Voltage_10 Power_10 RPM_10 TSR_10 most_prob_IR2_points_all_10
Vel_Def_mean_20000_10000_10 Vel_Def_mean2_20000_10000_10 };
xlswrite('Output_20000_10000.xls',A)
```

I.3 Read_data_20000_1000_10.m

```
%Read in Data
Data_coll_10 = input('[10 m/s] Enter data acquisiton speed in Hz');
Data_pts_10 = input('[10 m/s]Enter number of data points collected');
Atmos_press_10 = input('[10 m/s]Enter Atmospheric Pressure in kPa');
WT_Temp_10 = input('[10 m/s]Enter wind tunnel temperature in C');
Manom_10 = input('[10 m/s]Enter manometer reading in mm');
Resistance_10 = input('[10 m/s]Enter load bank total resistance in ohms');
strain_slope_10 = input('[10 m/s]Enter strain gauge calibration curve SLOPE');
strain_offset_10 = input('[10 m/s]Enter strain gauge calibration curve OFFSET');
Press_slope_10 = input('[10 m/s]Enter pressure gauge calibration curve SLOPE');
Press_offset_10 = input('[10 m/s]Enter pressure gauge calibration curve OFFSET');

time_step_10 = 1/Data_coll_10;
time_end_10 = (time_step_10 * Data_pts_10) - time_step_10;
Air_den_10 = Atmos_press_10*1000/(287.05*(WT_Temp_10+273.05));

%create time vector
time_10 = (0:time_step_10:time_end_10);
%time_10 = (0:0.001:0.999)';

Pitot_path = dlmread('Pitot_tube_path.txt');
%Convert to metric
Pitot_path = Pitot_path * 0.0254;

path('G:/Thesis/Matlab/data/Ampair Blade/2010-01-04 Single Axis 10ms',path)

%Read text files to define data matrix at one axial location
axloc1 = dlmread('Ten_mps_0_0_0.txt','\t',2,0);
axloc2 = dlmread('Ten_mps_0_1500_0.txt','\t',2,0);
axloc3 = dlmread('Ten_mps_0_3340_0.txt','\t',2,0);
axloc4 = dlmread('Ten_mps_0_4490_0.txt','\t',2,0);
axloc5 = dlmread('Ten_mps_0_5390_0.txt','\t',2,0);
axloc6 = dlmread('Ten_mps_0_6160_0.txt','\t',2,0);
axloc7 = dlmread('Ten_mps_0_6850_0.txt','\t',2,0);
axloc8 = dlmread('Ten_mps_0_7470_0.txt','\t',2,0);
axloc9 = dlmread('Ten_mps_0_8050_0.txt','\t',2,0);
```

```
axloc10 = dlmread('Ten_mps_0_8590_0.txt','\t',2,0);
axloc11 = dlmread('Ten_mps_0_9090_0.txt','\t',2,0);
axloc12 = dlmread('Ten_mps_0_9570_0.txt','\t',2,0);
axloc13 = dlmread('Ten_mps_0_10030_0.txt','\t',2,0);
axloc14 = dlmread('Ten_mps_0_10460_0.txt','\t',2,0);
axloc15 = dlmread('Ten_mps_0_10880_0.txt','\t',2,0);
axloc16 = dlmread('Ten_mps_0_11290_0.txt','\t',2,0);
axloc17 = dlmread('Ten_mps_0_11680_0.txt','\t',2,0);
axloc18 = dlmread('Ten_mps_0_12050_0.txt','\t',2,0);
axloc19 = dlmread('Ten_mps_0_12420_0.txt','\t',2,0);
axloc20 = dlmread('Ten_mps_0_12770_0.txt','\t',2,0);
axloc21 = dlmread('Ten_mps_0_13120_0.txt','\t',2,0);
axloc22 = dlmread('Ten_mps_0_13450_0.txt','\t',2,0);
axloc23 = dlmread('Ten_mps_0_13780_0.txt','\t',2,0);
axloc24 = dlmread('Ten_mps_0_14100_0.txt','\t',2,0);
axloc25 = dlmread('Ten_mps_0_14420_0.txt','\t',2,0);
axloc26 = dlmread('Ten_mps_0_14720_0.txt','\t',2,0);
axloc27 = dlmread('Ten_mps_0_15020_0.txt','\t',2,0);
axloc28 = dlmread('Ten_mps_0_15320_0.txt','\t',2,0);
axloc29 = dlmread('Ten_mps_0_15610_0.txt','\t',2,0);
axloc30 = dlmread('Ten_mps_0_15890_0.txt','\t',2,0);
axloc31 = dlmread('Ten_mps_0_16170_0.txt','\t',2,0);
axloc32 = dlmread('Ten_mps_0_16440_0.txt','\t',2,0);
axloc33 = dlmread('Ten_mps_0_16710_0.txt','\t',2,0);
axloc34 = dlmread('Ten_mps_0_16980_0.txt','\t',2,0);
axloc35 = dlmread('Ten_mps_0_17240_0.txt','\t',2,0);
axloc36 = dlmread('Ten_mps_0_17500_0.txt','\t',2,0);
axloc37 = dlmread('Ten_mps_0_17750_0.txt','\t',2,0);
axloc38 = dlmread('Ten_mps_0_18000_0.txt','\t',2,0);
axloc39 = dlmread('Ten_mps_0_18250_0.txt','\t',2,0);
axloc40 = dlmread('Ten_mps_0_18500_0.txt','\t',2,0);
axloc41 = dlmread('Ten_mps_0_18760_0.txt','\t',2,0);
axloc42 = dlmread('Ten_mps_0_19020_0.txt','\t',2,0);
axloc43 = dlmread('Ten_mps_0_19290_0.txt','\t',2,0);
axloc44 = dlmread('Ten_mps_0_19560_0.txt','\t',2,0);
axloc45 = dlmread('Ten_mps_0_19830_0.txt','\t',2,0);
axloc46 = dlmread('Ten_mps_0_20110_0.txt','\t',2,0);
axloc47 = dlmread('Ten_mps_0_20390_0.txt','\t',2,0);
axloc48 = dlmread('Ten_mps_0_20680_0.txt','\t',2,0);
axloc49 = dlmread('Ten_mps_0_20980_0.txt','\t',2,0);
axloc50 = dlmread('Ten_mps_0_21280_0.txt','\t',2,0);
axloc51 = dlmread('Ten_mps_0_21580_0.txt','\t',2,0);
axloc52 = dlmread('Ten_mps_0_21900_0.txt','\t',2,0);
axloc53 = dlmread('Ten_mps_0_22220_0.txt','\t',2,0);
axloc54 = dlmread('Ten_mps_0_22550_0.txt','\t',2,0);
axloc55 = dlmread('Ten_mps_0_22880_0.txt','\t',2,0);
axloc56 = dlmread('Ten_mps_0_23230_0.txt','\t',2,0);
axloc57 = dlmread('Ten_mps_0_23580_0.txt','\t',2,0);
axloc58 = dlmread('Ten_mps_0_23950_0.txt','\t',2,0);
axloc59 = dlmread('Ten_mps_0_24320_0.txt','\t',2,0);
axloc60 = dlmread('Ten_mps_0_24710_0.txt','\t',2,0);
axloc61 = dlmread('Ten_mps_0_25120_0.txt','\t',2,0);
axloc62 = dlmread('Ten_mps_0_25540_0.txt','\t',2,0);
axloc63 = dlmread('Ten_mps_0_25970_0.txt','\t',2,0);
axloc64 = dlmread('Ten_mps_0_26430_0.txt','\t',2,0);
axloc65 = dlmread('Ten_mps_0_26910_0.txt','\t',2,0);
axloc66 = dlmread('Ten_mps_0_27410_0.txt','\t',2,0);
axloc67 = dlmread('Ten_mps_0_27950_0.txt','\t',2,0);
```

```
axloc68 = dlmread('Ten_mps_0_28530_0.txt','\t',2,0);
axloc69 = dlmread('Ten_mps_0_29150_0.txt','\t',2,0);
axloc70 = dlmread('Ten_mps_0_29840_0.txt','\t',2,0);
axloc71 = dlmread('Ten_mps_0_30610_0.txt','\t',2,0);
axloc72 = dlmread('Ten_mps_0_31510_0.txt','\t',2,0);
axloc73 = dlmread('Ten_mps_0_32660_0.txt','\t',2,0);
axloc74 = dlmread('Ten_mps_0_34500_0.txt','\t',2,0);
axloc75 = dlmread('Ten_mps_0_36000_0.txt','\t',2,0);
axloc76 = dlmread('Ten_mps_0_37500_0.txt','\t',2,0);
axloc77 = dlmread('Ten_mps_0_39000_0.txt','\t',2,0);
axloc78 = dlmread('Ten_mps_0_40500_0.txt','\t',2,0);
axloc79 = dlmread('Ten_mps_0_42000_0.txt','\t',2,0);
axloc80 = dlmread('Ten_mps_0_43500_0.txt','\t',2,0);
axloc81 = dlmread('Ten_mps_0_45000_0.txt','\t',2,0);
axloc82 = dlmread('Ten_mps_0_46500_0.txt','\t',2,0);

%Compile datamatrix_10 for all axial locations
datamatrix_10(:,:,1) = axloc1;
datamatrix_10(:,:,2) = axloc2;
datamatrix_10(:,:,3) = axloc3;
datamatrix_10(:,:,4) = axloc4;
datamatrix_10(:,:,5) = axloc5;
datamatrix_10(:,:,6) = axloc6;
datamatrix_10(:,:,7) = axloc7;
datamatrix_10(:,:,8) = axloc8;
datamatrix_10(:,:,9) = axloc9;
datamatrix_10(:,:,10) = axloc10;
datamatrix_10(:,:,11) = axloc11;
datamatrix_10(:,:,12) = axloc12;
datamatrix_10(:,:,13) = axloc13;
datamatrix_10(:,:,14) = axloc14;
datamatrix_10(:,:,15) = axloc15;
datamatrix_10(:,:,16) = axloc16;
datamatrix_10(:,:,17) = axloc17;
datamatrix_10(:,:,18) = axloc18;
datamatrix_10(:,:,19) = axloc19;
datamatrix_10(:,:,20) = axloc20;
datamatrix_10(:,:,21) = axloc21;
datamatrix_10(:,:,22) = axloc22;
datamatrix_10(:,:,23) = axloc23;
datamatrix_10(:,:,24) = axloc24;
datamatrix_10(:,:,25) = axloc25;
datamatrix_10(:,:,26) = axloc26;
datamatrix_10(:,:,27) = axloc27;
datamatrix_10(:,:,28) = axloc28;
datamatrix_10(:,:,29) = axloc29;
datamatrix_10(:,:,30) = axloc30;
datamatrix_10(:,:,31) = axloc31;
datamatrix_10(:,:,32) = axloc32;
datamatrix_10(:,:,33) = axloc33;
datamatrix_10(:,:,34) = axloc34;
datamatrix_10(:,:,35) = axloc35;
datamatrix_10(:,:,36) = axloc36;
datamatrix_10(:,:,37) = axloc37;
datamatrix_10(:,:,38) = axloc38;
datamatrix_10(:,:,39) = axloc39;
datamatrix_10(:,:,40) = axloc40;
datamatrix_10(:,:,41) = axloc41;
```

```
datamatrix_10(:,:,42) = axloc42;
datamatrix_10(:,:,43) = axloc43;
datamatrix_10(:,:,44) = axloc44;
datamatrix_10(:,:,45) = axloc45;
datamatrix_10(:,:,46) = axloc46;
datamatrix_10(:,:,47) = axloc47;
datamatrix_10(:,:,48) = axloc48;
datamatrix_10(:,:,49) = axloc49;
datamatrix_10(:,:,50) = axloc50;
datamatrix_10(:,:,51) = axloc51;
datamatrix_10(:,:,52) = axloc52;
datamatrix_10(:,:,53) = axloc53;
datamatrix_10(:,:,54) = axloc54;
datamatrix_10(:,:,55) = axloc55;
datamatrix_10(:,:,56) = axloc56;
datamatrix_10(:,:,57) = axloc57;
datamatrix_10(:,:,58) = axloc58;
datamatrix_10(:,:,59) = axloc59;
datamatrix_10(:,:,60) = axloc60;
datamatrix_10(:,:,61) = axloc61;
datamatrix_10(:,:,62) = axloc62;
datamatrix_10(:,:,63) = axloc63;
datamatrix_10(:,:,64) = axloc64;
datamatrix_10(:,:,65) = axloc65;
datamatrix_10(:,:,66) = axloc66;
datamatrix_10(:,:,67) = axloc67;
datamatrix_10(:,:,68) = axloc68;
datamatrix_10(:,:,69) = axloc69;
datamatrix_10(:,:,70) = axloc70;
datamatrix_10(:,:,71) = axloc71;
datamatrix_10(:,:,72) = axloc72;
datamatrix_10(:,:,73) = axloc73;
datamatrix_10(:,:,74) = axloc74;
datamatrix_10(:,:,75) = axloc75;
datamatrix_10(:,:,76) = axloc76;
datamatrix_10(:,:,77) = axloc77;
datamatrix_10(:,:,78) = axloc78;
datamatrix_10(:,:,79) = axloc79;
datamatrix_10(:,:,80) = axloc80;
datamatrix_10(:,:,81) = axloc81;
datamatrix_10(:,:,82) = axloc82;

Pressure_10 = zeros(length(datamatrix_10),length(Pitot_path));
Strain_10 = zeros(length(datamatrix_10),length(Pitot_path));
IR1_10 = zeros(length(datamatrix_10),length(Pitot_path));
IR2_10 = zeros(length(datamatrix_10),length(Pitot_path));
Turb_Out_10 = zeros(length(datamatrix_10),length(Pitot_path));

for i=1:length(Pitot_path)
   Pressure_10(:,i) = datamatrix_10(:,1,i);
   Strain_10(:,i) = datamatrix_10(:,2,i);
   IR1_10(:,i) = datamatrix_10(:,3,i);
   IR2_10(:,i) = datamatrix_10(:,4,i);
   Turb_Out_10(:,i) = datamatrix_10(:,5,i);
end

clear datamatrix_10
```

```
Pressure_10_av_axloc = mean(Pressure_10); %mean of each axloc column
Pressure_10_av_all = mean(Pressure_10_av_axloc);

Strain_10_av_axloc = mean(Strain_10);
Strain_10_av_all = mean(Strain_10_av_axloc);

Turb_Out_10_av_axloc = mean(Turb_Out_10);
Turb_Out_10_av_all = mean(Turb_Out_10_av_axloc);
```

I.4 Calc_Force_20000_1000.m

```
%Calculate average Force of runs
%% 10 m/s
load Ampair_20000_10000_10 Strain_10_av_all strain_slope_10
Force_10 = mean(Strain_10_av_all)/strain_slope_10;
```

I.5 Calc_Power_20000_10000.m

```
%Calculate average Power for each run

load Ampair_20000_10000_10 Turb* Resistance*

%% 10 m/s
Voltage_10 = Turb_Out_10_av_all*2;
[Vrms] = RMS(Turb_Out_10);
Vrms_10 = Vrms;
Power_rms_10 = ((Vrms_10)^2)/Resistance_10;
Power_10 = ((Voltage_10)^2)/Resistance_10;
```

I.6 Calc_Current_20000_10000.m

```
%Calculate average Power for each run

%% 10 m/s
Current_10 = Voltage_10/Resistance_10;
```

I.7 Calc_WT_windspeed_20000_10000.m

```
%Calculate wind tunnel wind speed in m/s for each run

%% Load correction curves
horiz_buoy = dlmread('Horizontal buoyancy.txt','\t');

%% 10 m/s
load Ampair_20000_10000_10 Manom_10 Air_den_10
deltaP_WT_10 = 998*9.81*Manom_10*.001;
Wind_vel_WT_10 = sqrt(2*deltaP_WT_10/Air_den_10);

%Correct for wind tunnel location
Wind_vel_WT_mast_10 =
(interp1(horiz_buoy(:,1),horiz_buoy(:,2),Wind_vel_WT_10))*5.208+Wind_vel_WT_10;
```

I.8 Minima2.m

```
function [xmin,imin] = minima2(x)
%MINIMA   Gets the global minima points from a time series.
%   [XMIN,IMIN] = MINIMA2(X) returns the global minima
%   points of the vector X, where
%    XMIN - minima points
%    IMIN - indexes of the XMIN
```

```
%

xmin = [];
imin = [];

% Difference between subsequent elements:
dx = diff(x);

% Indexes where x changes
for j = 1:numel(dx)/length(dx)
   for i = 1:(length(dx))
      if dx(i,j)~=0
         a(i,j) = i;
      else
         a(i,j) = 0;
      end
   end
end

% Peaks?
for j = 1:numel(a)/length(a)
   for i = 1:(length(a))
      if a(i,j) > 0
         xa(i,j) = x(a(i,j),j);
      else
         xa(i,j) = 4.85;
      end
   end
end


b = (diff(xa) > 0);
% 1  =>  positive slopes (minima begin)
% 0  =>  negative slopes (maxima begin)

xb  = diff(b);
% -1 =>  maxima indexes (but one)
% +1 =>  minima indexes (but one)

% minima indexes
for j = 1:numel(xb)/length(xb)
   i = 1;
   while i <= length(xb)
      if xb(i,j) == +1
         imin(i,j) = 0;
         imin(i+1,j) = i+1;
         i = i+1;
      else
         imin(i,j) = 0;

      end
      i = i+1;
   end
end

if length(imin) > length(xb)
   imin(length(xb)+1,:) = [];
end
```

```
for j = 1:numel(xb)/length(xb)
   for i = 1:(length(xb))
      if imin(i,j) > 0
         xmin(i,j) = x(imin(i,j),j);
      else
         xmin(i,j) = 0;
      end
   end
end
```

I.9 Calc_RPM_20000_10000_10.m

```
%Use IR1 data (revolutions)

load Ampair_20000_10000_10 IR1_10 Pitot_path Data_coll_10 time_10

%Filter data so that the only minima are the voltage spikes.
q = zeros(length(IR1_10),length(Pitot_path));
for j = 1:length(Pitot_path)
   for i = 1:length(IR1_10)
     q(i,j) = IR1_10(i,j);
    if q(i,j) < 4.75
         q(i,j) = IR1_10(i,j);
    else
     q(i,j) = 4.85;
     end
   end
end

%Find minima
   [xmin,imin] = minima2(q);
   IR1imin_10 = imin;
   IR1xmin_10 = xmin;

clf

%Find RPM
for j = 1:length(Pitot_path)
   k = 1;
   clear t rev
   for i = 1:length(IR1imin_10)
      if IR1imin_10(i,j) > 0
         t(k) = IR1imin_10(i,j);
         k = k+1;
      end
   end

   rev = diff(t);

   %At the bottom of the IR1 signal peaks there is some noise that gives
   %several false minima.  Need to remove these extra signals.
   l = rev < 100;
   t(l==1) = [];

   rev = diff(t);

   X = 1:5000;
   n = hist(rev,X);
```

```
   rpm_data_10(j,:) = n;

   freq(:,j) = Data_coll_10/mean(rev);
   num_revs_10(:,j) = length(rev);
   rev_start_10(:,j) = t(1);
   rev_end_10(:,j) = t(end);
   plot(time_10',IR1_10(:,j)','k')
   hold on
   xlabel('Time (s)')
   ylabel('DAQ Output (Volts)')
   title(['IR Signal at axloc=',num2str(Pitot_path(j)),'m (Wind Speed = 10 m/s)'])
   plot(time_10',q(:,j),'b')
   plot(time_10(t),IR1xmin_10(t,j),'r*')
   hgsave(['Ten mps IR1 Signal ',num2str(j)])
   clf
end

rpm_data_10 = sum(rpm_data_10);
rpm_data_fig(rpm_data_10,10);
hgsave('Ten mps rpm data')

RPM_10 = mean(freq)*60;

TSR_10 = (RPM_10 * pi * 0.928)/(60 * Wind_vel_WT_10);
```

I.10 Calc_Velocity_20000_10000.m

```
%Calculate wind velocities of run from Kiel probe pressure data

load Ampair_20000_10000_10 Press* Data_pts* Air_den* Pitot*

deltaPmm_10 = (Pressure_10 - Press_offset_10)/Press_slope_10;
deltaPmm_av_10 = mean(deltaPmm_10,2); %mean of each axial location column
%Convert mmH2O to Pascal
deltaP_10 = 998*9.81*deltaPmm_10*.001;
deltaP_av_10 = mean(deltaP_10,2);

%Convert pressure to wind velocity m/s
%Note: negative pressures are not valid for pitot-tube theory.  However, to deal with the negative numbers
%they are interpreted as negative velocities.  The negative velocities will be removed by only graphing
%positive values.
for j = 1:length(Pitot_path)
   for i = 1:Data_pts_10
      if deltaP_10(i,j) < 0
         Wind_vel_10(i,j) = -(sqrt(2*abs(deltaP_10(i,j))/Air_den_10));
      else
         Wind_vel_10(i,j) = sqrt(2*deltaP_10(i,j)/Air_den_10);
      end
   end
end

Wind_vel_av_10 = mean(Wind_vel_10);
Wind_vel_av_all_10 = mean(Wind_vel_av_10);
```

I.11 Calc_mean_vel_def3_20000_10000.m

```
% Calculate mean wind speed by discrete integration using areas

load Ampair_20000_10000_3 Pitot*
```

```
% NEED TO FIND PITOT_PATH LOCATION WHERE VELOCITY BEGINS TO RISE
% 10-25 m/s at Pitot_path = 0.4313 (34)
% 5-9 m/s at Pitot_path = 0.4572 (38)
% 4.5 m/s at Pitot_path = 0.4635 (39)
% 4 m/s at Pitot_path = 0.4699 (40)
% 3 m/s at Pitot_path = 0.4765 (41)

% 10m/s
load Ampair_20000_10000_Vel_10 Wind_vel*
clear W
for n = 1:33
   if Wind_vel_av_10(n) < 0
      Wind_vel_av_10(n) = 0;
   end
   W(n) = Wind_vel_av_10(n) * (((Pitot_path(n+1))^2)-((Pitot_path(n))^2));
end

Vel_Def_mean2_20000_10000_10 = sum(W)/(Pitot_path(34)^2);

%% save
save Ampair_20000_10000_mean_vel_area
```

I.12 Calc_mean_vel_def3_20000_10000.m

```
% Calculate mean wind speed with hub wake subtracted by discrete integration using areas

load rel_vel_NR
load rel_vel_all

rel_vel_subNR_20000_10000_15 = (1-rel_vel_NR(:,3)) + rel_vel_20000_10000(:,10);
rel_vel_subNR_20000_10000_15b = (1-rel_vel_NRb(:,3)) + rel_vel_20000_10000b(:,10);

% NEED TO FIND PITOT_PATH LOCATION WHERE VELOCITY BEGINS TO RISE
% 10-25 m/s at Pitot_path = 0.4313 (34)
% 5-9 m/s at Pitot_path = 0.4572 (38)

% 10m/s
clear W
for n = 1:33
   if rel_vel_subNR_20000_10000_10(n) < 0
      rel_vel_subNR_20000_10000_10(n) = 0;
   end
   W(n) = rel_vel_subNR_20000_10000_10(n) * (((Pitot_path(n+1))^2)-((Pitot_path(n))^2));
end

Vel_Def_mean3_20000_10000_10 = sum(W)/(Pitot_path(34)^2);

%% save
save Ampair_20000_10000_mean_subNR_vel_area
```

I.13 Calc_Phase_averages_20000_10000_10.m

```
%Use IR2 data (blade passes)
%Filter data so that the only minima are the voltage spikes.

load Ampair_20000_10000_10 IR2_10 time_10 Pitot_path Data_pts_10 Data_coll_10 Press* Air_den_10
load Ampair_20000_10000_RPM rev* num*
```

```
% 10 m/s
clear imin
clear xmin
clf

r = zeros(Data_pts_10,length(Pitot_path));
for j = 1:length(Pitot_path)
   for i = 1:Data_pts_10
      r(i,j) = IR2_10(i,j);
      if r(i,j) < 4.6
         r(i,j) = IR2_10(i,j);
      else
         r(i,j) = 4.85;
      end
   end
end


%Find minima
[xmin,imin] = minima2(r);
IR2imin_10 = imin;
IR2xmin_10 = xmin;

for j = 1:length(Pitot_path)
   k = 1;
   clear u phase_imin_10 IR2_points_10 num_bp_10 n time_btw*
   clf
   for i = 1:length(IR2imin_10)
      if IR2imin_10(i,j) > 0
         u(k) = IR2imin_10(i,j);
         k = k+1;
      end
   end
   plot(time_10',IR2_10(:,j)','k')
   hold on
   xlabel('Time (s)')
   ylabel('DAQ Output (Volts)')
   title(['IR Signal at axloc=',num2str(Pitot_path(j)),'m (Wind Speed = 10 m/s)'])
   plot(time_10',r(:,j),'b')
   plot(time_10(u), IR2xmin_10(u,j),'r*')
   hgsave(['Ten mps IR2 Signal ',num2str(j)])
   close

   %At the bottom of the IR1 signal peaks there is some noise that gives
   %several false minima.  Need to remove these extra signals.
   faux = diff(u);
   l = faux < 10;
   u(l==1) = [];

   phase_imin_10 = u;
   %Truncate blade passes before start of first complete revolution
   while phase_imin_10(1) < (rev_start_10(j)-5)
      %+5 is to account for small inequalities between IR1 and IR2
      %signals
      phase_imin_10(1) = [];
   end
   %Truncate blade passes after end of last complete revolution
   m = length(phase_imin_10);
```

```
while phase_imin_10(m) > (rev_end_10(j)+5)
   %+5 is to account for small inequalities between IR1 and IR2
   %signals
   phase_imin_10(m) = [];
   m = m-1;
end
IR2_points_10 = diff(phase_imin_10);
num_bp_10 = length(IR2_points_10);

%for some reason there are cases where num_bp does not equal
%6*num_revs.  For these cases this switch is devised to make the number
%of elements match for reshaping into 6 columns
oddness = num_revs_10(j)*6 - num_bp_10;
 if oddness == 0
   time_btw_bp_10 = IR2_points_10/Data_coll_10;
   c = 1;
   for a = 1:num_bp_10/6
      for b = 1:6
         time_btw_bp2_10(a,b) = time_btw_bp_10(c);
         c = c+1;
      end
   end
   time_btw_X_10 = 1:num_bp_10/6;
elseif oddness > 0
   for odd = 1:oddness
      IR2_points_10(end+1) = IR2_points_10(end);
   end
   num_bp_10 = length(IR2_points_10);
   time_btw_bp_10 = IR2_points_10/Data_coll_10;
   c = 1;
   for a = 1:num_bp_10/6
      for b = 1:6
         time_btw_bp2_10(a,b) = time_btw_bp_10(c);
         c = c+1;
      end
   end
   time_btw_X_10 = 1:num_bp_10/6;
else
   for odd = 1:abs(oddness)
      IR2_points_10(end) = [];
   end
   num_bp_10 = length(IR2_points_10);
   time_btw_bp_10 = IR2_points_10/Data_coll_10;
   c = 1;
   for a = 1:num_bp_10/6
      for b = 1:6
         time_btw_bp2_10(a,b) = time_btw_bp_10(c);
         c = c+1;
      end
   end
   time_btw_X_10 = 1:num_bp_10/6;
end

plot(time_btw_X_10,time_btw_bp2_10(:,1),'k')
hold on
plot(time_btw_X_10,time_btw_bp2_10(:,2),'b')
plot(time_btw_X_10,time_btw_bp2_10(:,3),'r')
plot(time_btw_X_10,time_btw_bp2_10(:,4),'m')
```

```
plot(time_btw_X_10,time_btw_bp2_10(:,5),'g')
plot(time_btw_X_10,time_btw_bp2_10(:,6),'c')

xlabel('Revolution Number')
ylabel('Time Between Blade Passes (s)')
title(['Blade Pass Time at Radial Location=',num2str(Pitot_path(j)),' (Wind Speed = 10 m/s)'])
hgsave(['Ten mps BP time ',num2str(j)])
close

%Calculate PDF of number of points per blade pass for this axial
%location
x = 1:500;
n = hist(IR2_points_10,x);
%hist(IR2_points_10,x)
rev_data_10(j,:) = n;
K = find(n==max(n)); %for the case where there are 2 equal cases
most_prob_IR2_points_10(j) = round(mean(K));
%Construct Pressure signal array with equal number of points per blade
%pass based on the most probable number of points
clear E A C
E = zeros(most_prob_IR2_points_10(j)+1,2,num_bp_10);
for d = 1:num_bp_10
   clear B;
   B(1,:) = (0:(60/IR2_points_10(d)):60);
   B(2,:) = (0:(60/IR2_points_10(d)):60);

   A = B';

   e=1;
   for f = phase_imin_10(d):1:(phase_imin_10(d) + IR2_points_10(d))
      A(e,2) = Pressure_10(f,j);
      e = e+1;
   end
   clear D;
   D(1,:) = (0:(60/most_prob_IR2_points_10(j)):60);
   D(2,:) = (0:(60/most_prob_IR2_points_10(j)):60);

   C = D';

   for g = 1:most_prob_IR2_points_10(j)+1
      C(g,2,1) = interp1(A(:,1),A(:,2),C(g,1));
   end

   E(:,:,d) = C(:,:,1);
   %E is a matrix with column 1 as phase angles for one blade pass,
   %column 2 is the interpolated pressures at those angles, and each
   %page is a different blade pass.
   %Press_normalized takes the information from all pages of E and
   %lines them all up in just 2 columns
end
clear Press_normalized_10 deltaPmm_norm_10 deltaP_norm_10

d = 1;
for x = 0:most_prob_IR2_points_10(j):(num_bp_10-1)*most_prob_IR2_points_10(j)
   for y = 1:most_prob_IR2_points_10(j)
      Press_normalized_10((x+y),:) = E(y,:,d);
   end
   d = d+1;
```

```
end

%Convert Pressure DAQ readings to mm H2O
deltaPmm_norm_10 = (Press_normalized_10(:,2) - Press_offset_10)/Press_slope_10;
%Convert mm H2O to Pascal
deltaP_norm_10 = 998*9.81*deltaPmm_norm_10*0.001;
%Convert Pascal to wind speed
clear Wind_vel_norm_10
for z = 1:length(deltaP_norm_10)
   if deltaP_norm_10(z) < 0
      Wind_vel_norm_10(z) = -(sqrt(2*abs(deltaP_norm_10(z))/Air_den_10));
   else
      Wind_vel_norm_10(z) = sqrt(2*deltaP_norm_10(z)/Air_den_10);
   end
end

%Create matrix with each row is a blade pass and each column is a
%specific phase angle.  This matrix represents the current axial
%location (j)
clear Wind_vel_ph_10 phase_extended_10 phase_10 Wind_vel_ph_plot_10
clear Wind_vel_ph_av_10 Wind_vel_ph_av_plot_10

v = 0;
for w = 1:num_bp_10
   for x = 1:most_prob_IR2_points_10(j)
      Wind_vel_ph_10(w,x) = Wind_vel_norm_10(v+x);
   end
   v = v+most_prob_IR2_points_10(j);
end

bp_div_10(j) = 60/most_prob_IR2_points_10(j);
phase_extended_10 = 0:bp_div_10(j):((num_bp_10*60)-bp_div_10(j));
Wind_vel_ph_plot_10 = reshape(Wind_vel_ph_10',1,(most_prob_IR2_points_10(j)*num_bp_10));
fig_Wind_vel_ph_10(phase_extended_10,Wind_vel_ph_plot_10,Pitot_path(j))
hgsave(['Ten mps Vel phase av whole axloc ',num2str(j)])
close
%Average phase angle data over a single revolution
for a = 1:6
   for b = 1:most_prob_IR2_points_10(j)
      c = 1;
      for d = 1:6:(num_bp_10-6)
         value(c) = Wind_vel_ph_10((a+d-1),b);
         c = c+1;
      end
      Wind_vel_ph_av_10(a,b) = mean(value);
      %each row are the values across a 60 degree phase arc, i.e. one
      %blade pass.  Each column is the successive value at each phase
      %division
   end
end
Wind_vel_ph_av_plot_10 = reshape(Wind_vel_ph_av_10',1,(6*most_prob_IR2_points_10(j)));
phase_10 = 0:bp_div_10(j):(360-bp_div_10(j));
clf
fig_Wind_vel_ph_av_10(phase_10,Wind_vel_ph_av_plot_10,Pitot_path(j))
hgsave(['Ten mps Vel phase av one rev axloc ',num2str(j)])
close

%Standardize the length of the phase array
```

```
   Wind_vel_ph_av_plot_10(end+1) = Wind_vel_ph_av_plot_10(1);
   phase_10(end+1) = 360;
   phase_interp_10 = 0:0.2:360;
   Wind_vel_ph_av_interp_10 = interp1(phase_10,Wind_vel_ph_av_plot_10,phase_interp_10);

   %Compile individual locations into a single array
   Wake_10(j,:) = Wind_vel_ph_av_interp_10;
end

rev_data_10 = sum(rev_data_10);
rev_data_fig(rev_data_10,10);
hgsave('Ten mps rev data')
close

L = find(rev_data_10==max(rev_data_10)); %for the case where there are 2 equal cases
most_prob_IR2_points_all_10 = round(mean(L));

Wake_3D_fig(phase_interp_10,Pitot_path,Wake_10)
hgsave('Wake_10_3D_20000_10000')

Wake_2D_fig(phase_interp_10,Wake_10)
hgsave('Wake_10_2D_20000_10000')

% Make a matrix of velocity data at 1 degree intervals
e = 1;
for i = 1:5:length(Wake_10)
   f = 1;
   for j = 1:length(Pitot_path)
      phase_plot_10(e,f) = Wake_10(j,i);
      f = f+1;
   end
   e = e+1;
end
```

I.14 Calc_Ub.m

```
load Ampair_20000_10000_Vel_10 Wind_vel*

Ub_20000_10000_10 = mean(Wind_vel_av_10(55:78));
Ub_factor_20000_10000_10 = Ub_20000_10000_10/Wind_vel_WT_mast_10;
```

Appendix J: Wake Speed Uncertainty

The error involved in measuring wake speed was analyzed. There are two measurements involved to calculate wake wind speed using the Kiel probe. The first is air density using Equation 5. Then Equation 4 can be used to determine wind speed.

J.1 Air Density

Two measurements are involved in calculating air density. The mercury barometer measures atmospheric pressure and air temperature in the wind tunnel is measured with a thermocouple fitted with a digital display. The barometer error, ζ_P, is ±0.2 mm Hg, which corresponds to 26 Pa for this experiment. The thermocouple error, ζ_T, is ±0.05°C. The error involved in measuring air density is defined by Equation J.1. A typical error for air density is ±0.00036 kg/m^3.

$$\zeta_\rho = \sqrt{\left(\frac{d\rho}{dT_{air}}\zeta_T\right)^2 + \left(\frac{d\rho}{dP_{atm}}\zeta_P\right)^2} \quad \text{(Eq. J.1)}$$

J.2 Wind Speed

To calculate wind speed the error from measuring air density (as shown above) and dynamic pressure using the Kiel probe and pressure transducer are required. The sensitivity of the Validyne pressure transducers are listed in Table 2.7. The systematic error of wake wind speed, B_U, is calculated by Equation J.2.

$$B_U = \sqrt{\left(\frac{dU_W}{dP_d}\zeta_{Pd}\right)^2 + \left(\frac{dU_W}{d\rho}\zeta_\rho\right)^2} \quad \text{(Eq. J.2)}$$

There is also error in the average wind speed due to the variations in the signal over the 20,000 sample points. The random uncertainty, P_U, of the signal (using more than 30 measurements) is twice the standard deviation of the measurements. The total error on wake wind speed, ζ_U, is shown is Eq. J.3.

$$\zeta_U = \sqrt{B_U^2 + P_U^2} \quad \text{(Eq. J.3)}$$

The wake speed profiles are plotted with the errors in Figure J.1. The largest component of the error is due to the standard deviation in the Kiel probe signal. This error is an indication of how much turbulence is present. It can be seen that there is high turbulence in the area directly behind the wind turbine hub, and at 20 m/s (45

mph) freestream wind speed. The high errors help to explain the large variations in power at this wind speed.

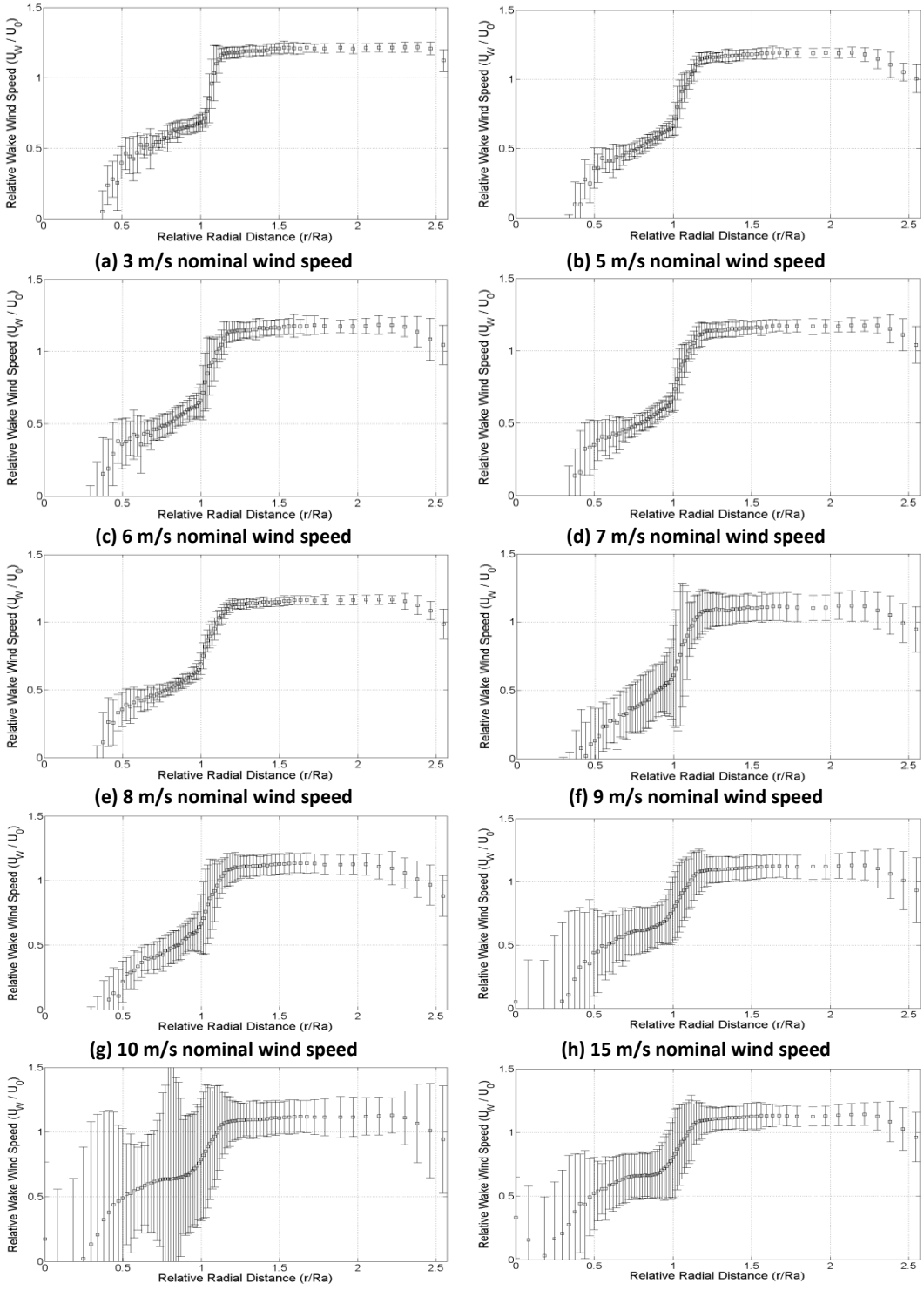

(a) 3 m/s nominal wind speed

(b) 5 m/s nominal wind speed

(c) 6 m/s nominal wind speed

(d) 7 m/s nominal wind speed

(e) 8 m/s nominal wind speed

(f) 9 m/s nominal wind speed

(g) 10 m/s nominal wind speed

(h) 15 m/s nominal wind speed

(i) 20 m/s nominal wind speed

(j) 25 m/s nominal wind speed

Figure J.1 – Wake profiles at various freestream wind speeds showing errors in Kiel probe measurement

Appendix K: Gaussian curves

Wake measurements were done on the wind turbine hub alone (with the rotor blades removed). The wake speed plots of the wind turbine hub are shown in Figure K.1. In the figure, it is shown that the relative velocity deficit (defined in Equation 25) in the wake behind the wind turbine hub can be fit with Gaussian curves. Radial distance from centerline, r, is non-dimensionalized by the rotor radius, Ra. Speed of the wake was recorded all the way to the wind tunnel wall (r/Ra = 2.54) but the figure was truncated at r/Ra =1.0 because there was no significant change in the data in that region besides the effect of the boundary layer. When determining the Gaussian best fit curves, points below r/Ra =0.183 were ignored because they lie directly behind the hub and the turbulent air did not give consistent results. Points above r/Ra =2.13 were also ignored as they showed increasing velocity deficit due to the boundary layer.

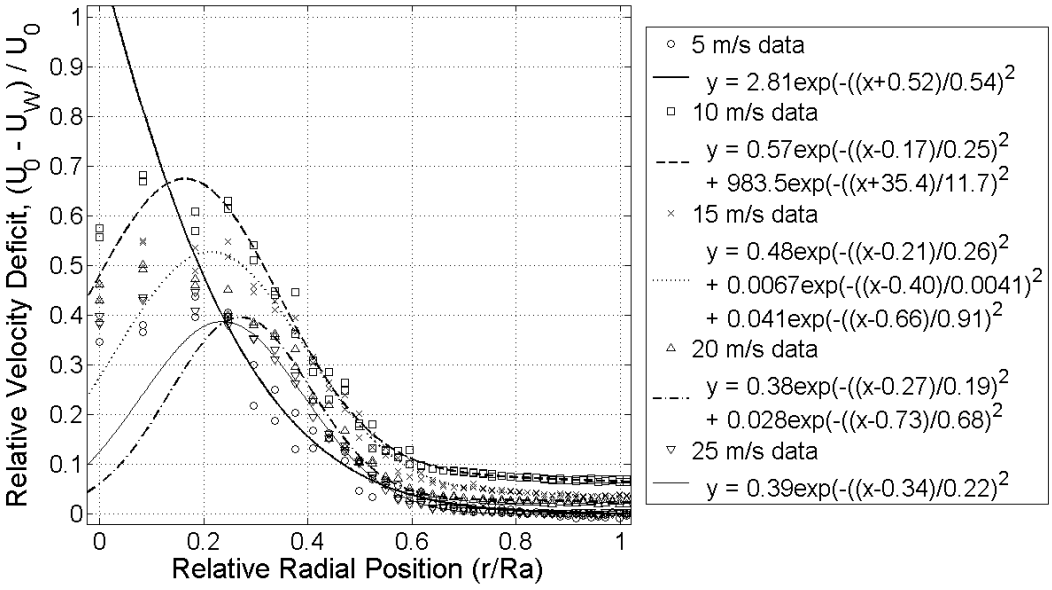

Figure K.1 - Velocity deficit in the wake behind the Ampair 100 hub and mast with no rotor blades installed

Appendix L: Equipment Installation for Laser Light Sheet in Wind Tunnel

The construction drawings for the modifications required to install a laser light sheet through the roof of the wind tunnel, including mounting arrangement of the laser emitter head and mirror, and drawings of laser trap are shown in Figure L.1.

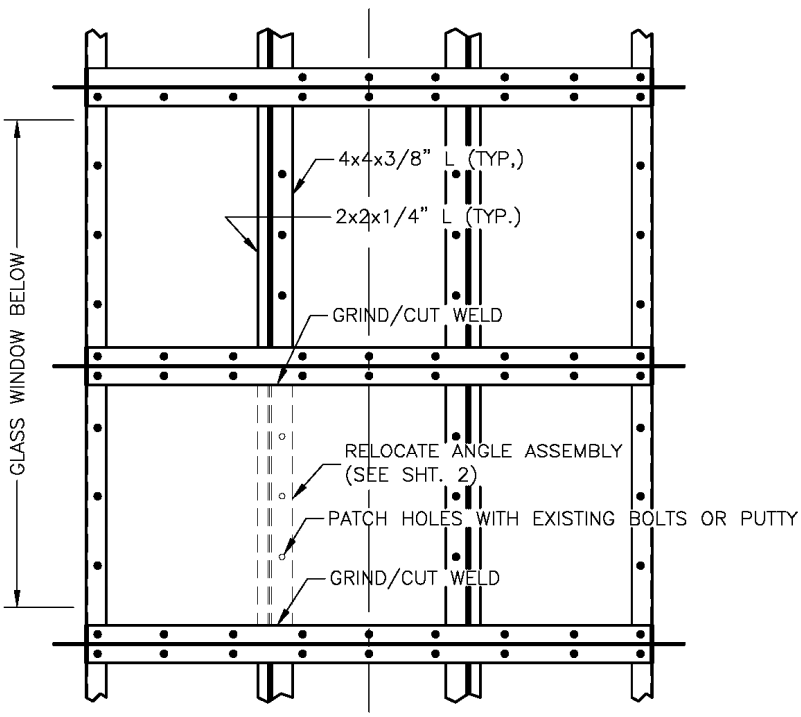

PLAN AT WIND TUNNEL ROOF

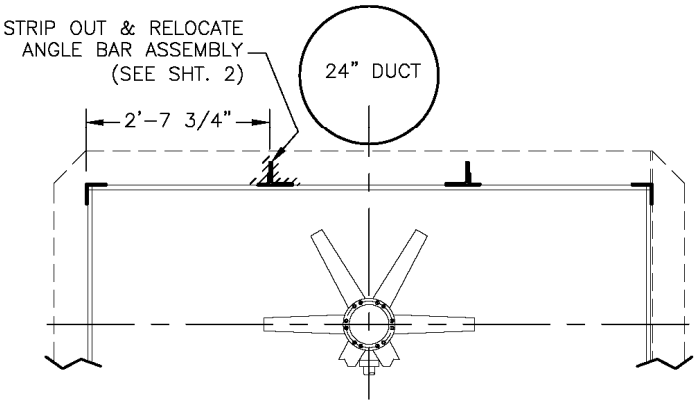

SECTION

LOOKING IN DIRECTION OF WIND

TITLE: WIND TUNNEL STRIP OUT			REV: 1	SHT: 1/13
NAME: G. COMYN	TEL: 492-3706	E-MAIL: gcomyn@ualberta.ca	DATE: 13 JAN 10	
SUPERVISOR: DR. B. FLECK	SPEED CODE: 40490		SCALE: 1/2"=1'=0"	

(a)

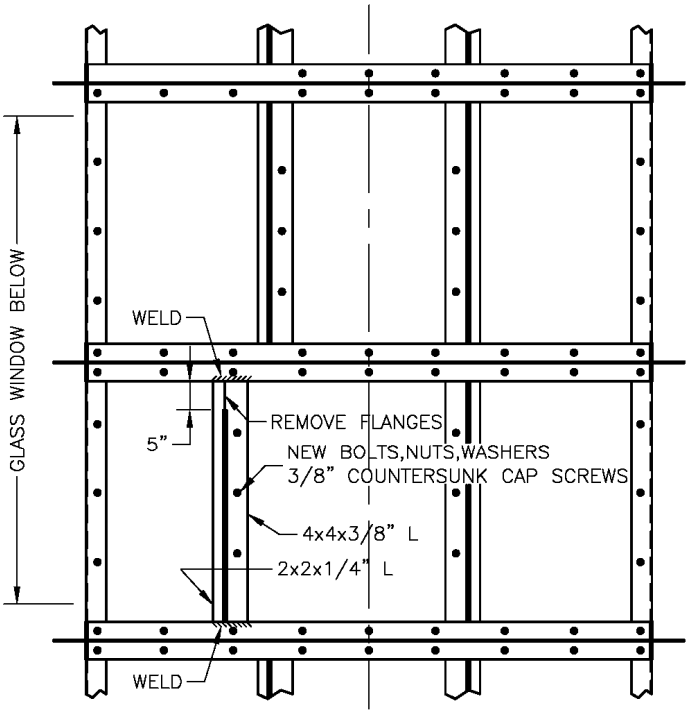

PLAN AT WIND TUNNEL ROOF

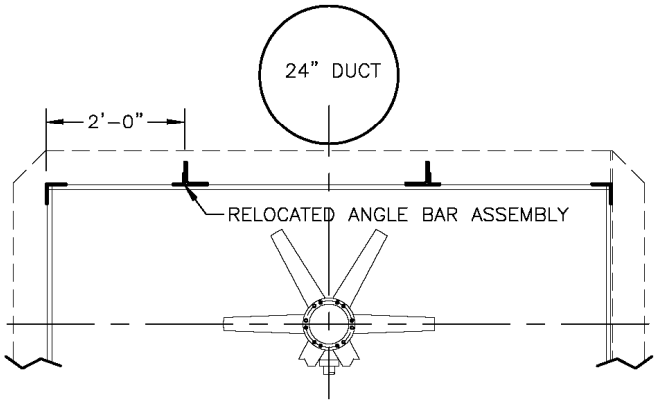

SECTION

LOOKING IN DIRECTION OF WIND

TITLE: WIND TUNNEL STRUCTURAL MODIFICATION			REV: 1	SHT: 2/13
NAME: G. COMYN	TEL: 492-3706	E-MAIL: gcomyn@ualberta.ca	DATE: 13 JAN 10	
SUPERVISOR: DR. B. FLECK	SPEED CODE: 40490		SCALE: 1/2"=1'=0"	

(b)

(c)

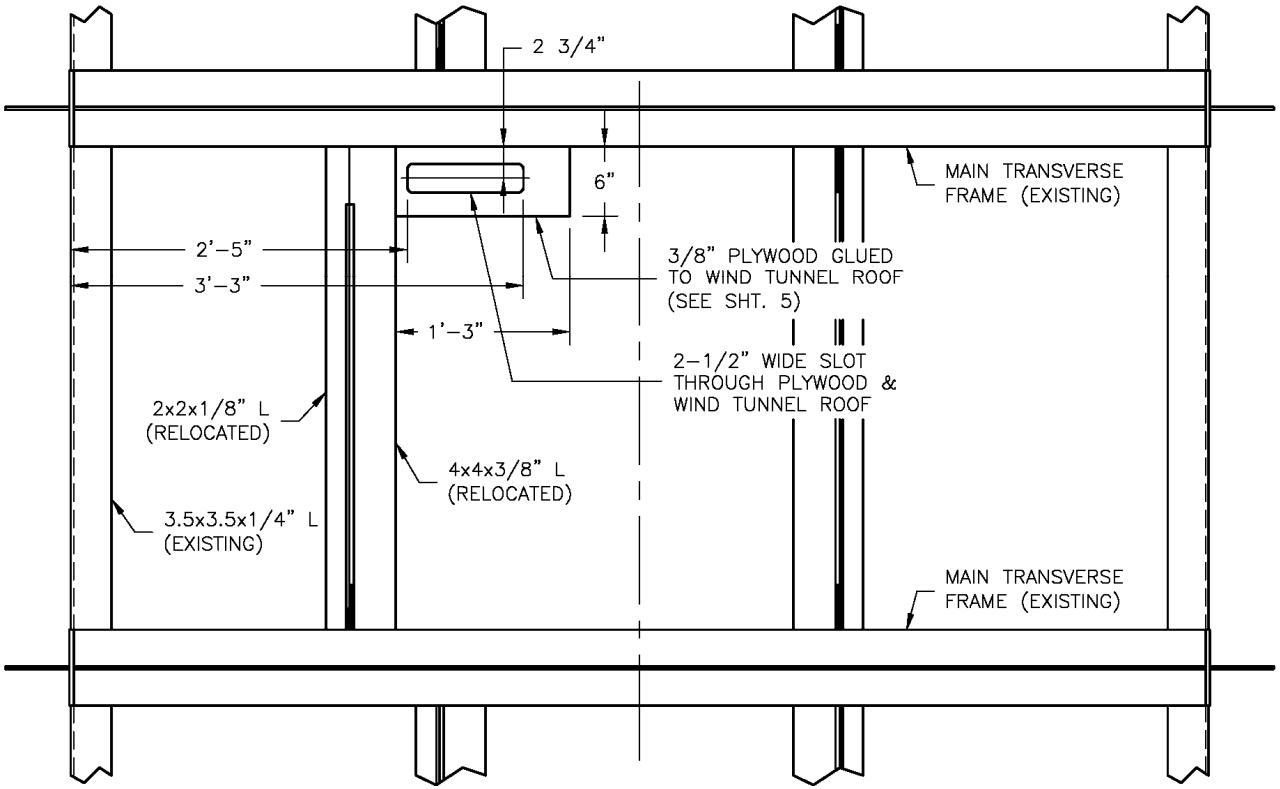

PLAN AT WIND TUNNEL ROOF

TITLE: WIND TUNNEL LASER SLOT			REV: 1	SHT: 3/13
NAME: G. COMYN	TEL: 492–3706	E–MAIL: gcomyn@ualberta.ca	DATE: 13 JAN 10	
SUPERVISOR: DR. B. FLECK	SPEED CODE: 40490		SCALE: 1"=1'=0"	

(d)

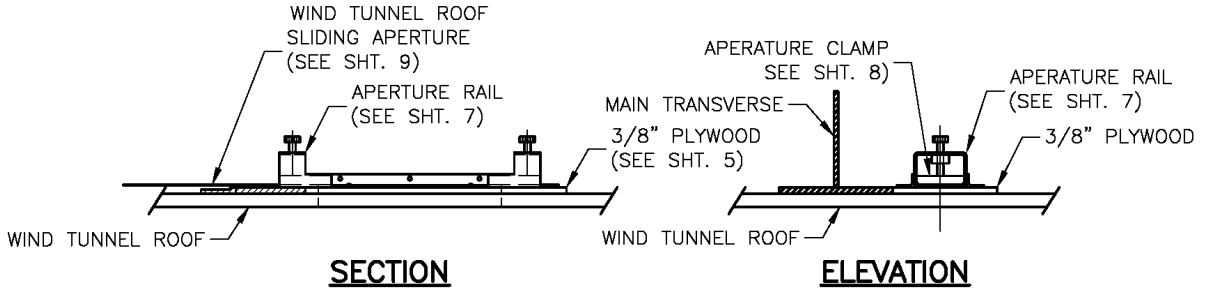

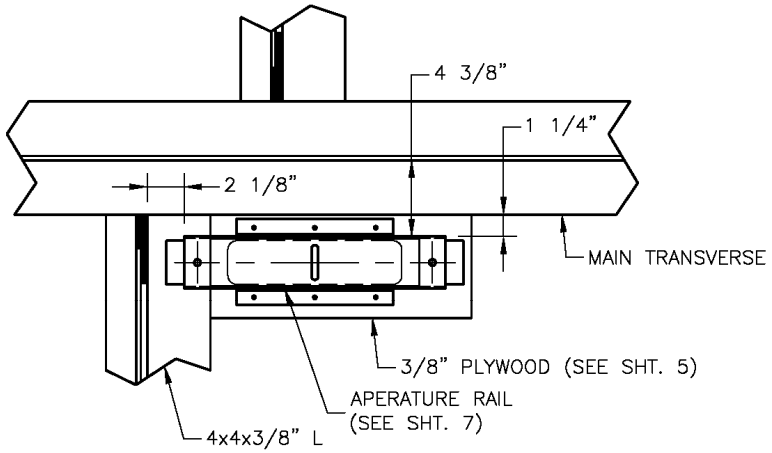

PLAN AT WIND TUNNEL ROOF

TITLE: LASER SLOT ASSEMBLY			REV: 1 / SHT: 4/13
NAME: G. COMYN	TEL: 492-3706	E-MAIL: gcomyn@ualberta.ca	DATE: 13 JAN 10
SUPERVISOR: DR. B. FLECK	SPEED CODE: 40490		SCALE: 1-1/2"=1'=0"

(e)

MATERIAL: 3/8" PLYWOOD
COATING: NONE

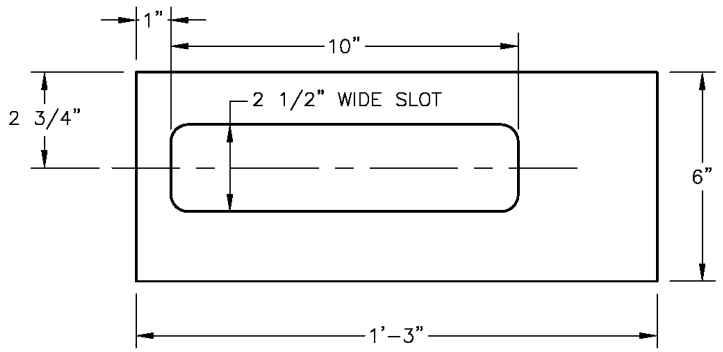

PLAN

TITLE: PLYWOOD MOUNTING BOARD			REV: 1 / SHT: 5/13
NAME: G. COMYN	TEL: 492-3706	E-MAIL: gcomyn@ualberta.ca	DATE: 13 JAN 10
SUPERVISOR: DR. B. FLECK	SPEED CODE: 40490		SCALE: 3"=1'=0"

(f)

MATERIAL: 1x1/2" FLAT BAR, STEEL OR ALUMINUM
COATING: PAINT BLACK

FABRICATE: 2 OFF

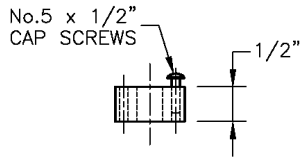

ELEVATION

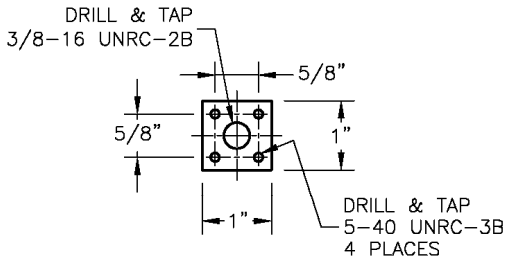

PLAN

TITLE: FIXED NUT			REV: 0 / SHT: 6/13
NAME: G. COMYN	TEL: 492-3706	E-MAIL: gcomyn@ualberta.ca	DATE: 13 JAN 10
SUPERVISOR: DR. B. FLECK	SPEED CODE: 40490		SCALE: 6"=1'=0"

(g)

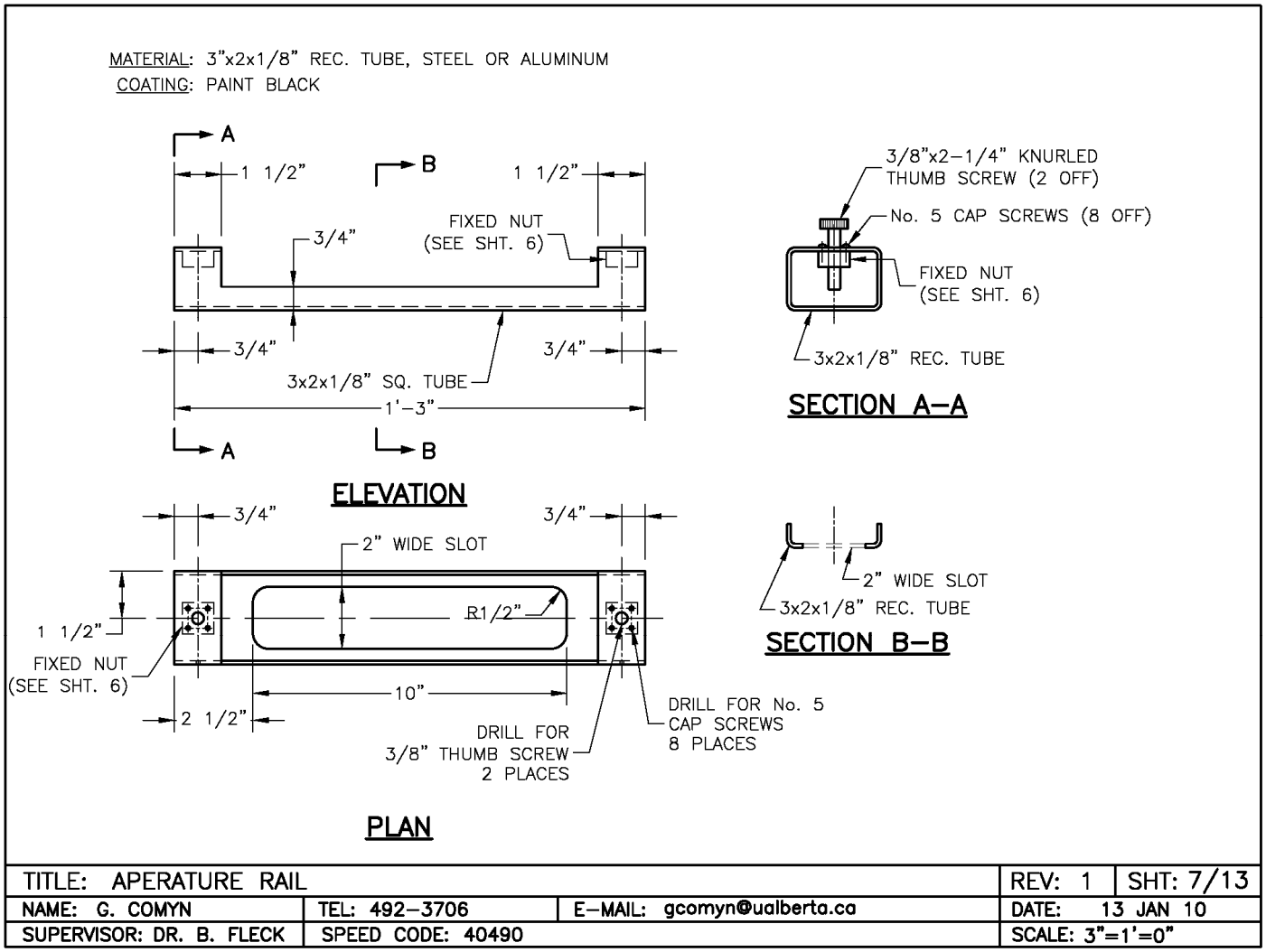

TITLE: APERATURE RAIL			REV: 1 / SHT: 7/13
NAME: G. COMYN	TEL: 492-3706	E-MAIL: gcomyn@ualberta.ca	DATE: 13 JAN 10
SUPERVISOR: DR. B. FLECK	SPEED CODE: 40490		SCALE: 3"=1'=0"

(h)

MATERIAL: STEEL OR ALUMINUM
COATING: PAINT BLACK

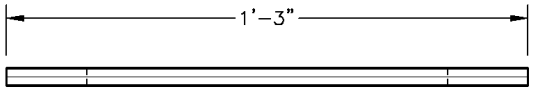

ELEVATION

NOTE: THIS PART SHOULD SLIDE FREELY IN APERTURE RAIL

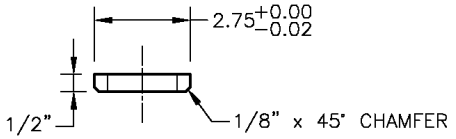

SECTION

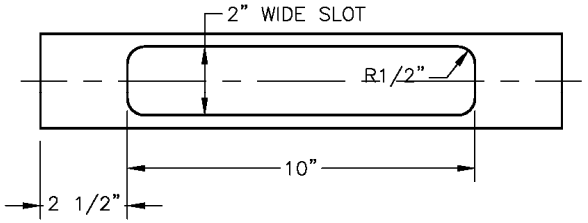

PLAN

TITLE: APERTURE CLAMP			REV: 1 / SHT: 8/13
NAME: G. COMYN	TEL: 492-3706	E-MAIL: gcomyn@ualberta.ca	DATE: 13 JAN 10
SUPERVISOR: DR. B. FLECK	SPEED CODE: 40490		SCALE: 3"=1'=0"

(i)

MATERIAL: 20 GAUGE SHEET STEEL

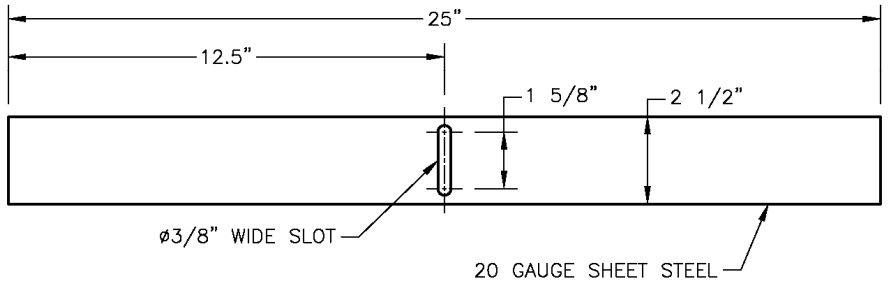

TITLE: SLIDING APERTURE			REV: 1 / SHT: 9/13
NAME: G. COMYN	TEL: 492-3706	E-MAIL: gcomyn@ualberta.ca	DATE: 13 JAN 10
SUPERVISOR: DR. B. FLECK	SPEED CODE: 40490		SCALE: 3"=1'=0"

(j)

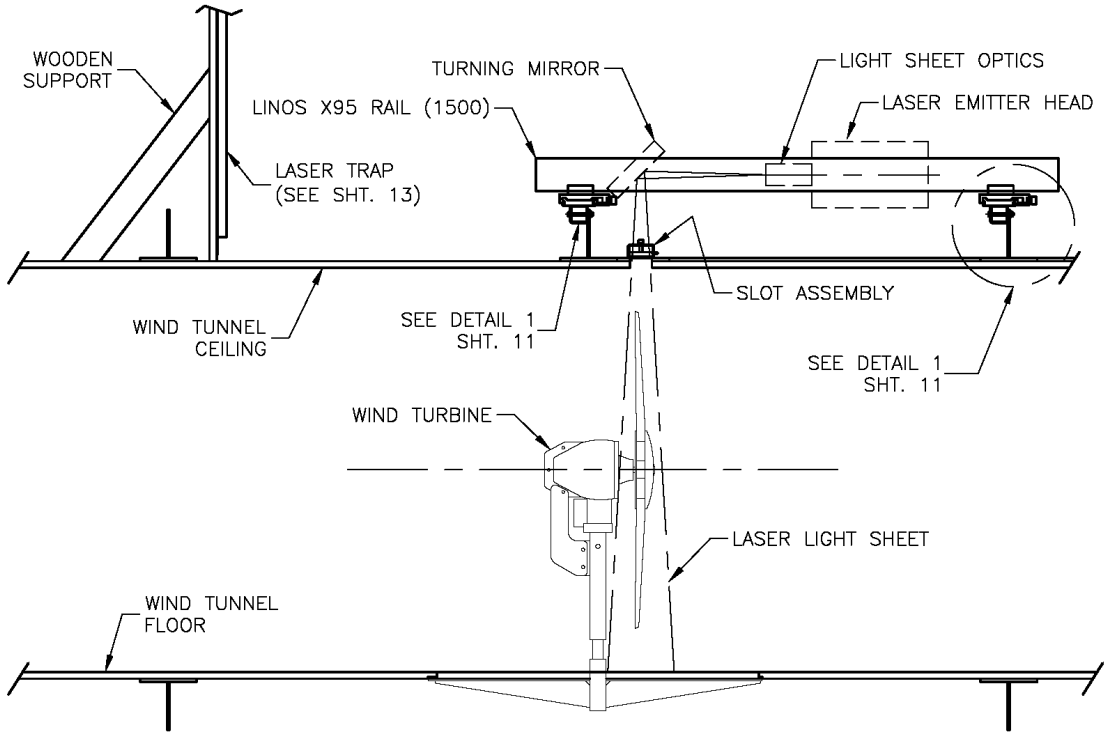

ELEVATION THROUGH WIND TUNNEL

TITLE: OPTICAL SYSTEM ARRANGEMENT			REV: 1	SHT:10/13
NAME: G. COMYN	TEL: 492-3706	E-MAIL: gcomyn@ualberta.ca	DATE: 13 JAN 10	
SUPERVISOR: DR. B. FLECK	SPEED CODE: 40490		SCALE: 3/4"=1'=0"	

(k)

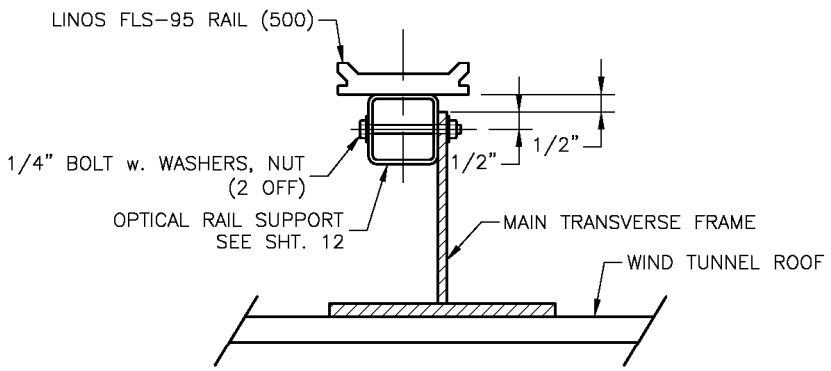

DETAIL 1

TITLE: OPTICAL SYSTEM ARRANGEMENT – DETAIL 1			REV: 1 SHT:11/13
NAME: G. COMYN	TEL: 492–3706	E–MAIL: gcomyn@ualberta.ca	DATE: 13 JAN 10
SUPERVISOR: DR. B. FLECK	SPEED CODE: 40490		SCALE: 3"=1'=0"

(I)

MATERIAL: 2x2x1/8" SQUARE TUBE, STEEL OR ALUMINUM
COATING: PAINT BLACK
FABRICATE: 2 OFF

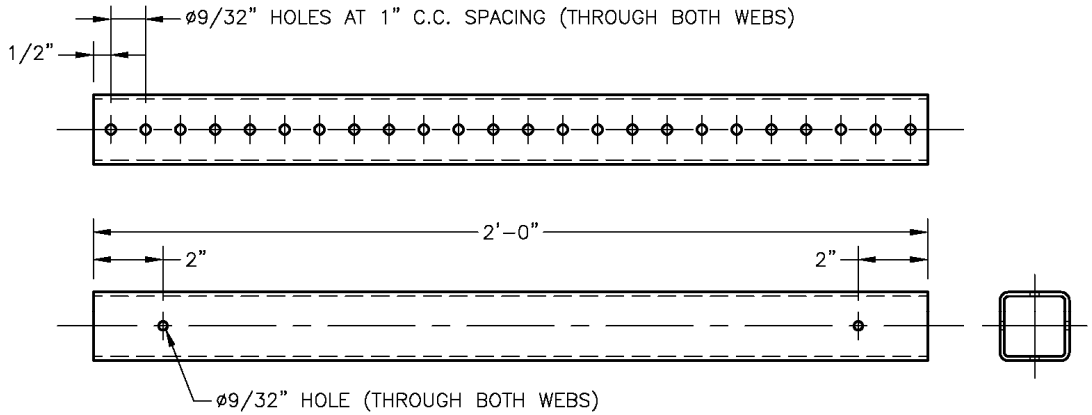

TITLE: OPTICAL RAIL SUPPORT			REV: 1	SHT:12/13
NAME: G. COMYN	TEL: 492-3706	E-MAIL: gcomyn@ualberta.ca	DATE: 12 JAN 10	
SUPERVISOR: DR. B. FLECK	SPEED CODE: 40490		SCALE: 3"=1'=0"	

(m)

MATERIAL: ø3/4" SCH. 5 PIPE (STEEL OR ALUMINUM) OR SIMILAR
1–1/4" x 1/8" FLAT BAR (STEEL OR ALUMINUM)
COATING: PAINT BLACK

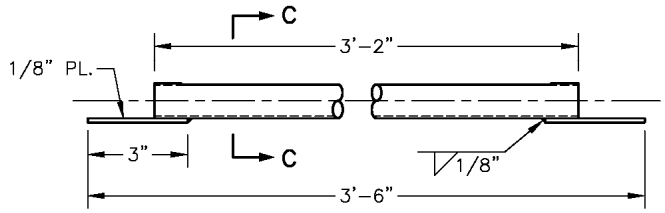

ELEVATION

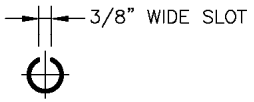

SECTION C–C

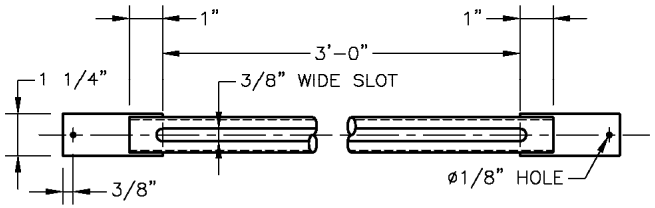

PLAN

TITLE: LASER TRAP			REV: 1 SHT:13/13
NAME: G. COMYN	TEL: 492–3706	E–MAIL: gcomyn@ualberta.ca	DATE: 13 JAN 10
SUPERVISOR: DR. B. FLECK	SPEED CODE: 40490		SCALE: 3"=1'=0"

Figure L.1 – Construction drawings for PIV optical arrangement and wind tunnel modifications

Appendix M: Method of Unwanted Image Removal from Water Droplet Tracking Data Sets

During the experiment in which water droplets were sprayed at the rotor, it was found that the rotor speed was decreasing and uneven over time. This resulted in a shifting position of the blade in the camera field of view. In order to improve the average vector field of the data set, it was necessary to determine an average position of the blade. This average position was used to define the stationary mask that would be applied to all images during the preprocessing phase. Images in which the blade position was 4 mm above or below this average value were discarded from the data set.

To determine the average position of the blade, the commercial software package was used to produce an average image of all the raw images. Laser reflection from the light sheet produced an area of high intensity at the blade leading edge that was used as the reference point. In the average image this reference point had the highest intensity in the position where the blade was most common. The blade was generally continually slowing down throughout the experiment (blade position was moving down in the field of view) so the upper edge of the range of maximum intensity was used in order to include more images. An example of the average image of a data set and location of average position is shown in Figure M.1.

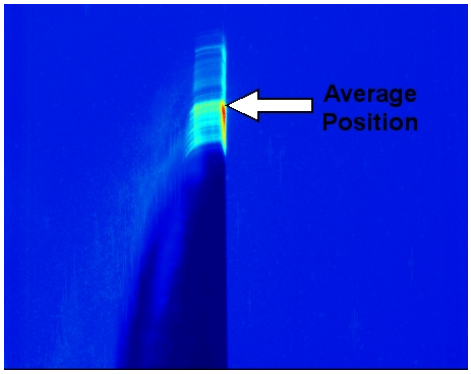

Figure M.1 - Average position of blade leading edge defined

The positions of the leading edge of the blade were recorded for each data set and are shown in Figure M.2. The vertical dimension of the field of view (FOV) ranged from -32.562 to 38.125 mm and the leading edge fell somewhere in this range. If the blade was not in the image, the figure does not display a value for that image. The dashed line in Figure M.2 represents the average position of the leading edge as defined by Figure M.1. The dash-dot lines in Figure M.2 represent the upper and lower ranges beyond which the images were discarded from the data set (±4 mm).

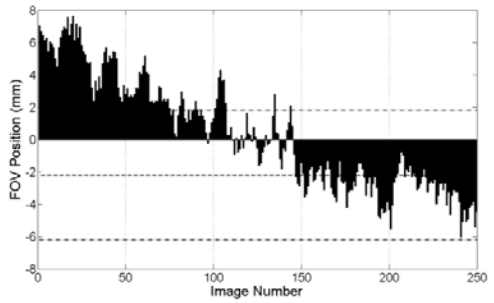

(a) 5 m/s nominal windn speed, trial A

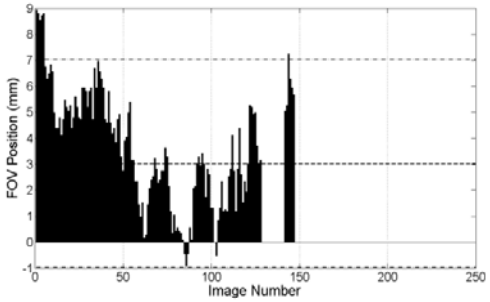

(b) 5 m/s nominal wind speed, trial B

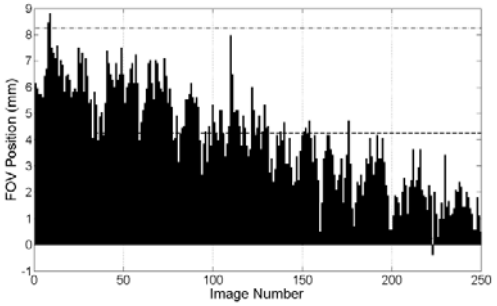

(c) 6 m/s nominal wind speed, trial A

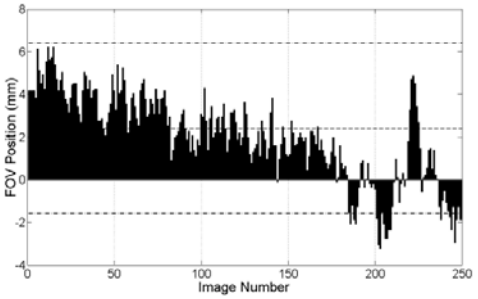

(d) 6 m/s nominal wind speed, trial B

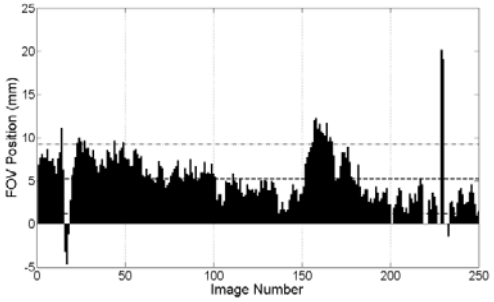

(e) 8 m/s nominal wind speed, trial A

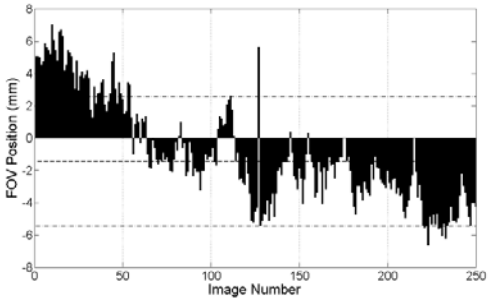

(f) 8 m/s nominal wind speed, trial B

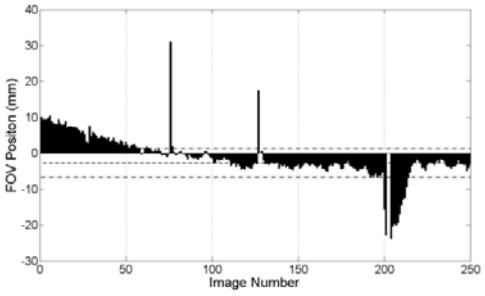

(g) 10 m/s nominal wind speed, trial A

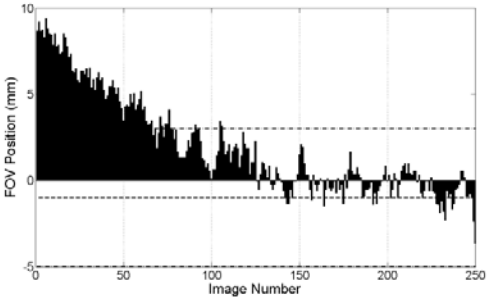

(h) 10 m/s nominal wind speed, trial B

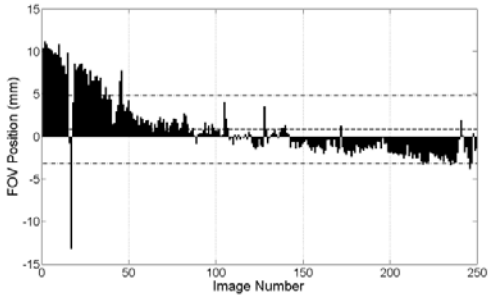

(i) 15 m/s nominal wind speed, trial A

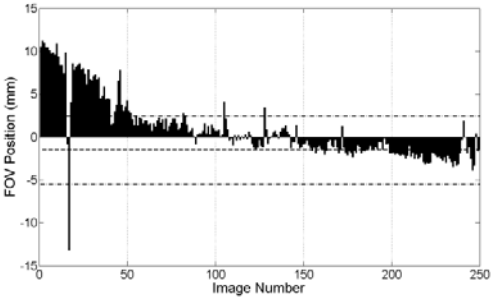

(j) 15 m/s nominal wind speed, trial B

Figure M.2 – Vertical position of blade leading edge in images. Images in which leading edge falls outside range of average position were removed from data set.